SAPIENZA
UNIVERSITÀ DI ROMA

Modeling and control of multibody flexible systems with application in complex space mission scenarios

David Paolo Madonna
Department of Mechanical and Aerospace Engineering
Sapienza University of Rome

Advisor:
Prof. Paolo Gasbarri

Co-Advisor:
Prof. Mauro Pontani

A dissertation submitted in fulfillment of the requirements for the degree of
Doctor of Philosophy in Aeronautical and Space Engineering

XXXVII Cycle
2022-2025

Contents

List of figures

List of tables

Introduction

Context and motivation of the work

In recent years, the field of space engineering has undergone significant evolution, with an increasing number of complex missions being designed and launched [1-5]. As space activities expand beyond traditional Earth-orbit applications toward more ambitious scenarios, spacecraft are becoming progressively more sophisticated and articulated. In many cases, these systems can no longer be modeled as simple rigid bodies but must instead be treated as multibody systems composed of multiple interconnected components, some of which exhibit significant structural flexibility. This trend is largely driven by the demand for deployable structures such as large-aperture antennas [6] – enabling high-performance Earth observation, deep-space astronomy, and telecommunications – together with solar panels [7], telescopic booms and robotic manipulators. These types of structures exhibit elastic behavior and require accurate modeling of their flexibility to predict deformations during deployment operations or reorientation maneuvers. Moreover, robotic arms and manipulators used for on-orbit servicing or assembly introduce additional complexity into the spacecraft architecture [8]. While these elements greatly expand mission capabilities, the evolution of space operations brings new challenges: elastic deformations can couple with the spacecraft attitude dynamics and the motion of appendages, degrading pointing accuracy, interfering with sensitive payload operations, compromising the performance of docking or assembly activities, and even threatening the structural integrity of the spacecraft itself.

An iconic example of a new-generation satellite that presents notable design challenges due to its unique configuration is the driving force behind this PhD project. In fact, this work was developed within the framework of an industrial collaboration with Thales Alenia Space Italia (TAS-I), responding to concrete industrial needs – specifically, the challenges posed by the CIMR (Copernicus Imaging Microwave Radiometer) mission, an ESA Earth Observation program dedicated to Arctic monitoring [10-12]. CIMR is an ambitious project featuring a satellite equipped with a large, rotating, and flexible antenna, a novel and demanding configuration compared to conventional Earth observation satellites. The presence of this large, rotating elastic appendage introduces significant challenges, requiring careful assessment of both payload behavior and the overall satellite dynamics [12]. These difficulties are further compounded by the innovative nature of this spacecraft configuration: among previously launched satellites, only the SMAP mission employs a similar architecture, though with a considerably smaller payload than that of CIMR [5]. Consequently, there arose a clear need for advanced modeling capabilities to analyze and manage these complex dynamic phenomena.

To address these challenges, the accurate modeling of flexible multibody dynamics is essential for both mission success and operational safety. High-fidelity models allow for the prediction of critical dynamic interactions, including the effects of structural flexibility on attitude and orbit control, as well as interactions between components during operations such as deployment or robotic manipulation. In addition, advanced guidance and control strategies are required to effectively manage the complex behavior encountered in modern space missions. In particular, attitude control and relative motion control during proximity operations are closely linked to the dynamic characteristics of flexible multibody satellites. This is especially true in applications such as on-orbit servicing or debris removal, where precise control is critical to ensure safe and efficient mission execution [13]. All these factors play an increasingly important role in both current and future space missions. They demand rigorous and comprehensive dynamic analysis, along with the development of advanced control techniques capable of addressing the challenges presented by diverse and evolving mission scenarios.

State of the art and thesis objectives

The objectives of this PhD work are closely linked to the challenges introduced by recent technological advancements in the space sector. By combining high-fidelity modeling techniques with efficient control strategies, the thesis aims to enable the simulation of complex space mission scenarios that address the emerging demands of the evolving space environment.

Modeling – On the modeling side, the goal is to develop a comprehensive capability for accurately representing multibody spacecraft, particularly those with flexible components and complex architectures.

The challenge of modeling multibody systems lies in describing the kinematics and dynamics of interconnected rigid or flexible bodies efficiently. Several approaches exist for formulating equations of motion, all with their own strengths and weaknesses [14]. Aerospace multibody dynamics has traditionally relied on three main families of methods: the Newton\Euler method, the Lagrangian formulations – whether embedded (minimal coordinates) or augmented (with multipliers) –, and Kane's method, all providing different ways to describe system dynamics [15, 16].

The Newton\Euler method, based on Newton's second law and Euler's rotational equations, results in a formulation that explicitly incorporates constraint forces. However, a fundamental computational drawback of this method is that it leads to a system of Differential Algebraic Equations (DAEs), requiring the inclusion of constraint equations alongside the system's dynamic equations. This increases computational complexity and can lead to numerical difficulties.

The Lagrange approach derives the dynamic equations by applying the Hamilton principle to the Lagrange function and expresses the system dynamics in terms of generalized coordinates [17]. The embedded Lagrange method minimizes the number of equations by reducing the system to a minimal set of Ordinary Differential Equations (ODEs), leading to faster computations [18]. However, despite this advantage, deriving the equations is less intuitive than in the Newton\Euler method and requires significant algebraic effort, especially for complex systems. In contrast, the augmented Lagrange formulation reintroduces additional equations to enforce constraints using Lagrange multipliers, resulting in a larger system of DAEs with the associated computational challenges. Although the introduction of multipliers can lead to numerical instability issues [19], this approach is systematically applicable and is widely adopted in commercial software.

Kane's method emerges as the optimal synthesis of these approaches [20]. It retains the intuitive equation derivation of Newton\Euler while achieving the computational efficiency of the embedded Lagrange formulation [21]. In fact, the dynamic equations are directly derived from the projection of Newton\Euler equations (excluding constraints) through the Kane's Jacobian. Moreover, by utilizing generalized speeds, Kane's method avoids the explicit inclusion of constraint forces while maintaining a minimal set of ODEs [22]. This results in a highly effective formulation, providing a computationally efficient framework for multibody dynamics analysis.

Building on this formulation, the thesis develops a versatile and systematic modeling capability able to handle spacecraft composed of both rigid and flexible bodies, across a wide range of configurations and interconnections. The primary objective is to establish a consistent and general framework that can accommodate the broadest possible variety of satellite architectures. Recent research – most notably from the Autonomous Vehicles Systems (AVS) Laboratory led by Hanspeter Schaub – has explored Kane's approach for spacecraft multibody dynamics, with emphasis on robotic manipulation and rendezvous [22, 23]. However, much of this literature treats predominantly rigid-body representations and relatively simple kinematic topologies. The present dissertation addresses these limitations by systematically extending Kane's method to include:

1. Flexible appendages, allowing accurate representation of structural elasticity and stress-stiffening phenomena. The approach remains strongly focused on the specific requirements of space applications. For example, it examines the interaction between gravitational forces and structural flexibility in flexible spacecraft, and incorporates modeling features required by the CIMR satellite, such as the evaluation of stiffness variations in the rotating antenna [25].

2. Closed-loop kinematic chains, which cannot be represented by tree-like topologies without additional treatment [26].

3. Other fundamental physical couplings, such as propellant sloshing via a sliding-particle representation [27].

4. Additional modeling and analysis features, as the derivation of constraint reactions, the implementation of kinematic laws, and the evaluation of both total momenta and center-of-mass motion. Unlike the standard literature, where these aspects are rarely presented together under a unified formulation, this work consolidates them in a coherent framework. This not only broadens the modeling possibilities for spacecraft dynamics but also provides a more systematic and versatile foundation for analysis, thereby enhancing the applicability of Kane's method to complex mission scenarios.

Control – On the control side, this thesis addresses both attitude and relative motion control. In both cases, nonlinear strategies based on feedback linearization are adopted. In fact, given the inherent nonlinearities present in spacecraft dynamics, particularly in attitude and orbital motion, nonlinear control methods can provide superior performance compared to classical linear control laws, as long as state estimation is sufficiently accurate [28].

For the attitude control problem, both triaxial and single-axis control strategies are investigated. The latter is typically employed when there is no requirement to align the remaining two axes of the spacecraft with specific directions, beyond the one already being controlled. As a result, single-axis maneuvers involve a shorter angular path compared to their triaxial counterparts, which translates into faster convergence when the same control effort is applied [29]. Nonlinear attitude control laws are typically presented together with a stability analysis, which is essential to establish their general validity. However, the maneuver performance is usually determined solely by the choice of control gains. In contrast, the objective of this work is to design nonlinear feedback control laws by directly modifying the structure of the error-dependent terms, thereby making more effective use of the available actuators. This approach enables faster convergence and improved overall performance compared to established benchmarks in the literature, for both triaxial and single-axis control scenarios. [30]. The proposed control laws are introduced together with their stability analysis, carried out using Lyapunov's theorem and LaSalle's invariance principle, which establish global asymptotic stability with respect to the desired state. Furthermore, the enhanced performance of attitude maneuvers achieved under these new laws is demonstrated through a comparison with the results obtained using current state-of-the-art solutions [31].

The control architecture is still based on feedback linearization even in the context of relative motion. In fact, the relative motion dynamics is strongly affected by nonlinearities in a wide variety of orbital configurations, except for nearly circular, quasi equatorial and low-perturbed orbits, where linearity assumption can be considered sufficiently representative [32, 33]. In contrast, feedback linearization can handle more complex scenarios, provided it relies on a high-fidelity dynamic model. The formulation of relative motion presented in this work allows the derivation of a chaser's trajectory relative to a target, even when both are on perturbed orbits. This represents a significant advancement over the standard Battin-Giorgi approach, which requires the target to follow a Keplerian orbit [34]. Specifically, the proposed method improves the numerical accuracy of relative motion computations. Building on this improved formulation, a novel feedback control law is introduced, denoted as Hybrid Predictive Control (HPC). Similar to the attitude control case, the goal of HPC is to enhance maneuver performance while accounting for actuator limitations. However, unlike the attitude control scenario, the relative motion problem features an unbounded state vector, which makes it more challenging to modify the structure of the error-dependent terms. Consequently, the HPC approach relies on a opportunely designed adaptive logic combined with a predictive strategy, which will be described in detail. Finally, the performance of the HPC law is extensively evaluated and compared to that of the classical feedback linearization controller, demonstrating significant improvement of the maneuvers performance.

Integration and validation – A major contribution of this work is the development of integrated applications that combine all the modeling and control techniques presented. The ultimate objective of the thesis is precisely this: to enable high-fidelity dynamic simulations of realistic and complex space missions that represent the future of the space sector. The five applications discussed in this work are representative of advanced space missions aligned with the new frontiers of space utilization and exploration. These scenarios demand advanced modeling and control capabilities to address their inherent dynamic complexities. In all these applications, the techniques developed in this thesis – both in flexible multibody modeling and in advanced nonlinear control – are systematically applied, demonstrating their effectiveness and their ability to be integrated into comprehensive simulation frameworks for complex space mission scenarios.

From an industrial perspective, beyond the developments specific to the CIMR mission, another key objective of this work is to provide a software tool capable of supporting dynamic analysis for a wide range of multibody spacecraft scenarios. The tool enables the automatic generation of dynamic models for any satellite configuration, directly within its operational environment, including orbital dynamics. This capability eliminates the need to rewrite dedicated code for each new scenario and allows even non-expert users to perform advanced simulations with ease. Moreover, the tool is designed to be more space-focused than general-purpose commercial software, offering better handling of space-specific issues such as orbit propagation. In general, the availability of in-house software simplifies the analysis process, as it is tailored to perfectly meet the user's needs, provides full understanding and transparency of the code, and avoids the need for complex co-simulation with external tools.

Thesis structure

This thesis is organized as follows. Chapter 1 presents a recursive and general formulation based on Kane's method to derive the dynamical equations of a multibody rigid spacecraft in an open-loop configuration. The application of constraints is then discussed, enabling the modeling of closed-loop configurations and complex dynamic phenomena such as fuel sloshing. Finally, the application of Kane's equations to space manipulator systems is examined; within this framework, a strategy for modeling a manipulator capturing another articulated body is introduced. Chapter 2 extends the results of the first chapter to the case of elastic bodies. In this context, the use of two different bases to represent elasticity – modal basis and finite element method (FEM) basis [35] – is explored. The possibility of treating a series of interconnected elastic bodies as a single elastic body within the elastic equations, while maintaining them as separate bodies in the rigid motion equations to simplify the dynamics, is also discussed. The chapter then presents an accurate modeling of the gravity-elasticity interaction and concludes with an analysis of the stress stiffening phenomenon. Chapter 3 focuses on nonlinear control techniques. It begins with attitude control, proposing new nonlinear control laws with their stability analysis for both triaxial and reduced-attitude reorientation cases. The performance of these laws is compared to existing ones from the literature, demonstrating their advantages. In this context, steering laws for control momentum exchange devices are also presented. The chapter then addresses relative orbit control, first introducing an advanced version of the Battin-Giorgi formulation [36], followed by a new feedback linearization-based relative motion control law called Hybrid Predictive Control, whose performance is evaluated in detail. Chapter 4 presents five applications that integrate the modeling and control techniques introduced in the previous chapters. These applications include:

- A space manipulator system performing the capture and de-spinning of a rotating, uncooperative target.
- A large flexible satellite executing tracking and collision avoidance maneuvers in a debris-dense environment.
- The CIMR satellite in its operational scenarios, with detailed analyses of structural deformations and stress stiffening effects.
- A large space infrastructure concept for future use, such as a modular space station equipped with telescopic booms.
- Proximity operations in cislunar space involving the future Gateway station.

Finally, an overview of the multibody simulation tool developed for Thales Alenia Space Italia is reported in the Appendix. It outlines the tool modeling capabilities, explains the multibody structure assembly logic, reviews the current state of the user interface, and presents an example application.

Original contribution of the Dissertation

The main original contributions of this Ph.D. work can be summarized as follows:

- **Application of Kane's method to flexible spacecraft modeling:** Development of a unified recursive formulation for multibody systems including flexible components, enabling the accurate modeling of elasticity (including stress stiffening phenomenon), and gravitational coupling effects in space dynamics. On this aspect, the detailed expression of gravitational terms are derived, removing the usual approximation of considering the gravitational action as concentrated in the center of mass of the bodies composing the spacecraft and adding the terms related to deformation to the gravity gradient torque. Moreover, the multibody formulation is reported in an explicit matrix form that facilitates the software implementation, and it is presented together with a set of modeling and analysis features that broaden its applicability to complex mission scenarios.

- **Inclusion of constraints:** Adaptation of Kane's equations to the presence of constraints. A modern approach from literature and based on Kane's methodology is applied to constrained spacecraft and compared to the classic Lagrange's multipliers approach. In this framework, two specific cases of interest are analyzed: (a) spacecraft configurations that cannot be represented by tree structures, thus extending the applicability of the method to articulated systems with closed kinematic loops, and (b) propellant sloshing effects that are captured through a contained-particle approach. Everything is made within the same dynamical formulation, preserving consistency across rigid, flexible, and fluid-coupled dynamics.

- **Advanced control strategies for nonlinear spacecraft dynamics:** Design and analysis of novel nonlinear feedback laws for spacecraft attitude and relative orbital motion, aimed at achieving faster convergence rates and higher actuator efficiency compared to classical approaches. On the attitude control side, both triaxial and single-axis control laws are developed by modifying the structure of the error-dependent terms. The stability of the proposed controllers is rigorously established through Lyapunov's theorem and LaSalle's invariance principle. Their superior performance is further demonstrated through an extensive set of numerical simulations. For the relative motion problem, an advancement of the nonlinear Battin-Giorgi formulation is introduced, enabling the representation of a chaser spacecraft dynamics relative to a target on a perturbed orbit (in contrast to the standard Keplerian assumption). Building on this framework, a new Hybrid Predictive Control (HPC) law is proposed. The effectiveness of the HPC law is validated by comparing its performance against a state-of-the-art maneuvering strategy, showing clear improvements in efficiency and accuracy.

- **End-to-end validation through realistic mission scenarios:** Application of the developed modeling and control techniques to five representative case studies, including the CIMR satellite, robotic capture of rotating debris, and deployable flexible structures. The modeling capabilities developed and presented in this work are applied to obtain reliable numerical simulations, enabling an accurate evaluation of the spacecraft dynamics along the various missions phases. In addition, the enhanced control techniques ensure an efficient use of the available actuation capacity of the satellites involved in the considered missions. Overall, these applications not only demonstrate the effectiveness of the proposed methods in scenarios of direct industrial and scientific relevance, but also provide valuable insights into spacecraft dynamics and control in next-generation mission scenarios, which are of growing importance in the current space environment.

- **Development of a generalized simulation tool:** Implementation of an in-house multibody simulation software tailored to space applications, capable of automatically generating dynamic models for complex spacecraft architectures, including orbital dynamics, and validated against commercial benchmarks.

Chapter 1

Kane’s dynamic equations for rigid multibody space applications

This chapter combines a review of Kane’s classical theory with original extensions specifically tailored to rigid multibody spacecraft dynamics. The general derivation of Kane’s equations and the recursive formulation for tree-topology systems follow the established literature, but all the kinematic and dynamic quantities are written in a matrix form where the reference frames are explicitly indicated, in order to facilitate the numerical implementation. Moreover, the Chapter collects a series of features that are particularly useful for the spacecraft dynamic analysis, such as the computation of linear and angular momenta and the motion of the center of mass, the computation of constraint reactions and the imposition of kinematic laws. Although these aspects are present separately in the literature, it is not common to find a text containing all of them in the context of a spacecraft-focused Kane-based multibody formulation. Moreover, particular emphasis is placed on novel adaptations developed by the author to address space-relevant scenarios such as closed-chain kinematic configurations, sloshing phenomena, and transient capture dynamics in robotic applications.

1.1. Vector notation

As a preliminary step, the notation used in this work to represent vectors is introduced. Specifically, the following relation holds:

$$\underset{\rightarrow}{\mathrm{x}} = \underline{\underline{\mathrm{A}}}\,\underline{\mathrm{x}}^{(\mathrm{A})} \tag{1.1}$$

where a physical vector $\underset{\rightarrow}{x}$ is expressed as the matrix multiplication of vectrix $\underline{\underline{\mathrm{A}}} = \begin{bmatrix} \hat{\mathrm{a}}_1 & \hat{\mathrm{a}}_2 & \hat{\mathrm{a}}_3 \end{bmatrix}$ and the 3x1 (component) column vector $\underline{\mathrm{x}}^{(\mathrm{A})} = \begin{bmatrix} \mathrm{x}_1^{(\mathrm{A})} & \mathrm{x}_2^{(\mathrm{A})} & \mathrm{x}_3^{(\mathrm{A})} \end{bmatrix}^{\mathrm{T}}$. Therefore, the vectrix embodies the set of right-handed unit vectors (i.e. the basis) used to express vector components. Physical unit vectors are denoted with superscript “ $\widehat{\ }$ ”. An analogous relation also exists for dyadics and 3x3 (component) matrices. Specifically, the following relation holds:

$$\underset{\rightarrow}{D} = \underline{\underline{A}}\, D^{(A)} \underline{\underline{A}}^T \tag{1.2}$$

where $\underset{\rightarrow}{D}$ is the dyadic, while $D^{(A)}$ is the 3x3 matrix obtained from the projection of the dyadic along vectrix $\underline{\underline{A}}$. Superscripts for 3x1 vectors and 3x3 matrices will be omitted when they are preceded by vectrices, to avoid redundancy in notation. Since vectrices represent reference frames, it is possible to define the rotation matrix from reference frame $\underline{\underline{A}}$ to reference frame $\underline{\underline{B}}$ as

$$\underset{B\leftarrow A}{R} = \underline{\underline{B}}^T \underline{\underline{A}} \tag{1.3}$$

leading to the following relations:

$$\underline{x}^{(b)} = \underset{B\leftarrow A}{R}\, \underline{x}^{(A)} \tag{1.4}$$

$$D^{(B)} = \underset{B\leftarrow A}{R}\, D^{(A)} \underset{B\leftarrow A}{R}^T \tag{1.5}$$

To conclude, the main vector operations can be written using both physical and component vectors. The scalar product is defined as

$$\underset{\rightarrow}{x} \cdot \underset{\rightarrow}{y} = \left(\underline{x}^{(A)}\right)^T \underline{y}^{(A)} = \left(\underset{A\leftarrow B}{R}\, \underline{x}^{(B)}\right)^T \underline{y}^{(A)} = \left(\underline{x}^{(A)}\right)^T \underset{A\leftarrow B}{R}\, \underline{y}^{(B)} \tag{1.6}$$

while for the vector product the following relation holds

$$\underset{\rightarrow}{x} \times \underset{\rightarrow}{y} = \underline{\underline{A}}\, \underline{\tilde{x}}^{(A)} \underline{y}^{(A)} = \underline{\underline{A}}\, \underline{\tilde{x}}^{(A)} \underset{A\leftarrow B}{R}\, \underline{y}^{(B)} = \underline{\underline{A}} \left(\underset{A\leftarrow B}{R}\, \underline{\tilde{x}}^{(B)} \underset{A\leftarrow B}{R}^T \right) \underline{y}^{(A)} \tag{1.7}$$

where

$$\underline{\tilde{x}}^{(A)} = \begin{bmatrix} 0 & -x_3^{(A)} & x_2^{(A)} \\ x_3^{(A)} & 0 & -x_1^{(A)} \\ -x_2^{(A)} & x_1^{(A)} & 0 \end{bmatrix} \tag{1.8}$$

is the skew-symmetric matrix associated with $\underline{x}^{(A)}$.

1.2. Kinematics

In this section, the main steps related to the Kane's formulation kinematics are discussed, with reference to tree-topology spacecraft. First, the constraints are classified to establish the field of application of Kane's method. Subsequently, the joint partials are introduced as useful operators to describe the relative motion among the spacecraft's bodies. Then, the key features of this formulation, i.e. partial velocities and remainder accelerations are presented.

1.2.1. Constraints of a mechanical system

In general, multibody spacecraft consist of multiple interconnected parts. For example, the connection point between two rigid bodies imposes a constraint, preventing them from moving freely as if they were separate. A mechanical system may be subject to [37]:

(a) Configuration constraints, which restrict positions;

(b) Motion constraints, which limit (linear and angular) velocities.

The configuration constraints refer only to the position vectors that describe a system. For a system consisting of N point masses, with $\vec{R}_i$ representing the position of the i-th mass relative to point O, the m holonomic constraints associated with the positions of these masses can be expressed in the following form:

$$\underline{\Phi}\left(\vec{R}_1,\ldots,\vec{R}_N,t\right)=\underline{0} \tag{1.9}$$

where $\underline{\Phi}$ is a vector of dimension $m\times 1$. A constraint is said to be holonomic if it involves constraints only on the position variables, like $\vec{R}_i$ (and not on the velocities). The degrees of freedom of this system are $3N-m$ (since each point mass has 3 translational degrees of freedom), and they correspond to $3N-m$ quantities that are sufficient to describe the system, i.e., the generalized coordinates. Holonomic constraints are classified into:

- Scleronomous or fixed, when $\underline{\Phi}$ does not depend on time;
- Rheonomous or time-dependent, when $\underline{\Phi}$ depends on time.

If $\underline{q}$ is the vector of generalized coordinates, the motion variables $\underline{u_M}$ can be obtained from the system of differential kinematic equations:

$$\underline{u_M} = Y(\underline{q}, t)\dot{\underline{q}} + \underline{z}(\underline{q}, t) \tag{1.10}$$

where Y is a square matrix and $\underline{z}$ is a vector, both chosen so that $\dot{\underline{q}}$ can be uniquely determined from $\underline{u_M}$ and $\underline{z}$. In many specific cases, the choices $Y = I_{3\times3}$ and $\underline{z} = \underline{0}$ simplify the system.

Thus, for a system of N point masses, in addition to the m holonomic constraints, there may also be m_M nonholonomic constraints on the velocities $\underset{\rightarrow}{v_i}$ of the masses, expressed as

$$\underline{f}\left(\underset{\rightarrow}{v_i}, \ldots, \underset{\rightarrow}{v_N}, t\right) = \underline{0} \tag{1.11}$$

where $\underline{f}$ is a vector of dimension $m_M \times 1$. These m_M additional constraint equations are not integrable in terms of position vectors; otherwise, they would be holonomic constraints and part of $\underline{\Phi}$. A system with nonholonomic constraints is called nonholonomic, whereas a system without them is holonomic. Nonholonomic constraint equations can be rewritten in terms of generalized coordinates and motion variables as

$$\underline{f}\left(\underline{u_M}, \underline{q}, t\right) = \underline{0} \tag{1.12}$$

If these equations can be expressed in a linear form with respect to the motion variables

$$A(\underline{q}, t)\underline{u_M} + \underline{b}(\underline{q}, t) = \underline{0} \tag{1.13}$$

then $\underline{u_M}$, a vector with $n = 3N - m$ components, can be decomposed into

$$\begin{cases} \underline{u}^T = \begin{bmatrix} u_1 & \cdots & u_p \end{bmatrix}^T \\ \underline{u_R}^T = \begin{bmatrix} u_{p+1} & \cdots & u_n \end{bmatrix}^T \end{cases} \tag{1.14}$$

where $p = 3N - m - m_M = n - m_M$, corresponding to the number of degrees of freedom of the system. The components of $\underline{u}$ are mutually independent (while those of $\underline{u_R}$ can be expressed in terms of $\underline{u}$ using the constraint equations) and are referred to as generalized velocities. In the form (1.13), the constraints are referred to as simple nonholonomic constraints. Otherwise, if $\underline{f}$ cannot be expressed in a linear form, the system is said to be subject to nonlinear nonholonomic constraints.

1.2.2. Multibody tree structure

Figure 1.1: International Space Station

A multibody spacecraft with a tree structure is a system composed of multiple interconnected rigid or flexible bodies, arranged hierarchically without closed kinematic loops [38]. Each body is connected to a parent body through rotary or prismatic joints, forming a branching structure resembling a tree. This representation is widely used in spacecraft modeling because most satellites consist of a central bus (main body) with appendages such as solar panels, antennas, robotic arms, or scientific instruments that are connected in a branching logic. The tree-structure model simplifies dynamic analysis, allowing for efficient computation of the system kinematics.

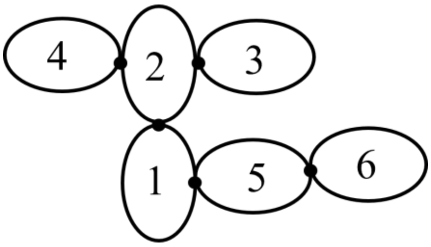

Figure 1.2: Example of tree-like structured multibody spacecraft

Considering the example in Figure 1.2, the kinematic and dynamic quantities of interest are determined by starting from the root body, i.e. the body with no parent, and progressing along the branches to the end body of each branch. Each path from the root body to an end body forms a column in the so-called configuration array [39]. For the given example, the configuration array has the following structure:

$$\begin{array}{ccc} 1 & 1 & 1 \\ 2 & 2 & 5 \\ 3 & 4 & 6 \end{array}$$

The configuration array represents the key to the recursive structure of multibody formulations. By following this structured approach, computations of motion and forces can be efficiently propagated through the system, enabling simulation of complex spacecraft dynamics. Although closed-loop structures may not initially conform to this configuration, they can be transformed into a tree-like structure by making strategic cuts to open the loops. This process, which will be discussed in Section 1.4.2, allows for the application of recursive multibody formulations even in systems with closed kinematic chains.

1.2.3. Degrees of freedom: generalized velocities

For a system of N unconstrained rigid bodies, the total number of degrees of freedom is $p = 6N$, since each body has 3 translational and 3 rotational degrees of freedom. In the presence of constraints,

(i) if m holonomic constraints are present, the number of degrees of freedom is

$$p = 6N - m$$

(ii) if m_M nonholonomic constraints are also present, the number of degrees of freedom becomes

$$p = 6N - m - m_M$$

The number of degrees of freedom corresponds to the number of generalized velocities. If $m_M = 0$, then the number of generalized velocities is equal to the number of generalized coordinates.

The tree-structured multibody satellite discussed in the previous section is a holonomic system since each joint imposes a set of holonomic constraints. Both rotary and prismatic joints allow between one and three rotational or translational degrees of freedom, respectively. Each joint, therefore, results in three to five configuration constraints. Specifically, the i-th joint, which connects the i-th body to its parent body (not necessarily labeled as i-1), is associated with the i-th joint velocity vector, defined as

a. $\underline{\dot{\theta}}_i = \dot{\theta}_{i1}$ or $\underline{\dot{\theta}}_i^T = \begin{bmatrix} \dot{\theta}_{i1} & \dot{\theta}_{i2} \end{bmatrix}^T$ or $\underline{\dot{\theta}}_i^T = \begin{bmatrix} \dot{\theta}_{i1} & \dot{\theta}_{i2} & \dot{\theta}_{i3} \end{bmatrix}^T$ in the case of rotary joints, or
b. $\underline{\dot{s}}_i = \dot{s}_{i1}$ or $\underline{\dot{s}}_i^T = \begin{bmatrix} \dot{s}_{i1} & \dot{s}_{i2} \end{bmatrix}^T$ or $\underline{\dot{s}}_i^T = \begin{bmatrix} \dot{s}_{i1} & \dot{s}_{i2} & \dot{s}_{i3} \end{bmatrix}^T$ in the case of prismatic joints.

The joint variables and their associated joint velocities can be defined in various ways, depending on the chosen convention and the reference frame used for their representation. Further details are provided in the next section.

1.2.4. Joint Partials

In the computation of recursive kinematics, it is fundamental to express the relative linear and angular velocities of a child body with respect to its parent as a function of the joint velocity vector. To do this, the joint partials are introduced [40]. By definition, they are obtained from the following relations:

$$ {}^{B_{i-1}}\underset{\rightarrow}{\omega}^{B_i} = \underline{\underline{B}}_i \, \Gamma_i \, \underline{\dot{\theta}}_i \tag{1.15}$$

$$ {}^{C_{i-1}}\underset{\rightarrow}{v}^{C_i} = \underline{\underline{B}}_{i-1} \, \Sigma_i \, \underline{s}_i \tag{1.16}$$

where ${}^{B_{i-1}}\underset{\rightarrow}{\omega}^{B_i}$ and ${}^{C_{i-1}}\underset{\rightarrow}{v}^{C_i}$ are the angular and linear velocity of the i-th body with respect to its parent body, which is now referred to as i-1 (but, in general, it could have any number lower than i). In the angular velocity, superscript "B" refers to the body reference frame, while superscript "C" in linear velocity is associated with the center of mass of the bodies. In Eqs. (1.15)-(1.16), matrices Γ_i and Σ_i are the angular and linear joint partials, respectively. It is often convenient to derive these terms from the projection of relative velocities along the parent or child body frames. Specifically, the angular relative velocity is typically projected along the child body frame, while the linear relative velocity is often more effectively referenced to the parent body frame. The following two examples illustrate the structure of these terms.

First, a 3-DOF spherical hinge that joins bodies 1 and 2 is considered. Supposing that the joint is characterized by a 3-1-2 sequence of rotations, the global rotation matrix is

$$ \underset{2\leftarrow 1}{R} = R_2(\theta_3) R_1(\theta_2) R_3(\theta_1) R_A \tag{1.17}$$

where R_A is the assembly rotation matrix, i.e. the matrix that describes the relative orientation between the body reference frames $\underline{\underline{B}}_1$ and $\underline{\underline{B}}_2$ when all joint angles are set to zero. Each rotation leads to a new reference frame, so Eq. (1.17) can be represented as

$$ \underline{\underline{B}}_1 \xrightarrow{R_A} \underline{\underline{B}}_{1'} \xrightarrow{R_3(\theta_1)} \underline{\underline{B}}_{1''} \xrightarrow{R_1(\theta_2)} \underline{\underline{B}}_{1'''} \xrightarrow{R_2(\theta_3)} \underline{\underline{B}}_2 \tag{1.18}$$

Hence, one can define the following rotation matrices:

$$\underset{2\leftarrow 1'''}{R} = R_2(\theta_3) = \begin{bmatrix} c_{\theta_3} & 0 & -s_{\theta_3} \\ 0 & 1 & 0 \\ s_{\theta_3} & 0 & c_{\theta_3} \end{bmatrix} \tag{1.19}$$

$$\underset{2\leftarrow 1''}{R} = R_2(\theta_3) R_1(\theta_2) = \begin{bmatrix} c_{\theta_3} & s_{\theta_2}s_{\theta_3} & -c_{\theta_2}s_{\theta_3} \\ 0 & c_{\theta_2} & s_{\theta_2} \\ s_{\theta_3} & -s_{\theta_2}c_{\theta_3} & c_{\theta_2}c_{\theta_3} \end{bmatrix} \tag{1.20}$$

$$\underset{2\leftarrow 1'}{R} = R_2(\theta_3) R_1(\theta_2) R_3(\theta_1) = \begin{bmatrix} c_{\theta_1}c_{\theta_3} - s_{\theta_1}s_{\theta_2}s_{\theta_3} & s_{\theta_1}c_{\theta_3} + c_{\theta_1}s_{\theta_2}s_{\theta_3} & -c_{\theta_2}s_{\theta_3} \\ -s_{\theta_1}c_{\theta_2} & c_{\theta_1}c_{\theta_2} & s_{\theta_2} \\ c_{\theta_1}s_{\theta_3} - s_{\theta_1}c_{\theta_2}c_{\theta_3} & s_{\theta_1}s_{\theta_3} - c_{\theta_1}s_{\theta_2}c_{\theta_3} & c_{\theta_2}c_{\theta_3} \end{bmatrix} \tag{1.21}$$

In this specific example, the relative angular velocity of body 2 with respect to body 1 is

$$\begin{aligned}
\underset{\longrightarrow}{{}^{B_1}\omega^{B_2}} &= \underline{\underline{B}}_{1'} \begin{bmatrix} 0 \\ 0 \\ 1 \end{bmatrix} \dot{\theta}_1 + \underline{\underline{B}}_{1''} \begin{bmatrix} 1 \\ 0 \\ 0 \end{bmatrix} \dot{\theta}_2 + \underline{\underline{B}}_{1'''} \begin{bmatrix} 0 \\ 1 \\ 0 \end{bmatrix} \dot{\theta}_3 = \\
&= \underline{\underline{B}}_2 \left\{ \underset{2\leftarrow 1'}{R} \begin{bmatrix} 0 \\ 0 \\ 1 \end{bmatrix} \dot{\theta}_1 + \underset{2\leftarrow 1''}{R} \begin{bmatrix} 1 \\ 0 \\ 0 \end{bmatrix} \dot{\theta}_2 + \underset{2\leftarrow 1'''}{R} \begin{bmatrix} 0 \\ 1 \\ 0 \end{bmatrix} \dot{\theta}_3 \right\} = \\
&= \underline{\underline{B}}_2 \left\{ \begin{bmatrix} \left(\underset{2\leftarrow 1'}{R}\right)_{j=3} & \left(\underset{2\leftarrow 1''}{R}\right)_{j=1} & \left(\underset{2\leftarrow 1'''}{R}\right)_{j=2} \end{bmatrix} \begin{bmatrix} \dot{\theta}_1 \\ \dot{\theta}_2 \\ \dot{\theta}_3 \end{bmatrix} \right\} = \\
&= \underline{\underline{B}}_2 \Gamma_2 \underline{\dot{\theta}}
\end{aligned} \tag{1.22}$$

with $\left(\underset{B\leftarrow A}{R}\right)_j$ is the j-th column of the rotation matrix. So, the angular joint partial matrix in this case corresponds to

$$\Gamma_2 = \begin{bmatrix} -c_{\theta_2}s_{\theta_3} & c_{\theta_3} & 0 \\ s_{\theta_2} & 0 & 1 \\ c_{\theta_2}c_{\theta_3} & s_{\theta_3} & 0 \end{bmatrix} \tag{1.23}$$

Following this general procedure, it is possible to find any configuration of angular joint partial.

Similarly, linear joint partials are derived. However, unlike the angular case, it is more convenient to express the components of relative velocity with respect to the parent body frame. For a 1-DOF prismatic joint, where body i slides along a linear guide on body i-1, the linear joint partial corresponds to the direction of the guide expressed in the (i-1)-th body frame. When increasing the joint's degrees of freedom – for example, allowing body i to move along a planar guide on body i-1 – the two columns of the joint partial matrix correspond to the unit vectors defining the plane in the parent body frame. To further justify this choice of reference frame, it is useful to examine the structure of the linear joint partial in the case of a circular guide.

In Figure 1.3 a circular guide located on body i-1 is depicted. Axes x and y are associated with $\underline{\underline{B}}_{i-1}$, while the joint connecting body i to body i-1 is located in Q_i. Hence, one can write that

$$ {}^{C_{i-1}}\underset{\rightarrow}{v}^{Q_i} = \underline{\underline{B}}_{i-1}\Sigma_i\dot{s}_i = \underline{\underline{B}}_{i-1}\begin{bmatrix} -\sin\theta \\ \cos\theta \\ 0 \end{bmatrix}\dot{s}_i = \underline{\underline{B}}_{i-1}\begin{bmatrix} -\sin(s_i/r) \\ \cos(s_i/r) \\ 0 \end{bmatrix}\dot{s}_i \tag{1.24} $$

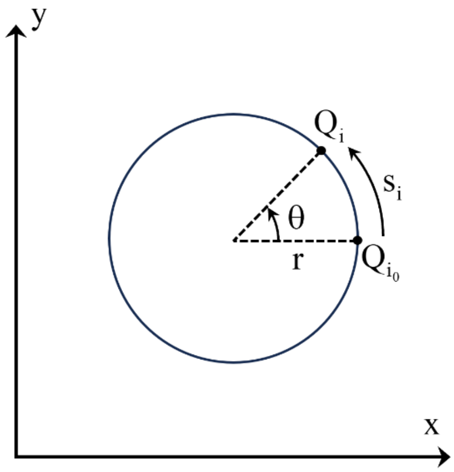

Figure 1.3: Sketch of a circular guide

It is worth noting that different choices can be made when selecting the reference frame for expressing joint partials. However, the choices proposed in this Section are believed to simplify the derivation of the recursive structure of multibody kinematics.

1.2.5. The Kane's Jacobian: linear and angular partial velocities

In Kane's formulation, partial velocities play a crucial role, as the dynamic equations are derived by projecting the Newton\Euler equations onto these vectors [20]. Partial velocities are defined as the vector coefficients that, when multiplied by the generalized velocities, yield the linear and angular velocities of the bodies in a multibody system. Aligned with the directions of motion, they are orthogonal to the constraint reactions. As a result, the constraint forces and torques exchanged between bodies can be disregarded in the derivation of the dynamic equations. This property is one of the key advantages of Kane's method.

Being $\underline{u}$ the vector of generalized velocities appearing in Eq. (1.14), it is possible to write that

$$\begin{cases} {}^{N}\vec{v}^{C_i} = \sum_{r=1}^{p} \vec{v}_r^{C_i} u_r + \vec{v}_t^{C_i} \\ {}^{N}\vec{\omega}^{B_i} = \sum_{r=1}^{p} \vec{\omega}_r^{i} u_r + \vec{\omega}_t^{i} \end{cases} \tag{1.25}$$

where ${}^{N}\vec{v}^{C_i}$ and ${}^{N}\vec{\omega}^{B_i}$ are the linear and angular velocity of the i-th body with respect to the inertial frame $\underline{\underline{N}}$ respectively, $\vec{v}_r^{C_i}$ and $\vec{\omega}_r^{i}$ are the linear and angular partial velocity vectors associated with the i-th body and the r-th degree of freedom of the system respectively, while $\vec{v}_t^{C_i}$ and $\vec{\omega}_t^{i}$ are the remainder terms, which do not depend on generalized velocities. If the system is holonomic, as in the case of multibody tree structures, then $n = p$ in Eq. (1.25). This Equation can be rewritten in the following matrix form:

$$\begin{bmatrix} {}^{N}\vec{v}^{C_i} \\ \vdots \\ {}^{N}\vec{v}^{C_N} \end{bmatrix} = \begin{bmatrix} \vec{v}_1^{C_1} & \cdots & \vec{v}_n^{C_1} \\ \vdots & \ddots & \vdots \\ \vec{v}_1^{C_N} & \cdots & \vec{v}_n^{C_N} \end{bmatrix} \begin{bmatrix} u_1 \\ \vdots \\ u_n \end{bmatrix} + \begin{bmatrix} \vec{v}_t^{C_1} \\ \vdots \\ \vec{v}_t^{C_N} \end{bmatrix} \tag{1.26}$$

$$\begin{bmatrix} {}^{N}\vec{\omega}^{B_i} \\ \vdots \\ {}^{N}\vec{\omega}^{B_N} \end{bmatrix} = \begin{bmatrix} \vec{\omega}_1^{1} & \cdots & \vec{\omega}_n^{1} \\ \vdots & \ddots & \vdots \\ \vec{\omega}_1^{N} & \cdots & \vec{\omega}_n^{N} \end{bmatrix} \begin{bmatrix} u_1 \\ \vdots \\ u_n \end{bmatrix} + \begin{bmatrix} \vec{\omega}_t^{1} \\ \vdots \\ \vec{\omega}_t^{N} \end{bmatrix} \tag{1.27}$$

If all physical vectors appearing in Eqs. (1.26)-(1.27) are transformed into 3x1 vectors, e.g. by projecting them along the frame associated with the body they refer, it is possible to rewrite these two equation as

$$\underline{v} = V\underline{u} + \underline{v}_t \tag{1.28}$$

$$\underline{\omega} = \Omega\underline{u} + \underline{\omega}_t \tag{1.29}$$

being $\underline{v}$ and $\underline{\omega}$ the vectors collecting the 3x1 velocity vectors of all bodies composing the multibody structure, so as $\underline{v}_t$ and $\underline{\omega}_t$ collect the remainder terms. Moreover, symbols V and Ω denote the linear and angular partial velocity matrices, respectively, collecting partial velocities already expressed in the body reference frames.

From Eqs. (1.26)-(1.29), it is clear that partial velocities serve as a crucial bridge between Eulerian kinematics – represented by the left-hand side, i.e., the linear and angular velocities of all bodies – and Lagrangian kinematics, characterized by the generalized velocities, which are directly derived from the generalized coordinates as shown in Eq. (1.10). As a final remark, it is worth noting that partial velocities are obtained by differentiating the velocities of the bodies with respect to the generalized velocities. For this reason, they are also referred to as "Kane's Jacobian".

1.2.6. Remainder accelerations

To complete the general description regarding the kinematics in Kane's formulation, remainder accelerations are now introduced. From time derivation of Eq. (1.25) one obtains that the angular and linear accelerations of the i-th body are expressed as

$$\begin{cases} {}^{N}\vec{a}^{C_i} \triangleq \dfrac{{}^{N}d\left({}^{N}\vec{v}^{C_i}\right)}{dt} = \displaystyle\sum_{r=1}^{n} \vec{v}_r^{C_i}\dot{u}_r + \sum_{r=1}^{n} \dfrac{{}^{N}d\left(\vec{v}_r^{C_i}\right)}{dt} u_r + \dfrac{{}^{N}d\left(\vec{v}_t^{C_i}\right)}{dt}^{N} \\ \vec{\alpha}^{B_i} \triangleq \dfrac{{}^{N}d\left({}^{N}\vec{\omega}^{B_i}\right)}{dt} = \displaystyle\sum_{r=1}^{n} \vec{\omega}_r^{i}\dot{u}_r + \sum_{r=1}^{n} \dfrac{{}^{N}d\left(\vec{\omega}_r^{i}\right)}{dt} u_r + \dfrac{{}^{N}d\left(\vec{\omega}_t^{i}\right)}{dt} \end{cases} \tag{1.30}$$

where ${}^{N}d/dt$ indicates that the time derivation is computed with respect the inertial frame. From Eq. (1.30) it is possible to distinguish two different contributions:

(i) terms $\sum_{r=1}^{n} \vec{v}_r^{C_i}\dot{u}_r$ and $\sum_{r=1}^{n} \vec{\omega}_r^{i}\dot{u}_r$ are linearly dependent on the time derivative of generalized velocities;

(ii) the remaining terms do not contain $\dot{\underline{u}}$: they are called "remainder accelerations".

It is worth noting that Eq. (1.30) can be rewritten in a more compact form, in the same way Eq. (1.25) is transformed into Eqs. (1.28)-(1.29). Specifically, one can write that

$$\underline{a} = V\dot{\underline{u}} + \underline{a}^{(R)} \tag{1.31}$$

$$\underline{\alpha} = \Omega\dot{\underline{u}} + \underline{\alpha}^{(R)} \tag{1.32}$$

where all vectors are expressed along the related body frame. Vectors $\underline{a}$ and $\underline{\alpha}$ collect the body accelerations, while $\underline{a}^{(R)}$ and $\underline{\alpha}^{(R)}$ correspond to the remainder acceleration vectors. Separating these two contributions enables the derivation of dynamic equations in which the only unknown is the time derivative of the generalized velocities, as will be discussed in Section 1.3.1.

1.2.7. Recursive kinematics in multibody tree-like structures

This section explores the recursive structure of partial velocities and remainder accelerations in a multibody system with a tree-like structure composed of rigid bodies. As previously mentioned, the bodies are assumed to be interconnected by rotary or prismatic joints.

In the case of a multibody spacecraft, the bus is typically chosen as the root body (body 1) of the structure. While this choice is not mandatory – other bodies could serve as the root – it is the most logical option, as it provides a clearer representation of the spacecraft's motion. Then, the first six generalized velocities of the system are the linear and angular velocities of the platform with respect to the inertial frame, both projected along the body 1 frame:

$$\underline{u}\big|_{1,\dots,6} = \begin{bmatrix} \underline{v}_{C_1}^{(1)T} & \underline{\omega}_1^{(1)T} \end{bmatrix}^T \tag{1.33}$$

Different choices can be made when selecting the reference frame employed to express the platform's velocities. From a computational perspective, projecting the linear velocity onto the inertial frame $\underline{\underline{N}}$ significantly reduces computational effort. This is because the characteristic timescale of velocity variation in the inertial frame is on the order of the spacecraft's orbital period. In contrast, expressing velocity in the body frame causes it to vary at the same rate as the spacecraft's angular motion, increasing both the numerical stiffness of the system and the computational cost. However, in this work, all velocities are expressed in their respective body frames, as this choice simplifies the representation of elastic motion (which will be discussed in the next chapter). Nonetheless, the computational drawback of this approach for generalized velocities is only apparent. It can be easily mitigated by transforming $\dot{\underline{v}}_{C_1}^{(1)}$ into the inertial frame after solving the dynamic equations and before the numerical integration, using the following operation:

$$\dot{\underline{v}}_{C_1}^{(N)} = \underset{N\leftarrow 1}{R}\left(\dot{\underline{v}}_{C_1}^{(1)} + \tilde{\underline{\omega}}_1^{(1)}\underline{v}_{C_1}^{(1)}\right) \tag{1.34}$$

This approach allows the system to be solved in the body frame while numerically integrating the velocity in the inertial frame, leveraging the advantages of both formulations.

Starting from the root body velocities, the tree configuration allows the possibility to reconstruct the velocity of each body by proceeding along the branches up to the end bodies. In fact, the following relations always hold:

$$\begin{cases} {}^{N}\underset{\rightarrow}{\omega}^{B_i} = \underline{\underline{B}}_i \underline{\omega}_i = {}^{N}\underset{\rightarrow}{\omega}^{B_{i-1}} + {}^{B_{i-1}}\underset{\rightarrow}{\omega}^{B_i} \\ {}^{N}\underset{\rightarrow}{v}^{C_i} = \underline{\underline{B}}_i \underline{v}_{C_i} = {}^{N}\underset{\rightarrow}{v}^{C_{i-1}} + {}^{N}\underset{\rightarrow}{\omega}^{B_{i-1}} \times \underset{\rightarrow}{r}_{C_{i-1}Q_i} + {}^{N}\underset{\rightarrow}{\omega}^{B_i} \times \underset{\rightarrow}{r}_{Q_iC_i} + {}^{C_{i-1}}\underset{\rightarrow}{v}^{C_i} \\ \qquad\qquad = {}^{N}\underset{\rightarrow}{v}^{C_{i-1}} + \underset{\longrightarrow}{\Delta v}^{C_i} \end{cases} \tag{1.35}$$

The relative velocities of child body with respect to the parent body are then obtained considering Figures 1.4-1.5, it is possible to write that

$$\begin{cases} {}^{B_{i-1}}\underset{\rightarrow}{\omega}^{B_i} = \underline{\underline{B}}_i \Gamma_i \dot{\underline{\theta}}_i \\ \underset{\longrightarrow}{\Delta v}^{C_i} = {}^{N}\underset{\rightarrow}{\omega}^{B_{i-1}} \times \underset{\rightarrow}{r}_{C_{i-1}Q_i} + {}^{N}\underset{\rightarrow}{\omega}^{B_i} \times \underset{\rightarrow}{r}_{Q_iC_i} = -\underline{\underline{B}}_{i-1} \tilde{\underline{r}}_{C_{i-1}Q_i} \underline{\omega}_{i-1} - \underline{\underline{B}}_i \tilde{\underline{r}}_{Q_iC_i} \underline{\omega}_i \\ \qquad = -\underline{\underline{B}}_{i-1} \tilde{\underline{r}}_{C_{i-1}C_i} \underline{\omega}_{i-1} - \underline{\underline{B}}_i \tilde{\underline{r}}_{Q_iC_i} \Gamma_i \dot{\underline{\theta}}_i \end{cases} \tag{1.36}$$

for the rotary joint, while

$$\begin{cases} {}^{B_{i-1}}\underset{\rightarrow}{\omega}^{B_i} = \underset{\rightarrow}{0} \\ \underset{\longrightarrow}{\Delta v}^{C_i} = {}^{N}\underset{\rightarrow}{\omega}^{B_{i-1}} \times \left(\underset{\rightarrow}{r}_{C_{i-1}Q_{i0}} + \underline{\underline{B}}_{i-1} \Sigma_i \underline{s}_i \right) + {}^{N}\underset{\rightarrow}{\omega}^{B_i} \times \underset{\rightarrow}{r}_{Q_iC_i} + \underline{\underline{B}}_{i-1} \Sigma_i \dot{\underline{s}}_i \\ \qquad = -\underline{\underline{B}}_{i-1} \left(\underline{r}_{C_{i-1}Q_i} + \Sigma_i \underline{s}_i \right)^{\sim} \underline{\omega}_{i-1i} - \underline{\underline{B}}_i \tilde{\underline{r}}_{Q_iC_i} \underline{\omega}_i + \underline{\underline{B}}_{i-1} \Sigma_i \dot{\underline{s}} \\ \qquad = \underline{\underline{B}}_{i-1} \left[-\left(\underline{r}_{C_{i-1}C_i} + \Sigma_i \underline{s}_i \right)^{\sim} \underline{\omega}_{i-1} + \Sigma_i \dot{\underline{s}}_i \right] \end{cases} \tag{1.37}$$

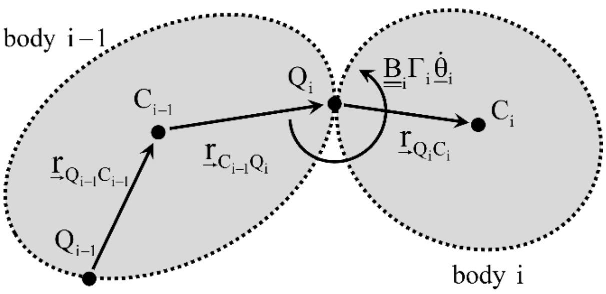

Figure 1.4: Two bodies interconnected via rotary joint

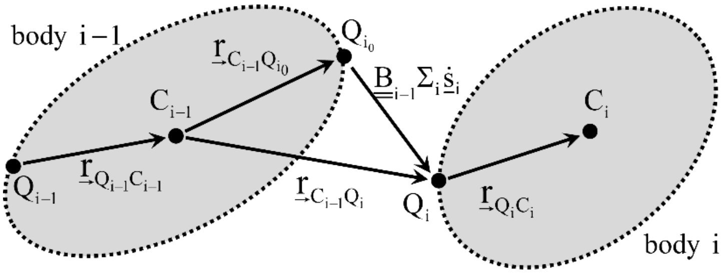

Figure 1.5: Two bodies interconnected via prismatic joint

For the prismatic joint. This implies that the remaining part of the generalized velocities vector is composed of the joint velocities' vectors:

$$\underline{u}\big|_{7,\dots,n} = \left[\left(\dot{\underline{\theta}}_i^{\,T} \vee \dot{\underline{s}}_i^{\,T}\right)_{i=2,\dots,N}\right]^T \tag{1.38}$$

where the (angular or linear) nature of the term in brackets depends on the joint interconnecting the i-th body to its parent body.

Recalling the definition of partial velocities – the vector coefficients that multiply generalized velocities to provide the velocities of the bodies composing the multibody structure – it is possible to use Eqs. (1.36) and (1.37) to obtain a general and recursive method to build matrices V and Ω appearing in Eqs. (1.28)-(1.29). In fact, considering that the i-th $3\times n$ block of these matrices, denoted as V_i and Ω_i, is associated with the i-th body, from inspection of Eqs. (1.36)-(1.37) it is possible to write that

$$V_i = \left[\underset{i\leftarrow 1}{R} \quad -\underset{i\leftarrow 1}{R}\,\tilde{\underline{r}}_{C_1C_i} \quad \left\{-\underset{i\leftarrow j}{R}\,\tilde{\underline{r}}_{Q_jC_i}\Gamma_j\right\}_{\text{revol}} \vee \left\{\underset{i\leftarrow j-1}{R}\,\Sigma_j\right\}_{\text{prism}}\right] \tag{1.39}$$

$$\Omega_i = \left[0_{3\times 3} \quad \underset{i\leftarrow 1}{R} \quad \left\{\underset{i\leftarrow j}{R}\,\Gamma_j\right\}_{\text{revol}} \vee \left\{0\right\}_{\text{prism}}\right] \tag{1.40}$$

where terms in curly brackets deserve to be further explained. In fact, while the first six columns are well-determined by the association with the rigid motion of the platform (root body), the remaining columns are built according to the root-to-end process previously mentioned. Starting from the seventh column, each column is associated with a specific joint degree of freedom that is related to a single body, called body j. If the j-th body belongs to the same branch of body i and is closer to the root than body i, or if $j=i$, the 3×1 column is filled by the expression in curly brackets, choosing the one related to the typology of the joint (rotary or prismatic) connecting body j to its parent. In the other case, the column is filled by a 3×1 null vector.

In the same way, recursive structure of remainder acceleration is identified. In fact, from the time derivation of Eqs. (1.36)-(1.37), the following expression for remainder accelerations are obtained for rotary and prismatic interconnections respectively:

$$\begin{cases} \underline{a}_{C_i}^{(R)} = \underset{i\leftarrow i-1}{R}\left[\underline{a}_{C_{i-1}}^{(R)} - \underline{\tilde{r}}_{C_{i-1}Q_i}\underline{\omega}_{i-1}^{*} - \underline{\tilde{\omega}}_{i-1}\underline{\tilde{r}}_{C_{i-1}Q_i}\underline{\omega}_{i-1}\right] - \underline{\tilde{r}}_{Q_iC_i}\underline{\omega}_{i}^{*} - \underline{\tilde{\omega}}_{i}\underline{\tilde{r}}_{Q_iC_i}\underline{\omega}_{i} \\ \underline{\alpha}_{i}^{(R)} = \underset{i\leftarrow i-1}{R}\underline{\alpha}_{i-1}^{(R)} + \dot{\Gamma}_i\dot{\theta}_i + \underline{\tilde{\omega}}_i\Gamma_i\dot{\theta}_i \end{cases} \tag{1.41}$$

$$\begin{cases} \underline{a}_{C_i}^{(R)} = \underset{i\leftarrow i-1}{R}\left[\underline{a}_{C_{i-1}}^{(R)} - \underline{\tilde{r}}_{C_{i-1}Q_i}\underline{\omega}_{i-1}^{*} - \underline{\tilde{\omega}}_{i-1}\left(2\Sigma_i\underline{\dot{s}}_i + \dot{\Sigma}_i\underline{s}_i + \underline{\tilde{r}}_{C_{i-1}Q_i}\underline{\omega}_{i-1}\right) + \dot{\Sigma}_i\underline{s}_i\right] \\ \qquad - \underline{\tilde{r}}_{Q_iC_i}\underline{\omega}_{i}^{*} - \underline{\tilde{\omega}}_{i}\underline{\tilde{r}}_{Q_iC_i}\underline{\omega}_{i} \\ \underline{\alpha}_{i}^{(R)} = \underset{i\leftarrow i-1}{R}\underline{\alpha}_{i-1}^{(R)} \end{cases} \tag{1.42}$$

All accelerations vectors are expressed in the reference frame of the body they refer to, for the same reasons previously discussed for the partial velocities case.

It is worth noting that, as suggested by Eq. (1.30), remainder accelerations could be computed though the multiplication of a matrix containing the time derivative with respect to the inertial frame of partial velocities by the generalized velocity vector. Other formulations employ this methodology instead of Eqs (1.41)-(1.42) [41]. However, recursive structure reported here guarantees shorter computational times, because of a lower number of algebraic operations. In fact, adopting this strategy implies that the accelerations of the i-th body are computed adding the contribution of the i-th body to its parent body accelerations, which are already available from the previous step of computation. Instead, in the formulation that employs the derivatives of partial velocities, the operation to compute the parent body accelerations are always repeated in the matrix multiplications $\dot{V}\underline{u}$ and $\dot{\Omega}\underline{u}$, leading to a larger number of operations.

1.2.8. Introduction of kinematic laws

In some cases, it may be preferable to prescribe the time histories of one or more degrees of freedom of the multibody system rather than computing them from the solution of the dynamic equations. For example, if the impact of a specific appendage motion on the overall satellite needs to be evaluated, and the control action required to induce that motion is not yet known, an initial analysis can be performed by kinematically prescribing the motion of the appendage. This type of analysis provides a preliminary indication of the system's actual kinematics and dynamics. However, to validate these results, a follow-up analysis is required in which the prescribed motion laws are replaced with dynamic forces that generate the desired motion. This step is essential because, in some cases, the prescribed motion may be unfeasible – given realistic control actions – due to dynamic couplings with the overall spacecraft or with the motion of other bodies in the same kinematic chain. Moreover, applying an unrealistic motion could incorrectly influence the behavior of other components within the multibody structure.

When the motion of one or more degrees of freedom is prescribed, the time histories of the corresponding generalized coordinate and generalized velocity are known. In the framework of Kane's methodology previously described, the prescribed velocities constitute terms $\underline{v}_t^{C_i}$ and $\underline{\omega}_t^i$ appearing in Eq. (1.25). Specifically, if the k-th DOF of the system is assigned, the remainder velocity terms are

$$\begin{cases} \underline{v}_t^{C_i} = \underline{v}_k^{C_i} u_k \\ \underline{\omega}_t^i = \underline{\omega}_k^i u_k \end{cases} \tag{1.43}$$

This means that the k-th component of the generalized speeds vector u_k must be removed from $\underline{u}$, and the k-th column of V and Ω, denoted as $V|_k$ and $\Omega|_k$ respectively, must be removed from the partial velocities matrices. This information is not lost but only transferred to the known-term side of the equations. In fact, the remainder accelerations are modified as

$$\underline{a}^{(R)} = \underline{a}_0^{(R)} + V|_k \, \dot{u}_k \tag{1.44}$$

$$\underline{\alpha}^{(R)} = \underline{\alpha}_0^{(R)} + \Omega|_k \, \dot{u}_k \tag{1.45}$$

where $\underline{a}_0^{(R)}$ and $\underline{\alpha}_0^{(R)}$ are the linear and angular remainder accelerations vectors computed considering all degrees of freedom as unprescribed. After these modifications to the kinematic quantities, the subsequent steps for deriving the dynamic equations (described in the next section) can be carried out in the same way as in the case of unassigned degrees of freedom. However, it is important to note that when the k-th DOF is prescribed, the forces and torques associated with that DOF – specifically, those applied to the body moved by the k-th DOF and acting along its direction of motion – must be removed from the system of equations. This is because the prescribed motion serves as the kinematic counterpart of a dynamic input, making those forces and torques redundant.

1.3. Dynamics

In this section, the dynamic equations for a multibody rigid spacecraft are derived using Kane's methodology. The relationship between Kane's equations and internal and external dynamic actions is discussed, with particular attention to constraint reactions. A method for reconstructing constraint forces and torques – either online or in post-processing – is presented, leveraging the properties of a tree-structured system. Finally, the computation of verification functions such as linear and angular momenta is addressed, along with a methodology for efficiently deriving the motion of the system's center of mass by taking advantage of the structure of Kane's equations.

1.3.1. External and internal contributing forces and torques

The peculiarity of partial velocities lies in the fact that they follow the directions of the degrees of freedom of the multibody system. For example, they are aligned with the axes of rotary joints and the directions of prismatic guides. As a result, their scalar product with the constraint reactions is zero. This orthogonality allows constraint reactions to be neglected in the computation of the dynamic equations, significantly simplifying their derivation. In fact, it is worth recalling here (and it will be further discussed in the next section) that Kane's equations are obtained by projecting the Newton-Euler equations onto the partial velocity vectors. Therefore, the only dynamic actions that must be considered when applying Kane's formulation are:

(i) the external forces and torques

(ii) the internal contributing forces and torques.

The first category includes all possible external actions, such as gravitational forces, aerodynamic drag, solar radiation pressure, or even contact with other bodies, as well as "external" control actions, such as those exerted by chemical or electric thrusters. In contrast, the second group of dynamic actions refers to internal forces and torques – those exchanged among the bodies of the multibody satellite – that are not orthogonal to the partial velocities. For example, the torque generated by a joint motor acts along the joint axis and must be included in Kane's equations of motion. All these contributions must be considered in building the $3N \times 1$ vectors $\underline{f}$ and $\underline{t}$, where the i-th 3×1 block contains the total external and contributing forces and torques, respectively, that act on the i-th body.

1.3.2. Derivation of the dynamic equations

Usually, Kane's equations are written in the following form:

$$f_{G_r} + f_{G_r}^* = 0, \text{ with } r = 1, \dots, n \tag{1.46}$$

where f_{G_r} and $f_{G_r}^*$ are the r-th generalized active and inertia force, respectively, associated with the multibody system. As previously discussed, Kane's equations are obtained from the projection of Newton-Euler multibody equations along the partial velocities directions. In fact, the generalized active and inertia forces are defined as

$$f_{G_r} = \sum_{i=1}^{N} \left(\underset{\rightarrow}{v}_r^{C_i} \cdot \underset{\rightarrow}{f}_i + \underset{\rightarrow}{\omega}_r^{i} \cdot \underset{\rightarrow}{t}_i \right) \tag{1.47}$$

$$f_{G_r}^{*} = -\sum_{i=1}^{N} \left[\underset{\rightarrow}{v}_r^{C_i} \cdot m_i \, {}^{N}\underset{\rightarrow}{a}^{C_i} + \underset{\rightarrow}{\omega}_r^{i} \cdot \left(\underset{\rightarrow}{J}_{C_i} \cdot {}^{N}\underset{\rightarrow}{\alpha}^{B_i} + {}^{N}\underset{\rightarrow}{\omega}^{B_i} \times \underset{\rightarrow}{J}_{C_i} \cdot {}^{N}\underset{\rightarrow}{\omega}^{B_i} \right) \right] \tag{1.48}$$

where m_i is the i-th body mass, while $\underset{\rightarrow}{J}_{C_i}$ is the inertia tensor of the i-th bod evaluated in its center of mass. It is evident that the generalized active and inertia forces are simply the projections of the external and contributing internal dynamic actions, and of the inertia forces and torques, respectively. Constraint reactions are excluded from $\underset{\rightarrow}{f}_i$ and $\underset{\rightarrow}{t}_i$ because of their orthogonality with partial velocities,

Eqs. (1.46)-(1.48) can be converted to a matrix form, after projecting the physical vectors onto specific reference frames. In fact, the generalized active forces of Eq. (1.47) can also be written as

$$\underline{f_G} = V^T f + \Omega^T \underline{t} \tag{1.49}$$

where $\underline{f_G}$ is the $n \times 1$ column vector collecting all the n generalized active forces. In the same way, generalized inertia forces can be rewritten as

$$\begin{aligned} \underline{f_G^*} &= -V^T M \underline{a} - \Omega^T \left\{ J_C \underline{\alpha} + [\underline{\tilde{\omega}} J_C \underline{\omega}] \right\} \\ &= -V^T M \left[V \underline{\dot{u}} + \underline{a}^{(R)} \right] - \Omega^T \left\{ J_C \left[\Omega \underline{\dot{u}} + \underline{\alpha}^{(R)} \right] + [\underline{\tilde{\omega}} J_C \underline{\omega}] \right\} \\ &= -\left\{ V^T M V + \Omega^T J_C \Omega \right\} \underline{\dot{u}} - V^T M \underline{a}^{(R)} - \Omega^T \left\{ J_C \underline{\alpha}^{(R)} + [\underline{\tilde{\omega}} J_C \underline{\omega}] \right\} \end{aligned} \tag{1.50}$$

where Eqs. (1.31)-(1.32) have been used. In Eq. (1.50), $\underline{f_G^*}$ is the $n \times 1$ generalized inertia forces column vector, while

$$M = \begin{bmatrix} m_1 I_{3\times3} & & & 0 \\ & m_2 I_{3\times3} & & \\ & & \ddots & \\ 0 & & & m_N I_{3\times3} \end{bmatrix} \tag{1.51}$$

$$
J_C = \begin{bmatrix} J_1^{(C_1)} & & & 0 \\ & J_2^{(C_2)} & & \\ & & \ddots & \\ 0 & & & J_N^{(C_N)} \end{bmatrix} \tag{1.52}
$$

$$
\left[\underline{\tilde{\omega}}\, J_C\, \underline{\omega}\right] = \begin{bmatrix} \underline{\tilde{\omega}}_1\, J_1^{(C_1)}\, \underline{\omega}_1 \\ \underline{\tilde{\omega}}_2\, J_2^{(C_2)}\, \underline{\omega}_2 \\ \vdots \\ \underline{\tilde{\omega}}_N\, J_N^{(C_N)}\, \underline{\omega}_N \end{bmatrix} \tag{1.53}
$$

where $J_i^{(C_i)}$ is the moment of inertia of the i-th body computed with respect to its center of mass. Thus, Eq. (1.46) becomes

$$
\underline{f}_G + \underline{f}_G^* = \underline{0} \tag{1.54}
$$

and, substituting Eqs. (1.49)-(1.50) the following matrix form of the dynamic equations for multibody systems is obtained:

$$
\left\{V^T M V + \Omega^T J_C \Omega\right\} \underline{\dot{u}} = V^T \left\{\underline{F} - M\underline{a}^{(R)}\right\} + \Omega^T \left\{\underline{T} - J_C \underline{\alpha}^{(R)} - \left[\underline{\tilde{\omega}}\, J_C\, \underline{\omega}\right]\right\} \tag{1.55}
$$

By solving Eq. (1.55), the time derivatives of the generalized velocities are obtained. However, the state vector is composed not only of generalized velocities but also of generalized coordinates. Therefore, to complete the system of equations to be integrated, kinematic relations must be added to Eq. (1.55). In the case of a multibody, tree-structured satellite, it is necessary to include the kinematic equations that relate the time derivatives of the generalized coordinates to the generalized velocities:

(i) the attitude kinematic equations associated with the root body. It depends on the specific set of parameters that are chosen to represent the orientation of the root body, and provides the time derivative of this parameter as a function of $\underline{\omega}_1$

(ii) the trajectory equation of the root body: $\underline{\dot{r}}_{C_1}^{(N)} = \underline{v}_{C_1}^{(N)}$

(iii) the kinematic equations associated with the joint variables.

The numerical integration of this set of equations fully describes the motion of the multibody satellite. This represents the minimal-dimension set of kinematic and dynamic equations, which minimizes the computational effort associated with the system's dimension. Moreover, reconstructing the "Eulerian" motion quantities from the time histories of the generalized coordinates and speeds is straightforward. In fact, the linear and angular velocities of the individual bodies composing the multibody satellite are directly obtained using relations (1.28)-(1.29). Unlike the Newton\Euler equations, constraint reactions are not directly obtained from the solution of the dynamic equations. However, these quantities can also be easily reconstructed by exploiting the characteristics of the tree-like configuration, as discussed in the next section.

1.3.3. Constraint reactions in Kane's equations

The absence of constraint reactions is a notable limitation of Kane's formulation. However, for spacecraft with a tree-topology configuration, it is possible to reconstruct the values of constraint reactions easily using an approach based on the Newton/Euler equations. Unlike Kane's method, the Newton/Euler formulation for multibody structures incorporates constraint reactions directly into the state vector. However, the increased number of equations leads to longer computation times. In contrast, Kane's method guarantees a minimal set of ODEs to be integrated, and constraint reactions can be computed using the approach presented in this section. This additional computation only increases the number of algebraic operations while keeping the ODE system unchanged. The procedure follows the subsequent steps:

(i) At a certain time instant, the state vector containing the generalized coordinates and velocities is known. Moreover, after the numerical solution of Kane's equations, one also obtains $\underline{\dot{u}}$.

(ii) Then, by utilizing the partial velocities and remainder accelerations, it is possible to obtain the values of velocities and accelerations for all bodies within the structure (cf. Eqs. (1.28)-(1.29) and (1.31)-(1.32)).

(iii) As a result, the constraint reactions become the only unknowns in the Newton/Euler equations that can be written for all bodies. During this operation, a top-down approach is necessary, starting from the bodies at the ends of the kinematic chains. This is because each of these bodies has only a single joint, and one can then proceed backward along the kinematic chain toward the root body. Specifically, at each iteration of this process (where body i is considered) the constraint reactions at joint Q_i interconnecting the i-th body with its parent are computed as

$$m_i \underline{a}_{C_i} = \underline{f}_i + \underline{f}_i^c \quad \Rightarrow \quad \underline{f}_i^c = m_i \underline{a}_{C_i} - \underline{f}_i \tag{1.56}$$

$$
\begin{aligned}
&\mathrm{J}_{\mathrm{C_i}}\,\underline{\alpha}_{\mathrm{i}}+\underline{\tilde{\omega}}_{\mathrm{i}}\mathrm{J}_{\mathrm{C_i}}\,\underline{\omega}_{\mathrm{i}}=\underline{\mathrm{t}}_{\mathrm{i}}+\sum_{\mathrm{j}}\underline{\tilde{\mathrm{r}}}_{\mathrm{C_iP_{ij}}}\,\underline{\mathrm{f}}_{\mathrm{ij}}+\underline{\mathrm{t}}_{\mathrm{i}}^{\mathrm{c}}+\underline{\tilde{\mathrm{r}}}_{\mathrm{C_iQ_i}}\,\underline{\mathrm{f}}_{\mathrm{i}}^{\mathrm{c}}\\
&\Rightarrow\quad \underline{\mathrm{t}}_{\mathrm{i}}^{\mathrm{c}}=\mathrm{J}_{\mathrm{C_i}}\,\underline{\alpha}_{\mathrm{i}}+\underline{\tilde{\omega}}_{\mathrm{i}}\mathrm{J}_{\mathrm{C_i}}\,\underline{\omega}_{\mathrm{i}}-\underline{\mathrm{t}}_{\mathrm{i}}-\sum_{\mathrm{j}}\underline{\tilde{\mathrm{r}}}_{\mathrm{C_iP_{ij}}}\,\underline{\mathrm{f}}_{\mathrm{ij}}-\underline{\tilde{\mathrm{r}}}_{\mathrm{C_iQ_i}}\,\underline{\mathrm{f}}_{\mathrm{i}}^{\mathrm{c}}
\end{aligned}
\tag{1.57}
$$

where $\underline{\mathrm{f}}_{\mathrm{i}}=\sum_{\mathrm{j}}\underline{\mathrm{f}}_{\mathrm{ij}}$ is broken down as the sum of all external and contributing internal forces applied at points $\mathrm{P_{ij}}$ belonging to body i. It is worth noting that now $\underline{\mathrm{f}}_{\mathrm{i}}$ and $\underline{\mathrm{t}}_{\mathrm{i}}$ contain also the constraint reactions at the joints interconnecting the i-th body to its children bodies, which are available from the previous steps of computation of this iterative process.

This procedure can be applied whether online, i.e. at each step of the numerical integration, or in a post-processing module. Moreover, it is also possible to switch on the computation only for limited time intervals. In general, this procedure offers the possibility to extract the constraint reactions in the framework of Kane’s equations applied to a multibody tree tropology satellite, guaranteeing a low computational effort.

1.3.4. Motion of the system center of mass

In the context of dynamical modeling for multibody structures, there are some cases where it is needed to evaluate the motion of the center of mass of the overall satellite. It is essential for example when the orbital motion of the spacecraft is considered. In that case, in fact, orbital parameters [42] must be evaluated with respect to the motion of the overall system’s center of mass. It may also be required to kinematically impose a precomputed orbital motion to the multibody spacecraft center of mass, if an accurate orbit propagator is employed in determining the spacecraft trajectory. Moreover, the motion of the center of mass is needed when the total linear and angular momenta must be computed to check if the results of the dynamic analysis are consistent.

While the motion of the centers of mass of each body are separately considered in the Kane’s equations, the motion of the center of mass of the entire spacecraft requires further processing to be computed. Hence, denoting with $\underline{\mathrm{v}}_{\mathrm{C}}^{(\mathrm{N})}$ the velocity of the overall center of mass written in components along the inertial frame, the following transformation holds:

$$
\underline{\mathrm{v}}_{\mathrm{C}}^{(\mathrm{N})}=\underset{\mathrm{N}\leftarrow 1}{\mathrm{R}}\left(\underline{\mathrm{v}}_{\mathrm{C_1}}^{(1)}+\underline{\tilde{\omega}}_{1}^{(1)}\underline{\mathrm{r}}_{\mathrm{C_1C}}^{(1)}+\underline{\dot{\mathrm{r}}}_{\mathrm{C_1C}}^{(1)}\right)
\tag{1.58}
$$

with

$$\underline{r}^{(1)}_{C_1C} = \frac{\sum_{i=1}^{N} m_i \underline{r}^{(1)}_{C_1C_i}}{\sum_{i=1}^{N} m_i} \tag{1.59}$$

$$\dot{\underline{r}}^{(1)}_{C_1C} = \frac{\sum_{i=1}^{N} m_i \dot{\underline{r}}^{(1)}_{C_1C_i}}{\sum_{i=1}^{N} m_i} \tag{1.60}$$

where $\underline{r}^{(1)}_{C_1C}$ and $\dot{\underline{r}}^{(1)}_{C_1C}$ collect the components (resolved in $\underline{\underline{B}}_1$) of the position and velocity of the center of mass of body i relative to the center of mass of body 1 (i.e. the root body). In particular, $\dot{\underline{r}}^{(1)}_{C_1C}$ is obtained, at each time step, using the following expression:

$$\dot{\underline{r}}^{(1)}_{C_1C} = \underset{1\leftarrow i}{R}\, V_i\left(\underline{u}\right)_{\underline{v}_{C_1}=\underline{0},\, \underline{\omega}_1=\underline{0}} \tag{1.61}$$

Setting the linear and angular velocity of the root body (bus) to 0 leads to obtaining the relative velocities of the other bodies with respect to the bus. In fact, from the time derivation of

$$\vec{r}_{C_i} = \vec{r}_{C_1} + \vec{r}_{C_1C_i} \tag{1.62}$$

(where $\vec{r}_{C_1}$ and $\vec{r}_{C_i}$ are the position vectors of the center of mass of the root body and of the i-th body, respectively, taken from the origin of the inertial frame) and from the definition of partial velocities (see Eqs. (1.25) and (1.28)), it is apparent that

$$\vec{v}_{C_i} = \vec{v}_{C_1} + {}^{N}\vec{\omega}^{B_1} \times \vec{r}_{C_1C_i} + \underline{\underline{B}}_1 \dot{\underline{r}}^{(1)}_{C_1C_i} = \underline{\underline{B}}_i V_i \underline{u} \tag{1.63}$$

Hence, to isolate $\dot{\underline{r}}^{(1)}_{C_1C}$, it is sufficient to set null bus velocities in Eq. (1.63), and Eq. (1.61) is obtained as a result.

1.3.5. Computation of the system linear and angular momenta

To check the absence of modeling or coding errors when simulating the motion of multibody spacecraft, it is useful to compute the linear and angular momenta of the system. In fact, in the absence of external forces and torques, the two momenta are conserved, and this behavior must be verified also in numerical simulations.

Linear and angular momenta can be directly computed taking advantage of the matrix form of the dynamic equations that has been presented in Section 1.3.2. In fact, from inspection of Eq. (1.55), it is possible to define

$$\hat{M} \triangleq V^T M V + \Omega^T J_C \Omega \tag{1.64}$$

as the system inertia matrix, or generalized mass matrix, of the multibody spacecraft. This matrix is of fundamental importance in computing the system's momenta. In fact, it can be proven that the following relation holds [43]:

$$\underline{m} = \hat{M}\underline{u} \tag{1.65}$$

where

$$\underline{m} = \begin{bmatrix} \underline{p}_{tot} \\ \underline{h}_{tot}^{C_1} \\ \left\{\underline{h}_i^{C_i}\right\}_{revol} \vee \left\{\underline{p}_i\right\}_{prism} \end{bmatrix} \tag{1.66}$$

is the generalized momentum vector, i.e. the vector containing the total linear momentum of the multibody spacecraft $\left(\underline{p}_{tot}\right)$, the total angular momentum of the system computed with respect to C_1 (the root body's center of mass) $\left(\underline{h}_{tot}^{C_1}\right)$, and the projection of the i-th body linear or angular momentum computed with respect to the i-th body's center of mass (depending on the joint connecting it to its parent body) along the i-th joint partial directions, i.e. the directions of the degrees of freedom allowed by the joint. If the joints allow only 1 degree of freedom, $\underline{h}_i^{C_i}$ and $\underline{p}_i$ are scalars.

The first six components of $\underline{m}$ are the system's total momenta and can be used to check the implementation of multibody equations in a numerical environment. Nonetheless, while the total linear momentum computed from Eq. (1.65) must be conserved and can be directly used, the angular momentum deserves further discussion. In fact, it is well known that, in absence of external dynamic actions, the total angular momentum evaluated with respect to the system center of mass must remain constant. However, the total angular momentum computed from Eq. (1.65) is evaluated with respect to the center of mass of the root body instead of the overall satellite. This happens because the choice of relevant kinematic quantities to describe the motion of the spacecraft led to partial velocities that are referred to the center of mass of the root body (cf. the second block in Eq. (1.39)). In fact, from the computation of Eq. (1.65) the vector $\underline{h}_{tot}^{C_1}$ is obtained, while conservation holds only for $\underline{h}_{tot}^{C}$ where C is the center of mass of the overall system. Thus, from the definition of angular momentum one obtains

$$\underline{h}_{tot}^{C} = \underline{h}_{tot}^{C_1} - \tilde{\underline{r}}_{C_1C}\,\underline{p}_{tot} \tag{1.67}$$

where all vectors are resolved in the root body frame. Specifically, $\underline{p}_{tot}$ and $\underline{h}_{tot}^{C_1}$ are already obtained in the frame $\underline{\underline{B}}_1$ from Eq. (1.65), while $\underline{r}_{C_1C}$ derives from Eq. (1.61).

1.4. Introduction of constraints

In the previous section, Kane's equations were introduced and discussed in the context of a multibody spacecraft, where the only constraints considered were those arising from the interconnections between bodies. These constraints are holonomic and are naturally incorporated into Kane's formulation through the projection of the dynamic equations onto the directions of the partial velocities. This approach effectively eliminates constraint forces and torques from the equations while ensuring that the compatibility conditions are fully satisfied. However, in many practical scenarios, it becomes necessary to introduce additional constraints – both holonomic and nonholonomic. This section addresses that need by presenting a technique that involves an additional projection of Kane's equations. Furthermore, two relevant examples of multibody spacecraft requiring the inclusion of such constraints are analyzed and solved. In both cases, the final equations are then compared to those obtained using the traditional method based on Lagrange multipliers.

1.4.1. A second Kane-like projection of dynamic equations for constrained systems

Once the multibody dynamic equations have been derived, the procedure for incorporating additional constraints remains the same, regardless of whether the unconstrained equations were obtained using Kane's method or the Lagrangian formulation. In fact, the dynamic equations produced by Kane's method are equivalent to those from Lagrange's formulation, provided that the generalized velocities are directly related to the time derivatives of the generalized coordinates. This condition is typically satisfied for the variables used in such simulations, with the exception of attitude representation, where the formulations may differ depending on the choice of parameters used to describe spacecraft orientation. Aside from this distinction, the two methods yield equivalent final equations, allowing constraints to be added using the same procedure in either case.

In the context of Lagrange's formulation, constraints are typically introduced using Lagrange multipliers [35, 36]. This involves adding a set of algebraic constraint equations to the system of ordinary differential equations (ODEs), resulting in an augmented system of differential-algebraic equations (DAEs). While this approach is widely adopted in the literature, it presents two main drawbacks: (i) an increase in the dimensionality of the system, and (ii) the introduction of DAEs, which can lead to challenges related to computational efficiency and numerical stability.

An alternative method for incorporating constraints into dynamic equations is presented in Ref. [46]. This approach is based on projecting the dynamic equations onto directions orthogonal to the additional constraints to be imposed. The underlying principle is analogous to the projection of Newton\Euler equations along the directions of the reaction forces associated with the interconnections between bodies. In this case, the projection is applied to Kane's equations, which themselves result from an initial projection that eliminates interconnection forces. This second projection is performed along directions orthogonal to the generalized constraint forces, which correspond to the projection of the additional constraint reactions onto the partial velocities. It is important to note that, as previously mentioned, this second projection could also be applied to the Lagrangian multibody equations without any loss of consistency. Nonetheless, the focus of this work remains on Kane's methodology, and the discussion is therefore framed within that context.

The general version of the Kane-like methodology to introduce further holonomic and nonholonomic constraints in the dynamic equations of a multibody spacecraft is now presented, with reference to Section 1.2.1 for what concerns the theory of constraints. A multibody system characterized by n generalized coordinated q_i (collected in the column vector $\underline{q}$) and n motion variables $u_{M,i}$ (collected in the column vector $\underline{u_M}$), which are linearly dependent on the time derivative of the generalized coordinates (cf. Eq. (1.10)), is considered. Before the application of the additional constraints, the number of generalized velocities corresponds to the number of motion variables, that is $\underline{u_M} = \underline{u}$. Then, if $m_M = n - p$ velocity constraints are imposed, the set of n motion variables can be divided into two subsets (see Eq. (1.14)): $\underline{u} = \underline{u_I} = \begin{bmatrix} u_1 & \cdots & u_p \end{bmatrix}^T$ and $\underline{u_R} = \underline{u_D} = \begin{bmatrix} u_{p+1} & \cdots & u_n \end{bmatrix}^T$ containing the independent and the dependent motion variables, respectively. Specifically, $\underline{u_I}$ corresponds to the actual set of generalized velocities of the constrained multibody system. The constraint equations can be expressed as

$$\underline{u_D} = A\left(\underline{q}, t\right)\underline{u_I} + \underline{b}\left(\underline{q}, t\right) \tag{1.68}$$

where $A \in \mathbb{R}^{(n-p)\times p}$ and $\underline{b} \in \mathbb{R}^{n-p}$ both depend on the generalized coordinates and time t. It can be proven that, under the constraint equations (1.68), the Kane's dynamical equations can be written as [46]

$$\underline{\tilde{f}_G} + \underline{\tilde{f}_G^*} = A_2\left(\underline{f_G} + \underline{f_G^*}\right) = \underline{0} \tag{1.69}$$

where $\underline{\tilde{f}_G}$, $\underline{\tilde{f}_G^*} \in \mathbb{R}^p$ are the vectors of generalized active forces and generalized inertia forces respectively defined for the constrained system, while $\underline{f_G}$, $\underline{f_G^*} \in \mathbb{R}^n$ are referred to the unconstrained system, and $A_2 = \begin{bmatrix} I_{p\times p} & A^T \end{bmatrix}$ where $I_{p\times p}$ is the identity matrix of dimension p. The generalized inertia force vector can be rewritten as (see Eq. (1.50))

$$\underline{f_G^*} = -\hat{M}\left(\underline{q}, t\right)\underline{\dot{u}_M} - \underline{c_{nl}}\left(\underline{q}, \underline{u_M}, t\right) \tag{1.70}$$

where $\hat{M} \in \mathbb{R}^{n\times n}$ is the generalized mass matrix, while $\underline{c_{nl}} \in \mathbb{R}^n$ is the vector of nonlinear terms of dynamics, which are the terms that do not linearly depend on the time derivative of the motion variables, i.e. (cf. Eq. (1.55))

$$\underline{c_{nl}} \triangleq V^T M \underline{a}^{(R)} + \Omega^T \left\{ J_C \underline{\alpha}^{(R)} + \left[\underline{\tilde{\omega}} J_C \underline{\omega}\right] \right\} \tag{1.71}$$

Substituting Eq. (1.70) in Eq. (1.69) one obtains

$$A_2 \hat{M} \underline{\dot{u}_M} = -A_2 \underline{c_{nl}} + A_2 \underline{f_G} \tag{1.72}$$

To incorporate constraint equation (1.68) into the system, it needs to undergo a time derivation to be expressed in the form of acceleration:

$$\underline{\dot{u}_D} = A\underline{\dot{u}_I} + \dot{A}\underline{u_I} + \underline{\dot{b}} \;\Rightarrow\; A_1 \underline{\dot{u}_M} = \dot{A}\underline{u_I} + \underline{\dot{b}} \tag{1.73}$$

where $A_1 = \begin{bmatrix} -A & I_{(n-p)\times(n-p)} \end{bmatrix}$. Hence, merging of Eqs. (1.72) and (1.73) leads to

$$T\underline{\dot{u}_M} = \left\langle \left[\dot{A}\underline{u_I} + \underline{\dot{b}}\right]^T \quad \left[A_2\left(-\underline{c_{nl}} + \underline{f}^*\right)\right]^T \right\rangle^T \tag{1.74}$$

where the matrix $T = \begin{bmatrix} A_1^T & \left(A_2\hat{M}\right)^T \end{bmatrix}^T \in \mathbb{R}^{n\times n}$ is invertible (the proof is provided in Ref. [46]). The new set of dynamic equations features the time derivatives of the motion variables – not the generalized velocities – as the unknowns. This is because the presence of additional velocity constraints implies that the generalized velocities are now part of the motion variables themselves. The total number of equations in the system is n > p, where p is the number of degrees of freedom (DOFs). Specifically, in the presence of velocity constraints, the minimal set of equations required to describe the system dynamics consists of p equations associated with the DOFs, and (n-p) additional equations arising from the constraints. It is important to note that the velocity constraints referenced here may be either holonomic or nonholonomic. In the case of holonomic constraints defined in terms of configuration variables, a time derivative is required to convert them into their velocity form.

Eq. (1.74) completely describes the motion of a constrained system, without however providing any information about the constraint reactions. To evaluate them, one can consider that, in the presence of additional constraints, the Kane's dynamic equations could be written as in Eq. (1.69) or, alternatively, as

$$\underline{\mathrm{f}_{\mathrm{G}}} + \underline{\mathrm{f}_{\mathrm{G}}^{*}} + \underline{\mathrm{f}_{\mathrm{G}}^{\mathrm{c}}} = \underline{0} \tag{1.75}$$

where $\underline{\mathrm{f}_{\mathrm{G}}^{\mathrm{c}}}$ is the generalized constraint reactions vector associated with the imposed constraints. In fact, in Eq. (1.69), A_2 is the operator of the projection of the Kane's dynamics equations along directions that are orthogonal to these additional constraints. In fact, it can be proven that

$$\mathrm{A}_2 \underline{\mathrm{f}_{\mathrm{G}}^{\mathrm{c}}} = \underline{0} \tag{1.76}$$

Hence, the generalized constraint forces can be obtained by substituting Eq. (1.70) in Eq. (1.75), obtaining that

$$\underline{\mathrm{f}_{\mathrm{G}}^{\mathrm{c}}} = -\underline{\mathrm{f}_{\mathrm{G}}} + \hat{\mathrm{M}}\underline{\dot{\mathrm{u}}_{\mathrm{M}}} + \underline{\mathrm{c}_{\mathrm{nl}}} \tag{1.77}$$

where $\underline{\dot{\mathrm{u}}_{\mathrm{M}}}$ is obtained from Eq. (1.74).

1.4.2. The closed-chain configuration

In the earlier part of this section, the focus was on multibody satellite configurations with a tree-like structure. In such configurations, all kinematic chains are open and form the branches of the tree. However, in some cases, this representation does not accurately reflect the physical scenario being modeled. Certain satellite designs may involve closed kinematic chains, characterized by one or more loops of interconnected bodies. A common example is a multi-armed satellite grasping a target [26]; in this case, the combined system of the chaser and target forms a closed chain, which requires a different modeling approach than that used for a simple tree-like configuration. Nonetheless, there are techniques to convert a closed-chain problem into an equivalent tree structure. One such method is the cut-joint approach [47]. This technique involves breaking the closed chain at an underactuated joint, thereby transforming it into two open chains, while simultaneously imposing kinematic constraints that replicate the behavior of the removed joint. The derivation of the dynamic equations is now presented for a specific case: the slider-crank mechanism. However, it is important to note that this method can be generalized and applied to any closed-chain structure.

The sketch of a slider-crank mechanism is reported in Figure 1.6, (a) before and (b) after the cut open procedure. In the open configuration, the generalized coordinate vector is $\underline{q} = [\theta_1 \quad \theta_2 \quad s_3]^T$ and the motion variables are chosen to be the time derivative of the generalized coordinates. Following the Lagrange or the standard Kane's methodology to derive the system dynamical equations, one obtains the same result, i.e.

$$\hat{M}\underline{\dot{u}_M} + \underline{c_{nl}} = \underline{f_G} + \underline{f_G^c} \tag{1.78}$$

where $\underline{f_G^c}$ is associated with the kinematic constraints that must be imposed to guarantee that the position of Q_3 always coincide C_3. These constraints can be written in the following form:

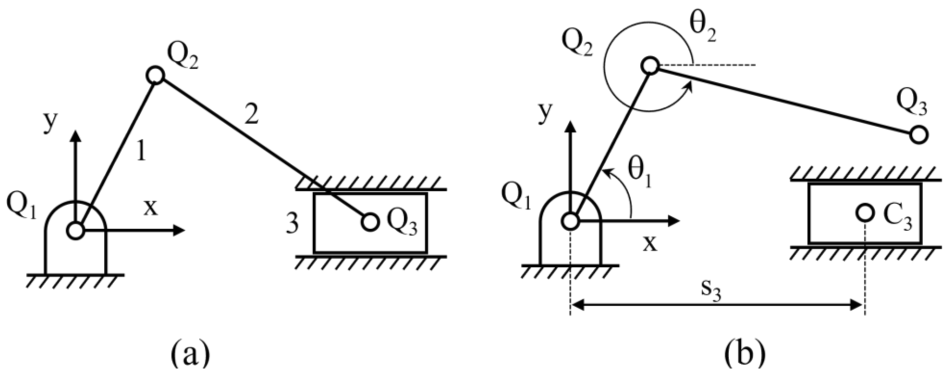

Figure 1.6: Sketch of a slider-crank mechanism (a) before and (b) after the cut open procedure

$$\underline{\Phi}(\underline{q}) = \underline{0} \;\Rightarrow\; \begin{cases} l_1 \cos\theta_1 + l_2 \cos\theta_2 - s_3 = 0 \\ l_1 \sin\theta_1 + l_2 \sin\theta_2 = 0 \end{cases} \tag{1.79}$$

where l_1 and l_2 are the lengths of the two links. Now, Eq. (1.79) can be incorporated in Eq. (1.78) using Lagrange's multipliers or following the Kane's logic described in the previous Section. In the first case, Eq. (1.79) is derived twice with respect to time to obtain

$$\underline{\ddot{\Phi}} \equiv D\underline{\dot{u}_M} = \underline{\gamma} \tag{1.80}$$

where $D \in \mathbb{R}^{(n-p)\times n}$ and $\gamma \in \mathbb{R}^{n-p}$, with $p = 1$ and $n = 3$. Since the vector of Lagrange multipliers $\underline{\lambda} \in \mathbb{R}^{n-p}$ is defined such that

$$\underline{f_G^c} = -D^T\underline{\lambda} \tag{1.81}$$

one finally retrieves the following DAE system:

$$\begin{bmatrix} \hat{M} & D^T \\ D & 0 \end{bmatrix} \begin{Bmatrix} \underline{\dot{u}_M} \\ \underline{\lambda} \end{Bmatrix} = \begin{Bmatrix} \underline{f_G} - \underline{c_{nl}} \\ \underline{\gamma} \end{Bmatrix} \tag{1.82}$$

which is composed of five differential-algebraic equations. On the other side, using the Kane's methodology presented in the previous section, at the beginning only one time derivation of Eq. (1.79) is carried out to obtain

$$\underline{\dot{\Phi}} \equiv C\underline{u_M} = \underline{\beta} \tag{1.83}$$

that can be reconducted to the form of Eq. (1.68). For the case of kinematic constraints imposed in the cut joint approach, both $\underline{B}$ and $\underline{\beta}$ are null vectors, so

$$C\underline{u_M} = \begin{bmatrix} C_I & C_D \end{bmatrix} \begin{bmatrix} \underline{u_I} \\ \underline{u_D} \end{bmatrix} = C_I\underline{u_I} + C_D\underline{u_D} = \underline{0} \ \Rightarrow\ A = -C_D^{-1}C_I \tag{1.84}$$

where $C_D \in \mathbb{R}^{(n-p)\times(n-p)}$ is invertible except at toggle configurations, where the choice of $\underline{u_I}$ must be opportunely modified to avoid singularity, and $C_I \in \mathbb{R}^{(n-p)\times p}$. Hence, following the steps described in the previous section, one obtains a system which expression coincides with Eq. (1.74). Differently from Eq. (1.82), the obtained system is composed of three ordinary differential equations that completely describe the motion of the mechanism. The system alone does not provide any information about constraint reactions, which however can be separately evaluated (in their generalized form) through Eq. (1.77) if required.

The adaptation of the second Kane's projection approach for constrained systems to closed-loop multibody structures, as presented here, has been developed within the framework of this Ph.D. research. Although the treatment of algebraic constraints in Kane's equations has been addressed in isolated contexts in the literature, applications of Kane's formulation to closed-loop spacecraft are uncommon, and the use of the second projection approach in this configuration is even rarer. The implementation of this technique, together with its integration into a general and recursive Kane's framework, constitutes an original contribution of this work.

1.4.3. The sloshing modeling

Various models exist for incorporating fuel sloshing effects into dynamic equations. Simplified approaches often represent sloshing using oscillators (spring mass or pendulum like models) [48]. However, these models do not accurately capture the complex behavior of the fuel inside the tank in microgravity environment. A higher-fidelity alternative is the sliding particle model, where the fuel is modeled as a point mass constrained to move along a predefined constraint surface. This surface, typically spherical or ellipsoidal depending on the tank geometry, is entirely contained within the tank. Its size varies with the fuel level – when the tank is less full, the constraint surface lies closer to the tank walls. To implement this model, it is necessary to enforce the sliding constraint on the fuel's point mass, a task that can be addressed using the projection-based technique introduced in this section.

An even more accurate representation is provided by the contained particle model [49, 50], which extends the sliding particle approach. In this model, the particle is permitted to leave the constraint surface if the inertial forces acting on it are directed toward the interior of the surface. When this occurs, the particle moves freely within the tank until it recontacts the surface, at which point it undergoes an impact and resumes sliding motion. Transitioning from the sliding particle model to the contained particle model is relatively straightforward and can be achieved by incorporating conditional logic into the simulation. Despite this added realism, the central modeling challenge remains the proper enforcement of sliding constraints, which is addressed in the following section.

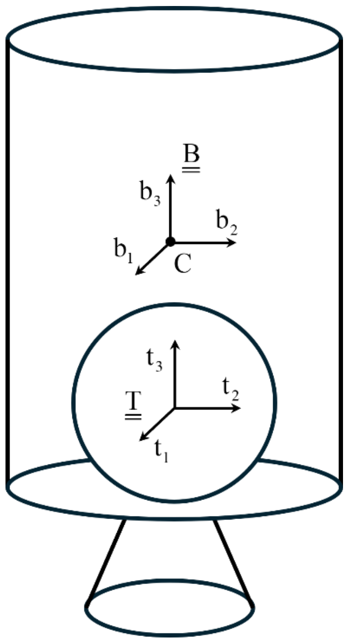

Figure 1.7: sketch of a spacecraft equipped with a tank

In Figure 1.7, a rigid spacecraft equipped with a fuel tank is represented. The bus and tank reference frames are denoted as $\underline{\underline{B}}$ and $\underline{\underline{T}}$ respectively. In this case, a spherical tank is considered, with the constraint surface modeled as a sphere whose radius is inversely proportional to the fill ratio. The fuel is represented as a particle that can either slide along this surface or move freely within it, depending on the acting inertial forces. Within the framework of assembling the spacecraft multibody equations, the system is modeled as a two-body spacecraft: the main body and the propellant. The propellant is a point mass connected to the main body via a 3-DOFs prismatic joint. Let the position vector of the propellant relative to the spherical tank frame be denoted as

$$\underline{\rho} = \begin{bmatrix} t_1 & t_2 & t_3 \end{bmatrix}^T \tag{1.85}$$

the sliding constraint in its velocity form can be expressed as

$$\dot{\underline{\rho}}^T \underline{\rho} = 0 \tag{1.86}$$

that means that the particle velocity must be tangent to the constraint surface. As in the previous Section, the procedure to enforce the constraint both using the Lagrange multipliers, and the presented Kane's-like formulation are discussed. If Eq. (1.86) is derived with respect to time, the following acceleration constraint is obtained:

$$\ddot{\underline{\rho}}^T \underline{\rho} + \dot{\underline{\rho}}^T \dot{\underline{\rho}} = 0 \tag{1.87}$$

The motion variables of the system, corresponding to the generalized velocities prior to the application of constraints, include the linear velocity of the platform's center of mass, the spacecraft's angular velocity, and the relative velocity of the fuel particle with respect to the platform, i.e.

$$\underline{u_M} = \begin{bmatrix} \underline{v}_C{}^T & \underline{\omega}^T & \dot{\underline{\rho}}^T \end{bmatrix}^T \tag{1.88}$$

Then, it is straightforward to reconduct the acceleration constraint in the form $D\dot{\underline{u}}_M = \underline{\gamma}$, with

$$D = \begin{bmatrix} 0_{1\times 6} & \underline{\rho}^T \end{bmatrix} \tag{1.89}$$

$$\underline{\gamma} = -\dot{\underline{\rho}}^T \dot{\underline{\rho}} \tag{1.90}$$

All the blocks to build the set of equations (1.82) are available. Instead, if Kane's formulation for constrained systems is applied, one must divide $\underline{u_M}$ into the independent and dependent sets. If, for example, $\underline{u_D} = \dot{t}_3$, the constraint matrix A is derived from Eq. (1.86) as

$$A = \begin{bmatrix} 0_{1\times 6} & -\dfrac{t_1}{t_3} & -\dfrac{t_2}{t_3} \end{bmatrix} \tag{1.91}$$

It is apparent that the second and third components of A assume very large values for t_3 close to 0. This could lead to numerical instability problems, which can however be avoided by changing the choice of $\underline{u}_D$ in the neighborhood of $t_3 = 0$. Matrix A is the only element needed to derive all the others appearing in the considered formulation. Following the steps reported in Section 1.4.1, it is then possible to obtain the set of dynamic equations of the constrained system.

If the sliding particle model is adopted, the equations of motion remain the same during all the simulation. It is worth noting that, beside the constraint force exchanged between the tank and the bus represented by (1.81), a further friction force exerted by the bus on the fuel mass particle must be included in the model as

$$\underline{f}_{b\to f}^{fr} = -\mu \dot{\underline{\rho}} \tag{1.92}$$

where μ is the friction coefficient [51]. On the other hand, when a more sophisticated model, such as the contained particle model, is considered, the equation of motion must be modified in a piecewise manner. The contained particle model alternates between the sliding motion and the free-floating motion of the fuel particle. Specifically, the sliding motion occurs when the force exerted by the particle on the tank wall (and consequently on the bus) has a positive radial component. In other words, if this reaction force is expressed as

$$\underline{f}_{f\to b}^{cr} = \lambda \underline{\rho} \tag{1.93}$$

where λ is the Lagrange multiplier and $\underline{\rho}$ represents the direction of the force, then the sliding phase lasts until $\lambda > 0$. When $\lambda \leq 0$ the model moves to the free-floating phase by removing the sliding kinematic constraint previously enforced. While in the Lagrange formulation the value of the multiplier is directly provided by the solution of the DAE system, for the Kane's version of constrained system equations it is obtained in two steps: first, the constraint generalized forces must be evaluated through Eq. (1.77), and then λ is computed from Eq. (1.81), with D available from Eq. (1.89). The free-floating motion is characterized by $\|\underline{\rho}\| < R$ with R radius of the tank, and continues until $\|\underline{\rho}\|$ reaches again the value of R. At this point, the impact between the fuel particle and the tank wall must be simulated using one of the well-known contact models, typically employing equivalent stiffness and damping coefficients [52]. After this short-term transient phase, the sliding constraint must be re-enforced, and the sequence of phases continues until the end of the simulation. The contained particle model is widely used to represent sloshing disturbances in space missions, as it strikes a balance between the high fidelity it offers – provided the coefficients are well-tuned – and the relative simplicity of incorporating it into a dynamic model.

The application of the second Kane-like projection to incorporate propellant sloshing effects through a contained-particle model represents another novel aspect of this dissertation. To the best of the author's knowledge, previous studies have included sloshing dynamics within Kane's equations for spacecraft analysis only by employing the Lagrange multipliers approach. The method developed here therefore constitutes a distinctive and original contribution of this work.

1.5. The application of Kane's method in robotics

The Kane's method is widely applied in the robotic framework, due to the computational advantages and the versatility that arises from being the synthesis of Newton\Euler and Lagrange methods. In this Section, the focus is posed on how the most peculiar object of the Kane's formulation, i.e. Kane's Jacobian, is related to some important aspects of robotic modeling. First, it is shown that once deriving the Kane's Jacobian, also the manipulator Jacobian is obtained at once. To complete the modeling of rigid multibody spacecraft, a simplified yet effective strategy is presented, which uses Jacobian matrices to represent a space manipulator system capturing another articulated object

1.5.1. Kane's vs manipulator Jacobian

The manipulator Jacobian plays a crucial role in several aspects of robotics [53]. Among its various applications, it is needed to remind that

(a) it is used to numerically solve the inverse kinematics problem, i.e. deriving the time histories of the joint variables from the end-effector trajectory in the cartesian space

(b) it allows evaluation of the singular or redundant configurations of the manipulator and is also used to compute the manipulability ellipsoids. All this information is of primary importance in the characterization of the manipulator workspace

(c) in statics problems, it is used to relate the end-effector forces to the joint torques, which are essential to opportunely size the joint motors

(d) in the control problems, several techniques are based on the manipulator Jacobian, as the Jacobian Transpose Control and the pseudoinverse techniques.

For all these reasons, the computation of the manipulator Jacobian is a fundamental step in robotic problems. However, when the model of the manipulator is constructed using Kane's formulation, its Jacobian can be obtained with minimal additional effort [54]. Here the Jacobian is defined as the matrix that relates the joint velocities to the linear and angular velocities of the end-effector. Therefore, it can be expressed as:

$$\begin{bmatrix} \underline{v}_E^{(E)} \\ \underline{\omega}_E^{(E)} \end{bmatrix} = \begin{bmatrix} J_P^m \\ J_A^m \end{bmatrix} \underline{u} = J^m \underline{u} \tag{1.94}$$

where symbols $\underline{v}_E^{(E)}$ and $\underline{\omega}_E^{(E)}$ denote the linear and angular velocity of the end-effector projected in the end-effector body frame, while J^m is the Jacobian matrix, composed of the two blocks J_P^m and J_A^m that are related to the position and attitude of the end-effector respectively. The vector of generalized velocities contains only joint variables for fixed-base manipulators. Instead, in the case of mobile robots the base DOFs are included in the generalized speeds and J^m is called "generalized" Jacobian matrix.

It is apparent that Eq. (1.94) is of the same form of Eqs.(1.28)-(1.29). In fact, both relate the same set of generalized speeds to the linear and angular velocities of the bodies composing the multibody structure. If the end-effector is located at one of the free ends of the i-th body of the, the Kane's linear and angular Jacobian obtained from Eqs. (1.39)-(1.40) are in the following relationship with J_P^m and J_A^m:

(i) $V_i \underline{u}$ does not provide the linear velocity of the end-effector, but the linear velocity of the center of mass of the body where the end effector is mounted.

(ii) $\Omega_i \underline{u}$ exactly provides the angular velocity of the end-effector reference frame.

So, while $J_A^m = \Omega_i$, a further but easy algebraic manipulation is need to be applied on V_i to obtain J_P^m. In fact, it is sufficient to consider, in Eq. (1.39), the position vectors that do not end in C_i but in the end-effector point E. With this simple modification, the Jacobian matrix associated with the end-effector position can be easily obtained. Differently from other formulations, when the dynamic model of the manipulator is derived using Kane's method, the robotic manipulator is automatically obtained without further computations.

1.5.2. Linear and angular momenta conservation to model space manipulator capture

Space Manipulator Systems (SMS) are often tasked with capturing a target, which can be either cooperative or non-cooperative [55-57]. In the previous part of this chapter, all the necessary elements to simulate an SMS during the phases before and after target capture have been provided, including cases where two or more arms of the manipulator connect with the target to form one or more closed loops. However, it is also crucial to model the transient capture phase to fully represent the dynamic scenario. If the analysis primarily focuses on the capture process, all the necessary elements for simulating this phase have already been provided. In this case, it is sufficient to introduce contact forces as generalized active forces on the bodies that are in contact. However, an accurate model is required to compute the correct contact forces. Additionally, the contact dynamics often involves high stiffness processes, leading to computational times that are one or more orders of magnitude greater than those associated with the rest of the system dynamics. On the other hand, if the capture is not the central focus of the simulation and is only considered a transition between the pre-grasping and post-grasping phases, a simplified yet valid model can be applied.

If the short-term dynamics of the grasping phase is neglected, the capture can be modeled as an anelastic impact between the target and the chaser. Thus, it is possible to link the kinematics immediately before and after the capture, that is approximated to happen in a single time instant [58, 59]. As specified before, this is not an accurate representation of the continuous grasping process, but an approximation to include the effect of grasping in the simulation, allowing the evaluation of both the appropriate kinematic condition that can be set as the aim to reach for the pre-grasping phase, and the initial conditions of the post-grasping phase simulation. When capture is the focus and must be modeled with high accuracy, more detailed models are employed to achieve the required level of fidelity. In these cases, the geometries of the end-effector and the target interface (e.g., a handle) are explicitly considered, and structural compliance is taken into account. Contact forces are modeled using the mathematical formulation that best fits the physical behavior observed in the real scenario [60].

Recalling Eqs. (1.49), (1.55), (1.64) and (1.71) the equations of motion of a manipulator can be written as

$$\hat{M}\underline{\dot{u}} + \underline{c_{nl}} = \underline{f_G} \tag{1.95}$$

Approximating the capture as an anelastic impact, an impulsive force can be considered applied to the space manipulator. This contribution is already contained in the generalized force vector, which can be broken down into

$$\underline{f}_G = \underline{f}_{G_0} + \left(J_P^m\right)^T \underline{f}_{imp}^{(E)} + \left(J_A^m\right)^T \underline{t}_{imp}^{(E)} = \underline{f}_{G_0} + \left(J^m\right)^T \begin{bmatrix} \underline{f}_{imp}^{(E)} \\ \underline{t}_{imp}^{(E)} \end{bmatrix} \tag{1.96}$$

where $\underline{f}_{imp}^{(E)}$ and $\underline{t}_{imp}^{(E)}$ are the impulsive impact force and torque in components with respect to the end-effector frame, while $\underline{f}_{G_0}$ is the remainder part of the generalized forces. It is worth noting that not only a force, but also an impulsive torque should be considered. In fact, the anelastic impact is seen as an instantaneous establishing of a locking interconnection between two bodies, where both relative and angular motion is impaired. Moreover, the use of the position-associated term of the Jacobian in deriving the generalized forces deserves a further discussion. In fact, as discussed in the previous section, the position part of the Jacobian corresponds to the linear partial velocities matrix associated with the end-effector location (instead of the body center of mass) in the end-effector body, which is the point where $\underline{f}_{imp}^{(E)}$ is applied. Although linear partial velocities not referred to the body center of mass are used, the term $\left(J_P^m\right)^T \underline{f}_{imp}^{(E)}$ is coherent with the previously discussed formulation, where generalized forces are obtained through Eq. (1.49). In fact, being (cf. Eqs. (1.39)-(1.40))

$$\begin{cases} V_E = \begin{bmatrix} \underset{E\leftarrow 1}{R} & -\underset{E\leftarrow 1}{R}\,\underline{\tilde{r}}_{C_1C_E} & \left\{-\underset{E\leftarrow j}{R}\,\underline{\tilde{r}}_{Q_jC_E}\Gamma_j\right\}_{revol} \vee \left\{\underset{i\leftarrow j-1}{R}\,\Sigma_j\right\}_{prism} \end{bmatrix} \\ \Omega_E = \begin{bmatrix} 0_{3\times 3} & \underset{E\leftarrow 1}{R} & \left\{\underset{E\leftarrow j}{R}\,\Gamma_j\right\}_{revol} \vee \left\{0\right\}_{prism} \end{bmatrix} \end{cases} \tag{1.97}$$

and, according to the definition provided in the previous section,

$$J_P^m = \begin{bmatrix} \underset{E\leftarrow 1}{R} & -\underset{E\leftarrow 1}{R}\,\underline{\tilde{r}}_{C_1E} & \left\{-\underset{E\leftarrow j}{R}\,\underline{\tilde{r}}_{Q_jE}\Gamma_j\right\}_{revol} \vee \left\{\underset{i\leftarrow j-1}{R}\,\Sigma_j\right\}_{prism} \end{bmatrix} \tag{1.98}$$

it derives that

$$\left(J_P^m\right)^T \underline{f}_{imp}^{(E)} = V_E{}^T \underline{f}_{imp}^{(E)} + \Omega_E{}^T \underline{t}_{eq}^{(E)} \tag{1.99}$$

where $\underline{t}_{eq}^{(E)} = \underline{\tilde{r}}_{C_EE}^{(E)} \underline{f}_{imp}^{(E)}$ is an additional impulsive torque term that must be applied when moving the point of application of $\underline{f}_{imp}^{(E)}$ from the end-effector location to the center of mass of the body containing the end-effector to maintain the equivalence of the dynamic systems.

If the capture is modeled as an anelastic contact that occurs in a time interval δt much shorter than the time scale of the examined dynamics, Eq. (1.95) can be integrated over the contact duration to obtain

$$\hat{M}\int_{t}^{t+\delta t}\underline{\dot{u}}\,d\tau+\int_{t}^{t+\delta t}\underline{c}_{nl}\,d\tau=\int_{t}^{t+\delta t}\underline{f}_{G_0}\,d\tau+\left(J^m\right)^T\int_{t}^{t+\delta t}\begin{bmatrix}\underline{f}_{imp}^{(E)}\\ \underline{t}_{imp}^{(E)}\end{bmatrix}d\tau \tag{1.100}$$

Terms $\underline{c}_{nl}$ and $\underline{f}_{G_0}$ can be considered constant in the time interval $\delta t \rightarrow 0$ and brought out of the integration, so the integrals associated with them vanish and finally one obtains

$$\hat{M}\delta\underline{u}=\left(J^m\right)^T\underline{f}_{\delta}^{(E)} \tag{1.101}$$

where

$$\delta\underline{u}=\left[\underline{u}(t+\delta t)-\underline{u}(t)\right] \tag{1.102}$$

is the variation of the generalized speeds caused by the capture, and

$$\underline{f}_{\delta}^{(E)}=\int_{t}^{t+\delta t}\begin{bmatrix}\underline{f}_{imp}^{(E)}\\ \underline{t}_{imp}^{(E)}\end{bmatrix}d\tau \tag{1.103}$$

is the impulse associated with the impact force. Using Eq. (1.94) it is possible to correlate the variation of the generalized speeds caused by the capture with the variation of the end-effector linear and angular velocity:

$$\begin{bmatrix}\delta\underline{v}_{E}^{(E)}\\ \delta\underline{\omega}_{E}^{(E)}\end{bmatrix}=J^m\delta\underline{u} \tag{1.104}$$

and, substituting Eq. (1.101), one obtains

$$\begin{bmatrix}\delta\underline{v}_{E}^{(E)}\\ \delta\underline{\omega}_{E}^{(E)}\end{bmatrix}=J^m\hat{M}^{-1}\left(J^m\right)^T\underline{f}_{\delta}^{(E)}=H\underline{f}_{\delta}^{(E)} \tag{1.105}$$

where

$$H\triangleq J^m\hat{M}^{-1}\left(J^m\right)^T \tag{1.106}$$

is the Jacobian inertia of the space manipulator associated with its end-effector [59]. The Jacobian inertia can be seen as an equivalent inertia matrix that allows connecting the end-effector kinematics with forces and torques acting on the end effector. It can be split into two contributions, such that

$$H=\begin{bmatrix}H_P & H_A\end{bmatrix} \tag{1.107}$$

with

$$\mathrm{H_P} = \mathrm{J^m}\hat{\mathrm{M}}^{-1}\left(\mathrm{J_P^m}\right)^{\mathrm{T}} \tag{1.108}$$

$$\mathrm{H_A} = \mathrm{J^m}\hat{\mathrm{M}}^{-1}\left(\mathrm{J_A^m}\right)^{\mathrm{T}} \tag{1.109}$$

where $\mathrm{H_P}$ and $\mathrm{H_A}$ are the position and attitude part of the Jacobian inertia, respectively, i.e. the matrices accounting for the effect of end-effector forces and torques separately on the overall robotic arm.

The present formulation allows to investigate the effect of the capture on the overall kinematics of the involved bodies, in the frame of multibody formulation. In the following, a chaser spacecraft is denoted as the spacecraft 1, while the target satellite is named spacecraft 2. The contact occurs between the end-effector point of the chaser and one handle point of the target. The handle can be treated like the end-effector, so a Jacobian inertia can be written to link the impulse on it to the overall kinematics of the articulated target body. Immediately before the capture, the chaser end-effector and the target handle have velocities $\left(\underline{\mathrm{v}}_{\mathrm{E},1}^{(\mathrm{E})}, \underline{\omega}_{\mathrm{E},1}^{(\mathrm{E})}\right)$ and $\left(\underline{\mathrm{v}}_{\mathrm{H},2}^{(\mathrm{H})}, \underline{\omega}_{\mathrm{H},2}^{(\mathrm{H})}\right)$ respectively, where subscript H refers to the handle point while superscript (H) indicates that the vector is expressed in the reference frame associated with the body containing the handle. Considering only the linear velocity – albeit the procedure is the same for the angular velocity –, immediately after the capture both the end effector and the handle must have the same velocity. Expressing all vectors in the end-effector reference frame without any loss of generality, one obtains that

$$\begin{cases} \underline{\mathrm{v}}_{\mathrm{E},1}^{(\mathrm{E})} + \delta\underline{\mathrm{v}}_{\mathrm{E},1}^{(\mathrm{E})} = \underset{\mathrm{E}\leftarrow\mathrm{H}}{\mathrm{R}}\left[\underline{\mathrm{v}}_{\mathrm{H},2}^{(\mathrm{H})} + \delta\underline{\mathrm{v}}_{\mathrm{H},2}^{(\mathrm{H})}\right] \\ \underline{\omega}_{\mathrm{E},1}^{(\mathrm{E})} + \delta\underline{\omega}_{\mathrm{E},1}^{(\mathrm{E})} = \underset{\mathrm{E}\leftarrow\mathrm{H}}{\mathrm{R}}\left[\underline{\omega}_{\mathrm{H},2}^{(\mathrm{H})} + \delta\underline{\omega}_{\mathrm{H},2}^{(\mathrm{H})}\right] \end{cases} \tag{1.110}$$

where $\underset{\mathrm{E}\leftarrow\mathrm{H}}{\mathrm{R}}$ is the rotation matrix from the handle to the end effector frame, which is known because it is considered the same of the time instant preceding the capture. Eq. (1.110) can be rearranged as

$$\begin{bmatrix} \delta\underline{\mathrm{v}}_{\mathrm{E},1}^{(\mathrm{E})} \\ \delta\underline{\omega}_{\mathrm{E},1}^{(\mathrm{E})} \end{bmatrix} - \begin{bmatrix} \underset{\mathrm{E}\leftarrow\mathrm{H}}{\mathrm{R}} & 0_{3\times3} \\ 0_{3\times3} & \underset{\mathrm{E}\leftarrow\mathrm{H}}{\mathrm{R}} \end{bmatrix} \begin{bmatrix} \delta\underline{\mathrm{v}}_{\mathrm{H},2}^{(\mathrm{H})} \\ \delta\underline{\omega}_{\mathrm{H},2}^{(\mathrm{H})} \end{bmatrix} = \begin{bmatrix} \underset{\mathrm{E}\leftarrow\mathrm{H}}{\mathrm{R}} & 0_{3\times3} \\ 0_{3\times3} & \underset{\mathrm{E}\leftarrow\mathrm{H}}{\mathrm{R}} \end{bmatrix} \begin{bmatrix} \underline{\mathrm{v}}_{\mathrm{H},2}^{(\mathrm{H})} \\ \underline{\omega}_{\mathrm{H},2}^{(\mathrm{H})} \end{bmatrix} - \begin{bmatrix} \underline{\mathrm{v}}_{\mathrm{E},1}^{(\mathrm{E})} \\ \underline{\omega}_{\mathrm{E},1}^{(\mathrm{E})} \end{bmatrix} \tag{1.111}$$

and substituting Eq. (1.105) – assuming the positive sign for the impulse acting on the end-effector – one obtains that

$$\mathrm{H}_1 \underline{\mathrm{f}_\delta}^{(\mathrm{E})} + \bar{\mathrm{R}}\mathrm{H}_2 \underline{\mathrm{f}_\delta}^{(\mathrm{H})} = \bar{\mathrm{R}} \begin{bmatrix} \underline{\mathrm{v}}_{\mathrm{H},2}^{(\mathrm{H})} \\ \underline{\omega}_{\mathrm{H},2}^{(\mathrm{H})} \end{bmatrix} - \begin{bmatrix} \underline{\mathrm{v}}_{\mathrm{E},1}^{(\mathrm{E})} \\ \underline{\omega}_{\mathrm{E},1}^{(\mathrm{E})} \end{bmatrix} \tag{1.112}$$

where

$$\bar{\mathrm{R}} = \begin{bmatrix} \underset{\mathrm{E}\leftarrow\mathrm{H}}{\mathrm{R}} & 0_{3\times3} \\ 0_{3\times3} & \underset{\mathrm{E}\leftarrow\mathrm{H}}{\mathrm{R}} \end{bmatrix} \tag{1.113}$$

and one can finally obtain

$$\underline{\mathrm{f}_\delta}^{(\mathrm{E})} = \left\{ \mathrm{H}_1 + \bar{\mathrm{R}}\mathrm{H}_2\bar{\mathrm{R}}^{\mathrm{T}} \right\}^{-1} \left\{ \bar{\mathrm{R}} \begin{bmatrix} \underline{\mathrm{v}}_{\mathrm{H},2}^{(\mathrm{H})} \\ \underline{\omega}_{\mathrm{H},2}^{(\mathrm{H})} \end{bmatrix} - \begin{bmatrix} \underline{\mathrm{v}}_{\mathrm{E},1}^{(\mathrm{E})} \\ \underline{\omega}_{\mathrm{E},1}^{(\mathrm{E})} \end{bmatrix} \right\} \tag{1.114}$$

Once the impulse $\underline{\mathrm{f}_\delta}^{(\mathrm{E})} = -\bar{\mathrm{R}}\underline{\mathrm{f}_\delta}^{(\mathrm{H})}$ acting on both translational and rotational dynamics is computed, Eq. (1.101) is used twice to evaluate the variation of the generalized speeds of both the caser and the target. After the capture, the two spacecraft form a single combined spacecraft composed of both spacecraft. The end-effector of the chaser and the handle of the target become connected via a locking joint. In the case of a different locking mechanism that impairs only relative translation but allows relative rotation, the entire previous procedure can still be applied, with the rotational equations associated with the degrees of freedom of the grasping mechanism being eliminated. In this case, only the linear velocity of the two interface bodies is equated after the capture, while part or all the angular velocity may differ, depending on the number of degrees of freedom of the rotary joint.

Although this approach is drawn from existing literature, integrating it within the framework of Kane's equations and including it among the modeling features presented in this thesis is expected to enhance the overall quality of the work, enabling the representation of a broad range of dynamic phenomena within a unified and coherent framework.

1.6. Concluding remarks

Chapter 1 presented a comprehensive and systematic formulation of the dynamics of rigid multibody space systems based on Kane's method. First, the motivation behind the choice of this formulation are outlined, also through a review of existing multibody modeling approaches, including Newton\Euler and (embedded and augmented) Lagrangian formulations. After evaluating their respective advantages and limitations, the choice of Kane's method was justified due to its balance between intuitive derivation and computational efficiency, particularly for space applications. The formulation adopted a recursive and modular structure that is particularly suited for multibody tree-like configurations, commonly encountered in spacecraft architectures. The kinematics of multibody systems is then addressed, detailing the classification of constraints, the definition of degrees of freedom and generalized velocities, and the introduction of joint partials as essential operators for describing the motion between interconnected bodies. The Kane's Jacobian, composed of linear and angular partial velocities, was derived as a key tool for efficiently projecting Newton\Euler equations along the directions of the system's degrees of freedom. The recursive computation of remainder accelerations was also introduced, enabling aa general and computationally efficient implementation. In the dynamics section, the formulation of generalized active and inertia forces was presented, highlighting how constraint reactions are inherently excluded from Kane's equations due to their orthogonality to partial velocities. This property simplifies the derivation of dynamic equations while enhancing the computational performance. Moreover, useful strategies were provided to compute the system linear and angular momenta, as well as the motion of the center of mass of the spacecraft, which are often of fundamental importance in the dynamic analysis of complex multibody spacecraft. A Kane-based procedure for introducing any constraints – even the nonholonomic ones – was discussed and compared to the more classic use of Lagrange multipliers. This formulation was then applied to model closed-chain configurations and fuel sloshing, further broadening the applicability of the methodology. Additionally, the chapter addressed the integration of kinematic laws, enabling partial prescription of the system motion where required. The chapter ended with the extension of Kane's method to space robotic applications, including a strategy to model capture maneuvers through the interaction of linear and angular momenta. The techniques introduced in Chapter 1 establish a consistent foundation for dynamic modeling of rigid multibody spacecraft, offering modularity, computational efficiency, and compatibility with a wide range of space mission scenarios.

It is important to clearly distinguish between the established theory and the original contributions introduced in this chapter. The general presentation of Kane's equations, their recursive implementation for tree-topology systems, and the fundamental background on multibody dynamics are provided as a review of the classical theory. In this work, however, the equations have been reformulated in an explicit matrix form, which facilitates the software implementation of a multibody dynamics code. In addition, the extension to closed-chain kinematic configurations and the systematic incorporation of sloshing dynamics – via the contained-particle approach and through the second Kane-like projection formulation – represent original contributions of this research. Furthermore, the integration of multiple features within a coherent Kane-based framework, including the ability to compute spacecraft constraint reactions, center-of-mass motion, linear and angular momenta, and the outcome of a manipulator capture, is considered a significant advancement. These developments extend the applicability of

Kane’s method both within and beyond the scope of existing literature, and provide the foundation for the elastic-body extensions presented in Chapter 2.

Chapter 2

Kane's dynamic equations of a multibody flexible spacecraft

In this chapter, the previously introduced Kane formulation is extended to spacecraft composed of both rigid and flexible bodies. The derivation is still carried out in an explicit matrix form for both the kinematic and dynamic equations. Flexible body deformations are modeled within the framework of linear elasticity theory, with particular attention to applications involving flexible appendages consisting of one or more bodies. Within this linear approximation, the stress stiffening effect is incorporated to enhance the reliability of the model. Furthermore, the interaction between gravitational forces and spacecraft elasticity is treated through a detailed formulation that avoids the common simplification of applying gravity at a single point of each body in the multibody structure, thereby improving the physical fidelity of the analysis.

2.1. Linear representations of elasticity

The elasticity of flexible bodies is introduced in the dynamic model by adding a certain number of degrees of freedom associated with the bodies deformation. These degrees of freedom directly derive from the definition of the elastic problem, i.e. the equations of motion associated with the elastic deformation of a flexible body. These equations are obtained from the weak form of the principle of virtual work in the virtual displacement version, i.e.

$$\delta W_S = \delta W_I + \delta W_E \tag{2.1}$$

where

$$\delta W_S = \int_V \underline{s}^T \delta \underline{\varepsilon} \, dV \tag{2.2}$$

is the virtual work of internal elastic forces expressed as a volume integral, being $\underline{s}$ and $\underline{\varepsilon}$ the second Piola-Kirchoff stress vector and the Green-Lagrange strain vector respectively [61]. Moreover,

$$\delta W_I = -\int_V \rho \underline{\ddot{r}}^T \delta \underline{r} \, dV \tag{2.3}$$

and δW_E are the virtual work of inertial and external forces respectively, being ρ and $\underline{r}$ the mass per unit volume and the position vector respectively. In this section, it is assumed that the elastic body is unaffected by rigid-body motion in order to derive the dynamic equations associated solely with the elastic degrees of freedom. When rigid-body motion is included, these equations are augmented to form a generalized system that also incorporates the rigid-body dynamics and the rigid-flexible coupling terms, which will be discussed in the following sections. Then, terms δW_S and δW_I in Eq. (2.1) can be expressed as a function of the only unknown $\underline{w}(\underline{r}, t)$, which is the elastic displacement of the flexible body represented as a vector field depending on time t. In doing this, it is assumed that the body shows a linear elastic behavior, and that only small deformations are admitted. These hypotheses are widely employed in several structural applications, and are considered also in this work, where elastic nonlinearities are not taken into account. Specifically, when accepting only small deformations, the second Piola-Kirchoff stress vector can be substituted with the Cauchy stress vector $\underline{\sigma}$ [61]. This assumption also permits the use of the linearized expression of the Green-Lagrange strain vector as a function of the elastic displacements:

$$\underline{\varepsilon} = D\underline{w} \tag{2.4}$$

where D is a differential operator containing partial derivatives with respect to the cartesian coordinates. Furthermore, under this assumption

$$\underline{\ddot{r}} = \underline{\ddot{w}} \quad \text{and} \quad \delta\underline{r} = \delta\underline{w} \tag{2.5}$$

because the only time-varying part of the position vector is the displacements induced by the elastic deformation. Moreover, if the further assumption of linear elastic material is made, it is possible to link the stress and strain vectors through the following constitutive equation:

$$\underline{\sigma} = C\underline{\varepsilon} = CD\underline{w} \tag{2.6}$$

where C is the symmetric matrix of elastic coefficients.

Once Eqs. (2.4)-(2.6) are substituted in Eq. (2.1) such that $\underline{w}(\underline{r},t)$ is the only unknown, a further manipulation is carried out by applying the separation of variables technique. In fact, the displacement field cam be expressed in terms of an infinite series of the following form:

$$\underline{w}(\underline{r},t)=\sum_{k=1}^{\infty}\underline{\psi}_k(\underline{r})q_{e,k}(t) \tag{2.7}$$

where $\underline{\psi}_k(\underline{r})$ is the k-th shape function, which forms an orthogonal basis that must be consistent with the boundary conditions, and $q_{e,k}(t)$ are the so-called elastic coordinates. Obviously, the representation of Eq. (2.7) must be approximated by truncating the series to n_F terms, obtaining the following matrix form:

$$\underline{w}(\underline{r},t)=\Psi(\underline{r})\underline{q_e}(t) \tag{2.8}$$

where $\Psi(\underline{r})\in\mathbb{R}^{3\times n_F}$ is the shape matrix containing the 3×1 basis vectors associated with point P, whose position is identified by $\underline{r}$, projected in the body frame $\underline{\underline{B}}$, and $\underline{q_e}\in\mathbb{R}^{n_F}$ is the column vector collecting all the considered elastic coordinates. Consequently, the error in the elastic displacement representation reduces as the number of terms in Eq. (2.7) increases. Substituting the truncated form of Eq. (2.7) into Eq. (2.1) under the assumption of linear elasticity, the equation of the linear structural elastic problem can be written as

$$M\underline{\ddot{q}_e}+K\underline{q_e}=\underline{f}_G \tag{2.9}$$

where

$$M=\int_V \rho\Psi^T\Psi dV \tag{2.10}$$

and

$$K=\int_V \Psi^T D^T C D\Psi\, dV \tag{2.11}$$

are the structural mass and stiffness matrices, while $\underline{f}_G$ is the generalized active (external) forces vector. The structural mass and stiffness matrices are obtained through a volume integration of the combination of shape functions and either the density distribution for the mass, or the elastic properties of the structure for the stiffness matrix. It is worth noting that the structural mass matrix is denoted with the same symbol that was used for the generalized mass matrix of Eq. (1.64). In fact, the structural mass matrix corresponds to the generalized mass matrix associated with a single body where the only allowed degrees of freedom are the elastic ones.

The choice of the basis in Eq. (2.7) determines the form of the mass and stiffness matrices. In the framework of Finite Element Method (FEM), for instance, the elastic body is discretized into a finite number of elements and nodes [62]. The elastic coordinates $\underline{q}_e$ represent the translational and rotational degrees of freedom at the body nodes. Each nodal degree of freedom $q_{e,k}$ is associated with a shape function $\underrightarrow{\psi}_k(\underline{r})$, which satisfies the Kronecker delta property: it equals 1 at the associated node's position vector $\underline{r}$, and 0 at the positions of all other nodes. Modeling elasticity through FEM nodal degrees of freedom can be directly employed in the derivation of the dynamic equations for a multibody structure. This approach enables the exact enforcement of boundary conditions, as it allows individual nodal degrees of freedom to be constrained according to the imposed physical restrictions. However, the main drawback of this method lies in the high dimensionality of the resulting elastic problem. Indeed, using FEM shape functions means that the total number of elastic degrees of freedom is equal to the number of nodes multiplied by the number of DOFs per node. Since accurately capturing the flexural behavior requires a sufficiently fine mesh, the number of elastic DOFs can quickly become very large, leading to computational challenges both in algebraic operations and in numerical time integration.

An alternative characterization of the body elasticity comes from the solution of the eigenproblem associated with the linear elastic equations (Eq. (2.9)) [63]. In fact, considering the homogeneous version of Eq. (2.9), i.e.

$$M\underline{\ddot{q}}_e + K\underline{q}_e = \underline{0} \tag{2.12}$$

if the associated solution is of the form

$$\underline{q}_e = \underline{z}\cos(\omega t) \tag{2.13}$$

one obtains that

$$\left(K - \omega^2 M\right)\underline{z} = \underline{0} \tag{2.14}$$

with $\underline{z} \in \mathbb{R}^{n_F}$ eigenvector in the space of the elastic coordinates, while ω^2 is the associated eigenvalue. The former corresponds to the natural mode of the structure, while the latter is the squared natural elastic frequency. From the solution of (2.14), n_F eigenvalues and eigenvectors are obtained. The eigenvectors can be collected in the matrix $Z \in \mathbb{R}^{n_F \times n_{F,red}}$, obtained from the horizontal concatenation of $n_{F,red} \leq n_F$ column eigenvectors. The choice of $n_{F,red}$, which represents the reduced number of elastic degrees of freedom that are used to represent the body flexibility, depends on the trade-off between the computational effort and the required model fidelity: the lower $n_{F,red}$ is, the shorter the computational time, but the less accurate the model becomes.

The new basis Z can be used to operate a change of coordinates. In fact, considering the following transformation

$$\underline{q}_e = Z\underline{q}_f \tag{2.15}$$

and pre-multiplying Eq. (2.12) by Z^T in order to project it along the orthogonal basis, one obtains that

$$Z^T M Z \ddot{\underline{q}}_f + Z^T K Z \underline{q}_f = \underline{0} \tag{2.16}$$

For the properties of Z,

$$\begin{cases} Z^T M\, Z = M_f \\ Z^T K\, Z = K_f \end{cases} \tag{2.17}$$

where

$$\begin{cases} M_f\big|_{kl} = m_k \delta_{kl} \\ K_f\big|_{kl} = m_k \omega_k^2 \delta_{kl} \end{cases} \tag{2.18}$$

where m_k is the k-th modal mass, ω_k is the k-th elastic frequency, and δ_{kl} is the Kronecker delta. If the eigenvectors are normalized with respect to the modal mass, then M_f becomes the identity matrix and the diagonal of K_f only contains the squared elastic frequencies. Finally, the modal shapes for the case of this parametrization of the elastic displacement are derived. Substituting Eq. (2.15) in Eq. (2.8) one obtains that

$$\underline{w} = \Psi \underline{q}_e = \Psi Z \underline{q}_f = \Phi\, \underline{q}_f \tag{2.19}$$

where, if Ψ is the FEM shape matrix, then $\Phi \in \mathbb{R}^{3 \times n_{F,red}}$ is the approximated modal shape matrix associated with the structural eigenmodes. It is approximated because it is obtained as an interpolation of the real modal shapes evaluated only in the nodes of the structure, as it appears from inspection of Figure 2.1 where $\underline{\phi}_k(\underline{r})$ is the k-th approximated modal shape – i.e., the physical vector associated with the k-th column of Φ .

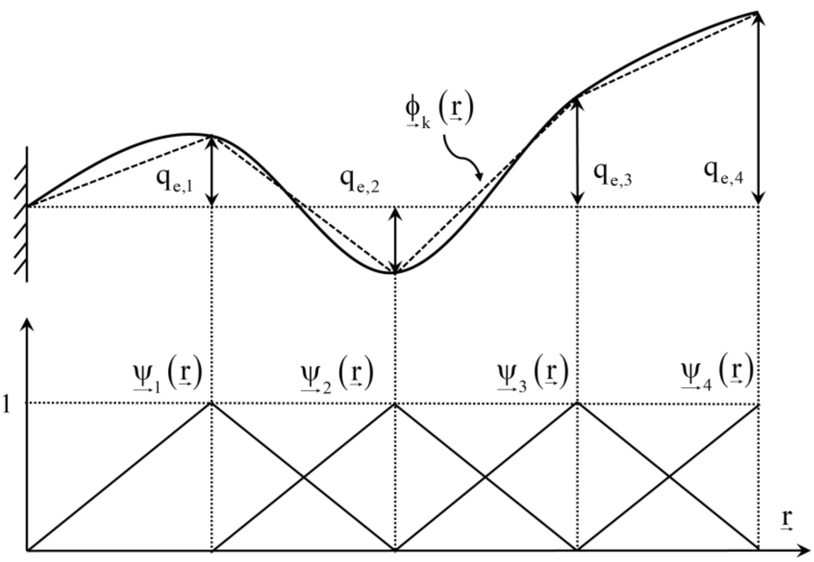

Figure 2.1: Approximated k-th natural mode shape of the elastic body expressed in terms of FEM elastic coordinates

Moreover, the new elastic coordinates $\underline{q_f}$ are also called modal amplitudes. It is important to note that the FEM and eigenmode-based discretization offer the same level of accuracy only when $n_{F,red} = n_F$. In fact, if $n_{F,red} < n_F$, this implies that some eigenmodes have been omitted from the representation of the elastic displacements, whereas the FEM formulation inherently accounts for the effects of all modes, including those associated with higher frequencies. Reducing the number of retained eigenmodes is a common strategy to decrease the computational cost of dynamic simulations. This reduction not only lowers the number of algebraic operations but also speeds up numerical integration, particularly when high-frequency modes are omitted. Typically, the discarded modes are those that have a negligible influence on the overall dynamic behavior of the elastic body.

2.2. Kinematics of multibody systems with elastic components

In the presence of elastic bodies, it is no longer convenient to express kinematic quantities with respect to the center of mass. This is because, as will be shown later, the dynamic equations for elastic bodies must be derived by integrating the generalized inertia and active forces over the body volume. In performing these volume integrals, it is useful to decompose the partial velocities of each body into two components: one independent of the body elastic deformation, and another that depends solely on the deformation [64]. Importantly, only the deformation-dependent component contributes to the volume integrals. To perform this decomposition, a common approach in multibody structure modeling is to express the kinematic quantities, such as partial velocities and remainder accelerations, with respect to the body root joint, i.e., the joint connecting the body to its parent. This choice naturally separates the motion that is independent of the body deformation – the motion of its root joint – from the component that arises exclusively due to the body's elastic deformation.

2.2.1. Recursive kinematics in the floating frame formulation

In this section, the kinematics of a multibody flexible spacecraft is developed within the framework of the floating frame formulation [65]. In this context, both the kinematic quantities and the resulting dynamic equations are expressed with respect to reference frames attached to the elastic bodies. Consistent with standard practice, the body reference frames are placed at the root joints, which connects the body to its parent. This choice ensures that the motion of the reference frame of the i-th body is not influenced by its elastic deformation. However, the refence frame motion may still depend on both the rigid and elastic motion of preceding bodies in the same kinematic chain. As a result, the elastic coordinates of the i-th body represent displacements relative only to its own undeformed configuration. This modeling approach is widely adopted in the literature on linear elasticity, as it yields dynamic equations in which the contributions of rigid and elastic motion are clearly separated.

The generalized velocities for the case of a multibody structure composed of flexible bodies correspond to the ones identified for the rigid case, incremented by the elastic degrees of freedom associated with the bodies deformation. Considering the root body velocities, in this more general version of the formulation any point of the root body can be selected as a reference to compute its linear velocity. Then, referring to this point as Q_1, the first six components of the generalized velocities vector are

$$\underline{u}\big|_{1,\dots,6} = \begin{bmatrix} \underline{v}_{Q_1}^{(1)T} & \underline{\omega}_1^{(1)T} \end{bmatrix}^T \tag{2.20}$$

and the same considerations about the integration of the linear acceleration with respect to the inertial frame (reported in Section 1.2.7) hold. Denoting as n_R the total number of rigid degrees of freedom of the multibody satellite such that the total number of DOFs is $n = n_R + n_F$, the $(n_R - 6)$ components of the generalized velocities vector are

$$\underline{u}\big|_{7,\dots,n_R} = \left[\left(\underline{\dot{\theta}}_i^{\,T} \vee \underline{\dot{s}}_i^{\,T} \right)_{i=2,\dots,N} \right]^T \tag{2.21}$$

that corresponds to Eq. (1.38). The remaining n_F DOFs are then the time derivatives of the elastic coordinates, i.e.

$$\underline{u}\Big|_{n_R,\dots,n} = \underline{\dot{q}}_e^{\ T} \tag{2.22}$$

where $\underline{q}_e$ is now used to denote the generic elastic coordinates, which could be the nodes' degrees of freedom in the case of FEM formulation, or the modal amplitudes of the natural modes of the structure.

Concerning partial velocities, they are obtained from the recursive expression of velocities of the i-th body with respect its parent, denoted as i-1 for simplicity. With respect to the rigid case, now the linear velocities are referred to the root joint, denoted as Q_i (cf. Figures 1.4-1.5), and deformation must be included in the evaluation of the body velocities. In general, the following relation holds:

$$\begin{cases} {}^N\underrightarrow{\omega}^{Q_i} = \underline{\underline{B}}_i \underrightarrow{\omega}_i = {}^N\underrightarrow{\omega}^{Q_{i-1}} + \underrightarrow{\Delta\omega}^{Q_i}\Big|_{flex} + \underrightarrow{\Delta\omega}^{Q_i}\Big|_{rot} \\ \qquad\qquad = {}^N\underrightarrow{\omega}^{Q_{i-1}} + \underrightarrow{\Delta\omega}^{Q_i} \\ {}^N\underrightarrow{v}^{Q_i} = \underline{\underline{B}}_i \underrightarrow{v}_{Q_i} = {}^N\underrightarrow{v}^{Q_{i-1}} + {}^N\underrightarrow{\omega}^{Q_i}_{B_{i-1}} \times \underrightarrow{r}_{Q_{i-1}Q_i} + \underrightarrow{\Delta v}^{Q_i}\Big|_{prism} + \underrightarrow{\Delta v}^{Q_i}\Big|_{flex} \\ \qquad\qquad = {}^N\underrightarrow{v}^{Q_{i-1}} + \underrightarrow{\Delta v}^{Q_i} \end{cases} \tag{2.23}$$

that is the version of Eq. (1.35) for the elastic case. In Eq. (2.23),

$$\underrightarrow{r}_{Q_{i-1}Q_i} = \underrightarrow{r}_{Q_{i-1}Q_i^*} + \sum_{k=1}^{n_F} \underrightarrow{\psi}_k\left(Q_i^*\right) q_{e,k} \tag{2.24}$$

where the asterisk in the superscript of Q_i^* indicates that the generic point in the structure is considered in the undeformed configuration of the body. In Eq. (2.24) symbol $\underrightarrow{\psi}_k$ denotes generically the k-th modal shape, regardless of the specific choice of the modeling of elasticity – e.g., FEM or eigenmodes formulations. When elasticity is considered, the angular velocity is no more a property of the whole body but depends on the point which it refers to. In fact, each point of the body is characterized by a specific value of the elastic rotation. For this reason, a subscript has been added to the symbols denoting angular velocities to specify which point it is referred to. In this framework, the following definitions are introduced:

$${}^N\underrightarrow{\omega}^{Q_i^*} \triangleq {}^N\underrightarrow{\omega}^{Q_{i-1}} + \underrightarrow{\Delta\omega}^{Q_i}\Big|_{rot} \tag{2.25}$$

is the angular velocity of Q_i if elastic rotation is neglected, while

$$ {}^{N}\underrightarrow{\omega}_{B_{i-1}}^{Q_i} \triangleq {}^{N}\underrightarrow{\omega}^{Q_{i-1}} + \underrightarrow{\Delta\omega}^{Q_i}\Big|_{flex} \tag{2.26} $$

is the total angular velocity of Q_i if it is considered to belong to the (i-1)-th body, so the relative rotation of the i-th body with respect the (i-1)-th one about the rotary joint is excluded. Then, the angular velocity can be evaluated as

$$ {}^{N}\underrightarrow{\omega}^{Q_i} = {}^{N}\underrightarrow{\omega}^{Q_i^*} + \sum_{k=1}^{n_F} \underrightarrow{\xi}_k\left(Q_i^*\right)\dot{q}_{e,k} \tag{2.27} $$

where

$$ {}^{N}\underrightarrow{\omega}^{Q_i^*} = {}^{N}\underrightarrow{\omega}^{Q_{i-1}} + \underrightarrow{\Delta\omega}^{Q_i}\Big|_{revol} \tag{2.28} $$

and where $\underrightarrow{\xi}_k$ is the k-th rotational shape function evaluated in Q_i. The rotational modal shapes can be derived considering that, under the assumption of small elastic deformations, the following relation between the elastic displacement $\underrightarrow{w}\left(\underrightarrow{r},t\right)$ and the elastic rotation $\underrightarrow{\gamma}\left(\underrightarrow{r},t\right)$ holds:

$$ \underrightarrow{\gamma}\left(\underrightarrow{r},t\right) \cong \frac{1}{2}\nabla\times\underrightarrow{w}\left(\underrightarrow{r},t\right) \tag{2.29} $$

where $\nabla\times(\;\;)$ is the rotor operator. Then, the rotational modal shapes are obtained from the “translational” ones, presented in the previous section, as

$$ \underrightarrow{\xi}_k = \frac{1}{2}\nabla\times\underrightarrow{\psi}_k \tag{2.30} $$

As in the previous chapter, two possible connections between the bodies are considered, i.e. prismatic and rotary joints. Through a time derivation of Eq. (2.23) for these two cases, one obtains

$$ \begin{cases} \underrightarrow{\Delta\omega}^{Q_i} = \underrightarrow{\Delta\omega}^{Q_i}\Big|_{flex} + \underrightarrow{\Delta\omega}^{Q_i}\Big|_{revol} = \underline{\underline{B}}_i\left[\underset{i\leftarrow i-1}{R}\sum_{k=1}^{n_F}\underline{\xi}_k\left(Q_i^*\right)\dot{q}_{e,k} + \Gamma_i\,\underline{\dot{\theta}}_i\right] \\ \underrightarrow{\Delta v}^{Q_i} = {}^{N}\underrightarrow{\omega}_{B_{i-1}}^{Q_i}\times\underrightarrow{r}_{Q_{i-1}Q_i} + \underrightarrow{\Delta v}^{Q_i}\Big|_{flex} = -\underline{\underline{B}}_{i-1}\left[\underline{\tilde{r}}_{Q_{i-1}Q_i}\,\underline{\omega}_{Q_i/B_{i-1}} + \sum_{k=1}^{n_F}\underline{\psi}_k\left(Q_i^*\right)\dot{q}_{e,k}\right] \end{cases} \tag{2.31} $$

for the rotary joint, and

$$
\begin{cases}
\underrightarrow{\Delta\omega}^{Q_i} = \underrightarrow{\Delta\omega}^{Q_i}\Big|_{flex} = \underline{\underline{B}}_{i-1}\sum_{k=1}^{n_F}\underline{\xi}_k\left(Q_i^*\right)\dot{q}_{e,k} \\
\underrightarrow{\Delta v}^{Q_i} = {}^{N}\underrightarrow{\omega}^{Q_i}_{B_{i-1}} \times \underrightarrow{r}_{Q_{i-1}Q_i} + \underrightarrow{\Delta v}^{Q_i}\Big|_{flex} + \underrightarrow{\Delta v}^{Q_i}\Big|_{prism} \\
\qquad = -\underline{\underline{B}}_{i-1}\left[\tilde{\underline{r}}_{Q_{i-1}Q_i}\,\underline{\omega}_{Q_i/B_{i-1}} + \sum_{k=1}^{n_F}\underline{\psi}_k\left(Q_i^*\right)\dot{q}_{e,k} + \Sigma_i\,\dot{\underline{s}}_i\right]
\end{cases}
\tag{2.32}
$$

for the prismatic interconnection. Symbol $\underline{\omega}_{Q_i/B_{i-1}}$ denotes the 3×1 vector counterpart of ${}^{N}\underline{\omega}^{Q_i}_{B_{i-1}}$. It is worth noting that, in the framework of the linearity assumption for the bodies elasticity, $q_{e,k}$ and its time derivatives are considered as infinitesimal. Then, making the term $\tilde{\underline{r}}_{Q_{i-1}Q_i}\,\underline{\omega}_{Q_i/B_{i-1}}$ explicit one obtains

$$
\begin{aligned}
\tilde{\underline{r}}_{Q_{i-1}Q_i}\,\underline{\omega}_{Q_i/B_{i-1}} &= \left(\tilde{\underline{r}}_{Q_{i-1}Q_i^*} + \sum_{k=1}^{n_F}\tilde{\underline{\psi}}_k q_{e,k}\right)\left(\underline{\omega}_{Q_{i-1}} + \sum_{k=1}^{n_F}\underline{\xi}_k\left(Q_i^*\right)\dot{q}_{e,k}\right) \\
&= \tilde{\underline{r}}_{Q_{i-1}Q_i^*}\,\underline{\omega}_{Q_{i-1}} + \tilde{\underline{r}}_{Q_{i-1}Q_i^*}\sum_{k=1}^{n_F}\underline{\xi}_k\left(Q_i^*\right)\dot{q}_{e,k} + \sum_{k=1}^{n_F}\tilde{\underline{\psi}}_k q_{e,k}\,\underline{\omega}_{Q_{i-1}}
\end{aligned}
\tag{2.33}
$$

where the term containing $q_{e,k}\dot{q}_{e,k}$ has been discarded as a second order infinitesimal.

From the recursive expressions for linear and elastic velocities, one can derive the partial velocity matrices in a general form. As discussed earlier, the linear and angular partial velocities are now referred to the joint locations and are denoted respectively by V_Q and Ω_Q. Analogous to the rigid case, the generic $3\times n$ block of the partial velocities matrices is expressed as:

$$
V_{Q_i} = \left[\underset{i\leftarrow 1}{R} \quad -\underset{i\leftarrow 1}{R}\,\tilde{\underline{r}}_{Q_1Q_i} \quad \left\langle \left\{-\underset{i\leftarrow j}{R}\,\tilde{\underline{r}}_{Q_jQ_i}\Gamma_j\right\}_{revol} \vee \left\{\underset{i\leftarrow j-1}{R}\,\Sigma_j\right\}_{prism}\right\rangle \quad \left\{V_{Q_i,k}\right\}_{k=1,\dots,n_F}\right]
\tag{2.34}
$$

$$
V_{Q_i,k} = \sum_{m=1}^{i-1}\underset{i\leftarrow m}{R}\left[\underline{\psi}_{m,k}\left(Q_{m+1}^*\right) - \tilde{\underline{r}}_{Q_mQ_i^*}\,\underline{\xi}_{m,k}\left(Q_{m+1}^*\right)\right]
\tag{2.35}
$$

$$
\Omega_{Q_i} = \left[0_{3\times 3} \quad \underset{i\leftarrow 1}{R} \quad \left\langle\left\{\underset{i\leftarrow j}{R}\,\Gamma_j\right\}_{revol} \vee \left\{0\right\}_{prism}\right\rangle \quad \left\{\Omega_{Q_i,k}\right\}_{k=1,\dots,n_F}\right]
\tag{2.36}
$$

$$
\Omega_{Q_i,k} = \sum_{m=1}^{i-1}\underset{i\leftarrow m}{R}\,\underline{\xi}_{m,k}\left(Q_{m+1}^*\right)
\tag{2.37}
$$

where $\underline{\psi}_{m,k}$ represents the modal shape associated with the m-th body and with the k-th elastic DOF. If the k-th elastic DOF does not influence the m-th body, $\underline{\psi}_{m,k} = \underline{0}$. The same logic to the rotational modal shapes $\underline{\xi}_{m,k}$. In Eqs. (2.35) and (2.37) the index m spans only the bodies that belong to the same kinematic chain as is i-th body.

The next step is to determine the remainder accelerations. By following a similar procedure to the rigid-body case, the remainder accelerations for rotary joints are given by:

$$\begin{cases} \underline{a}_{Q_i}^{(R)} = \underset{i\leftarrow i-1}{R}\left[\underline{a}_{Q_{i-1}}^{(R)} - \tilde{\underline{\omega}}_{Q_i/B_{i-1}}\tilde{\underline{r}}_{Q_{i-1}Q_i}\underline{\omega}_{Q_i/B_{i-1}} - \tilde{\underline{r}}_{Q_{i-1}Q_i}\underline{\omega}_{Q_i}^{\oplus} + 2\tilde{\underline{\omega}}_{Q_i/B_{i-1}}\sum_{k=1}^{n_F}\underline{\psi}_{i-1,k}\left(Q_i^*\right)\dot{q}_{e,k}\right] \\ \underline{\alpha}_{Q_i}^{(R)} = \underset{i\leftarrow i-1}{R}\left[\underline{\alpha}_{Q_{i-1}}^{(R)} + \tilde{\underline{\omega}}_{Q_i/B_{i-1}}\sum_{k=1}^{n_F}\underline{\xi}_{i-1,k}\left(Q_i^*\right)\dot{q}_{e,k}\right] + \dot{\Gamma}_i\underline{\dot{\theta}}_i + \tilde{\underline{\omega}}_{Q_i}\Gamma_i\underline{\dot{\theta}}_i \end{cases} \tag{2.38}$$

For prismatic joints, the remainder accelerations take the following form:

$$\begin{cases} \underline{a}_{Q_i}^{(R)} = \underset{i\leftarrow i-1}{R}\left[\underline{a}_{Q_{i-1}}^{(R)} - \tilde{\underline{\omega}}_{Q_i/B_{i-1}}\tilde{\underline{r}}_{Q_{i-1}Q_i}\underline{\omega}_{Q_i/B_{i-1}} - \tilde{\underline{r}}_{Q_{i-1}Q_i}\underline{\omega}_{Q_i}^{\oplus} + 2\tilde{\underline{\omega}}_{Q_i/B_{i-1}}\sum_{k=1}^{n_F}\underline{\psi}_{i-1,k}\left(Q_i^*\right)\dot{q}_{e,k}\right] \\ \quad + \tilde{\underline{\omega}}_{Q_i/B_{i-1}}\left(\dot{\Sigma}_i\underline{s}_i + 2\Sigma_i\underline{\dot{s}}_i\right) + \dot{\Sigma}_i\dot{s}_i \\ \underline{\alpha}_{Q_i}^{(R)} = \underset{i\leftarrow i-1}{R}\left[\underline{\alpha}_{Q_{i-1}}^{(R)} + \tilde{\underline{\omega}}_{Q_i/B_{i-1}}\sum_{k=1}^{n_F}\underline{\xi}_{i-1,k}\left(Q_i^*\right)\dot{q}_{e,k}\right] \end{cases} \tag{2.39}$$

where

$$\underline{\omega}_{Q_i}^{\oplus} = \underset{i\leftarrow 1}{\dot{R}}\,\underline{\omega}_1 + \sum_{m=2}^{i-1}\left(\underset{i\leftarrow m}{\dot{R}}\,\Gamma_m\underline{\dot{\theta}}_m + \underset{i\leftarrow m}{R}\,\dot{\Gamma}_m\underline{\dot{\theta}}_m\right) + \dot{\Gamma}_i\underline{\dot{\theta}}_i + \sum_{p=1}^{i-1}\left(\underset{i\leftarrow p}{\dot{R}}\sum_{k=1}^{n_F}\underline{\xi}_{p,k}\left(Q_{p+1}^*\right)\dot{q}_{e,k}\right) \tag{2.40}$$

In Eq. (2.40), the terms depending on the angular joint partial Γ and its time derivative are nonzero only if the m-th body is interconnected to its parent via a rotary joint. As with the partial velocities case, indices m and p proceed along the same kinematic chain of the i-th body, starting from the root of the body. Additionally, the time derivative of a rotation matrix is given by:

$$\underset{B\leftarrow A}{\dot{R}} = -\underline{\omega}_{AB}^{(B)}\underset{B\leftarrow A}{R} \tag{2.41}$$

where $\underline{\omega}_{AB}^{(B)}$ is the angular velocity of frame B with respect to frame A, in components with respect to frame B.

2.2.2. Assembling of elastic bodies

In certain situations, it may be advantageous to group a series of elastic bodies along the same kinematic chain and model them as a single equivalent elastic body for the purpose of describing flexible motion. Meanwhile, the relative rigid-body motion between individual elements is preserved within the overall kinematic framework. This approach is particularly useful in systems composed of repeated structural elements, such as telescopic booms. In such configurations, the individual segments may slide relative to one another via prismatic joints. However, for efficiency and clarity, it is often more practical to represent the elastic behavior of the entire structure as a whole, rather than reconstructing it from the deformation of each component element.

This assembling logic requires certain modifications to the formulation introduced in the previous section. The key idea is to adopt a generalized floating frame approach. When a group of bodies is treated as a single elastic body, the elastic displacement of a specific body within the group is no longer computed relative to its own undeformed configuration, but rather with respect to the undeformed configuration of the entire group. In the traditional, body-based formulation, the elastic displacement of the i-th body reflects only its own deformation. In contrast, the group-based formulation accounts for cumulative deformations, including those of preceding bodies along the same kinematic chain.

Shape functions are then defined for the entire system, either via the Finite Element Method (FEM) or the approximated modes approach (cf. Section 2.1). However, it is important to highlight a key distinction in the procedure:

(i) Approximated natural modes are defined with respect to a fixed, undeformed reference configuration. If the (undeformed) structure undergoes significant changes in its configuration over time due to the rigid joint motion regarding its components, the initially computed modes – valid only for the initial configuration – may become inaccurate. This requires recomputing the modes and their associated natural frequencies at each time step, accounting for the updated geometry and mass/stiffness distribution. Alternatively, one can perform an offline campaign of modal analyses across a fully representative set of possible configurations. This precomputed database of natural modes can then be used during multiple dynamic simulations, avoiding the need to recompute the modes at every time step.

(ii) In contrast, the FEM framework does not inherently require the computation of the structure natural modes. However, due to the typically large number of degrees of freedom, model reduction techniques are often necessary to make simulations computationally feasible (cf. Section 2.3.3). If a modal reduction is employed, the natural modes must be computed – potentially at each time step – to project the dynamics onto a reduced modal subspace, where the elastic unknowns are represented by the selected modal amplitudes. Nevertheless, the FEM approach offers a broader range of modeling capabilities, including the use of alternative reduction strategies and the ability to incorporate geometric or material nonlinearities.

It is worth noting that, within the framework of linear elasticity, there exist conditions that, if verified, lead the two approaches to be equivalent:

(a) The finite element discretization, i.e. the number and configuration of finite elements employed to compute the natural mode in (i), corresponds with the one used in (ii).

(b) A modal reduction technique is employed in (ii).

(c) The same natural modes of the structure are selected in both approaches.

Under these assumptions, the main discrepancy between the two approaches uniquely lies in the order of the operations. In the modal approach, the natural modes are computed first, and the dynamic equations are then derived in modal coordinates. In contrast, in the FEM-based approach, the full dynamic equations are first formulated in nodal coordinates, and, if a modal reduction is applied, the natural modes are computed afterward to reduce the system.

The key difference between the group-based approach and the traditional body-focused formulation lies in the employed reference frame. In the group-based method, elastic deformations are measured relative to the group's overall undeformed state, whereas in the body-based method they are measured locally for each individual body. In both the methodologies, shape functions and elastic coordinates are referred to the overall group frame rather than being associated with a single body. Specifically, the shape functions are resolved with respect to the group frame and are defined over all points of the group, referring to its undeformed configuration. Once the shape functions and elastic coordinates have been defined according to this group-based approach, the relevant kinematic quantities can be computed using the procedure outlined in the previous section, with the following modifications:

1. In the group-based approach, terms related to the flexibility of bodies that belong to the same group as the i-th body and preceding it along the kinematic chain must be removed from the expressions of partial velocities and remainder accelerations. Specifically, terms such as $V_{Q_i,k}$ and $\Omega_{Q_i,k}$ in Eqs. (2.34)-(2.36) must be replaced by zero vectors. This adjustment is necessary because, unlike in the body-focused formulation, nodal displacements and rotations are now computed with respect to the undeformed configuration of the group's root body – the most upstream body

in the group – rather than with respect to the immediately preceding body in the kinematic sequence. As a result, the elastic coordinates behave as absolute quantities within the group, and the corresponding partial velocities and remainder accelerations account only for the rigid-body motion of each body, not for internal elastic contributions from earlier bodies in the same group.

2. For the same reason, the body reference frames in the group-based approach are defined without accounting for relative elastic rotations. Only the relative rotations arising from rotary joints are considered when defining the orientation of each body frame, which is therefore associated purely with the rigid-body configuration. This convention does not exclude the effects of flexibility from the dynamic equations; rather, it reflects the specific choice of elastic coordinates, which express deformations with respect to the group undeformed configuration. As a result, the flexibility-related contributions are not embedded within the partial velocities and remainder accelerations but are treated separately through the elastic coordinates.

Aside from these adjustments, the subsequent steps in deriving the dynamic equations are largely the same for both the body-focused and group-focused approaches. The main differences lie in the expressions for the partial velocities and remainder accelerations, as discussed above. Accordingly, the remainder of this chapter continues with the derivation based on the traditional body-focused floating frame formulation. Nevertheless, the final expressions for the dynamic equations remain valid for the group-based approach and can be applied directly. A practical application of this group-based formulation is presented in Section 4.4, where the dynamics of a Telescopic Tubular Mast (TTM) structure are analyzed and discussed.

2.3. Dynamics

In this section, the dynamic equations governing a multibody flexible spacecraft are derived and analyzed within the framework of linear elasticity. A complete expression for the gravitational force acting on the flexible structure is presented, including the associated modal integrals that arise from the distributed deformation. Subsequently, a modal reduction technique is introduced to efficiently handle elasticity modeled through the FEM formulation within the multibody framework. Finally, the phenomenon of stress stiffening is examined, with key results illustrated for the case of a rotating cantilever beam.

2.3.1. Dynamical equations of a multibody flexible spacecraft

The general form of Kane's dynamic equations of motion, as given in Eq. (1.46), can be extended to multibody spacecraft that include flexible bodies. The key difference lies in the expressions for the generalized inertia and active forces, which are now obtained through volume integrals over all bodies in the system. This leads to a modified version of Eq. (1.46), now expressed with respect to the joints rather than the centers of mass of the bodies, and includes additional terms that capture the elastic behavior of the structure.

Being P_i the generic point belonging to the i-th body of the multibody spacecraft, the expression of the generalized inertia force associated with the i-th body and the r-th degrees of freedom of the system is

$$F^*_{G_r} = -\sum_{i=1}^{N} \left\langle \int_{B_i} \underset{\rightarrow}{v}_r^{P_i} \cdot {}^N\underset{\rightarrow}{a}^{P_i} dm_i + \int_{B_i} \underset{\rightarrow}{\omega}_r^{P_i} \cdot \left[\underset{\rightarrow}{dJ}_i \cdot {}^N\underset{\rightarrow}{\alpha}^{P_i} + {}^N\underset{\rightarrow}{\omega}^{P_i} \times \left(\underset{\rightarrow}{dJ}_i \cdot {}^N\underset{\rightarrow}{\omega}^{P_i} \right) \right] \right\rangle \tag{2.42}$$

which also accounts for the rotatory inertia associated with elastic motion. While this term improves the completeness of the dynamic model, its impact on simulation accuracy is typically marginal [66]. In most practical applications, especially where computational efficiency is a priority, such term is omitted as a compromise between model fidelity and analytical tractability. For this reason, the contribution of rotary inertia to elastic motion is generally neglected throughout the remainder of this work, and the dynamic equations are derived from the following expression of the generalized inertia forces:

$$F^*_{G_r} = -\sum_{i=1}^{N} \int_{B_i} \underset{\rightarrow}{v}_r^{P_i} \cdot {}^N\underset{\rightarrow}{a}^{P_i} dm_i \tag{2.43}$$

In this framework, it is worth remarking that only the effect of distributed rotatory inertia on the elastic motion is neglected, while the impact of the concentrated inertia is maintained. In fact, both the partial velocities and remainder accelerations include contributions from the rotational modal shapes (cf. Section 2.2). This plays a crucial role in improving the model accuracy: while the rotational inertia of an individual infinitesimal element is often negligible, this is not the case at the interface where a child body is attached to a parent flexible body [67]. In such instances, the elastic rotation at the connection point plays a critical role in determining the kinematics of not only the child body, but also all subsequent bodies in the downstream portion of the kinematic chain. Therefore, although rotary inertia is often excluded for computational simplicity, its influence must be preserved in the joint locations to correctly capture the propagation of elastic deformation and orientation along the multibody system.

As discussed in the previous section, the relevant kinematic quantities have been derived with respect to the root joint locations, allowing a clear distinction between the terms that are included in the volume integrals over the i-th body and those that are not. In fact, it is possible to break down the quantities appearing in Eq. (2.43) as

$$\underset{\rightarrow}{v}_r^{P_i} = \underset{\rightarrow}{v}_r^{Q_i} + \underset{\rightarrow}{\omega}_r^{Q_i} \times \left(\underset{\rightarrow}{r}_{Q_i P_i^*} + \sum_{k=1}^{n_F} \underset{\rightarrow}{\psi}_{i,k}\left(P_i^*\right) q_{e,k} \right) + \delta_{rs} \underset{\rightarrow}{\psi}_{i,s-n_R}\left(P_i^*\right) \tag{2.44}$$

$$\begin{aligned} {}^N\underset{\rightarrow}{a}^{P_i} = {}& {}^N\underset{\rightarrow}{a}^{Q_i} + {}^N\underset{\rightarrow}{\alpha}^{Q_i} \times \left(\underset{\rightarrow}{r}_{Q_i P_i^*} + \sum_{k=1}^{n_F} \underset{\rightarrow}{\psi}_{i,k}\left(P_i^*\right) q_{e,k} \right) + \sum_{k=1}^{n_F} \underset{\rightarrow}{\psi}_{i,k}\left(P_i^*\right) \ddot{q}_{e,k} \\ & + {}^N\underset{\rightarrow}{\omega}^{Q_i} \times \left[{}^N\underset{\rightarrow}{\omega}^{Q_i} \times \left(\underset{\rightarrow}{r}_{Q_i P_i^*} + \sum_{k=1}^{n_F} \underset{\rightarrow}{\psi}_{i,k}\left(P_i^*\right) q_{e,k} \right) + 2\sum_{k=1}^{n_F} \underset{\rightarrow}{\psi}_{i,k}\left(P_i^*\right) \dot{q}_{e,k} \right] \end{aligned} \tag{2.45}$$

where s is a second index referring to the degree of freedom, with the flexible degrees of freedom corresponding to those for which $s > n_R$, while δ_{rs} is the Kronecker delta. It is worth noting that, in Eqs. (2.44)-(2.45), the angular velocities and acceleration associated with point Q_i instead of point P_i appear. In fact, the elastic angular deformation is associated with the rotation of the nodal rigid body located in point P_i. However, this contribution does not affect the linear velocity and acceleration of the node located in P_i when it is seen a point mass. Substituting Eqs. (2.44) into Eq. (2.43) evaluated only for the i-th body one obtains that

$$\begin{aligned} F_{G_{r,i}}^* = {}& -\underset{\rightarrow}{v}_r^{Q_i} \cdot \int_{B_i} {}^N\underset{\rightarrow}{a}^{P_i} dm_i - \underset{\rightarrow}{\omega}_r^{Q_i} \cdot \int_{B_i} \left\langle \left(\underset{\rightarrow}{r}_{Q_i P_i^*} + \sum_{k=1}^{n_F} \underset{\rightarrow}{\psi}_{i,k}\left(P_i^*\right) q_{e,k} \right) \times {}^N\underset{\rightarrow}{a}^{P_i} \right\rangle dm_i \\ & - \delta_{rs} \int_{B_i} \left\langle \underset{\rightarrow}{\psi}_{i,l}\left(P_i^*\right) \cdot {}^N\underset{\rightarrow}{a}^{P_i} \right\rangle dm_i \end{aligned} \tag{2.46}$$

where index $l = s - n_R$ is introduced for a more compact form because $\underset{\rightarrow}{\psi}_{i,l}$ is defined only when $s > n_R$, and where the following properties of the mixed vector product has been employed:

$$\left(\underset{\rightarrow}{a} \times \underset{\rightarrow}{b}\right) \cdot \underset{\rightarrow}{c} = \underset{\rightarrow}{a} \cdot \left(\underset{\rightarrow}{b} \times \underset{\rightarrow}{c}\right) \tag{2.47}$$

Then, substituting Eq. (2.45) in Eq. (2.46) and considering that, from the definitions of partial velocities and remainder accelerations

$$\begin{cases} {}^N\underset{\rightarrow}{a}^{Q_i} = \underline{\underline{B}}_i \left(V_{Q_i} \underline{u} + \underline{a}_{Q_i}^{(R)} \right) \\ {}^N\underset{\rightarrow}{\alpha}^{Q_i} = \underline{\underline{B}}_i \left(\Omega_{Q_i} \underline{u} + \underline{\alpha}_{Q_i}^{(R)} \right) \end{cases} \tag{2.48}$$

the part of the generalized inertia force (associated with the r-th DOF and the i-th body) that linearly depends on the time derivative of the generalized speeds becomes

$$
\begin{aligned}
F^*_{G_{r,i}}\Big|_{lin} = &-\left(\underline{v}_r^{Q_i}\right)^T \left\langle V_{Q_i}\underline{\dot{u}}\, m_i + \left(\Omega_{Q_i}\underline{\dot{u}}\right)^{\sim} \int_{B_i}\left(\underline{r}_{Q_iP_i^*} + \sum_{k=1}^{n_F}\underline{\psi}_{i,k}\left(P_i^*\right)q_{e,k}\right)dm_i \right. \\
&\left. + \sum_{k=1}^{n_F}\int_{B_i}\underline{\psi}_{i,k}\left(P_i^*\right)dm_i\,\ddot{q}_{e,k}\right\rangle \\
&-\left(\underline{\omega}_r^{Q_i}\right)^T \left\langle \int_{B_i}\left(\underline{r}_{Q_iP_i^*} + \sum_{k=1}^{n_F}\underline{\psi}_{i,k}\left(P_i^*\right)q_{e,k}\right)^{\sim} dm_i V_{Q_i}\underline{\dot{u}} \right. \\
&-\int_{B_i}\left(\underline{r}_{Q_iP_i^*} + \sum_{k=1}^{n_F}\underline{\psi}_{i,k}\left(P_i^*\right)q_{e,k}\right)^{\sim}\left(\underline{r}_{Q_iP_i^*} + \sum_{k=1}^{n_F}\underline{\psi}_{i,k}\left(P_i^*\right)q_{e,k}\right)^{\sim} dm_i\left(\Omega_{Q_i}\underline{\dot{u}}\right) \\
&\left. + \sum_{k=1}^{n_F}\int_{B_i}\left(\underline{r}_{Q_iP_i^*} + \sum_{k=1}^{n_F}\underline{\psi}_{i,k}\left(P_i^*\right)q_{e,k}\right)^{\sim}\underline{\psi}_{i,k}\left(P_i^*\right)dm_i\,\ddot{q}_{e,k}\right\rangle \\
&-\delta_{rs}\left\langle \int_{B_i}\underline{\psi}_{i,l}^T\left(P_i^*\right)dm_i V_{Q_i}\underline{\dot{u}} - \int_{B_i}\underline{\psi}_{i,l}^T\left(P_i^*\right)\left(\underline{r}_{Q_iP_i^*} + \sum_{k=1}^{n_F}\underline{\psi}_{i,k}\left(P_i^*\right)q_{e,k}\right)^{\sim} dm_i\,\Omega_{Q_i}\underline{\dot{u}} \right. \\
&\left. + \sum_{k=1}^{n_F}\int_{B_i}\underline{\psi}_{i,l}^T\left(P_i^*\right)\underline{\psi}_{i,k}\left(P_i^*\right)dm_i\,\ddot{q}_{e,k}\right\rangle
\end{aligned}
\tag{2.49}
$$

The summation terms, as well as those involving the Kronecker delta, can be compactly expressed in matrix form. In particular,

$$
\sum_{k=1}^{n_F}\int_{B_i}\underline{\psi}_{i,k}\left(P_i^*\right)dm_i\,\ddot{q}_{e,k} = \underline{\Psi}_i\Delta\underline{\dot{u}} \tag{2.50}
$$

$$
\delta_{rs} = \Delta^T \tag{2.51}
$$

where $\underline{\Psi}_i$ is the modal shape matrix associated with the i-th body, and

$$
\Delta = \begin{bmatrix} 0_{n_F\times n_R} & I_{n_F\times n_F} \end{bmatrix} \tag{2.52}
$$

In this context, it is important to note that the k-th elastic degree of freedom does not contribute to the motion of the i-th body if it is not associated with that body. Based on Eq. (2.49), the generalized mass matrix of a multibody flexible spacecraft can then be expressed as:

$$\begin{aligned}\hat{M} = {} & V_Q{}^T\left[MV_Q - S_Q\Omega_Q + B\Delta\right] \\ & + \Omega_Q{}^T\left[S_QV_Q + J_Q\Omega_Q + C\Delta\right] \\ & + \Delta^T\left[B^TV_{Q,f} + G^T\Omega_{Q,f} + Y\Delta\right]\end{aligned} \tag{2.53}$$

Here, the matrices $V_{Q,f}$ and $\Omega_{Q,f}$ are the sub-blocks of the linear and angular partial velocities matrices, referring only to the flexible components of the structure. The matrices B and C contain the modal participation factors (MPFs)* [68] related to translational and rotational motion, respectively, while G aggregates the rotational MPFs along with cross-coupling terms that account for the interaction between rotational and elastic dynamics. The terms S_Q and J_Q represent the static and inertia-induced moments contributions for each flexible body, computed with respect to their corresponding joint locations Q_i. These include the effects of elastic deformation on the body's mass distribution and its dynamic response. Finally, the symbol Y is introduced to denote the structural mass matrix, distinguishing it from the overall generalized mass matrix. The structure of these matrices is reported in the following:

$$S = \begin{bmatrix} \underline{\tilde{s}}_{Q_1} & & & 0 \\ & \underline{\tilde{s}}_{Q_2} & & \\ & & \ddots & \\ 0 & & & \underline{\tilde{s}}_{Q_N} \end{bmatrix} \tag{2.54}$$

$$B = \begin{bmatrix} \underline{b}_{1,1} & \underline{b}_{1,2} & \cdots & \underline{b}_{1,n_F} \\ \underline{b}_{2,1} & \underline{b}_{2,2} & \cdots & \underline{b}_{2,n_F} \\ \vdots & \vdots & \vdots & \vdots \\ \underline{b}_{N_F,1} & \underline{b}_{N_F,2} & \cdots & \underline{b}_{N_F,n_F} \end{bmatrix} \tag{2.55}$$

$$C = \begin{bmatrix} \underline{c}_{1,1} & \underline{c}_{1,2} & \cdots & \underline{c}_{1,n_F} \\ \underline{c}_{2,1} & \underline{c}_{2,2} & \cdots & \underline{c}_{2,n_F} \\ \vdots & \vdots & \vdots & \vdots \\ \underline{c}_{N_F,1} & \underline{c}_{N_F,2} & \cdots & \underline{c}_{N_F,n_F} \end{bmatrix} \tag{2.56}$$

* Physical interpretation of Modal Participation Factors Modal participation factors quantify how much each elastic mode contributes to the overall motion – translational or rotational – of the flexible structure. Physically, they express the influence of a specific mode shape on the deformation energy and inertia distribution of the system. In dynamic terms, a high MPF for a particular mode indicates that this mode significantly shapes the system's response under motion or external loading, while modes with low MPFs contribute little. These factors are essential in capturing the coupling between rigid-body dynamics and structural flexibility, as they determine how vibrations and deformations propagate through the spacecraft structure and interact with the system overall movement.

$$G = \begin{bmatrix} \underline{g}_{1,1} & \underline{g}_{1,2} & \cdots & \underline{g}_{1,n_F} \\ \underline{g}_{2,1} & \underline{g}_{2,2} & \cdots & \underline{g}_{2,n_F} \\ \vdots & \vdots & \vdots & \vdots \\ \underline{g}_{N_F,1} & \underline{g}_{N_F,2} & \cdots & \underline{g}_{N_F,n_F} \end{bmatrix} \tag{2.57}$$

Being N_F the number of the flexible bodies composing the multibody structure. In the previous matrices, the following mass and modal integrals appear:

$$\underline{b}_{i,k} = \int_{B_j} \underline{\psi}_{i,k}\, dm \tag{2.58}$$

$$\underline{s}_{Q_i} = \int_{B_j} \underline{r}_{Q_i P_i^*}\, dm + \sum_{k=1}^{n_F} \underline{b}_{i,k} \tag{2.59}$$

$$\underline{c}_{i,k} = \int_{B_j} \tilde{\underline{r}}_{Q_i P_i^*}\, \underline{\psi}_{i,k}\, dm \tag{2.60}$$

$$\underline{g}_{i,l} = \underline{c}_{i,l} + \sum_{k=1}^{n_F} \underline{d}_{i,kl} \tag{2.61}$$

$$\underline{d}_{i,kl} = \int_{B_j} \tilde{\underline{\psi}}_{i,k}\, \underline{\psi}_{i,l}\, dm \tag{2.62}$$

$$N_{i,k} = -\int_{B_j} \tilde{\underline{\psi}}_{i,k}\, \tilde{\underline{r}}_{Q_i P_i^*}\, dm \tag{2.63}$$

$$J_{Q_i} = -\int_{B_j} \tilde{\underline{r}}_{Q_i P_i^*}\, \tilde{\underline{r}}_{Q_i P_i^*}\, dm + \sum_{k=1}^{n_F} \left(N_{i,k} + N_{i,k}{}^T \right) \tag{2.64}$$

For a better understanding of some of the reported modal integrals, it is important to recall the following vector identity:

$$-\tilde{\underline{a}}\tilde{\underline{b}} = \underline{a}^T \underline{b}\, I_{3\times 3} - \underline{a}\underline{b}^T \tag{2.65}$$

which resembles the definition of the moment of inertia.

Using the same methodology adopted for deriving the generalized mass matrix, the nonlinear dynamic terms can also be obtained. These terms arise specifically from the portion of the generalized inertia forces that do not depend on the time derivatives of the generalized velocities. In other words, they capture the velocity-dependent effects – such as Coriolis and centrifugal forces – that contribute to the system's dynamics but are not directly related to acceleration. For conciseness, the explicit derivation of these terms is omitted here. However, by appropriately grouping and reorganizing the resulting expressions into matrix form, the nonlinear dynamics vector takes the following form:

$$\begin{aligned}\underline{c}_{nl} &= V_Q{}^T\left\{M\underline{a}_Q^{(R)} - S_Q\underline{\alpha}_Q^{(R)} - \left[\tilde{\underline{\omega}}S\underline{\omega}\right] + 2\left[\tilde{\underline{\omega}}B\right]\right\} \\ &+ \Omega_Q{}^T\left\{S_Q\underline{a}_Q^{(R)} + J_Q\underline{\alpha}_Q^{(R)} + \left[\tilde{\underline{\omega}}J\underline{\omega}\right] + 2\left[N^T\underline{\omega}\right]\right\} \\ &+ \Delta^T\left\{B^T\underline{a}_{Q,f}^{(R)} + G^T\underline{\alpha}_{Q,f}^{(R)} - \left[\underline{\omega}^T L\underline{\omega}\right] - 2\left[\underline{\omega}^T\underline{d}\right]\right\}\end{aligned} \tag{2.66}$$

where $\underline{a}_{Q,f}^{(R)}$ and $\underline{\alpha}_{Q,f}^{(R)}$ are the remainder accelerations associated only with flexible bodies, and where the terms in square brackets show the following form:

$$\left[\tilde{\underline{\omega}}S\underline{\omega}\right] = \begin{bmatrix} \tilde{\underline{\omega}}_{Q_i}\tilde{\underline{s}}_{Q_i}\underline{\omega}_{Q_i} \\ \tilde{\underline{\omega}}_{Q_2}\tilde{\underline{s}}_{Q_2}\underline{\omega}_{Q_2} \\ \vdots \\ \tilde{\underline{\omega}}_{Q_N}\tilde{\underline{s}}_{Q_N}\underline{\omega}_{Q_N} \end{bmatrix} \tag{2.67}$$

$$\left[\tilde{\underline{\omega}}B\right] = \begin{bmatrix} \tilde{\underline{\omega}}_{Q_i}\sum_{k=1}^{n_F}\underline{b}_{1,k}\dot{q}_{e,k} \\ \tilde{\underline{\omega}}_{Q_2}\sum_{k=1}^{n_F}\underline{b}_{2,k}\dot{q}_{e,k} \\ \vdots \\ \tilde{\underline{\omega}}_{Q_N}\sum_{k=1}^{n_F}\underline{b}_{N,k}\dot{q}_{e,k} \end{bmatrix} \tag{2.68}$$

$$\left[\tilde{\underline{\omega}}J\underline{\omega}\right] = \begin{bmatrix} \tilde{\underline{\omega}}_{Q_i}J_{Q_i}\underline{\omega}_{Q_i} \\ \tilde{\underline{\omega}}_{Q_2}J_{Q_2}\underline{\omega}_{Q_2} \\ \vdots \\ \tilde{\underline{\omega}}_{Q_N}J_{Q_N}\underline{\omega}_{Q_N} \end{bmatrix} \tag{2.69}$$

$$\left[N^T\underline{\omega}\right] = \begin{bmatrix} \sum_{k=1}^{n_F}\left(N_{1,k}\right)^T\dot{q}_k\underline{\omega}_{Q_1} \\ \sum_{k=1}^{n_F}\left(N_{2,k}\right)^T\dot{q}_k\underline{\omega}_{Q_2} \\ \vdots \\ \sum_{k=1}^{n_F}\left(N_{N,k}\right)^T\dot{q}_k\underline{\omega}_{Q_N} \end{bmatrix} \tag{2.70}$$

$$\left[\underline{\omega}^{T} L \underline{\omega}\right]=\begin{bmatrix} \sum_{i=1}^{N} \underline{\omega}_{Q_i}{}^{T} L_{i,1} \underline{\omega}_{Q_i} \\ \sum_{i=1}^{N} \underline{\omega}_{Q_i}{}^{T} L_{i,2} \underline{\omega}_{Q_i} \\ \vdots \\ \sum_{i=1}^{N} \underline{\omega}_{Q_i}{}^{T} L_{i,n_F} \underline{\omega}_{Q_i} \end{bmatrix} \tag{2.71}$$

$$\left[\underline{\omega}^{T} \underline{d}\right]=\begin{bmatrix} \sum_{i=1}^{N} \underline{\omega}_{Q_i}{}^{T} \left(\sum_{k=1}^{n_F} \underline{d}_{i,1k} \dot{q}_{e,k}\right) \\ \sum_{i=1}^{N} \underline{\omega}_{Q_i}{}^{T} \left(\sum_{k=1}^{n_F} \underline{d}_{i,2k} \dot{q}_{e,k}\right) \\ \vdots \\ \sum_{i=1}^{N} \underline{\omega}_{Q_i}{}^{T} \left(\sum_{k=1}^{n_F} \underline{d}_{i,n_F k} \dot{q}_{e,k}\right) \end{bmatrix} \tag{2.72}$$

where

$$L_{i,k}=N_{i,k}-\sum_{l=1}^{n_F} q_{e,l} \int_{B_j} \underline{\tilde{\psi}}_{i,l} \underline{\tilde{\psi}}_{i,k} \, dm \tag{2.73}$$

Finally, the dynamic equations for a multibody flexible spacecraft can be written as

$$\hat{M} \underline{\dot{u}}+\hat{Z} \underline{u}+\hat{K} \underline{q}+\underline{c}_{nl}=\underline{f}_{G} \tag{2.74}$$

where $\hat{K}$ and $\hat{Z}$ represent the generalized stiffness and damping matrices, respectively. These are constructed as block diagonal matrices: the first block corresponds to the rigid-body degrees of freedom (DOFs) and is a zero matrix (since rigid motions have no associated stiffness or damping), while the second block contains the structural stiffness and damping matrices related to the flexible DOFs [62].

It is important to note that the number of generalized coordinates and generalized speeds associated with the rigid-body DOFs may differ. For instance, when using quaternions to represent spacecraft attitude, the generalized coordinate vector contains four components (the quaternion elements), whereas the corresponding generalized velocity vector contains only three components (those of the angular velocity). This mismatch implies that the dimensions of the generalized stiffness and damping matrices may differ accordingly. Additionally, the structural damping matrix $\hat{Z}$ is formulated based on the chosen physical damping model, which must be consistent with the selected modal representation. For example, if flexibility is modeled using natural modes, then the structural stiffness matrix contains the squared natural frequencies along the main diagonal. In that case, the damping matrix includes terms of the form $2\zeta_k\omega_k$ where ζ_k is the damping ratio and ω_k is the natural frequency of the k-th mode.

2.3.2. Generalized active forces: a focus on gravitational action

In Eq. (2.74), symbol $\underline{f}_G$ denotes the generalized active forces vector. In the framework of the formulation for elastic bodies, it is defined as

$$
\begin{aligned}
f_{G_{r,i}} = {} & \underrightarrow{v}_r^{Q_i} \cdot \int_{B_i} \underrightarrow{df}_i + \underrightarrow{\omega}_r^{Q_i} \cdot \int_{B_i} \left(\underrightarrow{r}_{Q_i P_i^*} + \sum_{k=1}^{n_F} \underrightarrow{\psi}_{i,k}\left(P_i^*\right) q_{e,k} \right) \times \underrightarrow{df}_i \\
& + \delta_{rs} \int_{B_i} \underrightarrow{\psi}_{i,l}\left(P_i^*\right) \cdot \underrightarrow{df}_i + \underrightarrow{\omega}_r^{P_i} \cdot \underrightarrow{T}_i
\end{aligned}
\tag{2.75}
$$

where $\underrightarrow{df}_i$ is the force applied on the infinitesimal element dm_i of the i-th body. If the external or the contributing force is applied on a specific point (i.e. concentrated force), then $\underrightarrow{df}_i$ is equal to the prescribed value in the point of application of the force, and zero in the other points. In that case, $\underrightarrow{df}_i$ can be brought out of the integrals, and the evaluation of the integrals in Eq. (2.75) is straightforward. Instead, in the case of a distributed force, $\underrightarrow{df}_i$ must remain inside the integrals, and their solution depends on the specific form of $\underrightarrow{df}_i$.

In the context of space operations, the gravity force plays a crucial role and deserves a dedicated discussion. Specifically, the infinitesimal gravitational force must be integrated over the body of interest, i.e. [20]

$$
\underrightarrow{df}_i^g = \mu \left\| \underrightarrow{p}_i \right\|^{-3} \underrightarrow{p}_i \, dm_i \tag{2.76}
$$

where μ is the Earth's gravitational constant, and

$$
\underrightarrow{p}_i = r_\oplus \hat{g} - \left(\underrightarrow{r}_{Q_1 Q_i} + \underrightarrow{r}_{Q_i P_i^*} + \sum_{k=1}^{n_F} \underrightarrow{\psi}_{i,k}\left(P_i^*\right) q_{e,k} \right) = r_\oplus \hat{g} - \underrightarrow{r}_{Q_1 P_i} \tag{2.77}
$$

is the position vector joining point P_i to the Earth's center of gravity, being $r_\oplus$ and $\hat{g}$ the magnitude and the direction respectively of the vector from the reference point of the platform Q_1 to the Earth's center of gravity. It is then possible to rewrite

$$\left\|\underrightarrow{p}_i\right\|^{-3} = \left(\left\|\underrightarrow{p}_i\right\|^2\right)^{-\frac{3}{2}} \tag{2.78}$$

and being

$$\left\|\underrightarrow{p}_i\right\|^2 = \underrightarrow{p}_i \cdot \underrightarrow{p}_i \tag{2.79}$$

one finally obtains

$$\left\|\underrightarrow{p}_i\right\|^{-3} = \left(r_\oplus\right)^{-3}\left[1 - \frac{2}{r_\oplus}\underrightarrow{r}_{Q_1P_i} \cdot \hat{g}\right]^{-\frac{3}{2}} \tag{2.80}$$

At this stage, the only approximation introduced in this discussion is the assumption that $r_\oplus \gg \left\|\underrightarrow{r}_{Q_1P_i}\right\|$, which is generally reasonable in the considered scenario. Thus, by applying the Maclaurin expansion series at the first order to Eq. (2.80), it becomes

$$\left\|\underrightarrow{p}_i\right\|^{-3} \cong \left(r_\oplus\right)^{-3}\left[1 + \frac{3}{r_\oplus}\underrightarrow{r}_{Q_1P_i} \cdot \hat{g}\right] \tag{2.81}$$

and, substituting in Eq. (2.76), one obtains

$$\underrightarrow{df}_i^{\,g} = \frac{\mu}{\left(r_\oplus\right)^2}\left\{\hat{g} - \frac{\underrightarrow{r}_{Q_1P_i}}{r_\oplus} + \frac{3}{r_\oplus}\left(\underrightarrow{r}_{Q_1P_i} \cdot \hat{g}\right)\hat{g}\right\}dm_i \tag{2.82}$$

where the infinitesimal of higher order – specifically, terms containing $\left(r_\oplus\right)^{-4}$ – have been neglected. Finally, Eq. (2.82) is used to obtain the three contributions of the gravitational force on translation, rotation and elastic motion appearing in Eq. (2.75) that become, after the projection of physical vectors along the i-th body frame

$$\int_{B_i} \underline{df}_i^{\,g} = \frac{\mu}{\left(r_\oplus\right)^2}\left\{m_i \underset{i\leftarrow 1}{R}\,\underline{g} - \frac{m_i \underset{i\leftarrow 1}{R}\,\underline{r}_{Q_1Q_i} + \underline{s}_{Q_i}}{r_\oplus} + \frac{3\underset{i\leftarrow 1}{R}\,\underline{g}\left[\underline{g}^T \underset{1\leftarrow i}{R}\left(m_i \underset{i\leftarrow 1}{R}\,\underline{r}_{Q_1Q_i} + \underline{s}_{Q_i}\right)\right]}{r_\oplus}\right\} \tag{2.83}$$

$$\int_{B_2} \tilde{\underline{r}}_{Q_iP_i}\,\underline{df}_i^{\,g} = \frac{\mu}{\left(r_\oplus\right)^2}\left\{\tilde{\underline{s}}_{Q_i} \underset{i\leftarrow 1}{R}\,\underline{g} - \frac{\tilde{\underline{s}}_{Q_i} \underset{i\leftarrow 1}{R}\,\underline{r}_{Q_1Q_i}}{r_\oplus} + \frac{3\left(\underset{i\leftarrow 1}{R}\,\underline{g}\right)^{\sim}\left[J_{Q_i}^{g} + \tilde{\underline{s}}_{Q_i}\left(\underset{i\leftarrow 1}{R}\,\underline{r}_{Q_1Q_i}\right)^T\right]\left(\underset{i\leftarrow 1}{R}\,\underline{g}\right)}{r_\oplus}\right\} \tag{2.84}$$

$$\int_{B_2} \underline{\psi}_{i,l}^{T} \underline{df}_{i}^{g} = \frac{\mu}{\left(r_{\oplus}\right)^{2}} \left\{ \underline{b}_{i,l}^{T} \underset{i\leftarrow 1}{R}\,\underline{g} - \frac{\underline{b}_{i,l}^{T} \underset{i\leftarrow 1}{R}\,\underline{r}_{Q_1Q_i} + n_{i,l}^{g}}{r_{\oplus}} \right.$$

$$\left. + \frac{3\left(\underset{i\leftarrow 1}{R}\,\underline{g}\right)^{T} \left[\underline{b}_{i,l} \left(\underset{i\leftarrow 1}{R}\,\underline{r}_{Q_1Q_i} \right)^{T} + L_{i,l}^{g} \right] \left(\underset{i\leftarrow 1}{R}\,\underline{g} \right)}{r_{\oplus}} \right\} \tag{2.85}$$

where the following "gravitational modal integrals" appear:

$$N_{i,k}^{g} = \int_{B_i} \underline{\psi}_{i,k}\left(P_i^*\right) \underline{r}_{Q_iP_i^*}^{T}\, dm_i \tag{2.86}$$

$$J_{Q_i}^{g} = \int_{B_i} \underline{r}_{Q_iP_i^*} \underline{r}_{Q_iP_i^*}^{T}\, dm_i + \sum_{k=1}^{n_F} \left(N_{i,k}^{g} + N_{i,k}^{g\,T} \right) q_{e,k} \tag{2.87}$$

$$L_{i,l}^{g} = N_{i,l}^{g} + \sum_{k=1}^{n_F} q_{e,k} \int_{B_i} \underline{\psi}_{i,l}\left(P_i^*\right) \underline{\psi}_{i,k}\left(P_i^*\right)^{T} dm_i \tag{2.88}$$

$$n_{i,l}^{g} = \int_{B_i} \underline{\psi}_{i,k}\left(P_i^*\right)^{T} \underline{r}_{Q_iP_i^*}\, dm_i + \sum_{k=1}^{n_F} y_{i,lk} q_{e.k} \tag{2.89}$$

$$y_{i,lk} = \sum_{k=1}^{n_F} q_{e,k} \int_{B_i} \underline{\psi}_{i,l}\left(P_i^*\right)^{T} \underline{\psi}_{i,k}\left(P_i^*\right) dm_i \tag{2.90}$$

It is worth noting that $y_{i,lk}$ is the component located in the l-th row and k-th column of the structural mass matrix associated with the i-th body. The terms obtained from Eqs. (2.83), (2.84) and (2.85) are then substituted into Eq.(2.75) to obtain the contribution of the gravitational action to the generalized active forces.

The introduction of gravitational modal integrals within the Kane's formulation for multibody flexible spacecraft is one of the major contributions of this work. In fact, the use of Eqs, (2.83)-(2.85) allows for the accurate inclusion of gravitational force contributions in the dynamic model. Such a level of accuracy is essential when modeling elastic space structures. Indeed, relying on a simplified model could lead to a misleading representation of the system elasticity, where elastic oscillations may appear not as a response to actual gravitational forces, but as artifacts of an incorrect representation of the gravity-elasticity interaction [69].

2.3.3. Modal reduction of the FEM system dimension

As discussed in the preceding sections, one of the primary limitations of the Finite Element Method (FEM) lies in the high dimensionality of the resulting system of dynamic equations. This arises because each elastic degree of freedom (DOF) corresponds to nodal displacements and rotations. To accurately capture the geometry and behavior of the structure, a large number of nodes is typically required. However, this leads to computational challenges, such as an increased number of algebraic operations and the inclusion of high-frequency elastic modes, which significantly increase the numerical stiffness of the system and consequently time integration. A viable solution to this problem is the adoption of a hybrid approach that incorporates modal reduction based on the solution of the structural eigenvalue problem [70]. This method reduces the system dimensionality while preserving the FEM ability to rigorously satisfy boundary conditions.

Considering the case of the group-based approach discussed in Section 2.2.2, an entire flexible appendage – comprising several elastic components – is modeled as a single deformable body, where the deformation is defined with respect to the rest configuration of the entire appendage. The use of FEM-derived shape functions ensures that the boundary conditions of each subcomponent are satisfied, though it still introduces the computational burdens noted earlier. Once the dynamic equations governing the spacecraft and its flexible appendage have been derived in the form of Eq. (2.74), the system size can be reduced by numerically solving the generalized eigenvalue problem. Specifically, if the generalized mass matrix $\left(\hat{\mathrm{M}}\right)$ and stiffness matrix $\left(\hat{\mathrm{K}}\right)$ are known, one can solve the generalized form of Eq. (2.14) to obtain the eigenvalues and eigenvectors of the system. The term "generalized" indicates that $\left(\hat{\mathrm{M}}\right)$ and $\left(\hat{\mathrm{K}}\right)$ include not only the elastic properties but also contributions from the rigid-body DOFs of the multibody system, whereas Eq. (2.14) pertains solely to the elastic submatrices.

The solution yields a total number of eigenvalues equal to the number of DOFs in the system. The first n_R eigenvalues – where n_R denotes the number of rigid-body DOFs – are exactly zero. Each corresponding eigenvector has all components equal to zero, except for a unit entry in the position associated with a specific rigid DOF. The remaining n_F eigenvalues correspond to the squared natural frequencies of the structure. Their associated eigenvectors contain zero entries for the rigid DOFs and non-zero components corresponding to the natural modes of the elastic body. Since the FEM elastic coordinates are defined by nodal displacements and rotations, the eigenvectors obtained from this modal analysis represent the modal shapes as a function of these elastic variables. This enables an efficient projection of the elastic motion onto a reduced modal basis, significantly lowering the computational cost while retaining dynamic accuracy.

To achieve this, the modal transformation matrix T – a generalized version of the matrix Z introduced in Eq. (2.15) – is constructed by concatenating the generalized eigenvectors corresponding to the selected elastic modes, along with those associated with the rigid-body DOFs. If $\hat{\mathrm{n}}_{\mathrm{F}}$ denotes the number of retained elastic modes and n_{R} the number of rigid-body DOFs, then $\mathrm{T} \in \mathbb{R}^{(\mathrm{n}_{\mathrm{R}}+\mathrm{n}_{\mathrm{F}})\times(\mathrm{n}_{\mathrm{R}}+\hat{\mathrm{n}}_{\mathrm{F}})}$ Once the modal transformation matrix is defined, the coordinate transformation is performed as follows:

$$\begin{cases} \underline{\mathrm{q}} = \mathrm{T}\underline{\hat{\mathrm{q}}} \\ \underline{\mathrm{u}} = \mathrm{T}\underline{\hat{\mathrm{u}}} \end{cases} \tag{2.91}$$

where $\underline{\mathrm{q}}$ is the original vector of generalized coordinates (typically including nodal displacements and rotations), and $\underline{\hat{\mathrm{q}}}$ is the reduced vector of modal coordinates, comprising both rigid-body motion and selected elastic modal amplitudes. Similarly, $\underline{\mathrm{u}}$ and $\underline{\hat{\mathrm{u}}}$ are the reduced and original vectors of the generalized velocities. This transformation enables the projection of the full-order dynamic model onto a reduced-order modal subspace, thereby yielding a compact and computationally efficient formulation suitable for simulation and control design. Then, the dynamic equations are projected onto the basis represented by T and become

$$\mathrm{T}^{\mathrm{T}}\hat{\mathrm{M}}\mathrm{T}\dot{\underline{\hat{\mathrm{u}}}} + \mathrm{T}^{\mathrm{T}}\hat{\mathrm{Z}}\mathrm{T}\underline{\hat{\mathrm{u}}} + \mathrm{T}^{\mathrm{T}}\hat{\mathrm{K}}\mathrm{T}\underline{\hat{\mathrm{q}}} + \mathrm{T}^{\mathrm{T}}\underline{\mathrm{c}_{\mathrm{nl}}} = \mathrm{T}^{\mathrm{T}}\underline{\mathrm{f}}_{\mathrm{G}} \tag{2.92}$$

The application of modal reduction results in a reduced-order system of dimension $\mathrm{n}_{\mathrm{R}} + \hat{\mathrm{n}}_{\mathrm{F}} < \mathrm{n}_{\mathrm{R}} + \mathrm{n}_{\mathrm{F}}$. This dimensionality reduction leads to significantly faster computations, particularly beneficial in time-domain simulations. Moreover, by selectively discarding only the higher-frequency/higher damped modes, which typically contribute less to the structural dynamics of interest, the numerical stiffness of the system is reduced, allowing for larger integration time steps if Runge-Kutta like algorithms are used [71]. As previously mentioned, this approach is commonly used to accelerate computations when one or more elastic bodies are modeled in the dynamic equations using FEM shape functions. In fact, it allows the natural modes, represented by the eigenvectors and eigenvalues, to be directly expressed in terms of the nodal displacements and rotations relative to the undeformed configuration of the body or group of bodies (cf. Figure 2.1 and Section 2.2.2).

This reduction corresponds to truncating the order of the shape functions when modal shapes are used to represent body elasticity. In both this case and in the modal reduction of a FEM-based approach, a certain number of modes (frequencies) are discarded in order to achieve a trade-off between accuracy and the computational cost of the numerical simulation. The appropriate choice consists of retaining only those modes that have a significant influence on the dynamics of interest. Typically, the lower-frequency modes dominate the deformation behavior of the structure, while higher-frequency modes often contribute less unless specifically excited. This aspect is particularly advantageous, since lower-frequency modes also impose less stringent restrictions on the timestep size of the numerical integration. A quantitative assessment of modal importance can be obtained from the modal participation factors (MPFs) or, equivalently, from the modal effective mass (or modal mass fraction) [61], which is derived directly from the MPFs and the system mass matrix. By inspecting these quantities, one can identify which modes have the greatest influence on system dynamics and define a threshold below which modes can safely be neglected. Finally, it is important to retain modes with natural frequencies close to the excitation frequencies, in order to avoid excluding potential resonance phenomena from the representation.

As a concluding remark, it is valuable to discuss the truncation procedure in the context of the assembling strategy discussed in Section 2.2.2. Considering a flexible appendage composed of several elastic substructures as a single elastic body allows for a more accurate and customizable characterization of its elastic behavior. In this formulation, one can directly select the modes (and their associated frequencies) that best capture the overall flexibility of the appendage. Conversely, if each sub-block is modeled as an individual elastic body, the number of retained modes for the entire appendage cannot be lower than the number of its components. For example, if only the lowest mode of each substructure is retained, the assembled system will necessarily include at least the first $\mathrm{N_B}$ frequencies, with $\mathrm{N_B}$ equal to the number of elastic sub-bodies. This approach introduces two main limitations: (i) it restricts the possibility of discarding unnecessary frequencies, and (ii) it does not allow a priori knowledge of which global appendage frequencies are represented in the final system without an additional modal analysis of the complete structure. For these reasons, in the case of structures discussed in Section 2.2.2 such as deployable booms, it is generally preferable to adopt the grouping strategy as it yields a clearer and more adjustable definition of the elastic properties of the appendage.

2.3.4. Stress stiffening in Kane's equations: the beam case

In Section 2.1, the structural flexibility of the system was modeled under the assumption of small elastic deformations and linear elastic material behavior. Within this framework, the dynamic equations were derived by neglecting all second-order infinitesimal terms, i.e., terms involving the products of elastic coordinates and/or their time derivatives. While this simplification is valid for small deformations, it removes the influence of stress stiffening effects from the equations. Stress stiffening refers to the phenomenon where the bending stiffness of a structure changes as a function of the internal normal stress state [72]. A classic example is buckling, where compressive axial stresses reduce the effective lateral stiffness of a structure, potentially causing instability. Conversely, tensile axial stresses increase the effective bending stiffness, as seen in pre-tensioned systems such as the strings of a guitar.

Crucially, this phenomenon does not require introducing geometric or material nonlinearities. It arises naturally from the correct linearization of the nonlinear kinematic description of the system. In other words, stress stiffening can be captured within a linear elastic model, provided that all the linear terms are retained in the equations. However, the dynamic equations derived in Section 2.3.1 do not account for stress stiffening. This omission stems from the sequence of linearization used. In those equations, the partial velocities were derived directly from already linearized expressions for the body velocities. As a result, the projection of the Newton\Euler equations onto the generalized coordinates fails to retain specific terms that are linear in the elastic coordinates but arise from nonlinear velocity expressions – terms that are essential to capture stress stiffening. In contrast, the correct procedure within Kane's methodology involves [63, 64]:

1. First deriving the nonlinear expressions of the body velocities, including all relevant coupling between rigid and elastic motion.

2. Then computing the nonlinear partial velocities from these expressions.

3. Finally, linearizing the resulting partial velocities and projecting the Newton\Euler equations accordingly.

By skipping the first two steps, the formulation in Section 2.3.1 can be described as "prematurely linearized", and thus, it misses the stress stiffening contributions.

Nonetheless, it is important to note that the formulation previously presented remains valid for many engineering applications, especially in complex three-dimensional geometries, where the nonlinear kinematic expressions of elastic deformations may be difficult (or even impossible) to express explicitly using separation of variables. In such cases, stress stiffening is typically reintroduced a posteriori, by incorporating additional stiffness terms into the model based on precomputed internal force distributions or stress states [74]. To provide a clearer illustration of how stress stiffening terms arise within Kane's framework, the case of a planar elastic beam is examined in the following part of the section [75]. This example enables the explicit derivation of nonlinear velocity expressions and offers a concrete demonstration of how stress stiffening modifies the dynamic behavior of the structure, even under linear elastic assumptions.

The case of the cantilever beam shown in Figure 2.2 is considered. The locked end is mounted on a rotor, that allows the rotation about an axis that can have generic direction.

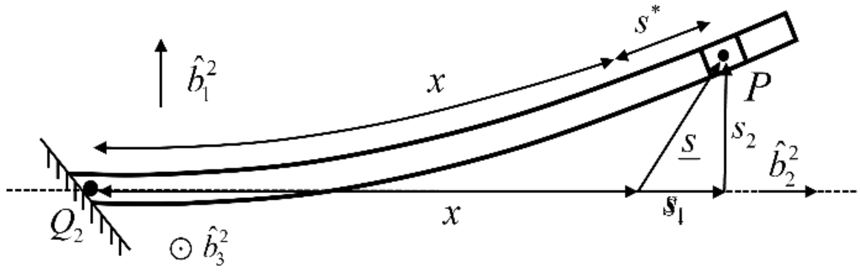

Figure 2.2: Schematics of the flexible boom (clamped-free) configuration

The flexible beam can undergo flexural bending deflection in all directions perpendicular to its longitudinal axis. The previously discussed natural modes decomposition technique is employed to describe its flexural response. Specifically, clamped-free boundary conditions are considered, to derive the modal shapes and natural frequencies of the beam. To account for the stress stiffening effect, it is essential to establish a relationship between the bending elastic displacement and the axial displacement, involving nonlinear elastic kinematics. Considering the overall nonlinear elastic kinematics, the length of a deformed infinitesimal element of the beam can be expressed as

$$\ell(x,t)dx = \sqrt{\left(1+\frac{\partial s_1}{\partial x}\right)^2 + \left(\frac{\partial s_2}{\partial x}\right)^2 + \left(\frac{\partial s_3}{\partial x}\right)^2}\,dx \tag{2.93}$$

where $\underline{s}(x,t) = [s_1 \quad s_2 \quad s_3]^T$ is the elastic displacement vector, whose components are written in the undeformed body frame $\left(\hat{b}_1, \hat{b}_2, \hat{b}_3\right)$. Therefore, with reference to Figure 2.2, the length of the beam from Q to P is determined through the following expression:

$$x + s^*(x,t) = \int_0^x \ell(\sigma,t)d\sigma \tag{2.94}$$

where σ is a dummy variable. If one adopts the following change of variable, i.e.

$$\zeta = x + s_1(x,t) \tag{2.95}$$

Eq. becomes

$$x + s^*(x,t) = \int_0^\zeta \hat{\ell}(\sigma,t)d\sigma \tag{2.96}$$

where

$$\hat{\ell}(\zeta,t) = \sqrt{1+\left(\frac{\partial s_2}{\partial \zeta}\right)^2 + \left(\frac{\partial s_3}{\partial \zeta}\right)^2} \tag{2.97}$$

The axial and bending components of the elastic displacement in the beam are expressed through a modal decomposition, using a set of predefined eigenfunctions. This approach allows the deformation field to be represented as a weighted sum of spatial mode shapes, each modulated by a time-dependent modal amplitude. The decomposition takes the following form:

$$s^*(x,t)=\sum_{i=1}^{n_F}\phi_{1i}(x)q_i(t) \tag{2.98}$$

$$s_2(x,t)=\sum_{i=1}^{n_F}\phi_{2i}(x)q_i(t) \tag{2.99}$$

$$s_3(x,t)=\sum_{i=1}^{n_F}\phi_{3i}(x)q_i(t) \tag{2.100}$$

where n_F denotes the number of flexible degrees of freedom of the beam, $q_i(t)$ is the *i*-th modal amplitude, while $\phi_{1i}(x)$, $\phi_{2i}(x)$ and $\phi_{3i}(x)$ are the i-th eigenfunction associated respectively with axial and the two orthogonal bending displacements.. These eigenfunctions are scalar-valued functions, each representing a spatial distribution corresponding to one component of the beam's elastic motion. The modal shape vectors $\underline{\phi}$ defined in Section 2.1, are constructed from combinations of these scalar eigenfunctions for each mode. By taking the time derivative of the total velocity expression (cf. Eq. (2.96)) and performing the necessary algebraic operations, the following expression is obtained:

$$\begin{aligned}\dot{s}_1 &= \frac{1}{\widehat{\ell}(\zeta,t)}\sum_{i=1}^{n_F}\Bigg\{\phi_{1i}(x)-\sum_{j=1}^{n_F}q_j(t)\int_0^{\zeta}\frac{1}{\widehat{\ell}(\sigma,t)}\\ &\quad\left[\phi'_{2i}(\sigma)\phi'_{2j}(\sigma)+\phi'_{3i}(\sigma)\phi'_{3j}(\sigma)\right]d\sigma\Bigg\}\dot{q}_i(t)\\ &=\sum_{i=1}^{n_F}\chi_i(x,t)\dot{q}_i(t)\end{aligned} \tag{2.101}$$

where $\dot{s}_1=\dot{\zeta}$ (from Eq. (2.95)), while χ_i denotes the coefficient that multiplies the time derivative of the i-th modal coordinate. The term $\chi_i(x,t)$ can be interpreted as the eigenfunction associated not with the axial displacement, but with the elastic displacement along the axis $\hat{b}_1$, which does not coincide with the deformed beam axis. Moreover, symbol $(\ )'$ in Eq. (2.101) denotes the derivative with respect to σ.

At this stage, it is possible to illustrate the process to directly derive a correct form of the linearized dynamic equations for the case of interest. Denoting as $\overline{\ell}$ the linearized version of $\widehat{\ell}$ (cf. Eq.(2.97)), it is apparent that

$$\overline{\ell}(\zeta,t)=\overline{\ell}(\sigma,t)=1 \tag{2.102}$$

because the squared terms appearing in Eq. (2.97) represent infinitesimal quantities of second order in the modal amplitudes. Thus, the linearization of Eq. (2.101) leads to

$$\dot{s}_1=\sum_{i=1}^{v}\left[\phi_{1i}-\sum_{j=1}^{n_F}q_j\left(\beta_{ij}+\gamma_{ij}\right)\right]\dot{q}_i=\sum_{i=1}^{v}\overline{\chi}_i\dot{q}_i \tag{2.103}$$

where

$$\beta_{ij}\triangleq\int_0^{\zeta}\phi_{2i}'(\sigma)\phi_{2j}'(\sigma)d\sigma \tag{2.104}$$

$$\gamma_{ij}\triangleq\int_0^{\zeta}\phi_{3i}'(\sigma)\phi_{3j}'(\sigma)d\sigma \tag{2.105}$$

and $\overline{\chi}_i$ is the linearized form of χ_i. It is apparent that a second order term in the modal coordinates and their time derivatives appears in Eq.(2.103), i.e.

$$-\sum_{i=1}^{v}\left[\sum_{j=1}^{n_F}\left(\beta_{ij}+\gamma_{ij}\right)q_j\right]\dot{q}_i \tag{2.106}$$

Hence, if Eq. (2.103) is employed to compute the linearized expression of the velocity field along the beam, the second-order coupling term described in Eq. (2.106) omitted. This leads to the simplified expression:

$$\dot{s}_1(x,t)=\dot{s}^*(x,t)=\sum_{i=1}^{n_F}\phi_{1i}(x)\dot{q}_i(t) \tag{2.107}$$

which suggests that the axial elastic displacement (along the undeformed longitudinal direction) s_1 is decoupled from the transverse bending displacements s_2 and s_3. However, this result is misleading, as it stems from a premature linearization. In reality, there is a geometric coupling between axial and transverse displacements due to the deformation of the beam, and this interaction must be preserved, at least in the computation of the partial velocities, to ensure the correct linearization of the dynamic equations. The component of partial velocities along $\hat{b}_1$ of the nonlinear partial velocity associated with the time derivative of the i-th modal coordinate is obtained from Eq. (2.103), and specifically corresponds to χ_i. Then, the linearized form of this partial velocity just corresponds to the term $\overline{\chi}_i$ appearing in Eq.(2.103). On the other hand, if the same linearized partial velocity were obtained from the linearized expression of the velocity along $\hat{b}_1$, it would consist only of the term ϕ_{1i} (cf. Eq. (2.107)). The critical insight here is that the axial elastic displacement, when expressed along the deformed axis, is indeed uncoupled from the bending displacements. However, this is not true when considering displacements along the undeformed axis, which is the conventional reference for modal expansions. In that context, Eq. (2.103) shows that the axial component of velocity includes contributions that depend on the bending modal amplitudes through the integrals in Eqs. (2.104) and (2.105). This understanding is essential for constructing a well-linearized set of dynamic equations that accurately incorporates stress stiffening effects. Specifically, it demonstrates that the correct projection of the Newton\Euler equations must be performed onto the properly linearized partial velocities, rather than onto prematurely simplified kinematic expressions. This approach ensures that Kane's equations retain the necessary coupling terms to capture stress stiffening in flexible structures.

To explicitly demonstrate the appearance of stress stiffening terms in the dynamic equations, a simplified case is analyzed. Consider the flexible beam depicted in Figure 2.2, modeled as a cantilevered boom rotating at a constant angular velocity ϖ about a fixed axis $\hat{b}_3^2$. Elasticity is represented by a single bending mode corresponding to in-plane deformation. For the sake of simplicity, the axial and out-of-plane deformations are neglected. Accordingly, the elastic displacement field reduces to:

$$s^*(x,t) = 0 \tag{2.108}$$

$$s_2(x,t) = \phi_{21}(x)q_1(t) \tag{2.109}$$

$$s_3(x,t) = 0 \tag{2.110}$$

The linear velocity of a generic point P on the beam, expressed in the body-fixed reference frame, is given by:

$$\underline{v}_P = \tilde{\underline{\varpi}}\underline{r}_{QP} + \dot{\underline{s}}(P,t) \tag{2.111}$$

where $\underline{\varpi} = [0 \quad 0 \quad \varpi]^T$ and $\underline{r}_{QP}$ is the distance from Q to P in the deformed configurations. From Eq. (2.111), it is possible to isolate the nonlinear partial velocity with respect to the generalized coordinate, which needs to be linearized with respect to small elastic displacements. The final form is By applying a linearization in the limit of small elastic displacements, we obtain:

$$V = [-\beta_{11}q_1 \quad \phi_{21} \quad 0]^T \tag{2.112}$$

where

$$\beta_{11} \triangleq \int_0^{\zeta}\left(\frac{\partial \phi_{21}(\sigma)}{\partial \sigma}\right)^2 d\sigma \tag{2.113}$$

Once the linearized partial velocities have been obtained, the acceleration field of the beam can be obtained from the time derivative of (2.111), i.e.

$$\underline{a}_P = \overline{V}\ddot{q}_1 + \underline{a}_P^{(R)} \tag{2.114}$$

where $\overline{V} = [0 \quad \phi_{21} \quad 0]^T$ is the prematurely linearized expression of Eq. (2.112), while $\underline{a}_P^{(R)}$ encompasses the terms of $\underline{a}_P$ that do not rely on the time derivatives of generalized velocities. Projecting the Newton–Euler equations onto the linearized partial velocities yields Kane's dynamic equations in the form:

$$\int_0^L \rho V^T \underline{a}_P \, dx + \omega_b^2 q_1(t) = \int_0^L \rho V^T \overline{V} \, dx \, \ddot{q}_1(t) + \int_0^L \rho V^T \underline{a}_P^{(R)} \, dx + \omega_b^2 q_1(t) = 0 \tag{2.115}$$

where L is the beam length, $\rho(x)$ is the beam mass per unit length, and ω_b is the frequency of the first bending mode. Then, one obtains the final governing equation,

$$\ddot{q}_1(t) + \left\{\omega_b^2 - \varpi^2 + \lambda\varpi^2\right\} q_1(t) = -\dot{\varpi}\int_0^L \rho(x) x \phi_{21}(x) dx \tag{2.116}$$

where the term

$$\lambda = \int_0^L \rho(x)\beta_{11}(x) x \, dx > 1 \tag{2.117}$$

is responsible for the stress stiffening and reflects how centrifugal effects – arising from the beam's rotation – induce axial tension, thereby increasing the effective stiffness of the structure. In Eq. (2.117), the quantity $\beta_{11}(x)$ is expressed as a function of x. This can be easily derived from Eq. (2.113) by applying the variable transformation outlined in Eq. (2.95).

This analysis reveals two competing effects resulting from the interaction between rigid-body rotation and elastic deformation:

1) The term $\left\{\omega_b^2 - \varpi^2\right\} q_1(t)$ associated with the flexible dynamics, tends to reduce the internal restoring force.
2) The stress stiffening effects $\left\{\lambda\varpi^2\right\} q_1(t)$ associated with centrifugal stretching, acts to increase the beam's stiffness.

Importantly, omitting the stress stiffening term would imply that the beam's effective stiffness could vanish under certain conditions – particularly for rapidly rotating systems – resulting in a grossly inaccurate dynamic model. This underscores the necessity of including stress stiffening in any realistic representation of rotating flexible structures.

The introduction of stress stiffening modeling capabilities within the Kane's formulation is not an original contribution of this work [75]. However, due to its relevance in various dynamic scenarios, it has been included in the theoretical discussion of the multibody formulation. This capability is also employed in one of the applications presented in Chapter 4, where it enables a more accurate evaluation of the elastic displacements of the CIMR's rotating antenna. Since the analysis of such dynamic effects in the CIMR case study represents a valuable contribution of this work, the detailed modeling required for this analysis is presented in this chapter, even though it does not constitute an original contribution of the thesis.

2.4. Concluding remarks

Chapter 2 extended the methodology presented in Chapter 1 to the domain of flexible multibody space systems. The main objective was to formulate dynamic equations that accurately represent the coupled rigid-elastic behavior of complex spacecraft architectures. The chapter began with an overview of linear representations of elasticity, comparing two primary modeling approaches: the modal basis and the finite element (FEM) basis. These representations enable the modeling of elastic deformations in flexible components, such as large deployable antennas or solar arrays. The kinematics of flexible multibody systems were formulated using a floating frame approach, with the recursive structure from Chapter 1 adapted to handle the presence of elastic components. The assembling of elastic bodies was addressed, enabling both single-body and multi-body elastic configurations to be modeled effectively. An important modeling choice discussed was the possibility of treating interconnected elastic bodies as a single equivalent elastic entity for the purpose of elastic deformation analysis, while maintaining separate rigid-body representations to simplify the overall dynamics. In the dynamics section, the derivation of the equations of motion for multibody flexible spacecraft was presented. Particular attention was given to the accurate modeling of generalized active forces, with a focus on gravitational interactions. The inclusion of gravity-elasticity coupling effects is in fact essential for predicting deformations and dynamic behavior during orbital maneuvers. The chapter also introduced modal reduction techniques for reducing FEM-based dynamic system dimensions, thereby improving computational efficiency without significantly sacrificing accuracy. Finally, the stress stiffening phenomenon, particularly relevant for rotating flexible structures, was analyzed and integrated into the Kane-based formulation. This capability was introduced in order to increase the modeling accuracy for realistic configurations such as the CIMR satellite with its large rotating antenna. Overall, Chapter 2 generalized the Kane's approach to include flexible dynamics, thereby enabling a unified modeling framework for both rigid and flexible multibody spacecraft. The results of this chapter provide the essential tools for analyzing the coupled dynamics of advanced space systems in realistic operational scenarios.

Chapter 3

Nonlinear techniques for attitude and relative orbit control

This chapter presents new enhancements to feedback nonlinear control techniques for both attitude control and relative motion control. For attitude control, the proposed laws are derived from existing approaches by modifying the structure of the error-dependent terms, in both triaxial and single-axis cases. Their stability is analyzed using Lyapunov's theorem and LaSalle's invariance principle. In the attitude control framework, the steering laws for the two most common categories of momentum exchange devices – i.e., reaction wheels and single-gimbal control momentum gyroscopes – are provided. The presented laws include additional terms with respect to the literature solutions, leading to a more accurate tracking of the desired control torque by the actuator systems. For the relative motion case, a more accurate dynamic formulation is introduced to represent the chases dynamics with respect to a target on a perturbed orbit, and a new control strategy, denoted as Hybrid Predictive Control (HPC), is proposed. In both domains, the novel control strategies are benchmarked against state-of-the-art solutions, clearly demonstrating the performance improvements achieved with the proposed methods.

3.1. Control aspects in space missions involving multibody satellites

Multibody spacecraft have become increasingly relevant in modern space missions due to their versatility and adaptability, particularly in scenarios that require physical interaction with other objects in space. These platforms often include deployable structures, articulated mechanisms, or robotic manipulators, making them especially suitable for complex operations such as on-orbit servicing (OOS), which encompasses tasks like inspection, refueling, repair, assembly, and debris removal [76, 77]. The inherent complexity of these missions places stringent demands on the spacecraft ability to perform precise and coordinated control of both attitude and relative orbital motion. In the context of OOS missions, attitude control is critical not only for maintaining proper orientation with respect to communication links or payload pointing but also for enabling fine alignment during docking and berthing procedures. Simultaneously, relative orbital motion control is necessary to approach, rendezvous with, and operate safely around a target object [78]. For multibody spacecraft, the challenge is amplified due to the internal dynamics introduced by their articulated appendages or moving components, which can influence both the spacecraft mass distribution and its control response.

To address these challenges, this chapter discusses trajectory and attitude control as distinct subsystems, each with its own control objectives and algorithms. This separation is intentional: the proposed control laws are designed to be general-purpose and thus applicable to a wide variety of missions, including those involving single rigid-body spacecraft, rather than being tailored exclusively to multibody platforms. Nevertheless, when applied to multibody spacecraft – as illustrated in the case studies of Chapter 4 – these techniques have proven effective in meeting mission requirements. This is due to several factors:

(a) The novel control techniques presented in this chapter generally demonstrate better performance compared to classical control approaches.

(b) Nonlinear attitude controllers can inherently handle variations in the inertia matrix.

(c) Realistic design choices provide favorable conditions. For instance, the motion of articulated parts is not excessively fast, as in actual operations. Moreover, their motion is planned to keep the spacecraft center of mass as closely aligned as possible with the thruster line of action, thereby reducing imbalances that can nonetheless be compensated by the attitude control system.

(d) OOS operations are assumed to be conducted in a free-floating mode in the very last phases, where attitude control remains active while translational thruster actuation is avoided near the target to ensure safety.

Accordingly, the following sections of this chapter present attitude and relative orbit motion control strategies separately, highlighting the key techniques used in each domain. Their coordinated integration, which is crucial in multibody OOS scenarios [79], will instead be demonstrated through the application examples discussed in Chapter 4.

This work focuses on nonlinear control techniques due to their strong suitability for the class of problems under consideration. In particular, nonlinear control strategies offer the advantage of ensuring global or quasi-global stability in many relevant scenarios, such as those involving large rotational maneuvers or rendezvous operations with spacecraft in highly elliptical and perturbed orbits [80, 81]. These characteristics make nonlinear control especially effective for multibody spacecraft operations, where the system dynamics are inherently nonlinear and require globally consistent behavior across a wide range of configurations. As such, the control strategies presented in the following sections are developed within a fully nonlinear framework, aligning with the specific demands of advanced space missions.

The first part of this chapter focuses on attitude control. It begins by presenting the most commonly used parametrizations for describing attitude kinematics, followed by the main relationships among them. The concept of error kinematics is then introduced, along with the fundamental kinematic and dynamic equations governing attitude motion. Next, triaxial control is addressed by introducing one of the most widely adopted nonlinear attitude control techniques, together with its stability analysis. An enhanced version of this control law is subsequently presented, with a corresponding stability assessment. The discussion then shifts to the reduced-attitude control problem. A nonlinear control law from the literature is introduced, and its stability properties are analyzed. An improved version of this control strategy is also presented, and its stability is similarly assessed. The advantages introduced by the enhanced control laws are then discussed, supported by a numerical analysis. Finally, the chapter reviews attitude actuators, with a specific focus on momentum exchange devices. Steering laws are presented for both reaction wheels and single-gimbal control moment gyroscopes (CMGs), including a singularity avoidance algorithm for the latter.

The second part of the chapter addresses the modeling and control of the relative orbital motion of a chaser spacecraft with respect to a target. The modeling is approached using the Battin-Giorgi formulation, which ensures numerical stability and high-fidelity motion representation. An enhanced version of this formulation is also presented to further improve numerical accuracy. A nonlinear control strategy based on feedback linearization is then introduced. In addition, an improved variant of this control law – denoted as Hybrid Predictive Control (HPC) – is derived, featuring adaptive gains designed to intelligently saturate the control effort. The performance of this adaptive control is analyzed and compared to a traditional saturation approach based solely on control magnitude scaling.

3.2. Attitude kinematics and dynamics

The attitude of a spacecraft can be defined using different parametrizations. First, the definition of attitude comes with the definition of rotation matrix, which has been already presented in Eq. (1.3). Specifically, if $\underline{\underline{N}} = \begin{bmatrix} \hat{n}_1 & \hat{n}_2 & \hat{n}_3 \end{bmatrix}$ is the vectrix associated with the inertial frame, and $\underline{\underline{B}} = \begin{bmatrix} \hat{b}_1 & \hat{b}_2 & \hat{b}_3 \end{bmatrix}$ is the one associated with the spacecraft – modeled as a rigid body or in its undeformed configuration – frame, the attitude of the spacecraft is described by the rotation matrix

$$\underset{B\leftarrow N}{R} = \underline{\underline{B}}^T \cdot \underline{\underline{N}} = \begin{bmatrix} \left(\underline{b}_1^{(N)}\right)^T \\ \left(\underline{b}_2^{(N)}\right)^T \\ \left(\underline{b}_3^{(N)}\right)^T \end{bmatrix} \tag{3.1}$$

Moreover, the time derivation of Eq. (3.1) leads to the kinematic equation (2.41), which in the case at hand becomes [82]

$$\underset{B\leftarrow N}{\dot{R}} = -\underline{\tilde{\omega}}^{(B)} \underset{B\leftarrow N}{R} \tag{3.2}$$

where $\underline{\omega}^{(B)} = \underline{\omega}_{NB}^{(B)}$ is the angular velocity of the spacecraft with respect to the inertial frame, expressed in components with respect to the spacecraft frame.

The rotation matrix does not suffer from singularity issues, but it requires the largest number of parameters to determine the spacecraft attitude. In fact, although it consists of 9 components, only 6 are independent due to its orthogonality and normalization constraints. To reduce the number of parameters used for attitude representation, alternative parametrizations have been proposed. One of the most widely used is the eigenrotation, based on Euler's rotation theorem. According to this theorem, any rotation of a reference frame in three-dimensional space, with one point fixed (typically the origin), can be represented as a single rotation by a certain angle about a fixed axis passing through that point. This axis $\hat{e}$ is known as the Euler axis or eigenaxis, while the angle of rotation ϕ is referred to as the Euler angle or eigenangle. Since the eigenaxis is a unit vector, only two parameters are needed to define it because [82]

$$e_1^2 + e_2^2 + e_3^2 = 1 \tag{3.3}$$

with the third parameter being the eigenangle. Together, these three parameters uniquely define the spacecraft attitude. The relation between the eigenrotation parametrization and the rotation matrix is expressed by the following equation:

$$\underset{B\leftarrow N}{R} = \cos\phi \, I_{3\times 3} + (1-\cos\phi)\underline{e}\underline{e}^T - \sin\phi \, \underline{\tilde{e}} \tag{3.4}$$

where $\underline{e} = \underline{e}^{(N)} = \underline{e}^{(B)}$. Moreover, the following kinematic equations can be obtained that link the time derivatives of the eigenrotation parameters to the angular velocity:

$$\underline{\dot{e}}^{(B)} = \frac{1}{2}\left[\underline{\tilde{e}} - \arctan\frac{\phi}{2}\underline{\tilde{e}}\underline{\tilde{e}}\right]\underline{\omega}^{(B)} \tag{3.5}$$

$$\dot{\phi} = 1 - 2\sin^2\frac{\phi}{2} \tag{3.6}$$

where it is worth noting that the derivative of the eigenaxis components are not the same in the two considered reference frames. Then, at every time instant a new eigenaxis can be identified that links the two frames in their new relative configuration. The eigenaxis remains the same only if the angular velocity is parallel to the eigenaxis, that is $\hat{e} \cdot \underset{\rightarrow}{\omega} = |\underline{\omega}|$.
For the sake of completeness, the inverse of the previous equations is reported, i.e. the relation providing the angular velocity from the eigenrotation parameters and their time derivatives

$$\underline{\omega}^{(B)} = \dot{\phi}\underline{e} - (1 - \cos\phi)\underline{\tilde{e}}\underline{\dot{e}}^{(B)} + \sin\phi\underline{\dot{e}}^{(B)} \tag{3.7}$$

However, this set encounters singularities issues. In fact, from Eq. (3.4) one obtains

$$\cos\phi = \frac{1}{2}\left(\left\{\underset{B\leftarrow N}{R}\right\}_{11} + \left\{\underset{B\leftarrow N}{R}\right\}_{22} + \left\{\underset{B\leftarrow N}{R}\right\}_{33} - 1\right) \tag{3.8}$$

$$\underline{e} = \frac{1}{2\sin\phi}\begin{bmatrix} \left\{\underset{B\leftarrow N}{R}\right\}_{23} - \left\{\underset{B\leftarrow N}{R}\right\}_{32} \\ \left\{\underset{B\leftarrow N}{R}\right\}_{31} - \left\{\underset{B\leftarrow N}{R}\right\}_{13} \\ \left\{\underset{B\leftarrow N}{R}\right\}_{12} - \left\{\underset{B\leftarrow N}{R}\right\}_{21} \end{bmatrix} \tag{3.9}$$

As a result, the eigenaxis components are not defined for $\phi \to 0$. In fact, using only three parameters inevitably leads to singularities. To overcome this limitation, a four-parameter representation known as quaternions is often used. Derived directly from the axis-angle (eigenrotation) formulation, quaternions allow attitude to be described compactly while avoiding singularities. They are defined as

$$q_0 = \cos\frac{\phi}{2} \tag{3.10}$$

$$\underline{q} = \underline{e}\sin\frac{\phi}{2} \tag{3.11}$$

with the following constraint

$$q_0^2 + \underline{q}^T\underline{q} = 1 \tag{3.12}$$

The quaternions (or Euler parameters) are related to the rotation matrix through the following equation:

$$\underset{B\leftarrow N}{R} = \left(q_0^2 - \underline{q}^T\underline{q}\right)I_{3\times3} + 2\underline{q}\underline{q}^T - 2q_0\underline{\tilde{q}} \tag{3.13}$$

from which the kinematic equation is obtained as

$$\dot{q}_0 = -\frac{1}{2}\underline{q}^T\underline{\omega}^{(B)} \tag{3.14}$$

$$\underline{\dot{q}} = \frac{1}{2}\left[q_0 I_{3\times3} + \underline{\tilde{q}}\right]\underline{\omega}^{(B)} \tag{3.15}$$

All the discussed parametrizations refer to the orientation of a spacecraft frame relative to an inertial frame. However, there are situations where it is useful to define the attitude of the body-fixed frame with respect to a non-inertial frame, both having their own orientations relative to the inertial frame. This is the case, in attitude control, where the actual attitude of the spacecraft is expressed relatively to a commanded body frame $\underline{\underline{C}} = \left[\hat{c}_1 \quad \hat{c}_2 \quad \hat{c}_3\right]$, representing the desired attitude. In that case, everything is analogous with the already presented formulation. The attitude parameters are called "error" rotation matrix, eigenaxis, eigenangle and quaternion, and are defined as the rotation from the commanded frame to obtain the body frame. Moreover, the error angular velocity that appears in the kinematic relations is the angular velocity of frame B with respect to frame C in components with respect to frame B, i.e.

$$\underline{\omega_E}^{(B)} \triangleq \underline{\omega}_{CB}^{(B)} = \underline{\omega}_{NB}^{(B)} - \underset{B\leftarrow C}{R}\,\underline{\omega}_{NC}^{(C)} \tag{3.16}$$

where $\underset{B\leftarrow C}{R} = \underset{B\leftarrow N}{R}\,\underset{C\leftarrow N}{R}^T$ is the error rotation matrix. The error eigenaxis and eigenangle and the error quaternion are obtained from the error rotation matrix using Eqs. (3.8), (3.9) and (3.14)-(3.15). It is also possible to bypass the computation of the error rotation matrix and directly obtain the error representation in alternative parametrizations using specific formulas. These allow the error to be computed from the same parameters that describe the orientation of the two frames with respect to the inertial frame. For example, in the case of quaternions, the error quaternion can be computed directly from the quaternions representing the orientation of each frame relative to the inertial frame, as

$$\begin{cases} q_{E,0} = q_{C,0}q_{B,0} + \underline{q}_C^{\,T}\underline{q}_B \\ \underline{q_E} = -q_{B,0}\underline{q}_C + q_{C,0}\underline{q}_B + \underline{\tilde{q}}_B\underline{q}_C \end{cases} \tag{3.17}$$

with the subscript in the quaternions indicating the frame each quaternion is associated with. As a final remark, it is worth noting that even the kinematic equations for the error parameter have the same form of the ones previously presented. For instance, the time derivative of the error quaternions are obtained as

$$\dot{q}_{E,0} = -\frac{1}{2}\underline{q_E}^T \underline{\omega_E}^{(B)} \tag{3.18}$$

$$\underline{\dot{q}_E} = \frac{1}{2}\left[q_{E,0}I_{3\times3} + \underline{\tilde{q}_E}\right]\underline{\omega_E}^{(B)} \tag{3.19}$$

In this work, nonlinear feedback laws for attitude control are considered. These laws are widely discussed in the literature and, apart from the specific choice for attitude parametrization, they often show a canonical form. They are derived from the Euler equation of the spacecraft, evaluated with respect to the spacecraft's center of mass, that is

$$J_C\underline{\dot{\omega}} + \dot{J}_C\underline{\omega} + \underline{\tilde{\omega}}J_C\underline{\omega} = \underline{m} + \underline{t} \tag{3.20}$$

where J_C is the moment of inertia of the spacecraft with respect to the center of mass, while $\underline{m}$ and $\underline{t}$ are the disturbance and control torques respectively. In Eq. (3.20), all component vectors and matrices are referred to the spacecraft body frame. Before proceeding with the derivation, it is necessary to point out that Eq. (3.20) completely describes the rotation dynamics of a rigid spacecraft where the position to the center of mass remain fixed with respect to a body reference frame. This is the case of spacecraft mounting momentum exchange devices, i.e. gimbaled wheels that are used to provide the needed control torque (cf. Section 3.6) or mounting a pair of appendages symmetric with respect to the center of mass and moving in a specular way. In fact, the variation of the inertia tensor is accounted by term $\dot{J}_C\underline{\omega}$. However, if the motion of the appendices of an articulated spacecraft leads to move the center of mass with respect to the spacecraft body frame, Eq. (3.20) is no more sufficient to completely model the system dynamics because of the coupling between the attitude and trajectory motion. This implies that, during such appendages motions the control torque does not guarantee the perfect alignment with the desired attitude. However, once the spacecraft has reached a new configuration and stopped moving its appendages, Eq. (3.20) with respect to the new position of the center of mass in the body frame is again sufficient to completely model the spacecraft attitude dynamics, and the control torque is again able to guarantee the spacecraft stability with respect to the desired attitude.

3.3. Triaxial attitude tracking

This section addresses the problem of triaxial attitude tracking, in which all three body axes must align with the corresponding axes of a commanded body frame that may also rotate with a desired angular velocity. First, the standard form of the nonlinear feedback control law is introduced [37, 83], along with its stability analysis. Next, the procedure for selecting the control gains is discussed. Finally, an improved version of the triaxial control law is developed, and its stability properties are analyzed.

3.3.1. Feedback law

In the following, error quaternions are used to describe the difference between the commanded and actual attitude, but other parametrizations can be used. The target set of attitude tracking is then written as

$$q_{E,0} = 1 \qquad \underline{q_E} = [0,0,0]^T \qquad \underline{\omega_D} = \underline{0} \tag{3.21}$$

where $\underline{\omega_D} = \underline{\omega}^{(B)} - \underline{\omega}_C^{(C)}$ is a different version of the error angular velocity reported in Eq. (3.16).

Proposition 1. Let A and B denote two constant positive definite matrices; A is also symmetric. The feedback control law,

$$\underline{t_c} = \tilde{\underline{\omega}} J_C \underline{\omega} - \underline{m} + \dot{J}_C \underline{\omega_C} + J_C \dot{\underline{\omega}}_C - J_C A^{-1}\left[B\underline{\omega_D} + \operatorname{sgn}^+\{q_{E,0}(t_0)\}\underline{q_E}\right] \tag{3.22}$$

with

$$\operatorname{sgn}^+\{x\} = \begin{cases} 1 & \text{if } x \geq 0 \\ -1 & \text{if } x < 0 \end{cases} \tag{3.23}$$

drives the dynamical system governed by Eqs. (3.14), (3.15), and (3.20) toward the attracting set associated with $\underline{\omega_D} = \underline{0}$.

Proof. Because of the sign function appearing in Eq. (3.22), the proof is instead provided for the two control laws

$$\underline{t_c} = \tilde{\underline{\omega}} J_C \underline{\omega} - \underline{m} + \dot{J}_C \underline{\omega_C} + J_C \dot{\underline{\omega}}_C - J_C A^{-1}\left[B\underline{\omega_D} \pm \underline{q_E}\right] \tag{3.24}$$

If both of them are proven to drive the system toward the desired state with global asymptotic stability, the same statement must hold for law (3.22). First, the following two candidate Lyapunov functions [84] are proposed:

$$V = \frac{1}{2}\underline{\omega_D}^T A \underline{\omega_D} + 2\left(1 \mp q_{E,0}\right) \tag{3.25}$$

It is apparent that these functions are always positive definite and vanishes only in the target set. Second, they have continuous partial derivatives except in $q_{E,0}=0$, where a discontinuity occurs and the partial derivative with respect to is not defined. Then the time derivative of V is computed

$$\begin{aligned}\dot{V} &= \underline{\omega_D}^T A \underline{\dot{\omega}_D} \mp 2\dot{q}_{E,0} \\ &= \underline{\omega_D}^T A\left(\underline{\dot{\omega}}-\underline{\dot{\omega}_C}\right) \pm \underline{\omega_D}^T \underline{q_E} \\ &= \underline{\omega_D}^T A\left[\left(J_C\right)^{-1}\left(-\dot{J}_C\underline{\omega}-\underline{\tilde{\omega}}J_C\underline{\omega}+\underline{m}+\underline{t_c}\right)-\underline{\dot{\omega}_C}\right] \pm \underline{\omega_D}^T \underline{q_E}\end{aligned} \tag{3.26}$$

where Eq. (3.20) and a modified version of Eq. (3.18) have been applied. In fact,

$$\dot{q}_{E,0} = -\frac{1}{2}\underline{q_E}^T \underline{\omega_E} = -\frac{1}{2}\underline{q_E}^T\left(\underline{\omega}^B - \underset{B\leftarrow C}{R}\,\underline{\omega_C}^{(C)}\right) \tag{3.27}$$

but it can be easily proven that

$$\underline{q_E}^T \underset{B\leftarrow C}{R} = \underline{q_E}^T \tag{3.28}$$

and then Eq. (3.27) becomes

$$\dot{q}_{E,0} = -\frac{1}{2}\underline{q_E}^T\left(\underline{\omega}^{(B)} - \underline{\omega_C}^{(C)}\right) = -\frac{1}{2}\underline{q_E}^T \underline{\omega_D} \tag{3.29}$$

Thern, substituting the control laws (3.24) in Eq. (3.26) one obtains

$$\dot{V} = -\underline{\omega_D}^T B \underline{\omega_D} \tag{3.30}$$

that is always lower than zero except for $\underline{\omega_D}=\underline{0}$. This means that V are actually Lyapunov function. □

Proposition 1 is not sufficient to prove the convergence toward the complete target set. In fact, with the Lyapunov method alone it is possible to prove only the convergence toward the desired angular velocity and not toward the desired attitude. To do that, it is needed to apply the LaSalle invariance principle to identify the invariant set [84].

Proposition 2. The control law (3.22) drives the dynamical system described by Eqs. (3.14), (3.15) and (3.20) toward the invariant set that corresponds to the target set (3.21).

Proof. First, a compact set of the state must be identified where all feasible states are contained and where the Lyapunov function is continuously differentiable and always less than a certain value. By their definition, the quaternions are variables defined in a compact set, since $\left|q_{E,0}\right| \le 1$ and $\left\|\underline{q_E}\right\| \le 1 \ \forall t$ by definition (cf. Eq. (3.12)). Because $\dot{V} \le 0$, then $V(t) \le V(t_0) \ \forall t$, i.e.

$$\begin{aligned} &\frac{1}{2}\underline{\omega_D}(t)^T A\underline{\omega_D}(t) + 2\left[1 \mp q_{E,0}(t)\right] \\ &\le \frac{1}{2}\underline{\omega_D}(t_0)^T A\underline{\omega_D}(t_0) + 2\left[1 \mp q_{E,0}(t_0)\right] \\ &\le \frac{1}{2}\underline{\omega_D}(t_0)^T A\underline{\omega_D}(t_0) + 4 = c \end{aligned} \tag{3.31}$$

and

$$\Omega = \left\{\left(\underline{\omega}, q_0, \underline{q}\right) \in \mathbb{R}^7 \middle| V \le c\right\} \tag{3.32}$$

is the sought compact set. Then, it is needed to identify E, which is the set in Ω where $\dot{V} = 0$:

$$E = \left\{\left(\underline{\omega}, q_0, \underline{q}\right) \in \Omega \middle| \underline{\omega_D} = \underline{0}\right\} \tag{3.33}$$

Finally, the largest invariant set in E must be found. Recall that the invariant set is by definition the subset where the solution remains once it is there. Because in the invariant set $\underline{\omega_D} = \underline{0} \ \forall t$, then also $\underline{\dot{\omega}_D} = \underline{0} \ \forall t$. Hence, by substituting these two conditions in Eq. (3.20), where the control law (3.22) has been previously substituted, one obtains that

$$\begin{aligned} &J_C\underline{\dot{\omega}} = J_C\underline{\omega_C} - J_C A^{-1}\mathrm{sgn}^+\left\{q_{E,0}(t_0)\right\}\underline{q_E} \\ &\Rightarrow J_C\underline{\dot{\omega}_D} = -J_C A^{-1}\mathrm{sgn}^+\left\{q_{E,0}(t_0)\right\}\underline{q_E} \\ &\Rightarrow \underline{q_E} = \underline{0} \end{aligned} \tag{3.34}$$

This step is the reason behind the use of a modified sign function, which restitutes a nonzero value even if its argument is zero. Therefore, the largest invariant set in E is the one that comprises both the conditions for $\underline{\omega_D}$ and $q_{E,0}$, i.e.

$$S = \left\{\left(\underline{\omega}, q_0, \underline{q}\right) \in E \middle| \underline{\omega_D} = \underline{0},\ q_{E,0} = \pm 1\right\} \tag{3.35}$$

where the conditions $q_{E,0} = +1$ and $q_{E,0} = -1$ represent the same attitude. □

The last step proves that convergence is quasi-global because $\left\{\underline{\omega}(t_0), q_0(t_0), \underline{q}(t_0)\right\}$ that form c in Eq. (3.31) are arbitrary; "quasi" is due to the fact that convergence occurs towards two possible final conditions, i.e. $q_{E,0} = \pm 1$. If convergence toward the closest final condition is sought, which corresponds to the shortest angular path (and a faster transient behavior), then it may be desirable selecting $q_{E,0} = +1$ or $q_{E,0} = -1$ as the target condition. This is the reason why the term $\operatorname{sgn}^+\left\{q_{E,0}\left(t_0\right)\right\}$ has been introduced in the control law: if the initial value of $q_{E,0}$ is positive, the attitude will converge toward $q_{E,0} = +1$ that is the closest one, and vice versa.

3.3.2. Gain selection

The feedback control law (3.22) is defined in terms of two constant, positive definite matrices, i.e. A and B. Selection of these matrices affects the transient behavior and the convergence time of the actual attitude toward the commanded one. With no loss of generality, it is possible to select these two matrices assuming that both are diagonal and written as

$$A^{-1} = c_1 I_{3\times 3} \quad \text{and} \quad B = c_2 I_{3\times 3} \tag{3.36}$$

where c_1 and c_2 are two positive constants. The motion driven by the control law (3.22) can be approximated as an eigenaxis rotation with constant direction of the eigenaxis. In fact, the term $-J_C A^{-1} \underline{q_E}$ provides a torque which is opposite to the error eigenaxis $\underline{e_E}$ that is obtained from the rotation matrix $\underset{B\leftarrow C}{R}$ from the body to the commanded frame, i.e. the same rotation matrix associated with the error quaternion. The other terms of the control law deviate the motion from a simple eigenaxis rotation, which however remains an acceptable approximation for the gain selection process. Hence, after substituting Eq. (3.22) in (3.20) and neglecting the sign of the scalar component of the error quaternion at t_0, one obtains

$$\underline{\dot{\omega}_D} + A^{-1} B \underline{\omega_D} + A^{-1} \underline{q_E} = \underline{0} \tag{3.37}$$

Introducing the approximation of the eigenaxis rotation, the following relations hold:

$$\underline{\dot{\omega}_D} = \ddot{\phi}_E \underline{e_E} \qquad \underline{\omega_D} = \dot{\phi}_E \underline{e_E} \qquad \underline{q_E} = \sin\left(\frac{\phi_E}{2}\right)\underline{e_E} \tag{3.38}$$

where ϕ_E is the error eigenangle. Thus, Eq. (3.37) becomes

$$\ddot{\phi}_E + c_1 c_2 \dot{\phi}_E + c_1 \sin\left(\frac{\phi_E}{2}\right) = 0 \tag{3.39}$$

whose linearized form is

$$\ddot{\phi}_E + c_1 c_2 \dot{\phi}_E + c_1 \frac{\phi_E}{2} = 0 \tag{3.40}$$

This expression shows the structure of a second-order system, where

$$c_1 = 2\omega_n^2 \qquad c_2 = \frac{2\zeta\omega_n}{c_1} \tag{3.41}$$

with ω_n natural frequency and ζ damping factor. Selection of these two parameters, directly related to the transient behavior, leads to obtaining matrices A and B. This procedure allows to connect the gain selection to the actual performance of the controlled system, which is one of the major issues when dealing with nonlinear control laws.

3.3.3. Improved feedback law

An improved version of control law (3.22) is provided in this section. This enhanced law represents one of the novel contributions of this work. The difference consists of a new rewriting of the term depending on the attitude error, which now is defined using the eigenrotation parametrization instead of the quaternions. This means that $\underline{e_E}$ and ϕ_E are introduced as the error eigenangle and eigenaxis associated with $\underset{B \leftarrow C}{R}$, whose time evolution is governed by the following equations:

$$\underline{\dot{e}_E}^{(B)} = \frac{1}{2}\left[\underline{\tilde{e}_E} - \arctan\frac{\phi_E}{2}\underline{\tilde{e}_E}\,\underline{\tilde{e}_E}\right]\underline{\omega_E}^{(B)} \tag{3.42}$$

$$\dot{\phi}_E = 1 - 2\sin^2\frac{\phi_E}{2} \tag{3.43}$$

In this case, the target set is defined as

$$\phi_E = 0 \quad \text{and} \quad \underline{\omega_D} = 0 \tag{3.44}$$

Before presenting the control law, it is important to clarify that the inclusion of a term expressed in eigenrotation parameters does not pose a problem. Although this parametrization becomes singular at $\phi_E = 0$ and $\phi_E = \pi$, where the eigenaxis is undefined (see Eq. (3.9)), this issue can be circumvented. Specifically, one can use error quaternions – which are free from singularities – to represent the attitude and convert them into axis-angle form only when evaluating the terms of the control law.

Proposition 3. Let A and B denote two constant positive definite matrices; A is also symmetric. The feedback control law,

$$\underline{t}_c = \underline{\tilde{\omega}} J_C \underline{\omega} - \underline{m} + \dot{J}_C \underline{\omega}_C + J_C \underline{\dot{\omega}}_C - J_C A^{-1} \left[B \underline{\omega}_D + \underline{e}_E \sin \phi'_E \right] \tag{3.45}$$

where ϕ'_E is a modified error eigenangle, defined as

$$\begin{cases} \phi'_E = \gamma \phi_E & \text{if} \quad 0 \le \phi_E < \dfrac{\pi}{2\gamma} \\ \phi'_E = \dfrac{\pi}{2} & \text{if} \quad \dfrac{\pi}{2\gamma} \le \phi_E \le \pi \end{cases} \qquad \text{with } \gamma \ge \frac{1}{2} \tag{3.46}$$

drives the dynamical system governed by Eqs. (3.14), (3.15) and (3.20) toward the attracting set associated with $\underline{\omega}_D = \underline{0}$.

Proof. The following piecewise Lyapunov function is employed:

$$V = \begin{cases} \dfrac{1}{2} \underline{\omega}_D{}^T A \underline{\omega}_D + k_1 \left[1 - \cos\left(\gamma \phi_E \right) \right], & 0 \le \phi_E < \dfrac{\pi}{2\gamma} \\ \dfrac{1}{2} \underline{\omega}_D{}^T A \underline{\omega}_D + k_2 \phi_E, & \dfrac{\pi}{2\gamma} \le \phi_E \le \pi \end{cases} \tag{3.47}$$

where k_1 and k_2 are two positive arbitrary constants. V is a positive definite that vanishes only when the state coincides with the target set. Second, V has continuous partial derivatives only if

$$\gamma k_1 = k_2 \tag{3.48}$$

because

$$\left. \frac{\partial V}{\partial \phi_E} \right|_{\phi_E = \frac{\pi}{2\gamma}} = \begin{cases} \gamma k_1 \\ k_2 \end{cases} \tag{3.49}$$

Through the time derivation of Eq. (3.47) and substituting the dynamic equation (3.20) and the control law (3.45) one obtains

$$
\begin{aligned}
\dot{V} &= \begin{cases} \underline{\omega_D}^T A\left(\underline{\dot{\omega}} - \underline{\dot{\omega}}_C\right) + k_1 \sin\left(\gamma\phi_E\right)\gamma\dot{\phi}_E \\ \underline{\omega_D}^T A\left(\underline{\dot{\omega}} - \underline{\dot{\omega}}_C\right) + k_2\dot{\phi}_E \end{cases} \\
&= \begin{cases} -\underline{\omega_D}^T B\,\underline{\omega_D} - \underline{\omega_D}^T \underline{e_E} \sin\phi'_E + k_1 \sin\left(\gamma\phi_E\right)\gamma\dot{\phi}_E \\ -\underline{\omega_D}^T B\,\underline{\omega_D} - \underline{\omega_D}^T \underline{e_E} \sin\phi' + k_2\dot{\phi}_E \end{cases} \\
&= \begin{cases} -\underline{\omega_D}^T B\,\underline{\omega_D} - \left[\underline{\omega_D}^T \underline{e_E} - k_1\gamma\dot{\phi}_E\right]\sin\left(\gamma\phi_E\right) \\ -\underline{\omega_D}^T B\,\underline{\omega_D} - \left[\underline{\omega_D}^T \underline{e_E} - k_2\dot{\phi}_E\right] \end{cases} \\
&= \begin{cases} -\underline{\omega_D}^T B\,\underline{\omega_D} - \left[1 - k_1\gamma\right]\dot{\phi}_E \sin\left(\gamma\phi_E\right), & 0 \le \phi_E < \dfrac{\pi}{2\gamma} \\ -\underline{\omega_D}^T B\,\underline{\omega_D} - \left[1 - k_2\right]\dot{\phi}_E, & \dfrac{\pi}{2\gamma} \le \phi_E \le \pi \end{cases}
\end{aligned}
\tag{3.50}
$$

where it has been considered, passing from the second to the third step, that

$$
\begin{cases} \sin\phi'_E = \sin\left(\gamma\phi_E\right) & \text{if} \quad 0 \le \phi_E < \dfrac{\pi}{2\gamma} \\ \sin\phi'_E = 1 & \text{if} \quad \dfrac{\pi}{2\gamma} \le \phi_E \le \pi \end{cases}
\tag{3.51}
$$

Moreover, to pass from the third to the final step of Eq. (3.50) it has been considered that

$$
\underline{\omega_D}^T \underline{e_E} = \dot{\phi}_E \tag{3.52}
$$

This relation is proven in two steps. First, the following identity holds:

$$
\underline{\omega_D}^T \underline{e_E} = \left(\underline{\omega}^T - \underline{\omega}_C^T\right)\underline{e_E} = \left(\underline{\omega}^T - \underline{\omega}_C^T \underset{C\leftarrow B}{R}\right)\underline{e_E} = \left(\underline{\omega} - \underset{B\leftarrow C}{R}\,\underline{\omega}_C\right)^T \underline{e_E} = \underline{\omega_E}^T \underline{e_E} \tag{3.53}
$$

because $\underline{e_E}^{(B)} = \underline{e_E}^{(C)} = \underline{e_E}$ by definition. Then, from the error version of Eq. (3.7), which is

$$
\underline{\omega_E}^{(B)} = \dot{\phi}_E \underline{e_E} - \left(1 - \cos\phi_E\right)\underline{\tilde{e}_E}\,\underline{\dot{e}_E}^{(B)} + \sin\phi_E\,\underline{\dot{e}_E}^{(B)} \tag{3.54}
$$

one obtains that

$$
\underline{\omega_E}^T \underline{e_E} = \dot{\phi}_E \tag{3.55}
$$

because both $\underline{\tilde{e}_E}\,\underline{\dot{e}_E}$ and $\underline{\dot{e}_E}$ are orthogonal to $\underline{e_E}$, the former because of the definition of cross product, while the latter because the time derivative of a unit vector is always perpendicular to it. Referring back to Eq. (3.50), if one sets $k_1 = 1/\gamma$ and $k_2 = 1$ – which is in accordance with condition (3.48) – the time derivative of the Lyapunov function becomes

$$\dot{V} = -\underline{\omega_D}^T B \underline{\omega_D} \tag{3.56}$$

that is always lower than zero except for $\underline{\omega_D} = \underline{0}$. This means that V is actually a Lyapunov function. □

The previous proof holds for all values of ϕ_E between 0 and 180 degrees. Restricting the error eigenangle ϕ_E to only positive values does not limit the validity of the stability analysis. This is because, for any given rotation, there are two mathematically equivalent ways to represent the eigenrotation: one with a positive angle ϕ_E comprised between o and 180 degrees and an axis $\underline{e_E}$, and the other with a negative angle $-\phi_E$ between 0 and -180 degrees and the axis $-\underline{e_E}$, pointing in the opposite direction. Since both representations describe the same physical rotation, it is always possible to choose the one with a positive angle without any loss of generality.

Also in this case, Proposition 3 is not sufficient to prove the convergence toward the complete target set, and the LaSalle invariance principle must be applied to identify the invariant set.

Proposition 4. The control law (3.45) drives the dynamical system described by Eqs. (3.14), (3.15) and (3.20) toward the invariant set that corresponds to the target set (3.44).

Proof. First, a compact must be sought. Because $\dot{V} \le 0$, then $V(t) \le V(t_0)\ \forall t$, i.e.

$$\begin{cases} \frac{1}{2}\underline{\omega_D}(t)^T A \underline{\omega_D}(t) + \frac{1}{\gamma}\left[1-\cos\left(\gamma\phi_E(t)\right)\right] \le \frac{1}{2}\underline{\omega_D}(t_0)^T A \underline{\omega_D}(t_0) + 2, & 0 \le \phi_E < \frac{\pi}{2\gamma} \\ \frac{1}{2}\underline{\omega_D}(t)^T A \underline{\omega_D}(t) + \phi_E(t) \le \frac{1}{2}\underline{\omega_D}(t_0)^T A \underline{\omega_D}(t_0) + \pi, & \frac{\pi}{2\gamma} \le \phi_E \le \pi \end{cases} \tag{3.57}$$

with $\gamma \ge 1/2$. Thies leads to write that

$$V(t) \le \frac{1}{2}\underline{\omega_D}(t_0)^T A \underline{\omega_D}(t_0) + \pi = c, \qquad 0 \le \phi_E \le \pi \tag{3.58}$$

and the expression of Ω and E coincide with Eqs. (3.32) and (3.33). The largest invariant set in E is found with a similar procedure reported in Eq. (3.34), i.e. substituting the control law (3.45) in Eq. (3.20) and applying the conditions $\underline{\omega_D} = \underline{0}$ and $\underline{\dot{\omega}_D} = \underline{0}$:

$$J_C \underline{\dot{\omega}_D} = -J_C A^{-1} \underline{e_E} \sin\phi'_E \Rightarrow \sin\phi'_E = 0 \Rightarrow \phi_E = 0 \tag{3.59}$$

where the final result is obtained considering Eq. (3.46) and that ϕ_E only assumes values between 0 and 180 degrees. Thus, the largest invariant set in E is

$$S = \left\{ \left(\underline{\omega}, q_0, \underline{q}\right) \in E \middle| \underline{\omega_D} = \underline{0},\ \phi_E = 0 \right\} \tag{3.60}$$

that clearly coincides with target set (3.44). □

3.4. Reduced attitude tracking

In many cases, it is not necessary to control all three axes of the spacecraft: often, only one axis needs to be managed [85, 86]. This is typical for satellites that need to align only the payload axis with a desired direction, where rotation about the payload axis does not affect mission performance. In such cases, a different control law can be employed that focuses solely on steering the payload axis, resulting in maneuvers with shorter angular paths compared to those that also align the other two axes. This leads to advantages such as reduced reorientation time and lower torque requirements, as will be discussed in the following sections.

3.4.1. Feedback law

It is assumed that the body axis that has to be oriented is $\hat{b}_1$, which must be aligned with axis $\hat{c}_!$ of the commanded frame. From the error dual of Eq. (3.13), i.e.

$$\begin{aligned} \underset{B\leftarrow C}{R} &= \left(q_{E,0}^2 - \underline{q_E}^T \underline{q_E}\right) I_{3\times 3} + 2\underline{q_E}\,\underline{q_E}^T - 2q_{E,0}\underline{\tilde{q}_E} \\ &= \begin{bmatrix} 1-2\left(q_{E,2}^2+q_{E,3}^2\right) & 2\left(q_{E,0}q_{E,3}+q_{E,1}q_{E,2}\right) & 2\left(q_{E,1}q_{E,3}-q_{E,0}q_{E,2}\right) \\ 2\left(q_{E,1}q_{E,2}-q_{E,0}q_{E,3}\right) & 1-2\left(q_{E,1}^2+q_{E,3}^2\right) & 2\left(q_{E,0}q_{E,1}+q_{E,2}q_{E,3}\right) \\ 2\left(q_{E,0}q_{E,2}+q_{E,1}q_{E,3}\right) & 2\left(q_{E,2}q_{E,3}-q_{E,0}q_{E,1}\right) & 1-2\left(q_{E,1}^2+q_{E,2}^2\right) \end{bmatrix} \end{aligned} \tag{3.61}$$

one obtains – also employing the property (3.12) – that

$$\left\{\underset{B\leftarrow C}{R}\right\}_{11} = \hat{b}_1 \cdot \hat{c}_1 = 1 - 2\left(q_{E,2}^2 + q_{E,3}^2\right) \tag{3.62}$$

that is the term representing the misalignment between the controlled body and its desired direction. This leads the target set of the sought control law to be

$$1-2\left(q_{E,2}^2+q_{E,3}^2\right)=1\Leftrightarrow q_{E,2}^2+q_{E,3}^2=0 \quad \text{and} \quad \underline{\omega_E}=\underline{0} \tag{3.63}$$

Proposition 5. Let A and B denote two constant positive definite matrices; A is also symmetric. The feedback control law,

$$\underline{t_c}=\underline{\tilde{\omega}}J_C\underline{\omega}-\underline{m}+\dot{J}_C\underline{\omega_C}+J_C\left[\underset{B\leftarrow C}{R}\underline{\dot{\omega}_C}-\underline{\tilde{\omega}_E}\underset{B\leftarrow C}{R}\underline{\omega_C}\right]-J_C A^{-1}\left[B\underline{\omega_E}+\underline{f}\left(q_{E,0},\underline{q_E}\right)\right] \tag{3.64}$$

where

$$\underline{f}\left(q_{E,0},\underline{q_E}\right)=\begin{bmatrix}0\\ q_{E,0}q_{E,2}+q_{E,1}q_{E,3}\\ q_{E,0}q_{E,3}-q_{E,1}q_{E,2}\end{bmatrix} \tag{3.65}$$

drives the dynamical system governed by Eqs. (3.14), (3.15), and (3.20) toward the attracting set associated with $\underline{\omega_D}=\underline{0}$.

Proof. First, the candidate Lyapunov function is identified as

$$V=\frac{1}{2}\underline{\omega_E}^T A\underline{\omega_E}+q_{E,2}^2+q_{E,3}^2 \tag{3.66}$$

which is positive definite in all the state domain except for the case when the state coincides with the target set. Moreover, this function has continuous partial derivatives with respect to the state components. The time derivative of (3.66) leads to

$$\begin{aligned}\dot{V}&=\underline{\omega_E}^T A\underline{\dot{\omega}_E}+2\left(\dot{q}_{E,2}+\dot{q}_{E,3}\right)\\ &=\underline{\omega_E}^T A\left(\underline{\dot{\omega}}-\underset{B\leftarrow C}{R}\underline{\dot{\omega}_C}-\underset{B\leftarrow C}{\dot{R}}\underline{\omega_C}\right)+2\left(\dot{q}_{E,2}+\dot{q}_{E,3}\right)\\ &=\underline{\omega_E}^T A\left[\left(J_C\right)^{-1}\left(\dot{J}_C\underline{\omega}-\underline{\tilde{\omega}}J_C\underline{\omega}+\underline{m}+\underline{t_c}\right)\right]\\ &\quad-\underline{\omega_E}^T A\left(\underset{B\leftarrow C}{R}\underline{\dot{\omega}_C}-\underline{\tilde{\omega}_E}\underset{B\leftarrow C}{R}\underline{\omega_C}\right)\\ &\quad+\left(q_{E,0}q_{E,2}+q_{E,1}q_{E,3}\right)\omega_{E,2}+\left(q_{E,0}q_{E,3}-q_{E,1}q_{E,2}\right)\omega_{E,3}\end{aligned} \tag{3.67}$$

where Eqs. (3.18), (3.19), and (3.20) have been applied. Then, by substitution of the control law (3.64) one obtains that

$$\dot{V}=-\underline{\omega_E}^T B\underline{\omega_E} \tag{3.68}$$

that is always lower than zero except for $\underline{\omega_E} = \underline{0}$. This means that V is actually a Lyapunov function. □

Proposition 6. The control law (3.64) drives the dynamical system described by Eqs. (3.14), (3.15), and (3.20) toward the invariant set composed of the following two subsets:

(1) $\underline{\omega_E} = \underline{0}$ and $\left\{ \underset{B \leftarrow C}{R} \right\}_{11} = +1 \Leftrightarrow q_{E,2}^2 + q_{E,3}^2 = 0$

(2) $\underline{\omega_E} = \underline{0}$ and $\left\{ \underset{B \leftarrow C}{R} \right\}_{11} = -1 \Leftrightarrow q_{E,0}^2 + q_{E,1}^2 = 0$

Proof. The compact set is defined as in the triaxial case, i.e. through Eq. (3.32), where the constant c is found as

$$\begin{aligned} &\frac{1}{2}\underline{\omega_E}^T A \underline{\omega_E} + q_{E,2}^2 + q_{E,3}^2 \\ &\le \frac{1}{2}\underline{\omega_E}(t)^T A \underline{\omega_E}(t) + q_{E,2}^2(t) + q_{E,3}^2(t) \\ &\le \frac{1}{2}\underline{\omega_E}(t_0)^T A \underline{\omega_E}(t_0) + 1 = c \end{aligned} \tag{3.69}$$

Then, the set in Ω where $\dot{V} = 0$ is

$$E = \left\{ \left(\underline{\omega}, q_0, \underline{q}\right) \in \Omega \middle| \underline{\omega_E} = \underline{0} \right\} \tag{3.70}$$

and the largest invariant set in E is such that $\underline{\omega_E} = \underline{0}\ \ \forall t$, leading to $\underline{\dot{\omega}_E} = \underline{0}$. Substituting the control law (3.64) in the dynamic equation (3.20) and applying these two conditions one obtains that

$$\begin{aligned} &J_C \underline{\dot{\omega}} = J_C \left[\underset{B \leftarrow C}{R} \underline{\dot{\omega}_C} - \underline{\tilde{\omega}_E} \underset{B \leftarrow C}{R} \underline{\omega_C} \right] - J_C A^{-1} \left[B \underline{\omega_E} + \underline{f}\left(q_{E,0}, \underline{q_E}\right) \right] \\ &\Rightarrow J_C \underline{\dot{\omega}_E} = -J_C A^{-1} \left[B \underline{\omega_E} + \underline{f}\left(q_{E,0}, \underline{q_E}\right) \right] \\ &\Rightarrow \underline{f}\left(q_{E,0}, \underline{q_E}\right) = \underline{0} \end{aligned} \tag{3.71}$$

that translates into the two following conditions:

$$\begin{cases} q_{E,0} q_{E,2} + q_{E,1} q_{E,3} = \dfrac{1}{2}\left\{ \underset{B \leftarrow C}{R} \right\}_{13} = 0 \\ q_{E,0} q_{E,3} - q_{E,1} q_{E,2} = -\dfrac{1}{2}\left\{ \underset{B \leftarrow C}{R} \right\}_{12} = 0 \end{cases} \tag{3.72}$$

where Eq. (3.61) has been considered. This means that the large invariant set in E, also identified as the attracting set according to the LaSalle's principle, is

$$S=\left\{\left(\underline{\omega},q_0,\underline{q}\right)\in E\middle|\underline{\omega}_E=\underline{0},\ \left\{\underset{B\leftarrow C}{R}\right\}_{11}=\pm 1\right\} \tag{3.73}$$

This means that S includes two subsets:

(1) $\underline{\omega}_E=\underline{0}$ and $\left\{\underset{B\leftarrow C}{R}\right\}_{11}=+1\Leftrightarrow q_{E,2}^2+q_{E,3}^2=0$, and

(2) $\underline{\omega}_E=\underline{0}$ and $\left\{\underset{B\leftarrow C}{R}\right\}_{11}=-1\Leftrightarrow q_{E,0}^2+q_{E,1}^2=0$ □

Hence, the invariant set includes two subsets, denoted with (1) and (2). It is apparent that subset (1) is the target set, whereas subset (2) corresponds to the alignment of body axis 1 toward a direction opposite to the desired one. However, convergence toward subset (2) is only theoretical. In fact,

$$q_{E,0}^2+q_{E,1}^2=0\Leftrightarrow q_{E,2}^2+q_{E,3}^2=1 \tag{3.74}$$

And this implies that V has a maximum in subset (2) (cf. Eq. (3.66)). Although $\dot{V}=0$ in subset (2), if $q_{E,2}^2+q_{E,3}^2=1-\varepsilon$ (where ε is a positive and arbitrarily small constant), then $\dot{V}<0$, and the reduction of V leads the dynamical system to converge toward the subset (1), which coincides with the target set. This circumstance has the very interesting practical consequence that – from the numerical point of view – the dynamical system of interest enjoys global convergence toward the desired alignment conditions, provided that the feedback control law (3.64) is adopted. As a concluding remark, it is worth noting that the gain selection procedure is identical to the one discussed for the triaxial case.

3.4.2. Improved feedback law

It remains to report the improved version of the reduced-attitude control law. Even this enhanced law represents one of the novel contributions of this work. It is based on the rewriting of the term depending on the attitude error using the following parameters:

$$\phi_R=\cos^{-1}\left(\hat{b}_1\cdot\hat{c}_1\right)=\cos^{-1}\left[\left(\underline{b}_1^{(B)}\right)^T\underline{c}_1^{(B)}\right] \tag{3.75}$$

$$\hat{e}_R=\frac{\hat{b}_1\times\hat{c}_1}{\left\|\hat{b}_1\times\hat{c}_1\right\|}\Rightarrow \underline{e}_R^{(B)}=\underline{e}_R^{(C)}=\underline{e}_R=\frac{\tilde{\underline{b}}_1^{(B)}\underline{c}_1^{(B)}}{\left\|\tilde{\underline{b}}_1^{(B)}\underline{c}_1^{(B)}\right\|}=\frac{\tilde{\underline{b}}_1^{(B)}\underline{c}_1^{(B)}}{\sin\phi_R} \tag{3.76}$$

which are the reduced-attitude counterpart of the error eigenaxis and eigenangle defined in the triaxial case. Then, the target set becomes

$$\phi_R = 0 \quad \text{and} \quad \underline{\omega_E} = 0 \tag{3.77}$$

Proposition 7. Let A and B denote two constant positive definite matrices; A is also symmetric. The feedback control law,

$$\underline{t_c} = \underline{\tilde{\omega}} J_C \underline{\omega} - \underline{m} + \dot{J}_C \underline{\omega_C} + J_C \left[\underset{B\leftarrow C}{R} \underline{\dot{\omega}_C} - \underline{\tilde{\omega}_E} \underset{B\leftarrow C}{R} \underline{\omega_C} \right] - J_C A^{-1} \left[B \underline{\omega_E} + \underline{e_R} \sin\phi'_R \right] \tag{3.78}$$

with

$$\begin{cases} \phi'_R = \gamma\phi_R & \text{if} \quad 0 < \phi_E < \dfrac{\pi}{2\gamma} \\ \phi'_R = \dfrac{\pi}{2} & \text{if} \quad \dfrac{\pi}{2\gamma} \le \phi_R \le \pi \end{cases} \qquad \text{with} \;\; \gamma \ge \frac{1}{2} \tag{3.79}$$

drives the dynamical system governed by Eqs. (3.14), (3.15) and (3.20) toward the toward the invariant set that corresponds to the target set (3.77).

The proof of Proposition 7 is identical to the ones provided for Propositions 3 and 4, and is not developed for the sake of brevity. Here it is only reported the candidate Lyapunov function, which is

$$V = \begin{cases} \dfrac{1}{2} \underline{\omega_E}^T A \underline{\omega_E} + k_1 \left[1 - \cos\left(\gamma\phi_R\right) \right], & 0 < \phi_R < \dfrac{\pi}{2\gamma} \\ \dfrac{1}{2} \underline{\omega_E}^T A \underline{\omega_E} + k_2 \phi_R, & \dfrac{\pi}{2\gamma} \le \phi_R \le \pi \end{cases} \tag{3.80}$$

3.5. Performance comparison of the nonlinear control laws

The concept of the improved laws arises from the analysis of the terms of the two control laws (3.22) and (3.64) that depend on the error between the desired and the actual orientation of the spacecraft, i.e. $-J_C A^{-1} \underline{q_E}$ and $-J_C A^{-1} \underline{f}\left(q_{E,0}, \underline{q_E}\right)$ respectively. The inertia matrix can be excluded from the analysis because it simplifies when the control laws are substituted into the dynamic equations, as it is clear from inspection of Eq. (3.37). Moreover, unitary gains are considered. Starting with term $-\underline{q_E}$, it provides a torque opposite to the error eigenaxis associated with $\underset{B\leftarrow C}{R}$, because (cf. Eq. (3.11))

$$-\underline{q}_E = \underline{e}_E \sin\frac{\phi_E}{2} \tag{3.81}$$

Instead, term $-\underline{f}\left(q_{E,0}, \underline{q}_E\right)$ deserves a deeper insight. It is not associated with the eigenrotation dividing the body and the commanded frame. Instead, it refers only to the angle between the driven body axis and its desired direction – the body axis 1 in the case previously discussed. In fact, being

$$\underset{B \leftarrow C}{R} = \left[\underline{c}_1^{(B)} \quad \underline{c}_2^{(B)} \quad \underline{c}_3^{(B)}\right] \tag{3.82}$$

it is straightforward to prove that

$$-\underline{f}\left(q_{E,0}, \underline{q}_E\right) = \frac{1}{2}\tilde{\underline{b}}_1^{(B)} \underline{c}_1^{(B)} \tag{3.83}$$

with $\underline{b}_1^{(B)} = \begin{bmatrix}1 & 0 & 0\end{bmatrix}^T$. From relation (3.83) it is apparent that term $-\underline{f}\left(q_{E,0}, \underline{q}_E\right)$ provides a torque orthogonal to the plane that contains $\hat{b}_1$ and $\hat{c}_1$, with direction associated with the angle (in the range $[0, \pi]$) that separates $\hat{b}_1$ from $\hat{c}_1$. This rotation is parametrized using the previously defined quantities in Eqs. (3.75)-(3.76). Them, Eq. (3.83) can be rewritten as a function of these parameters, i.e.

$$-\underline{f}\left(\underline{e}_R, \phi_R\right) = \frac{1}{2}\underline{e}_R \sin\phi_R \tag{3.84}$$

As previously mentioned, the main advantage of reduced-attitude control lies in the lower number of requirements – specifically, the need to orient only one axis – which can be exploited to achieve the desired attitude with shorter angular paths. In fact, given any pair of frames $\underline{\underline{B}}$ and $\underline{\underline{C}}$, from the definitions of ϕ_E and ϕ_R it is apparent that

$$\phi_R \leq \phi_E \tag{3.85}$$

However, comparing Eqs. (3.81) and (3.84), reveals that the two control law terms related to the attitude error exhibit different dependencies on the error angle. The trends of these two terms as a function of the error angle are depicted in Figure 3.1.

From inspection of this figure, it is evident that the presence of a second subset within the invariant set for the reduced-attitude case influences the torque generated by the control law. Although the system cannot converge to the configuration where the controlled body

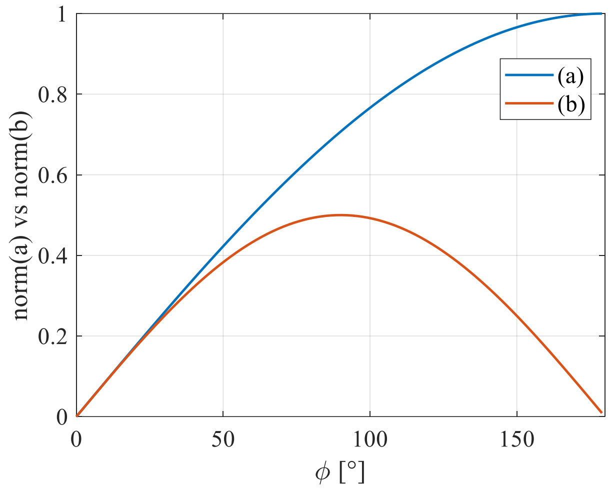

Figure 3.1: (a) $\left\|\underline{q}_E\right\|$ vs (b) $\left\|\underline{f}\right\|$ as a function of the respective error angle

axis is opposite to the desired direction – since this represents an unstable equilibrium point (a maximum of the Lyapunov function) – this point still affects the torque component associated with the attitude error. Specifically, while the triaxial control law produces a torque that increases monotonically with the angular error, the presence of the second equilibrium point in the reduced-attitude control results in a decreasing torque trend between 90° and 180°. This behavior contradicts the expected need for higher torques at larger angular displacements (relative to the commanded attitude), which is essential for executing fast maneuvers. These considerations led to modify the structure of the terms that depend on the attitude error in order to

1. avoid the existence of a second equilibrium point in the system governed by the reduced-attitude control law;
2. ensure that both control laws exhibit the same dependence on their respective error angles, enabling consistent comparisons;
3. achieve faster maneuvers without increasing actuator effort or modifying the actuation system

These improvements are achieved through the enhanced control laws previously presented, which introduce customized attitude error terms. It is worth noting that, for the reduced-attitude case, the enhancement of the control law leads to a more effective use of the actuation devices, while avoiding the existence of a second equilibrium point.

The enhanced laws present a modification in the term depending on the error in the attitude. For instance, with reference to Eq. (3.46), the function $\sin\phi'_E$ is monotonically increasing, starting from 0 when $\phi_E = 0$, and reaching 1 when ϕ_E reaches a certain angle between 0° and 180°, which can be set by appropriately choosing the free parameter γ. Beyond this point, up to $\phi_E = 180°$, the value of $\sin\phi'_E$ remains equal to 1, maximizing this term when the attitude is far from the desired one. The choice of the parameter γ strongly affects the performance of the controlled system. In fact, the parameter γ defines the threshold beyond which the term dependent on the attitude error reaches its maximum effect. Compared to the blue curve in Figure 3.1 – which represents a term that delivers its maximum effort only at $\phi_E = 180°$ – setting $\gamma > 1/2$ shifts this threshold to lower angles. This allows the attitude-error-dependent term to reach its maximum contribution even for lower, yet still significant, angular misalignments.

To demonstrate the improvements in attitude maneuver performance achieved by the enhanced control laws introduced in this chapter, numerical tests are performed and the results are compared with those obtained using the standard version of the control laws (3.22) and (3.64). Specifically, a Monte Carlo campaign comprising 1000 simulations is conducted, in which the spacecraft is reoriented toward a fixed target attitude, identical across all simulations and corresponding to

$$q_{T,0} = 1 \quad \underline{q_T} = \begin{bmatrix} 0 & 0 & 0 \end{bmatrix} \tag{3.86}$$

The variations lie in the initial conditions, namely the orientation and angular velocity. The initial attitudes are generated by applying an eigenaxis rotation to the inertial frame, where the eigenaxis is uniformly distributed over the unit sphere and the rotation angle (eigenangle) is uniformly distributed between 0 and 180 degrees. Moreover, the initial angular velocity components follow a Gaussian distribution with zero mean and a standard deviation of 0.5°/s, truncated at ±3σ. The spacecraft considered in the simulations have the following inertia matrix

$$J_C = \begin{bmatrix} 1200 & 100 & -200 \\ 100 & 2200 & 300 \\ -200 & 300 & 3100 \end{bmatrix} \mathrm{kg} \cdot \mathrm{m}^2 \tag{3.87}$$

and $\hat{b}_1$ the axis controlled in the reduced-attitude scenarios. The attitude performance is evaluated using two parameters:

1. The time to reach convergence, defined as the time at which the maneuver is considered complete. Convergence is reached when the attitude error – quantified by ϕ_E in the triaxial case and ϕ_R in the reduced-attitude case – falls below 0.1°, and the norm of the angular velocity error is less than 0.01°/s;

2. The maximum control torque, defined as the peak value reached by the control torque over the entire duration of the simulation.

Both of these parameters are computed for each simulation. However, the resulting data is highly scattered, making it difficult to clearly compare the performance of different control strategies. To address this, the results are smoothed using a moving-average filter, defined by the following relation:

$$y_i = \frac{1}{\bar{w}}\left[x_i + x_{i-1} + \ldots + x_{i-w+1}\right], \text{ with } \begin{cases} \bar{w} = i, & \text{if } i < w \\ \bar{w} = w, & \text{if } i \geq w \end{cases} \tag{3.88}$$

where x denotes the vector of data to be filtered, and w is the window size over which the moving average is computed. As a final note, all comparisons are performed using the same gain matrices, which in this case are determined through the gain selection procedure previously discussed by setting $\omega_b = 0.04$ and $\zeta = 1$.

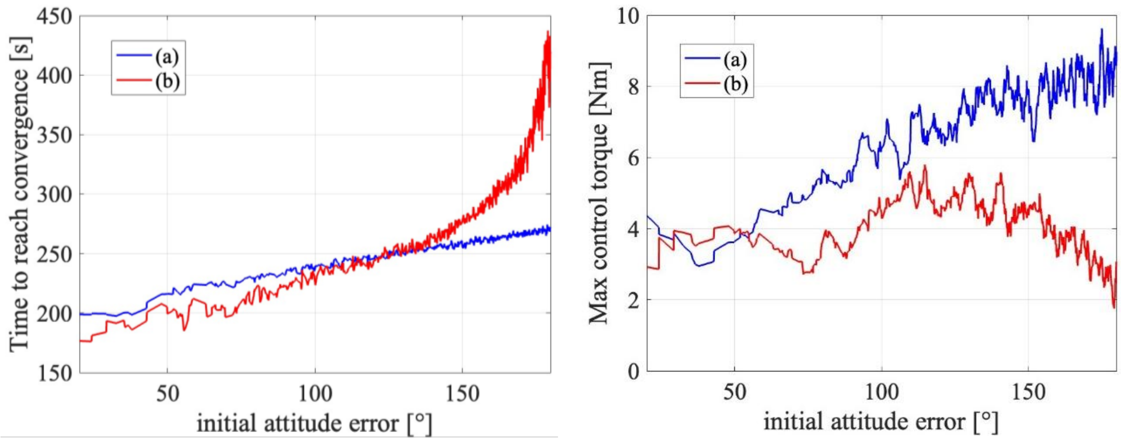

Figure 3.2: Convergence time and maximum torque comparison between control laws (a) and (b)

First, the results obtained for the standard laws (3.22) and (3.64) presented are compared. They are denoted with symbol (a) for the triaxial control law reported in Eq. (3.22) and (b) for the reduced attitude control law of Eq. (3.64). Results are reported in Figure 3.2 where the initial attitude error corresponds to $\phi_E(t_0)$ and $\phi_R(t_0)$ for triaxial and reduced-attitude cases respectively. As previously discussed, the comparison between the two control laws is not entirely consistent due to differences in how the attitude error is defined. The advantage of using the reduced-attitude control law, in terms of maneuver agility, is evident only when the initial angular distance from the desired orientation is below a certain threshold, approximately 125° in this case. Beyond that, the presence of a secondary equilibrium point in the reduced-attitude control law causes a significant increase in convergence time. However, it is also evident that the reduced-attitude control law results in lower control torque. This determines the inconsistency of the comparison, as the convergence times should ideally be evaluated under the same actuator capabilities – i.e., both control laws should operate under the same maximum torque constraints to ensure a fair assessment. To carry out a consistent comparison, the reduced control law (3.64) is substituted by the law (3.78) where parameter γ is set to 1/2, such that

$$\underline{e_R} \sin \phi'_R = \underline{e_R} \sin \frac{\phi_R}{2} \tag{3.89}$$

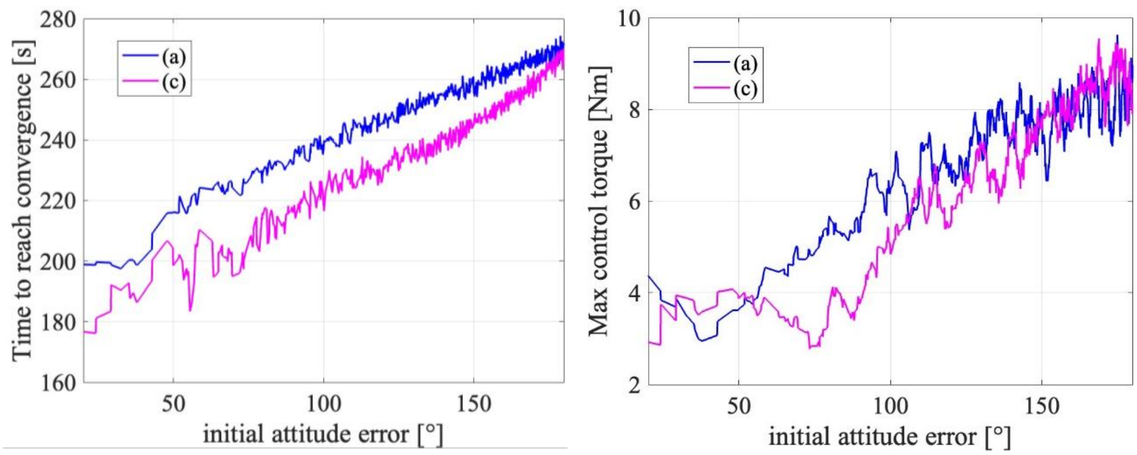

Figure 3.3: Convergence time and maximum torque comparison between control laws (a) and (c)

which has the same form of Eq. (3.81). This law is denoted with symbol (c), and the results are reported in Figure 3.3.

This comparison clearly highlights the advantage of the reduced-attitude control over the triaxial control: the convergence time is shorter due to the reduced angular path the spacecraft must follow. The use of the control law (3.78) removes the second equilibrium point from the reduced-attitude logic, avoiding the final blow-up in the convergence time. Moreover, it is worth noting that, for initial angular error close to 180 degrees, the results are similar both in terms of convergence time and maximum control torque, because the shortening of the angular path has a relative lower impact for longer maneuvers.

Finally, the role of parameter γ is investigated. The improved triaxial and reduced-attitude control laws are employed, both with $\gamma = 1$. They are denoted with symbols (d) and (e) respectively, and results are depicted in Figure 3.4. The results are similar to the ones reported in Figure 3.3. The main difference lies in the reduction of convergence time observed for both the triaxial and reduced-attitude control laws. This improvement is due to the effect of increasing the parameter γ, which causes the controller to apply the

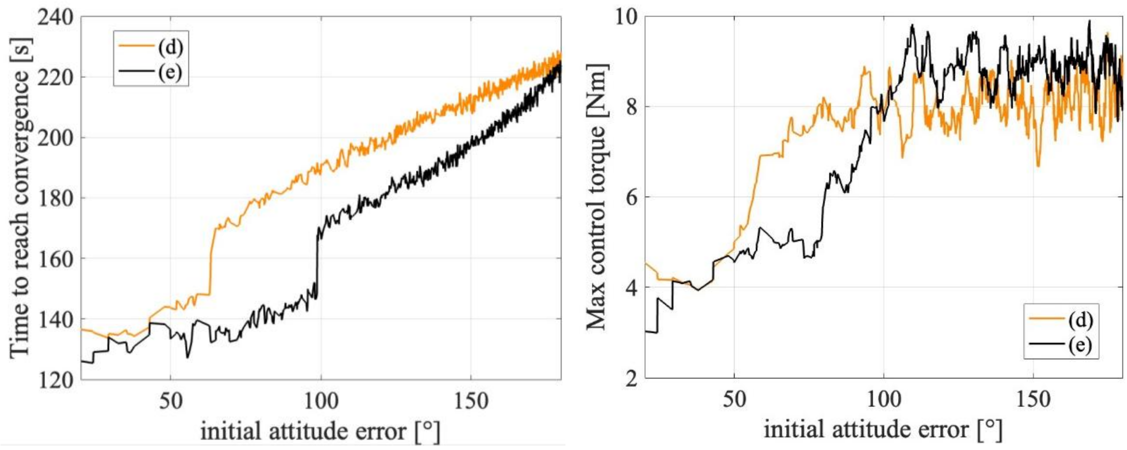

Figure 3.4: Convergence time and maximum torque comparison between control laws (d) and (e)

maximum torque associated with the orientation error whenever this error exceeds a certain threshold. This threshold depends on the value of γ and decreases as γ increases. However, excessively increasing this parameter is not advisable. A value that is too large causes the controller to apply maximum torque even when the spacecraft is already close to the target attitude. This leads to an unnecessarily high angular velocity toward the target, which the angular velocity error term

$$-J_C A^{-1} B \underline{\omega_D} \quad \text{or} \quad -J_C A^{-1} B \underline{\omega_E} \tag{3.90}$$

may not be able to sufficiently compensate for. As a result, the system can oscillate around the desired orientation. In fact, as $\gamma \to \infty$, the control law remains asymptotically stable, but the attitude error term

$$-J_C A^{-1} \underline{e_E} \sin \phi'_E \quad \text{or} \quad -J_C A^{-1} \underline{e_R} \sin \phi'_R \tag{3.91}$$

becomes permanently maximized. In this regime, the term (3.90) effectively acts as a damper, mitigating the oscillations induced by the excessive torque saturation.

As a concluding remark, all the results presented in this section are summarized in Figure 3.5. Apart from the red curve representing the control law (3.64), all the other laws are characterized by a similar maximum control torque – that almost reaches 10 Nm –, meaning that the results in term of convergence time are obtained considering the same actuators' sizing. In fact, the actuator sizing must be carried out considering the maximum possible value of the required control torque, which corresponds to the maxima of the curves reported in the right plot. It is apparent that, with same actuation, the improved

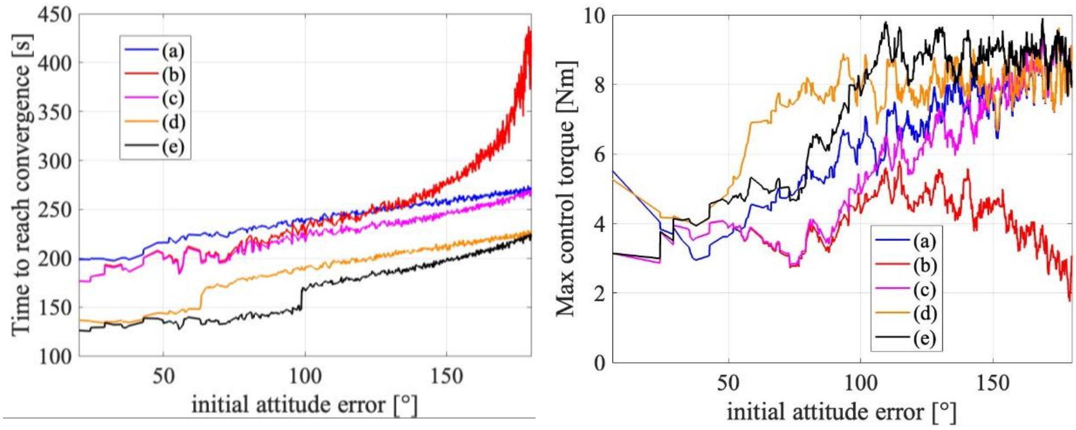

Figure 3.5: Convergence time and maximum torque comparison among all the discussed control laws

control laws where $\gamma = 1$ offer the best performance both for the triaxial (d) and the reduced-attitude (e) cases. A better choice of γ can be identified through numerical simulations, for example by performing additional Monte Carlo campaigns similar to those presented in this section and determining the value of γ that minimizes the average convergence time. As previously discussed, such a minimum exists: while an initial increase of γ from $\gamma = 1$ reduces the convergence time, excessively large values of γ eventually cause the convergence time to increase again due to oscillatory behavior around the desired attitude.

3.6. Actuation: steering laws for momentum exchange devices

The control laws discussed in the previous sections generate the inputs to the attitude actuation system, which ultimately drives the spacecraft orientation. While various types of actuators exist, they can generally be divided into two categories:

(i) Actuators that interact with the external environment to generate the required control torque. This category includes magnetic torquers, which exploit Earth's magnetic field, as well as electric and chemical thruster pairs, which provide torque by exchanging mass with the environment.

(ii) Momentum exchange devices, which reorient the spacecraft by exchanging angular momentum internally, without any interaction with the external environment.

This work focuses primarily on the second category, as these actuators are widely used because of the high pointing precision they can guarantee. Especially gyroscopes are also frequently employed when agile reorientation is required, since they can provide high torque levels and rapidly modulate them [87]. These devices are often mounted in medium and large-sized spacecraft systems in which dynamic effects are significant and must be modeled using multibody flexible dynamics. Additionally, the internal complexity of these actuators aligns well with the objective of analyzing the dynamics of complex spacecraft systems.

Among these devices, reaction wheels (RW) and single-gimbal control momentum gyroscopes (SG-CMG) are two categories commonly employed in space missions. The former simply consists of wheels that are accelerated or decelerated via internal torques operated by the spacecraft, which receives back a torque equal in magnitude and opposite in direction that leads it to rotate. The axis of rotation of the wheels remains fixed, differently from what happens in the case of the SG-CMGs. In fact, in this second case a torque is applied to an axis perpendicular to the rotation axis of the wheel, which usually rotates with constant angular rate, and the torque received by the spacecraft mainly correspond to the gyroscopic torque that arises from the rotation of the rotation axis of the wheel. This torque received by the spacecraft is larger than the torque employed by the spacecraft, and this phenomenon is known as "gyroscopic amplification" [88]. The sketch of a SG-CMG is depicted in Figure 3.6. With reference to this figure, the wheel rotates about the axis $\hat{w}_2$ with angular rate $\dot{\theta}_2$ (usually maintained constant), while the spacecraft applies a net motor torque about axis $\hat{w}_1$ making the whole device rotate with angular velocity $\dot{\theta}_1$. The resulting gyroscopic torque that the device transfers to the spacecraft – usually much larger than the net motor torque about $\hat{w}_1$ and consequently than the reaction torque transferred to the spacecraft – is parallel or opposite to $\hat{w}_2$, depending on the sense of rotation of the wheel about axis $\hat{w}_1$.

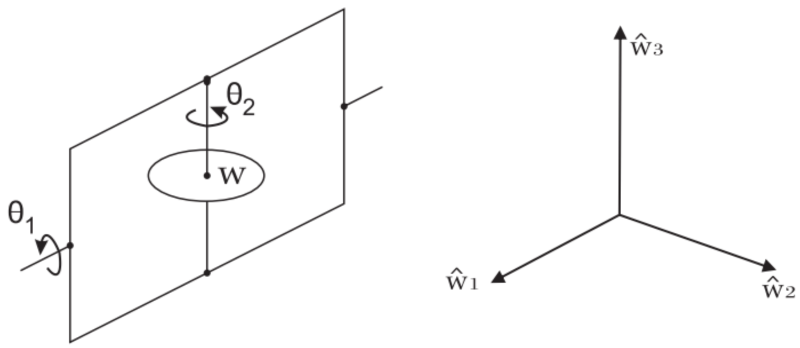

Figure 3.6 Sketch of a SG-CMG and the associated frame

A single device can provide a torque only in one direction, which is fixed with respect to the spacecraft frame in the case of reaction wheels, while it moves for the SG-CMG because $\hat{w}_3$ rotates jointly with the wheel. These peculiarity of the SG-CMG leads to the occurrence of singular configurations, i.e. configurations where the device or the array of devices cannot provide the desired torque. The presence of singularities represents the main drawback of these actuators, which otherwise offer the advantage of gyroscopic torque amplification. Singularity issues can be mitigated through dedicated avoidance algorithms or by increasing the number of devices in the array.

In practice, both reaction wheels and SG-CMGs are arranged in arrays composed of multiple devices configured to act as a single attitude control actuator. To generate torque in any desired direction, at least three devices – considering constant rotor speed SG-CMGs – are required. However, it is common to include an additional device for redundancy. In the case of reaction wheels, this redundancy is primarily for safety, since three wheels are sufficient to provide full three-axis control. In contrast, for SG-CMGs, redundancy also plays a critical role in reducing the probability of encountering singular configurations. The goal of a momentum exchange device array is to generate a torque that closely matches the control torque computed by the laws presented in the previous sections. To achieve this, appropriate steering laws must be developed to relate the devices kinematic parameters to the array overall output torque, ensuring the wheels move in a way that produces the desired control effect. Accurate modeling of the interaction of momentum exchange devices reveals that some gyroscopic effects exist that alter the actual torque transferred to the spacecraft. These effects must be evaluated and compensated, if possible.

3.6.1. Reaction wheels

Beginning with the case of a spacecraft equipped with an array of reaction wheels, the dynamic equations reveal that the actuator torque generated by the array takes the following form:

$$\underline{t}_a = -\underline{\tilde{\omega}} A \underline{\omega}_s - A_s \underline{\dot{\omega}}_s \tag{3.92}$$

where

$$A_s = \left[I_s^{(1)} \underline{a}_1^{(B)} \quad \dots \quad I_s^{(N)} \underline{a}_N^{(B)} \right] \tag{3.93}$$

is the assembly matrix of the array composed of N wheels, $\underline{a}_j^{(B)}$ the vector oriented along the j-th wheel's axis of rotation expressed in the spacecraft frame, while $I_s^{(j)}$ is the axial inertia of the j-th wheel. Moreover, $\underline{\omega}_s$ is the vector containing the angular rate of the wheels. It is then necessary to find a way to move the wheel such that the actuator torque $\underline{t}_a$ is equal to the commanded torque $\underline{t}_c$. From Eq. (3.92) one obtains that

$$-\underline{\tilde{\omega}} A \underline{\omega}_s - A_s \underline{\dot{\omega}}_s = \underline{t}_c \Rightarrow A_s \underline{\dot{\omega}}_s = -\underline{t}_c + \underline{\tilde{\omega}} A \underline{\omega}_s \tag{3.94}$$

If A_s is a 3×3 square nonsingular matrix, meaning that the array is composed of three reaction wheels aligned such that vectors $\underline{a}$ form a basis of $\mathbb{R}^3$, the solution of Eq. (3.94) is

$$\underline{\dot{\omega}_s} = -A_s^{-1}\left(\underline{t_c} - \underline{\tilde{\omega}}A\underline{\omega_s}\right) \tag{3.95}$$

Instead, for redundant arrays (where N > 3), the redundant degrees of freedom leads to the possibility of minimizing a cost function. Usually, it is chosen to minimize the angular velocities of the wheels, and this results in computing the Moore-Penrose pseudoinverse [89] of the matrix A_s, leading to

$$\underline{\dot{\omega}_s} = -A_s^T\left(A_sA_s^T\right)^{-1}\left(\underline{t_c} - \underline{\tilde{\omega}}A\underline{\omega_s}\right) \tag{3.96}$$

It is worth noting that, in the case of reaction wheels, it is possible to drive the wheels angular accelerations to precisely generate the desired torque, provided that this torque does not exceed the physical limits of the actuators. In fact, additional terms are included in the torque model used to derive the steering law, compared to what is commonly found in the literature – i.e. $\underline{t_a} = -A_s\underline{\dot{\omega}_s}$ [87] –, leading to higher accuracy in tracking the commanded torque. The term $\underline{\tilde{\omega}}A\underline{\omega_s}$, which represents an undesired effect due to the gyroscopic coupling between the spacecraft attitude motion and the wheels spin rates, is taken into account and compensated for within the steering law.

3.6.2. Single-Gimbal CMG

In the case of SG-CMGs, a similar procedure is followed, although with added complexity due to the more intricate dynamics of the gyroscopes and the presence of singularities. These factors require appropriately designed modifications to the steering law to properly account for their effects. As a first step, the torque generated by an array of SG-CMGs is computed using the dynamic model of the spacecraft equipped with the array, and is given by [37]:

$$\begin{aligned}\underline{t_a} = &\sum_{j=1}^{N}\left[I_s^{(j)}\omega_R^{(j)}\left(c_{\theta_1}^{(j)}\underline{r_{A2}}^{(j)} + s_{\theta_1}^{(j)}\underline{r_{A3}}^{(j)}\right) - \underline{\tilde{\omega}}J_t^{(j)}\underline{r_{A1}}^{(j)}\right]\dot{\theta}_1^{(j)} + \\ &+\underline{\tilde{\omega}}\sum_{j=1}^{N}\omega_R^{(j)}I_s^{(j)}\left[s_\theta^{(j)}\underline{r_{A2}}^{(j)} - c_\theta^{(j)}\underline{r_{A3}}^{(j)}\right] + \\ &-\sum_{j=1}^{N}I_t^{(j)}\underline{r_{A1}}^{(j)}\ddot{\theta}_1^{(j)}\end{aligned} \tag{3.97}$$

where $\dot{\theta}_1^{(j)}$ and $\ddot{\theta}_1^{(j)}$ are respectively the angular velocity and acceleration of the gimbal axis – $\hat{w}_1$ in Figure 3.6 – , $s_{\theta_1}^{(j)}$ and $c_{\theta_1}^{(j)}$ are respectively the sine and the cosine of the gimbal angle, $I_s^{(j)}$ and $I_t^{(j)}$ are axial and transverse moments of inertia of the wheels, $\omega_R^{(j)}$ is the constant rotor speed. Finally, $\underline{r_{A1}}^{(j)}$, $\underline{r_{A2}}^{(j)}$ and $\underline{r_{A3}}^{(j)}$ are the three unit vectors of the SG-CMG frame $\underline{\underline{W}} = \left[\hat{w}_1 \quad \hat{w}_2 \quad \hat{w}_3\right]$ in the configuration when $\theta_1^{(j)} = 0$ and projected in the spacecraft body frame $\underline{\underline{B}}$. They can also be seen as the rows of the rotation matrix $\underset{W_0 \leftarrow B}{R}$ where $\underline{\underline{W}} = \left[\hat{w}_1|_{\theta_1^{(j)}=0} \quad \hat{w}_2|_{\theta_1^{(j)}=0} \quad \hat{w}_3|_{\theta_1^{(j)}=0}\right]$. Finding a steering law from this complex model is a relatively complicated task. However, the last term of Eq. (3.97) can be neglected because usually it is of lower order of magnitude compared to the remaining terms. Hence, $\underline{t_a}$ can be rewritten as

$$\underline{t_a} = \left(A_s - \tilde{\underline{\omega}} B_s\right)\underline{\dot{\theta}_s} + \underline{t_a}^{(R)} = A_s^+ \underline{\dot{\theta}_s} + \underline{t_a}^{(R)} \tag{3.98}$$

where vector $\underline{\dot{\theta}_s}$ collects the gimbal angular velocities of the N devices, and

$$A_s = \left[I_s^{(1)}\omega_R^{(1)}\underline{f_1} \quad \cdots \quad I_s^{(N)}\omega_R^{(N)}\underline{f_N}\right] \tag{3.99}$$

$$B_s = \left[I_t^{(1)}\underline{r_{A1}}^{(1)} \quad \cdots \quad I_t^{(N)}\underline{r_{A1}}^{(N)}\right] \tag{3.100}$$

$$\underline{t_a}^{(R)} = \tilde{\underline{\omega}} \sum_{j=1}^{N} \omega_R^{(j)} I_s^{(j)} \left[s_{\theta_1}^{(j)} \underline{r_{A2}}^{(j)} - c_{\theta_1}^{(j)} \underline{r_{A3}}^{(j)}\right] \tag{3.101}$$

where $\underline{f_j}$ is the actual direction of $\hat{w}_2$ - considering the gimbal rotation – resolved in the spacecraft body frame, i.e.

$$\underline{f_j} = c_{\theta_1}^{(j)} \underline{r_{A2}}^{(j)} + s_{\theta_1}^{(j)} \underline{r_{A3}}^{(j)} \tag{3.102}$$

Under these assumptions, the gimbal angular velocities are sought such that

$$A_s^+ \underline{\dot{\theta}} + \underline{t_a}^{(R)} = \underline{t_c} \quad \Rightarrow \quad A_s^+ \underline{\dot{\theta}} = \underline{t_c^+} \tag{3.103}$$

where $\underline{t_c^+} = \underline{t_c} - \underline{t_a}^{(R)}$. In Eq. (3.98) an almost complete model of the actuators torque is considered: additional terms are included with respect to what one can commonly find in the literature [87], i.e. $\underline{t_a} = A_s \underline{\dot{\theta}_s}$, leading to higher accuracy in tracking the commanded torque.

The Moore-Penrose pseudoinverse solves the preceding equation when N > 3, while minimizing the norm of the gimbal angular velocity vector $\underline{\dot{\theta}_s}$,

$$\underline{\dot{\theta}_s} = A_s^{+T}(A_s^+ A_s^{+T})^{-1}\underline{t_c^+} \tag{3.104}$$

As previously discussed, an array of SG-CMGs may suffer from singularity issues, depending on the number of devices constituting the array and their orientation and actioning. A singularity occurs when $\det(A_s^+ A_s^{+T})$ is close to zero, leading to numerical instability of the inversion process. In fact, the parameter

$$m = \sqrt{\det(A_s^+ A_s^{+T})} \tag{3.105}$$

is known as the singularity measure of the array. Different strategies to tackle the problem of occurrence of singularities exist. Among them, one of the most employed consists of computing the singularity direction avoidance pseudoinverse. It is a modification of the Moore-Penrose pseudoinverse, where an additional term is added to exit the neighborhood of a singularity. This error obviously deviates the actuator torque from the desired commanded control torque. Then, to reduce it, it is applied only to the direction of the smallest singular value of A_s^+ in order to regularize it. In fact, the singular value decomposition of A_s^+ is

$$A_s^+ = U\Sigma V^T \tag{3.106}$$

with $U \in \mathbb{R}^{3\times 3}$ left singular vectors matrix, $\Sigma \in \mathbb{R}^{3\times N}$ singular values matrix, and $V \in \mathbb{R}^{N\times N}$ right singular vector matrix. The algorithm consists of modifying Eq. (3.104) as follows:

$$\underline{\dot{\theta}_s} = A_s^{+T}(A_s^+ A_s^{+T} + X)^{-1}\underline{t_c^+} \tag{3.107}$$

where

$$X = U\begin{bmatrix} 0 & 0 & 0 \\ 0 & 0 & 0 \\ 0 & 0 & \alpha \end{bmatrix}U^T \tag{3.108}$$

with

$$\alpha = \alpha_0 \exp\left\{-\mu\sqrt{\det(A_S^+ A_S^{+t})}\right\} \tag{3.109}$$

where α_0 and μ are two positive constants, to properly tune. In fact, substitution of Eqs. (3.106) and (3.108) into Eq. (3.107) – and considering that U and V are orthogonal – leads to

$$\underline{\dot{\theta}_s} = V \begin{bmatrix} \frac{1}{\sigma_1} & 0 & 0 \\ 0 & \frac{1}{\sigma_1} & 0 \\ 0 & 0 & \frac{\sigma_3}{\sigma_3^2 + \alpha} \\ & 0_{(N-3)\times 3} & \end{bmatrix} U^T \underline{t_c^+} \tag{3.110}$$

where σ_i are the singular values of matrix A_s^+ (ordered with decreasing magnitudes as *i* increases). The torque error introduced if the steering law (3.110) is adopted corresponds to

$$\underline{t_e} = \underline{t_c^+} - A_s^+ \underline{\dot{\theta}_s} = U \begin{bmatrix} 0 & 0 & 0 \\ 0 & 0 & 0 \\ 0 & 0 & \alpha/\left(\sigma_3^2 + \alpha\right) \end{bmatrix} U^T \underline{t_c^+} \tag{3.111}$$

and is only limited to the singular direction associated with the smallest singular value. When matrix A_s^+ is far from singularity, $\sigma_3 \gg \alpha$ and the torque error is negligible. In this case, the outcome of Eq. (3.110) corresponds to the one of the classic Moore-Penrose pseudoinverse of Eq. (3.104). However, the procedure of using the singular value decomposition can be still maintained to fasten the inversion of $A_s^+ A_s^{+T}$.

3.7. Relative orbital motion (Battin-Giorgi formulation)

Successful rendezvous maneuvers require a high-fidelity model of the chaser spacecraft motion relative to the target. Several approaches have been developed to describe this relative motion. One of the most widely used is based on linear orbit theory – specifically, the Hill-Clohessy-Wiltshire (HCW) equations [90]. These equations result from a linearization of the relative motion dynamics around the target nominal trajectory and are therefore accurate only when the chaser remains sufficiently close to the target. Furthermore, the HCW model assumes the absence of perturbations and a target spacecraft on a circular orbit with zero inclination. A well-known generalization of the HCW equations to elliptical orbits is provided by the Tschauner-Hempel formulation [36, 91], which, however, still relies on the same simplifying assumptions regarding perturbations, inclination and relative distance.

When more general scenarios are considered – such as highly elliptical and inclined or significantly perturbed orbits – it becomes necessary to adopt nonlinear models. One of the most established alternatives is the Battin-Giorgi (BG) approach [36], which avoids any linearization and therefore imposes no constraints on the distance between the chaser and the target. The classical BG formulation describes the motion of a perturbed spacecraft relative to a reference body moving on a Keplerian orbit. Consequently, to determine the relative motion of a chaser with respect to a target on a perturbed trajectory, one must separately compute the motion of both spacecraft with respect to a virtual reference body following a Keplerian path. The difference between their relative positions with respect to the virtual spacecraft yields the nonlinear relative motion between chaser and target. However, when the target trajectory deviates significantly from a Keplerian orbit (because of the perturbations), frequent updates of the reference path are required, making the method impractical. In the following, a modified version of the BG approach is introduced, in which the reference orbit is no longer restricted to being Keplerian. This enables a more direct and practical modeling of spacecraft motion with respect to perturbed target orbits.

In a generic inertial reference frame, the target acceleration is

$$\ddot{\underline{r}}_t = -\frac{\mu}{r_t^3}\underline{r}_t + \underline{a}_{p,t} \tag{3.112}$$

$\underline{r}_t$ the inertial position vector of the target and r_t its norm, μ the gravitational constant and $\underline{a}_{p,t}$ the sum of all relevant perturbing accelerations acting on the target. In a similar way, for the chaser

$$\ddot{\underline{r}}_c = -\frac{\mu}{r_c^3}\underline{r}_c + \underline{a}_{p,c} + \underline{a}_{t,c} \tag{3.113}$$

where $\underline{r}_c$ is the position vector of the chaser, $\underline{a}_{p,c}$ the perturbation acceleration acting on the chaser, and $\underline{a}_{t,c}$ the thrust acceleration of the chaser, i.e. the control variable. The relative position is defined as

$$\underline{\rho} = \underline{r}_c - \underline{r}_t \tag{3.114}$$

and then

$$\ddot{\underline{\rho}} = -\frac{\mu}{r_c^3}\underline{r}_c + \frac{\mu}{r_t^3}\underline{r}_t + \underline{a}_{p,c} - \underline{a}_{p,t} + \underline{a}_{t,c} \tag{3.115}$$

The following manipulation can be carried out:

$$-\frac{\mu}{r_c^3}\underset{\rightarrow}{r}_c+\frac{\mu}{r_t^3}\underset{\rightarrow}{r}_t=-\frac{\mu}{r_c^3}\underset{\rightarrow}{\rho}-\frac{\mu}{r_c^3}\underset{\rightarrow}{r}_t+\frac{\mu}{r_t^3}\underset{\rightarrow}{r}_t=\frac{\mu}{r_t^3}\underset{\rightarrow}{r}_t\left[1-\frac{r_t^3}{r_c^3}\right]-\frac{\mu}{r_c^3}\underset{\rightarrow}{\rho} \tag{3.116}$$

However, since $1-r_t^3/r_c^3$ becomes very small when $r_c \approx r_t$, it can lead to numerical issues that impair the accuracy of the integration. To mitigate this and improve numerical stability, the expression can be further rearranged as:

$$1-\frac{r_t^3}{r_c^3}=1-\frac{r_t^3}{\left|\underset{\rightarrow}{\rho}+\underset{\rightarrow}{r}_t\right|^3}=1-\frac{r_t^3}{\left(\rho^2+r_t^2+2\underset{\rightarrow}{\rho}\cdot\underset{\rightarrow}{r}_t\right)^{3/2}} \tag{3.117}$$

and the following parameter is introduced:

$$q=\frac{\rho^2+2\underset{\rightarrow}{\rho}\cdot\underset{\rightarrow}{r}_t}{r_t^2} \tag{3.118}$$

Then, the BG equations of the relative motion assume the form

$$\ddot{\underset{\rightarrow}{\rho}}=\frac{\mu}{r_t^3}\frac{q\left[2+q+\sqrt{1+q}\right]}{(1+q)^{3/2}\left[\sqrt{1+q}+1\right]}\underset{\rightarrow}{r}_t-\frac{\mu}{r_c^3}\underset{\rightarrow}{\rho}+\underset{\rightarrow}{a}_{p,c}-\underset{\rightarrow}{a}_{p,t}+\underset{\rightarrow}{a}_{t,c} \tag{3.119}$$

In the previous relation, $\ddot{\underset{\rightarrow}{\rho}}={}^{N}\ddot{\underset{\rightarrow}{\rho}}\triangleq\left.\frac{d^2}{dt^2}\right|_N\left(\underset{\rightarrow}{\rho}\right)$ is the relative acceleration vector obtained from a double time derivation of the relative position vector computed in the inertial reference frame. However, for relative motion, the Local Vertical Local Horizontal (LVLH) frame centered in the target is preferred with respect to an inertial frame. If the Earth Centered Inertial frame is denoted with unit vectors $\hat{c}_i$, the axes of the LVLH frame are defined as reported in Figure 3.7, where symbols Ω, i and θ_t indicate the RAAN (Right Ascension of the Ascending Node), inclination, and argument of latitude of the spacecraft orbit. Specifically, the LVLH is centered in the spacecraft's center of mass and

- $\hat{r}$ is parallel to the position vector of the spacecraft with respect to the central body;
- $\hat{\theta}$ is directed toward the spacecraft orbital velocity;
- $\hat{h}$ is aligned with the spacecraft angular momentum;

Since the LVLH frame associated with the target spacecraft (denoted as LVLH-T) is rotating, the relative acceleration between chaser and target computed with respect to the LVLH-T reference frame is obtained by applying twice the transport theorem

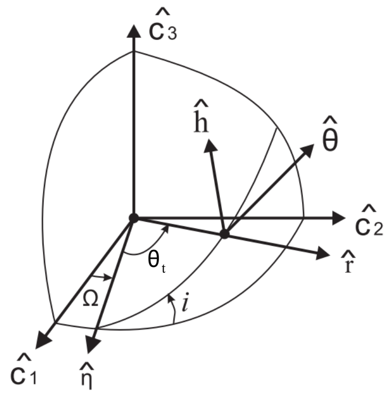

Figure 3.7: Orientation of the LVLH frame with respect to the ECI frame

$$^{N}\dot{\underset{\rightarrow}{\rho}} = {}^{L}\dot{\underset{\rightarrow}{\rho}} + {}^{N}\underset{\rightarrow}{\omega}_t^{L} \times \underset{\rightarrow}{\rho} \Rightarrow {}^{N}\ddot{\underset{\rightarrow}{\rho}} = {}^{L}\ddot{\underset{\rightarrow}{\rho}} + 2\,{}^{N}\underset{\rightarrow}{\omega}_t^{L} \times {}^{L}\dot{\underset{\rightarrow}{\rho}} + {}^{N}\dot{\underset{\rightarrow}{\omega}}_t^{L} \times \underset{\rightarrow}{\rho} + {}^{N}\underset{\rightarrow}{\omega}_t^{L} \times {}^{N}\underset{\rightarrow}{\omega}_t^{L} \times {}^{L}\dot{\underset{\rightarrow}{\rho}} \tag{3.120}$$

where ${}^{N}\underset{\rightarrow}{\omega}_t^{L}$ is the orbital angular velocity – and not the spacecraft angular velocity – of the LVLH-T frame with respect to the inertial frame. It can be expressed in the LVLH-T frame as a function of the Classical Orbit Elements (COE) and their time derivatives

$$^{N}\underset{\rightarrow}{\omega}^{L} = \begin{bmatrix} \hat{r} & \hat{\theta} & \hat{h} \end{bmatrix} \begin{bmatrix} \dot{\Omega}\sin i \sin\theta_t + \dot{i}\cos\theta_t \\ \dot{\Omega}\sin i cos\theta_t - \dot{i}\sin\theta_t \\ \dot{\Omega}\cos i + \dot{\theta}_t \end{bmatrix} \tag{3.121}$$

where the time derivatives of the COE are provided by the Gauss Variational Equations:

$$\begin{aligned} \dot{i} &= r\frac{\cos\theta_t}{h}a_h \\ \dot{\Omega} &= r\frac{\sin\theta_t}{h\sin i}a_h \\ \dot{\theta}_t &= \sqrt{\frac{\mu}{p^3}}\left(1+e\cos\nu\right)^2 - r\frac{\sin\theta_t\cos i}{h\sin i}a_h \end{aligned} \tag{3.122}$$

where r is the spacecraft radius, e is the eccentricity, ν the true anomaly, θ_* the argument of pericenter, and $\left(a_{r,}a_\theta, a_t\right)$ are the components of the non-Keplerian acceleration acting on the spacecraft resolved in the LVLH-T frame. Thus, substituting Eq. (3.120) in Eq. (3.119), one obtains the BG equations with kinematic quantities computed in the LVLH-T frame

$$
\begin{aligned}
{}^{L}\ddot{\underset{\rightarrow}{\rho}} = & -2\,{}^{N}\underset{\rightarrow}{\omega}_t^{L} \times {}^{L}\dot{\underset{\rightarrow}{\rho}} - {}^{N}\dot{\underset{\rightarrow}{\omega}}_t^{L} \times \underset{\rightarrow}{\rho} - {}^{N}\underset{\rightarrow}{\omega}_t^{L} \times {}^{N}\underset{\rightarrow}{\omega}_t^{L} \times {}^{L}\dot{\underset{\rightarrow}{\rho}} \\
& + \frac{\mu}{r_t^3} \frac{q\left[2+q+\sqrt{1+q}\right]}{(1+q)^{3/2}\left[\sqrt{1+q}+1\right]} \underset{\rightarrow}{r}_t - \frac{\mu}{r_c^3} \underset{\rightarrow}{\rho} + \underset{\rightarrow}{a}_{p,c} - \underset{\rightarrow}{a}_{p,t} + \underset{\rightarrow}{a}_{t,c}
\end{aligned}
\tag{3.123}
$$

In the following sections, this version of the Battin-Giorgi equations will be primarily referenced, and the superscripts will be omitted to simplify the notation. The term ${}^{N}\dot{\underset{\rightarrow}{\omega}}_t^{L}$ is computed numerically: the time history of the components of ${}^{N}\underset{\rightarrow}{\omega}_t^{L}$ obtained from Eq. (3.121) are propagated and then interpolated and derived with respect to time to obtain the components of ${}^{N}\underset{\rightarrow}{\omega}_t^{L}$.

The main difference introduced with respect to the classical Battin-Giorgi scheme lies in the choice of the reference orbit. In this formulation, the reference is the actual trajectory of the target, which inherently accounts for the perturbations acting upon it. The absence of a virtual Keplerian reference spacecraft significantly improves the numerical performance of the integration. In fact, in the standard approach, the relative motion of the chaser with respect to the target is obtained as the difference between their respective motions relative to a virtual Keplerian spacecraft, i.e.:

$$
\underset{\rightarrow}{\rho} = \underset{\rightarrow}{\rho}_c - \underset{\rightarrow}{\rho}_t \quad \text{with} \quad \begin{cases} \underset{\rightarrow}{\rho}_c = \underset{\rightarrow}{r}_c - \underset{\rightarrow}{r}_k \\ \underset{\rightarrow}{\rho}_t = \underset{\rightarrow}{r}_t - \underset{\rightarrow}{r}_k \end{cases}
\tag{3.124}
$$

with $\underset{\rightarrow}{r}_k$ position vector of the Keplerian spacecraft. This implies that, in the standard formulation, two sets of Battin-Giorgi equations must be integrated: one for the chaser and one for the target, each relative to the virtual Keplerian spacecraft. Additionally, the Keplerian orbit of the virtual spacecraft itself must be propagated. However, if the perturbations acting on both the chaser and the target cause them to drift together away from the virtual spacecraft – while maintaining a small relative distance between each other due to the similar effect of the perturbations – the standard approach ends up operating with $\left|\underset{\rightarrow}{\rho}_c\right|, \left|\underset{\rightarrow}{\rho}_t\right| \gg \left|\underset{\rightarrow}{\rho}\right|$, degrading numerical accuracy compared to the proposed approach, which works directly with $\underset{\rightarrow}{\rho}$. In fact, in the standard scheme, when such divergence occurs, the virtual Keplerian reference orbit is typically re-centered on the updated target trajectory. This correction step, however, is entirely unnecessary in the proposed formulation.

3.8. Relative orbital control

Achieving a successful rendezvous maneuver relies on accurately controlling the relative trajectory between the chaser and the target, as described by Eq. (3.123). Within the context of nonlinear control methods, feedback linearization stands out as a well-established and effective strategy. This technique enables precise trajectory tracking even in the presence of strong nonlinearities and perturbations, provided that the system's state vector is accurately known. For these reasons, it is adopted here as a suitable approach for relative trajectory control. First, the classical control law based on feedback linearization is presented. Then, a novel adaptive-gain control law incorporating a predictive logic, referred to as Hybrid Predictive Control (HPC), is introduced, and the performance of the two approaches is compared through numerical analysis.

3.8.1. Feedback linearization

The relative motion equations can be written in the following form where all the components vectors are resolved in the LVLH-T frame, recognizing a Multi-Input Multi Output system:

$$\underline{\ddot{\rho}} = \underline{f}\left(\underline{\rho}, \underline{\dot{\rho}}\right) + \underline{a}_{t,c} \tag{3.125}$$

with

$$\begin{aligned} \underline{f}\left(\underline{\rho}, \underline{\dot{\rho}}\right) &= -2\,\underline{\tilde{\omega}}_t \underline{\dot{\rho}} - \underline{\dot{\tilde{\omega}}}_t \underline{\rho} - \underline{\tilde{\omega}}_t \underline{\tilde{\omega}}_t \underline{\rho} \\ &\quad + \frac{\mu}{r_t^3} \frac{q\left[2 + q + \sqrt{1+q}\right]}{(1+q)^{3/2}\left[\sqrt{1+q} + 1\right]} \underline{r}_t - \frac{\mu}{r_c^3} \underline{\rho} + \underline{a}_{p,c} - \underline{a}_{p,t} \end{aligned} \tag{3.126}$$

The term $\underline{f}\left(\underline{\rho}, \underline{\dot{\rho}}\right)$ is a nonlinear vector function. The control acceleration $\vec{a}_{p,t}$ must drive the chaser to follow a desired trajectory defined by $\vec{\rho}_d(t)$, $\vec{\dot{\rho}}_d(t)$ and $\vec{\ddot{\rho}}_d(t)$. Generally, a PD-like structure is employed in the feedback linearization strategy. If the relative trajectory error is defined as

$$\underline{e} \triangleq \underline{\rho} - \underline{\rho_d} \tag{3.127}$$

then, the chaser thrust acceleration will assume the following form [92]:

$$\underline{a}_{t,c} = -\underline{f} + \underline{\rho_d} - K_d \underline{\dot{e}} - K_p \underline{e} \tag{3.128}$$

where $K_p = k_p I_{3\times3}$ and $K_d = k_d I_{3\times3}$ are 3×3 diagonal and constant gain matrices. The closed loop system is obtained by substituting Eq. (3.128) into Eq. (3.125), leading to

$$\ddot{\underline{e}} + k_d \dot{\underline{e}} + k_p \underline{e} = 0 \tag{3.129}$$

The control law yields a decoupled and linear second-order system, where $\underline{e} = \underline{0}$ and $\dot{\underline{e}} = \underline{0}$ constitute the target set that enjoys global asymptotic stability properties. Moreover, the transient behavior can be easily controlled by proper tuning of the gains. In fact, the i-th scalar equation

$$\ddot{e}_i + k_d \dot{e}_i + k_p e_i = 0 \tag{3.130}$$

can be rewritten introducing the natural frequency ω_n and the damping factor ζ, leading to the following relations:

$$\begin{cases} k_p = \omega_n^2 \\ k_d = 2\zeta\omega_n \end{cases} \tag{3.131}$$

3.8.2. Hybrid predictive control

The control law (3.128) is perfectly capable of driving the chaser toward the desired position with respect to the target spacecraft. However, from a performance point of view, it provides – for most of the mission duration – a thrust acceleration that is much lower than the maximum available one. This happens because usually $\left|-\underline{f} + \ddot{\underline{\rho}}_d\right|$ equals a fraction of the maximum thrust acceleration, denoted as u_{max} in the following. Then, if the gains are set at the beginning of the orbit maneuver such that $\left|\underline{a}_{t,c}(t_0)\right| = u_{max}$, it follows that $\left|\underline{a}_{t,c}(t)\right|$ rapidly decreases with the reduction of the relative position and velocity errors operated by the control itself. As a consequence of that, larger thrust are used only in the very first seconds of the maneuver.

To contrast this effect, a saturation logic can be applied to control law (3.128) in order to have $\left|\underline{a}_{t,c}\right| = u_{max}$ not only at the initial time, but for a certain time interval. However, this approach presents two main issues:

(i) The choice of the gains cannot be opportunely a-priori operated, if not by computing a numerical parametric analysis, which however may be in contrast with real-time applications;

(ii) In the scaling operated by the classic saturation process, the term $\left(-\underline{f}+\underline{\ddot{\rho}}_d\right)$ – which compensates for the dynamic nonlinearities and perturbations, and allow for the closed loop system to assume form reported in Eq. (3.130) – is reduced in magnitude, losing the peculiarity of the feedback linearization strategy

In this work, a novel adaptive version of (3.130) is proposed, which analytically finds the opportune gain values in the saturation intervals, while maintaining term $\left(-\underline{f}+\underline{\ddot{\rho}}_d\right)$ unaltered. The proportional and derivative gains are obtained at each time instant by setting

$$\left|\underline{a}_{t,c}\right| = \left|-\underline{f}+\underline{\rho}_d - k_d\underline{\dot{e}} - k_p\underline{e}\right| = u_{max} \tag{3.132}$$

and, considering that $k_d = 2\zeta\sqrt{k_p}$ (cf. Eq. (3.131)), Eq. (3.132) becomes

$$\left|-\underline{f}+\underline{\rho}_d - 2\zeta k\underline{\dot{e}} - k^2\underline{e}\right| = u_{max} \tag{3.133}$$

where the auxiliary variable $k=\sqrt{k_p}$ is introduced. From Eq. (3.133), one obtains that

$$\begin{aligned} &\left|\underline{e}\right|^2 k^4 + 4\zeta\underline{\dot{e}}^T\underline{e}k^3 + \left[4\zeta^2\left|\underline{\dot{e}}\right|^2 - 2\left(-\underline{f}+\underline{\rho}_d\right)^T\underline{e}\right]k^2 \\ &\qquad -4\zeta\left(-\underline{f}+\underline{\rho}_d\right)^T\underline{\dot{e}}k + \left|-\underline{f}+\underline{\rho}_d\right|^2 - u_{max}^2 = 0 \end{aligned} \tag{3.134}$$

Once the damping ratio is selected according to the desired performance – typically set to 1 to achieve critical damping condition – the result is a fourth-degree equation in the scalar unknown k, representing the gain of the control law.

Solving Eq. (3.134) at the beginning of the rendezvous maneuver allows the enforcement of a feedback linearization control that exploits the maximum available thrust acceleration at the starting time. As previously discussed, the classic feedback linearization adopts constant gains, which implies that the thrust magnitude is saturated only at the very beginning, while it reduces at subsequent times. To obtain saturated thrust over a finite time interval, a hybrid predictive control can be implemented, which uses adaptive gains in a first phase, then switches to a second phase that employs constant-gain feedback linearization. In particular, Eq. (3.134) is solved at any time in the saturation phase, to find the gains k_p and k_d that guarantee maximum thrust. As detailed in [93], the longer the saturation time, the higher the peak of the thrust acceleration magnitude of the constant-gain feedback linearization at the beginning of the second phase. This happens because the more the saturation phase lasts, the higher is the relative velocity at the end of the saturation phase. Then, at the beginning of the constant-gain phase the relative position error continues to decrease, while the relative velocity error increases; if the velocity error grows enough quickly – and this always happens after a certain saturation time sufficiently long –, it leads to a subsequent peak in thrust magnitude. This behavior is taken into account for the definition of the stop criterion for the first saturation phase. In fact, a predictive integration during the saturation phase can be carried out using constant-gain feedback linearization after the end of saturation. The saturation phase stops when the thrust acceleration magnitude in the subsequent (constant-gain) phase reaches a peak value that overcomes u_{max} – or a threshold that is set slightly below u_{max} for safety reason.

Before discussing the performance of this control law, it is needed to prove the existence of a positive real root of Eq. (3.134). Letting

$$\begin{cases} \underline{w} \triangleq -2\zeta k \dot{\underline{e}} - k^2 \underline{e} \\ \underline{c} \triangleq -\underline{f} + \underline{\ddot{\rho}_d} \end{cases} \tag{3.135}$$

Eq. (3.132) can be rewritten as

$$\left| \underline{w} + \underline{c} \right| = u_{max} \tag{3.136}$$

As a first step, provided that $\dot{\underline{e}} = \underline{0}$ and $\underline{e} = \underline{0}$ do not hold at the same time, a positive gain k always exists such that $\underline{w}$ has a specified (nonzero) magnitude. To prove the preceding statement, it is assumed that $\dot{\underline{e}} \neq \underline{0}$. If $\underline{e} = \underline{0}$ or $\underline{e}$ aligned with $\dot{\underline{e}}$, then it is straightforward to obtain the positive value of k corresponding to the desired magnitude w. If $\underline{e} \neq \underline{0}$ and the two vectors $\underset{\to}{e}$ and $\underset{\to}{\dot{e}}$ – associated with $\underline{e}$ and $\dot{\underline{e}}$ – are not aligned, then they identify a plane. Two unit vectors are introduced, i.e. $\hat{\xi}$, aligned with $-\underset{\to}{\dot{e}}$, and $\hat{\chi}$, coplanar with $\underset{\to}{e}$ and orthogonal to $\hat{\xi}$. In this plane, vector

$$-\underset{\to}{e} \triangleq n_\xi \hat{\xi} + n_\chi \hat{\chi} \tag{3.137}$$

while

$$-\underset{\to}{\dot{e}} \triangleq m\hat{\xi} \tag{3.138}$$

with m > 0. Using these definitions,

$$\underset{\to}{w} = \left(k^2 n_\zeta + 2\zeta k m \right) \hat{\xi} + k^2 n_\chi \hat{\chi} \tag{3.139}$$

If w_ξ and w_χ denote the two components of $\underset{\rightarrow}{w}$ in the plane at hand, elimination of k from Eq. (3.139) yields the following equation for the curve described by $\underset{\rightarrow}{w}$:

$$k^2 = \frac{w_\chi}{n_\chi} \Rightarrow w_\xi = 2\zeta m \sqrt{\frac{w_\chi}{n_\chi}} + \frac{n_\xi}{n_\chi} w_\chi \tag{3.140}$$

where n_ξ and w_ξ have the same sign due to Eq. (3.139). The derivative of w_ξ with respect to w_χ is

$$\frac{dw_\xi}{dw_\chi} = \frac{m}{\sqrt{w_\chi n_\chi}} + \frac{n_\xi}{n_\chi} \tag{3.141}$$

Because the first term tends to 0 as $w_\chi n_\chi \left(= k^2 n_\chi^2\right)$ increases, the second term in Eq. (3.141) dominates, and the geometrical locus described by vector $\underset{\rightarrow}{w}$ is radially unbounded as a result. Because $\underset{\rightarrow}{w}$ has zero magnitude at k = 0, due to continuity of w_ξ and w_χ as functions of k, in conjunction with radial unboundedness of $\underset{\rightarrow}{w}$, a positive value of k certainly exists such that $\underset{\rightarrow}{w}$ has prescribed magnitude.

In light of the preceding conclusion, the existence of a real positive value of k is transformed into the problem of finding a vector $\underset{\rightarrow}{w}$ (with components in the LVLH-T frame collected in $\underline{w}$) such that its magnitude w fulfills Eq. (3.136). To do this, vector $\underset{\rightarrow}{c}$

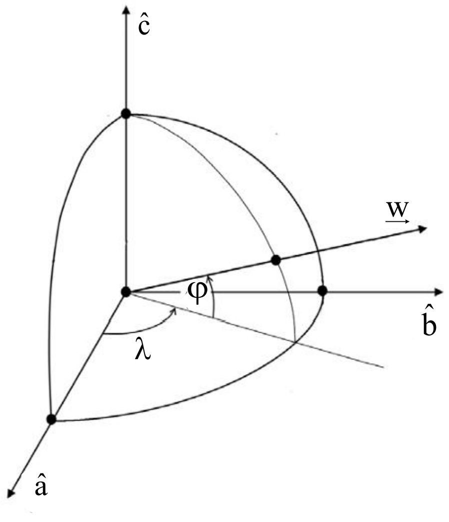

Figure 3.8: Vector $\underset{\rightarrow}{w}$ in the frame $\left(\hat{a}, \hat{b}, \hat{c}\right)$

is recalled as the physical vector counterpart of $\underset{\sim}{c}$ defined in Eq. (3.135), and an auxiliary reference frame, associated with unit vectors $\left(\hat{a}, \hat{b}, \hat{c}\right)$ (cf. Figure 3.8), is introduced. The unit vector $\hat{c}$ points toward $\underset{\rightarrow}{c}$, whereas $\left(\hat{a}, \hat{b}\right)$ are arbitrary, provided that they form a right-hand sequence together with $\hat{c}$. If $\hat{w}$ denotes the unit vector associated with $\underset{\rightarrow}{w}$, then its components $\left(w_a, w_b, w_c\right)$ can be written as (cf. Figure 3.8)

$$\begin{cases} w_a = w\cos\varphi\cos\lambda \\ w_b = w\cos\varphi\sin\lambda \\ w_c = w\sin\varphi \end{cases} \tag{3.142}$$

and Eq. (3.136) leads to

$$w^2 + 2wc\sin\varphi + c^2 - u_{max}^2 = 0 \tag{3.143}$$

which admits a positive real root if $u_{max} > c$, i.e. if the maximum available thrust is sufficient to compensate for nonlinearities and perturbations, to provide the feedforward term corresponding to the desired relative acceleration.

3.8.3. Performance evaluation of the Hybrid Predictive Control law

To evaluate the actual benefits of the Hybrid Predictive Control law (HPC) introduced in the previous section, a numerical analysis is performed. Specifically, two Monte Carlo campaigns, each consisting of 100 simulations, are conducted. The performance of the orbital maneuver achieved using the adaptive control law is compared against that obtained with a constant-gain feedback control law incorporating saturation logic. Since the adaptive-predictive control law implements a fundamentally different approach to handling saturation, it is essential to compare it with the standard saturation method typically used in constant-gain controllers in order to accurately assess its advantages. In fact, if the HPC is compared with the constant-gain controller applied without saturation, the HPC always outperforms because it applies the maximum thrust acceleration when the error in the state vector is larger, leading to a faster convergence.

As specified in the previous section, while the adaptive control law computes the gain values at each time step, a suitable gain must be determined for the constant-gain control law with saturation to enable a consistent comparison. The procedure begins by simulating the maneuver using the adaptive controller and recording the time instant where the passage from the adaptive-gain to the constant-gain phase occurs – denoted as t_{switch}. The value of t_{switch} is selected such that the second peak in the thrust norm is maximized without exceeding the thrust limit – or a certain percentage of it, if a margin factor is introduced –, in accordance with the predictive logic previously discussed. Subsequently, the maneuver governed by the constant-gain feedback linearization with saturation is simulated multiple times through a parametric study on the control gains. The gain value k used for comparison is selected based on a two-level criterion:

1. If a second peak in the thrust norm appears after the saturation phase ends, the gain k is selected so that the magnitude of this peak matches that observed in the HPC case. However, unlike the HPC law – which is observed to always produce a second peak – the constant-gain feedback linearization with saturation does not always exhibit this behavior. Moreover, maintaining saturation for excessively long durations can lead to a deterioration in maneuver performance. Therefore, if no second peak is observed even when saturation is extended up to a threshold of $1.5 \cdot t_{switch}$, the second criterion is applied:

2. The value of k is adjusted so that the saturation time matches t_{switch}, ensuring consistent comparison conditions.

This choice prioritizes the qualitative behavior of the thrust acceleration profile. If the standard saturated approach exhibits a time history of thrust acceleration similar to that of the HPC law, the comparison is carried out by allowing both controllers to operate under the same mode. Otherwise, the comparison is performed by enforcing the same saturation duration in both cases. It is worth noting that the HPC law consistently exhibits the same qualitative behavior, characterized by the appearance of a second peak in the thrust acceleration, which constitutes an additional advantage. This consistency makes the HPC law more predictable compared to constant-gain strategies, whose behavior can vary significantly depending on the boundary conditions.

In all the simulations, the target spacecraft travels on a Low Earth Orbit (LEO) characterized by the COE reported in Table 3.1.

Table 3.1: COE of the target spacecraft

Semimajor axis	7000 km
Eccentricity	0.01
Inclination	11°
RAAN	0°
Argument of periapsis	0°
True anomaly at t_0	0°

The initial relative position and velocity conditions of the chaser with respect to the target are defined by separately sampling the direction and magnitude of the corresponding vectors. For the direction, both the initial position and velocity vectors are assigned random orientations drawn from a uniform distribution on the unit sphere. The magnitude of the initial position vector is sampled from a truncated Gaussian distribution with a mean of 200 m and a standard deviation of 50 m, limited to the range $[50, 350]\,\mathrm{m}$ (i.e., truncated at 3σ). The initial velocity magnitude is also drawn from a Gaussian distribution, with a mean of 0.5 m/s and a standard deviation of 0.2 m/s, but with an asymmetric truncation over the interval $[0.01, 1]\,\mathrm{m/s}$. Moreover, the maximum available thrust acceleration is generally set to $u_{max} = 0.5\,\mathrm{N/ton}$. However, if this value is lower than $1.2\left|\underline{f}\left(t_0\right)\right|$ – the value of the dynamic nonlinearities at the initial time, increased by 20% – then $u_{max} = 1.2\left|\underline{f}\left(t_0\right)\right|$. The reduced level of the thrust acceleration is intentionally introduced to compare the two control laws under challenging conditions, thereby emphasizing differences in their control dynamics. In fact, with reference to Eq. (3.135), if $\left|\underline{w}\right| \gg \left|\underline{c}\right|$ the two control laws exhibit similar performance, since the primary difference between them lies in the treatment of the term $\underline{c}$: it is preserved unaltered in the HPC logic, whereas it is uniformly scaled in the constant-gain approach. However, if the thrust acceleration results too modest, the condition $u_{max} = 1.2\left|\underline{f}\left(t_0\right)\right|$ restores an acceptable margin of the control capabilities. Moreover, in a few simulations, the condition $\left|\underline{f}\left(t\right)\right| > u_{max}$ occurs despite the fact that $\left|\underline{f}\left(t_0\right)\right| > u_{max}$ holds, due to specific initial conditions. In such cases, the maximum available thrust acceleration is doubled for both control laws.

Before presenting the results of the two Monte Carlo campaigns, the results of a single case that proves the large discrepancy of performance between the HPC law and a constant-gain law without saturation are reported. This difference clearly appears from inspection of Figures 3.9-3.10. The gains of the constant-gain law without saturation are chosen to provide the maximum torque only at the first time instant of the rendezvous. The HPC significantly outperforms the non-saturated constant-gain law, and this always verifies because the control effort between the two laws are remarkably different. In the following, a saturation logic is applied to the constant-gain law according to the strategy previously discussed, and results are reported and analyzed.

In the first Monte Carlo campaign, the rendezvous maneuver is executed following a setpoint-based logic: only the final state is defined as the target condition, without specifying the exact time at which it must be reached. Starting from the same initial time and with the same maximum available thrust acceleration, the control law that reaches the target setpoint in the shortest time is considered the outperforming one. The position of the final set point is a vector defined relatively to the target position: the direction is

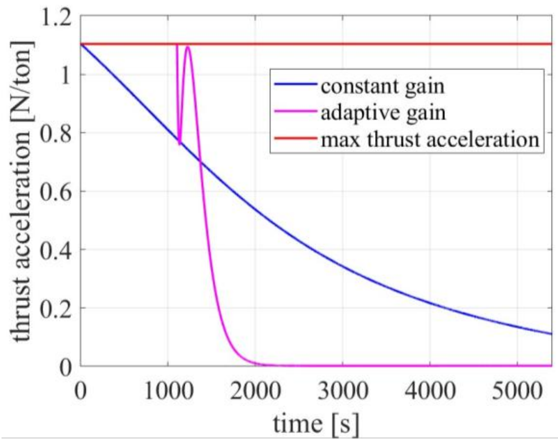

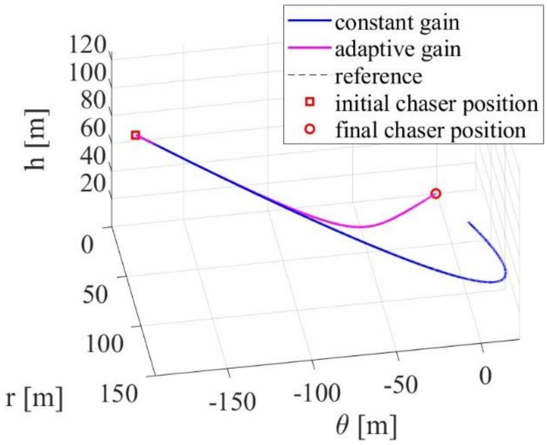

Figure 3.9: Comparison of thrust acceleration (left) and chaser trajectories (right) in a single case – HPC vs constant-gain without saturation

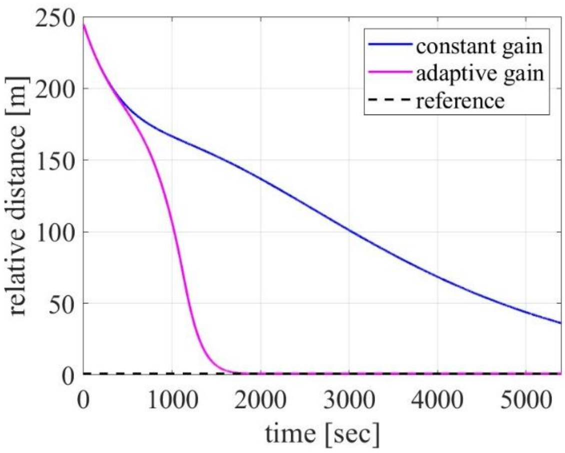

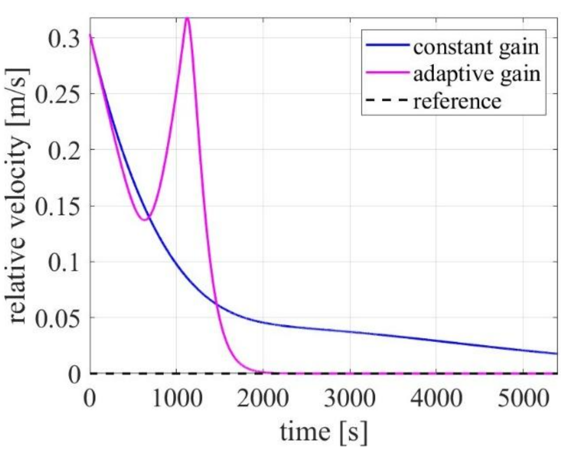

Figure 3.10: Comparison relative distance (left) and relative velocity norm (right) in a single case – HPC vs constant-gain without saturation

sampled uniformly on the unit sphere, while the magnitudes is fixed to 1 m. The relative velocity at the setpoint is equal to zero. The results show that the HPC law provides better performance in 72 cases. In the remaining 28 cases, the performance of the HPC law or worse in 27 of them, while in 1 case the two laws provide practically the same outcome.

The results for a single case when the HPC outperforms the constant-gain control with saturation is reported in Figures 3.11-3.12. The peak after the saturated interval is evident for the HPC law, while the constant-gain law does not show this behavior. Convergence is achieved in a lower time for the HPC law, despite both laws are characterized by the same saturation time interval. Qualitatively speaking, cases when the constant-gain law achieves slower convergence are the one where the peak after the

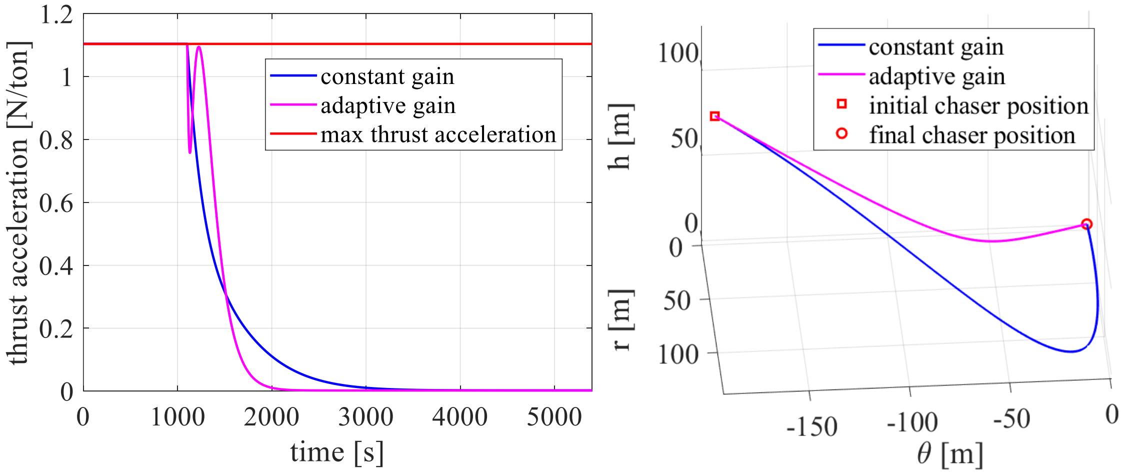

Figure 3.11: Comparison of thrust acceleration (left) and chaser trajectories (right) in a single case where the adaptive law (HPC) shows better performance – setpoint

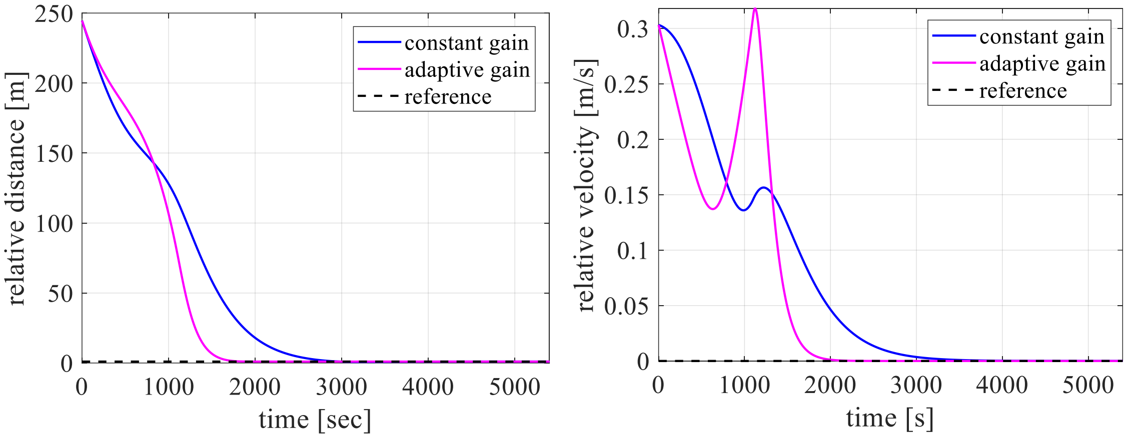

Figure 3.12: Comparison of relative distance (left) and relative velocity norm (right) in a single case where adaptive law (HPC) shows better performance – setpoint

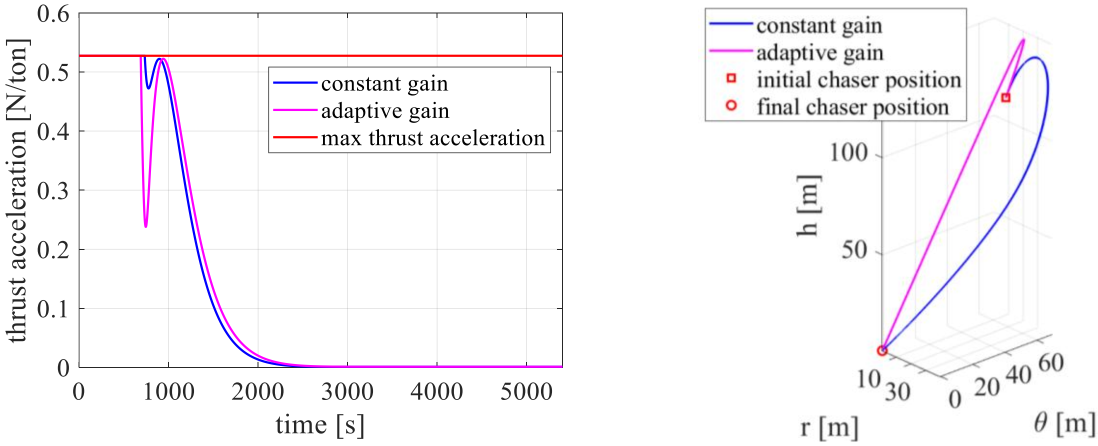

Figure 3.13: Comparison of thrust acceleration (left) and chaser trajectories (right) in a single case where the adaptive law (HPC) shows worse performance – setpoint

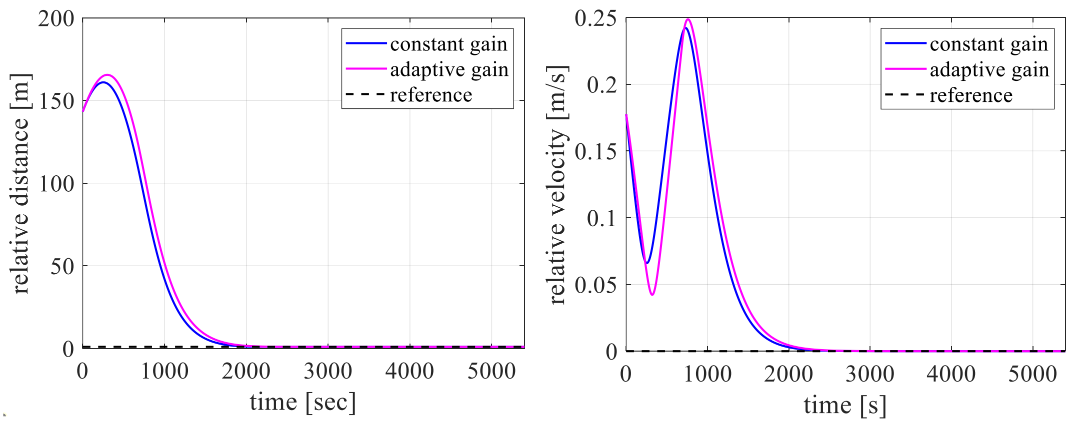

Figure 3.14: Comparison of relative distance (left) and relative velocity norm (right) in a single case where adaptive law (HPC) shows worse performance – setpoint

saturation interval does not appear. Conversely, cases when using the HPC law appears not to be convenient are the ones where this peak arises also in the constant-gain law. In cases similar to the ones reported in Figures 3.13-3.14, the HPC law achieves a slower convergence with respect to the constant-gain counterpart. However, the analysis of the results reveals that the performance gains achieved by the HPC law in favorable cases are generally much greater than the performance losses observed in the less favorable ones, as it appears by comparing Figures 3.12-3.14.

The fact that the HPC law does not always provide a performance advantage depends on the specific physics of the problem. The HPC law consistently compensates for dynamic nonlinearities and orbital perturbations, which can be interpreted as a form of "wind" – i.e., an external dynamic action – acting on the spacecraft. However, in certain cases, these effects may actually assist the rendezvous rather than hinder it, e.g. if the wind blows toward the desired target. Even in such situations, the adaptive controller still compensates for them, potentially counteracting helpful contributions. Nonetheless, such favorable cases represent a minority of scenarios. This is why, overall, the HPC law delivers superior performance in the majority of situations. Furthermore, due to its specific structure, the HPC law ensures that the trajectory remains confined to the plane defined by the unit vectors $\hat{\xi}$ and $\hat{\chi}$, as introduced at the end of the previous section. In contrast, the trajectory resulting from the constant-gain controller is less predictable. This regularity in the system response under HPC constitutes an additional advantage, as it enhances the predictability and understanding of the closed-loop dynamics.

When the set-point logic is replaced with a reference trajectory, the results may vary depending on the specific choice of the reference. However, the HPC law continues to demonstrate superior performance. A second Monte Carlo campaign is conducted, with all parameters varying as in the first campaign. The only difference lies in the guidance strategy: a reference trajectory is introduced, defined as a straight-line path connecting the initial and final positions of the chaser spacecraft. This trajectory is uniformly mapped over the time domain, meaning that each point along the path is associated with a specific time at which the spacecraft is expected to be there. The maneuver duration is set to 30 minutes, after which the chaser must reach the desired final position. In this framework, the control law that brings the chaser closest to the final position after 30 minutes is considered to have better performance. A draw is declared if the final positions obtained by the two control laws differ by less than 1 cm. The same criteria used previously are applied to select the gain of the constant-gain controller.

The results show that a draw occurs in 65 out of 100 cases. Among the remaining 35 cases, the HPC law outperforms the constant-gain law in 23, while it is outperformed in the remaining 12. Although the performance gap between the two approaches is reduced in this scenario, this outcome strongly depends on the specific definition of the reference trajectory, its duration, and its temporal mapping. Nevertheless, the HPC law maintains a

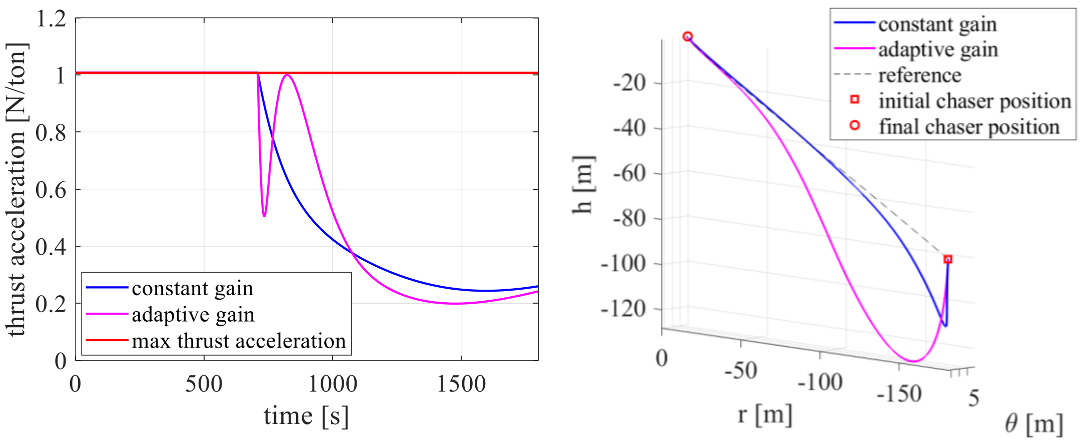

Figure 3.15: Comparison of thrust acceleration (left) and chaser trajectories (right) in a single case where the adaptive law (HPC) shows better performance – linear reference trajectory

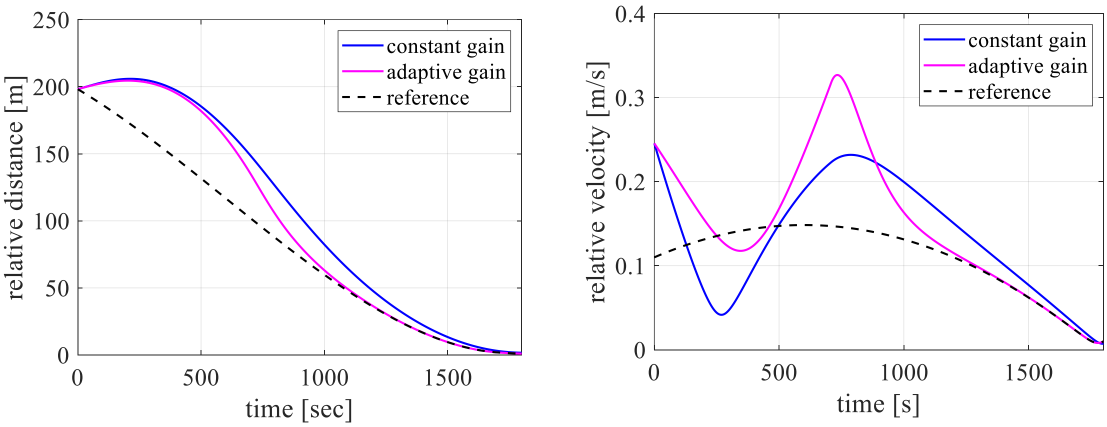

Figure 3.16: Comparison of relative distance (left) and relative velocity (right) in a single case where adaptive law (HPC) shows better performance – linear reference trajectory

clear advantage. As in the set-point case, the trajectory under HPC remains confined to the plane defined by the same unit vectors, and all previous considerations remain valid. An example of a case where the HPC law outperforms the constant-gain law is illustrated in Figures 3.15-3.16. It is worth noting that, although the 3D trajectories may suggest that the constant-gain law exhibits better behavior, the time histories of the distance to the reference trajectory provide a more accurate picture. In fact, the 3D plot does not convey the time associated with each point along the trajectories. As a result, although the chaser controlled by the constant-gain law may appear to stay closer to the reference path, it actually follows the reference trajectory less accurately over time.

3.9. Concluding remarks

Chapter 3 addressed the nonlinear control of spacecraft attitude and relative orbital motion, focusing on advanced techniques. The first part of the chapter was dedicated to attitude control. A detailed formulation of attitude kinematics and dynamics was provided, followed by the development of two nonlinear feedback control laws – one representing the state-of-the-art standard, the other consisting of a novel enhancement of the former – for triaxial attitude tracking. The stability of these control laws was rigorously analyzed, and guidelines for gain selection were presented. The chapter further addressed reduced-attitude tracking, a useful approach in scenarios where only single-axis attitude control is required (e.g., payload pointing), again providing a new improved control law supported by stability proofs. A comparative performance analysis of the proposed nonlinear control laws was carried out, demonstrating their superior performance relative to existing solutions in the literature, particularly in terms of faster convergence for a given actuator configuration. The chapter also introduced enhanced steering laws for momentum exchange devices, including reaction wheels and single-gimbal control moment gyroscopes (CMGs), enabling the practical implementation of the proposed nonlinear control strategies. In the second part of the chapter, the focus shifted to relative orbital motion. An advanced version of the Battin-Giorgi formulation was introduced for describing relative orbits in a fully nonlinear framework. Building on this, an innovative Hybrid Predictive Control (HPC) law was proposed for relative orbital control. The HPC law was shown to effectively combine feedback linearization with predictive control concepts, achieving robust and precise control of relative motion even in dynamically challenging scenarios. A detailed performance evaluation of the HPC law confirmed its effectiveness and highlighted its advantages over classical control methods. In conclusion, Chapter 3 demonstrated the development and validation of advanced nonlinear control laws for both attitude and relative orbital motion. The results of this chapter are critical for achieving high-performance guidance and control in future space applications, particularly in proximity operations, on-orbit servicing, and debris removal scenarios.

Chapter 4

Mission scenarios

In this chapter, several mission scenarios are presented, each demonstrating the application of the theoretical framework developed in the previous chapters. Some scenarios focus primarily on modeling aspects, others emphasize control strategies, while some highlight the integration of both modeling and control. The chapter begins with an analysis of a rendezvous and berthing operation, which includes the despinning of orbital debris. This is followed by a case study involving a large, flexible spacecraft performing agile attitude maneuvers. Next, a scenario involving a spacecraft equipped with a large rotating antenna is examined, with particular reference to the CIMR mission – of specific interest to Thales Alenia Space Italy. This case explores key dynamic characteristics, such as stress stiffening. Additionally, the elastic modeling using Finite Element Methods (FEM) is discussed in the context of a large spacecraft carrying two Telescopic Tubular Mesh structures. The chapter concludes with a mission scenario involving a rendezvous with the Gateway space station in the cislunar environment.

4.1. Rendezvous and berthing of a space manipulator system with a rotating debris

This section presents a study dedicated to the development of a robotic on-orbit servicing mission aimed at contributing to long-term space sustainability through the removal or stabilization of noncooperative debris in low Earth orbit. The mission focuses on the autonomous execution of rendezvous, close approach, and berthing operations using a spacecraft equipped with two articulated robotic arms. Once the chaser vehicle is brought into proximity with the target, a coordinated maneuver involving attitude and robotic control enables the arms to perform a precise manipulation that allows a stable grasp, accounting for the target uncontrolled motion. The capture conditions are achieved through careful planning of the manipulator trajectory, ensuring a smooth engagement despite the dynamic interaction between the arms and the spacecraft. Subsequently, the system transitions to a closed kinematic chain, with both arms securing the object. This setup enables a final despinning operation, during which the residual rotation of the captured debris is gradually reduced, allowing the system to reach a stable and safe post-capture condition.

4.1.1. Vehicle description

The space manipulator system considered in this application is modeled as a rigid multibody structure, made up of a parallelepiped-shaped bus and two anthropomorphic arms. Each of them is composed of two links connected via rotary joints. An illustrative sketch of the entire vehicle is reported in Figure 4.1.

With reference to Figure 4.1, joints Q_2 and Q_4 provide a 2-DOF rotation with θ_{21} and θ_{41} defined as the rotations around the axis aligned with $\pm\hat{b}_3$ and normal to the bus lateral surface, whereas joints Q_3 and Q_5 only allow a single degree of freedom rotation. Angles θ_{22} and θ_3 are coplanar, as well as the angles θ_{42} and θ_5. In total, each arm possesses 3 degrees of freedom, enabling the desired positioning of the end effectors. The problem of end-effector orientation is not addressed in this work and is assumed to be managed by means of a spherical wrist, which is not explicitly modeled.

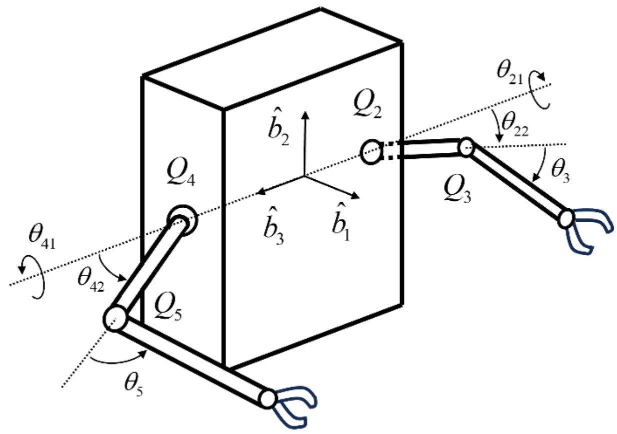

Figure 4.1: Geometry and elements of the Space Manipulator System

Furthermore, the spacecraft is equipped with the following actuators:

1. joint motors for the correct maneuvering of the robotic arms. The dynamics introduced by the joint motors leads to joints flexibility, which is modeled in this work;
2. a pyramidal array comprising four single-gimbal control momentum gyroscopes (SG-CMG) with constant rotor speed, to supply the necessary attitude control torque;
3. a non-steerable thruster aligned with the spacecraft axis $\hat{b}_2$ for trajectory control in the relative motion scenario.

Geometry, sizing, and inertia parameters (i.e. total mass and principal inertia moments J_1, J_2, J_3) of the spacecraft are inspired by the space manipulator proposed in Ref. [94].

Specifications for the bus are shown in Table 4.1, whereas the geometric and inertia characteristics of the four links are reported in Table 4.2. The major data of the joint motors are instead collected in Table 4.3 [95]. Moreover, Table 4.4 includes the specifications of a particular commercial array of SG-CMGs, selected for its performance suitability in the relevant dynamical scenarios [96]. Symbols h, I_s, ω_r, $\dot{\theta}_{max}$, T_{max} denote the axial angular momentum, inertia moment, rotor angular velocity, and maximum torque of the commercial device selected for this application. With regard to orbit control, a throttleable 1 N Hall ion thruster is considered [97]. Its specifications are reported in Table 4.5. Finally, the target is assumed spherical, with diameter of 1.2 meters.

Table 4.1: Bus specifications

Main Body (BUS)	
width (m)	1.5
height (m)	2.2
depth (m)	1.0
mass (kg)	1000
J_1 (kg m^2)	590.83
J_2 (kg m^2)	270.83
J_3 (kg m^2)	486.67

Table 4.2: Specifications of the arms links

Links	
length (m)	1
radius (cm)	3.5
mass (kg)	30

Table 4.3: Joint elasticity specifications

Joint motors	
inertia (kg m^2)	0.12
stiffness (Nm/rad)	40000
damping factor (Nms/rad)	0.02

Table 4.4: SG-CMG specifications

SG-CMG M50 Honeywell	
h (Nm sec)	75
I_s (kg m^2)	0.22
ω_r (rpm)	6500
$\dot{\theta}_{max}$ (rad/sec)	1
T_{max} (Nm)	75
mass (Kg)	33.1

Table 4.5: Thruster specifications

Hall ion thruster	
specific impulse (s)	1600
maximum thrust level (N)	1

4.1.2. Trajectory planning and control of the robotic arms

The trajectory planning algorithm used in this study case is identified through the following steps:

- first, the path points of the end effector must be defined in the operational (Cartesian) space;
- second, the path points must be translated into the joint space through an inverse kinematics procedure;
- lastly, the interpolation of the path points in the joint space provides the desired trajectory.

The choice of end effector path points in the operational space depends on the mission scenario, and this issue is discussed in the upcoming section. Furthermore, it is worth noting that a trajectory in the operational space can be more precisely followed by the end effector as the number of path points used for discretization increases. However, this also entails a higher computational burden. Consequently, there exists a computational cost constraint that imposes an upper limit on the total number of path points. Once the via-points are defined, the inverse kinematics algorithm is employed to transfer them to the joint space. Due to the specific configuration of the 3-DOF anthropomorphic arm, a closed-form solution of the inverse kinematics exists and is extensively described in [53]. However, for each end effector position, there exist four admissible solutions, which are coincident in pairs. The distinction between these two pairs of solutions lies in the opposite positions of the elbow joint. Therefore, a specific criterion must be applied to select only a single solution. The choice follows these two steps:

(a) first, the pair of solutions where the elbow is closer to the target envelope is discarded to prevent collisions with the target;
(b) second, between the two equivalent solutions, the one closest to the initial configuration is selected.

After defining the path points in the joint space, a spline interpolation technique is employed, to create the reference trajectories. This interpolation ensures continuity conditions for the cubic polynomials, as well as their first and second derivatives at the internal path points. Moreover, the interpolation conditions are finalized by setting the value of the first derivative (joint angular velocity) to zero, at both the starting and final points. The resulting planned path allows for the extraction of the first and second derivatives, which are essential inputs for the control algorithm discussed in the following section.

The two anthropomorphic arms of the manipulator need to be effectively controlled to perform precise grasping of the target. A joint space control strategy is chosen due to its computational advantages over operational space control. Joint space control only needs inverse kinematics computation during trajectory planning, whereas operational space control involves additional inverse kinematic operations within the feedback loop, resulting in increased computational complexity. Moreover, a feedback linearization approach is employed in this context as well [53]. The dynamical system of Eq. (1.95), associated with the complete motion of the Space Manipulator System – thus including also the base motion – can be rewritten as

$$\mathrm{A}\underline{\dot{u}} = \underline{b} \tag{4.1}$$

where

$$\mathrm{A} \triangleq \hat{\mathrm{M}} \qquad \left(\mathrm{n_{DOF}} \times \mathrm{n_{DOF}}\right) \tag{4.2}$$

$$\underline{b} \triangleq -\underline{nl} + \underline{f}_G \qquad \left(\mathrm{n_{DOF}} \times 1\right) \tag{4.3}$$

Vector $\underline{f}_G$ in Eq. (4.3) does not include the control torque obtained via feedback linearization, which is still to be computed. After removing the rows and columns not associated with the joints degrees of freedom from A and after doing the same operation with the rows of $\underline{\dot{u}}$ and $\underline{b}$, one obtains the following reduced system:

$$\mathrm{A_r}\underline{\ddot{\theta}} = \underline{b_r} + \underline{c} \tag{4.4}$$

whose dimension corresponds to the joint DOFs and where $\ddot{\underline{\theta}}$ can replace $\dot{\underline{u}}$. In fact, the remaining generalized velocities are the time derivatives of the joint variables θ_j and the robotic motion control vector $\underline{c}_r$ appears in Eq. (4.4). Hence, if the control law

$$\underline{c} = A_r\left[\ddot{\underline{\theta}}_d - K_D\left(\dot{\underline{\theta}} - \dot{\underline{\theta}}_d\right) - K_P\left(\underline{\theta} - \underline{\theta}_d\right)\right] - \underline{b}_r \tag{4.5}$$

is substituted in Eq. (4.4), it becomes

$$\ddot{\underline{e}} + K_D\dot{\underline{e}} + K_P\underline{e} = \underline{0} \tag{4.6}$$

where K_D and K_P are diagonal and constant matrices with positive elements, $\underline{\theta}_d$ is the vector of the desired joint variables and $\underline{e} = \underline{\theta}_d - \underline{\theta}$ is the joint error vector. Also in this case, feedback linearization ensures the convergence of the state toward the desired values, while the transient performance can be controlled through proper setting of the control gains.

4.1.3. Mission scenario

In this application, an end-to-end simulation of a complete rendezvous and berthing mission is performed. In this framework, one can distinguish five specific types of operations:

1. close-range rendezvous, i.e. approach of the chaser toward the target from a certain direction;

2. reorientation maneuver, i.e. the action of driving the operational axis of the chaser toward the desired direction;

3. arms opening, i.e. the first motion of the arms that pass from the stowed configuration to the desired initial condition for the manipulation phase;

4. spin rate synchronization, i.e. the chaser must reach the same spin angular velocity of the target to guarantee safe grasping;

5. manipulation, i.e. the actual grasping phase.

Close-range rendezvous – Starting from an initial relative distance of 20 m, the aim of close-range rendezvous is to reduce this distance to a desired value d_{op}, which is set to 1.5 m. Furthermore, the desired relative position must be aligned with the spin axis of the target $\hat{h}_{sp}$. In fact, the target is supposed to rotate about a certain axis, which does not change its orientation in the inertial frame. This assumption represents the condition of flat spin rotation of the target, while the long-term disturbances induced by gravity gradient torque and other environmental effects are neglected.

The rendezvous maneuver is carried out using a low-thrust throttleable electric actuator, with an upper bound on the thrust magnitude. Hence, the control gains of Eq. (3.128) are chosen not to exceed the threshold value of $1\,\mathrm{N/ton}$, which can be considered as a threshold for the normalized low thrust. In fact, in this study case a constant-gain control law is employed for the sake of simplicity, since the scenario does not require saturation to achieve the desired performance with the equipped thruster.

To ensure safe approach, the relative distance between chaser and target must not reduce below a certain safety threshold d_{op}, which is set to 1.4 m. To fulfill this requirement, the rendezvous trajectory is chosen between two different options. In fact, the desired alignment can be achieved with two different final points, one in the same direction of $\hat{h}_{sp}$ and one in the opposite, which means

$$\underline{X}_d = \pm \underset{L\leftarrow N}{R}\, \underline{h}_{sp}^{(N)} d_{op} \tag{4.7}$$

$$\underline{\dot{X}}_d = \pm \underset{L\leftarrow N}{\dot{R}}\, \underline{h}_{sp}^{(N)} d_{op} \tag{4.8}$$

$$\underline{\ddot{X}}_d = \pm \underset{L\leftarrow N}{\ddot{R}}\, \underline{h}_{sp}^{(N)} d_{op} \tag{4.9}$$

where $\underset{L\leftarrow N}{R}$ is the rotation matrix from the inertial to the LVLH-T frame and $\underline{h}_{sp}^{(N)}$ collects the components of $\hat{h}_{sp}$ resolved in inertial frame. Because the thruster is aligned with body axis $\hat{b}_2$, during the rendezvous operations this axis is supposed to be aligned with

$$\underline{b}_{C_2}^{(N)} = \frac{\underset{N\leftarrow L}{R}\, \underline{a}_{t,c}}{\left\| \underline{a}_{t,c} \right\|} \tag{4.10}$$

where $\underline{b}_{C_2}^{(N)}$ contains the components (in the inertial frame) of the commanded direction of body axis $\hat{b}_2$ and $\underline{a}_{t,c}$ the components of the thrust acceleration vector, obtained from Eq. (3.128). The other two commanded axes can be arbitrarily defined with the only requirement to form a right-hand triad, because the reduced-attitude control logic is utilized. Hence, the rotation matrix from the inertial frame to the commanded frame $\underline{\underline{C}}$ is obtained as

$$\underset{C\leftarrow N}{R} = \begin{bmatrix} \underline{b}_{C_1}^{(N)T} \\ \underline{b}_{C_2}^{(N)T} \\ \underline{b}_{C_3}^{(N)T} \end{bmatrix} \tag{4.11}$$

leading to the commanded quaternion $\left[q_{C,0}, \underline{q}_C\right]$. From the cubic spline interpolation of the commanded quaternion, it is straightforward to obtain the time derivative $\left[\dot{q}_{C,0}, \underline{\dot{q}}_C\right]$. From the inversion of the kinematics equation of the quaternions (cf. Eq. (3.15)), one obtains the commanded angular velocity. Then, $\underline{\dot{\omega}}_C$ – required for attitude tracking – is obtained from the analytical time derivation of the spline-interpolated expression of $\underline{\omega}_C$. It is worth noting that, during this phase, the spacecraft is kept in a stowed configuration, with its center of mass aligned with the thruster line of action, thereby avoiding imbalances and couplings between attitude and relative motion control.

Reorientation maneuver – Once the desired position is reached, the thruster is turned off and remains inactive for the rest of the mission, to avoid any interference with attitude maneuvers and robotic motion. Immediately after turning off the thruster, a reorientation maneuver is executed to align the body axis $\hat{b}_1$ with the target, thus facilitating the subsequent manipulation. The procedure for determining this maneuver is analogous to the one used for aligning the thruster with the trajectory, as described in the previous section. The only difference consists in the definition of the desired direction: in this case, Eq. (4.10) must be replaced by

$$\underline{b}_{C_1}^{(N)} = \frac{\underset{N\leftarrow L}{R}\,\underline{\rho}}{\left\|\underline{\rho}\right\|} \tag{4.12}$$

where $\underline{\rho}$ is the relative position vector in the LVLH-T frame defined in Section 3.7, which is parallel to the spin axis of the target until the thrusters are switched off. Moreover the gain matrix of the attitude control law are chosen to avoid exceeding the maximum torque supplied by the array of actuators.

Arms opening – Initially, the robotic arms are supposed to be in a stowed configuration. Then, the arms must assume a new configuration, which represents the initial condition of the grasping phase. The arm opening maneuver is divided into two subphases. First, the motion regards only the joint variables θ_{22}, θ_3, θ_{42} and θ_5 in order to align the two arms with $\hat{b}_3$. Then, a rotational motion in terms of angles θ_{21} and θ_{41} is carried out in order to align the joint axes corresponding to the preceding angles with $\hat{b}_2$. In each of the two phases, the joint variables that are not involved in the maneuver are considered locked.

Trajectory planning for the purpose of opening the two arms is much easier than the grasping phase, because no specific constraints must be fulfilled by the end effector position. No intermediate via points are introduced because it is sufficient to consider only the initial and final conditions, which are interpolated through a cubic polynomial. The maneuver duration is selected so that joint flexibility does not affect the motion of the arm. Specifically, first and second subphases are planned to take 60 s and 45 s, respectively.

It is preferable to carry out the opening maneuver before the spin rate synchronization, otherwise synchronization would be lost, because of the changes in angular velocity due to the variation of the moment of inertia about $\hat{b}_1$. In the latter case, successive corrections could be necessary before starting the manipulation phase. Besides this requirement, no other constraints exist for this maneuver. Established this, two different choices of the sequence of operations remain available:

(i) arms opening can be completed after the reorientation maneuver, or

(ii) arms opening can occur during the last part of the rendezvous.

The first option aims at reducing the reorientation duration by taking advantage of lower moments of inertia in the stowed configuration. In contrast, the second option involves excluding the entire arms opening time by performing this maneuver within a subinterval of a longer phase. Both cases will be discussed in the following section.

In conclusion, it is worth noting that arms opening is designed in such a way that the overall center of mass moves uniquely along the thruster axis $\hat{b}_2$. Therefore, arms opening can be carried out while the thruster is ignited, because no disturbance torques arise due to misalignment of the center of mass and thrust direction.

Spin rate synchronization – To ensure safe grasping, the chaser must synchronize its spinning angular rate with that of the target. Specifically, the spin axis of the chaser is $\hat{b}_1$, which is the axis aligned with the chaser-target direction.

Spin synchronization can be achieved by using a cubic time history for the first component of $\underline{\omega}_{C.}$ and $\dot{\underline{\omega}}_C$ that appear in the attitude control law. The spinup maneuver is set to 60 s, with the aim of carrying out the maneuver in short time while avoiding excessive torque and dynamical loads. During this maneuver, the direction of $\hat{b}_1$ is maintained aligned with the chaser-target direction.

Manipulation – After the synchronization phase is completed, the grasping phase can start. The trajectory is first defined in the operational space for the end effector and then mapped into the joint space through an analytical inverse kinematics algorithm. Unlike the opening phase, in this situation the criterion previously described is employed, to choose the best solution for the joint variables (among the four existing solutions).

With regard to the operational space, different trajectories are considered. For the trajectory of the end effector, three options are considered:

(a) a linear trajectory (cf. Figure 4.2);

(b) an elliptic arc trajectory lying in the plane that contains the shoulder joint and the initial and the final positions of the end effector; one of the two semimajor axes coincides with the distance between the shoulder joint and the initial position of the end effector (c.f. Figure 4.3);

(c) a mixed trajectory composed of (i) a circular arc lying in the plane that contains the shoulder joint, the initial and the final positions of the end effector; its radius equals the distance between the elbow joint and the initial position of the end effector; the arc ends when the tangent direction is directed toward the grasping point, and (ii) a segment tangent to the arc and directed toward the grasping point (c.f. Figure 4.4).

The shape of the trajectories is dictated by two main requirements:

1. reduction of motor torque amplitude and oscillations: for a safe and effective arms motion, the motor torque should be limited and smooth. Hence, trajectories (b) and (c) appear to be preferable, because the motion they require is easier to pursue rather than the linear path (a);

2. capability of updating the trajectory: because the chaser and the target are subject to relative motion even during the manipulation phase, uncertainties on the relative position require continuous updates of the relative position and the resulting path of the end effector. To do this, linear trajectories represent the simplest solutions. In the end, paths (a) and (c) appear to be suitable solutions for this task. In particular, for trajectory (c) updating occurs only in the (second) linear part.

With regard to point 1, it is apparent that a Chebyschev distribution of the via points in the operational space represents a suitable strategy to further reduce motor torque amplitude and oscillations, regardless of the shape of the trajectory. In fact, a Chebyschev distribution implies that the terminal phases of the manipulation are executed more slowly with respect to the use of a linear distribution. Hence, if (x_0, y_0, z_0) and (x_f, y_f, z_f) denote the coordinate of the initial and final end effector position, the $n+1$ points of the Chebyschev distribution are obtained using the following relation:

$$x_k = x_0 + \frac{x_f - x_0}{\cos\theta_f - \cos\theta_0}\left[\cos\left(\theta_0 - k\frac{\theta_0 - \theta_f}{n}\right) - \cos\theta_0\right], \quad k = 0,1,\ldots,n \qquad (4.13)$$

where θ_0 and θ_f are the initial and final angle of the upper half of the trigonometric circle, which is traveled clockwise from π to 0. To consider the entire interval, they are set to π and 0 respectively. The manipulation duration is set to 120 seconds, to allow safe grasping, while reducing the dynamical interaction between attitude motion of the chaser and the motion of the robotic arms. In Figures 4.2-4.4, the three trajectories are reported for the left arm in the case of a Chebyschev distribution of 30 points.

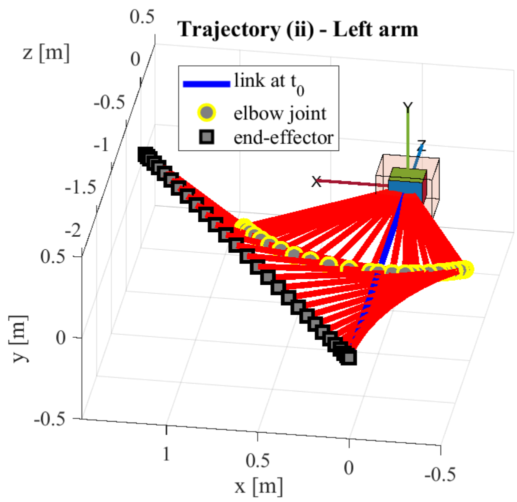

Figure 4.2: Linear trajectory for the left arm

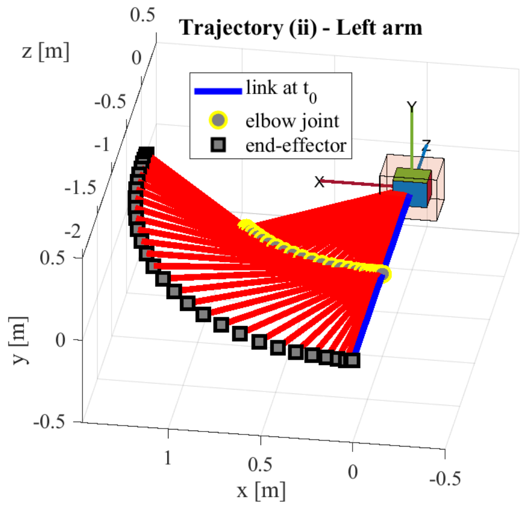

Figure 4.3: Elliptic trajectory for the left arm

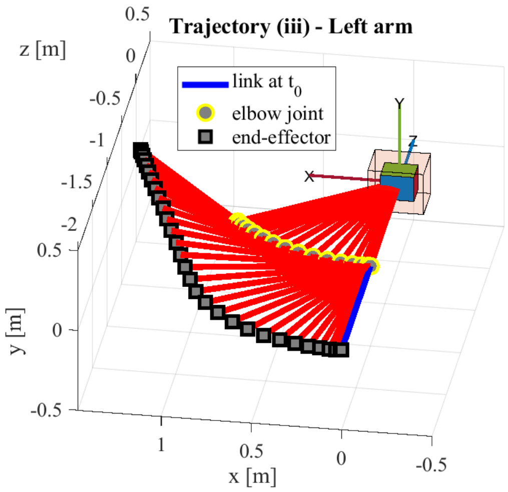

Figure 4.4: Mixed trajectory for the left arm

4.1.4. Close-range rendezvous and reorientation maneuver

At time $t_0 = 0$, the rendezvous operations start. The initial conditions chosen for this example are reported in Tables 4.6-4.7. Specifically, the order of magnitude of relative position and velocity are inspired by the closing phase of the ATV docking sequence [98]. Using the constant-gain feedback linearization control law described in Section 3.8.1, Figures 4.5-4.6 are obtained. The rendezvous maneuver is assumed to end when the error on the relative distance is lower than 1 mm and the error on the relative velocity is lower than 0.1 mm/s. Figure 4.5 shows the time history of the relative distance between target and chaser and the misalignment angle (i.e. the angular displacement) between the spinning axis of the target and the actual direction of the target-to-chaser direction. Moreover, the left plot in Figure 4.6 depicts the time histories of the three components of the thrust. It is apparent that the maneuver is carried out without overcoming the thrust limit imposed by the low-thrust actuator. The right plot in Figure 4.6 reports the motion of the chaser relative to the target during the entire

Table 4.6: Orbit elements of the reference orbit

semimajor axis (km)	7000
Eccentricity	0.01
inclination (deg)	11
RAAN (deg)	0
arg. of periapsis (deg)	0
true anomaly at t_0 (deg)	0

Table 4.7: Initial conditions on the relative motion

ρ_x [m]	11.09
ρ_y [m]	14.78
ρ_z [m]	7.65
$\dot{\rho}_x$ [cm/s]	3.61
$\dot{\rho}_y$ [cm/s]	1.00
$\dot{\rho}_z$ [cm/s]	0.17

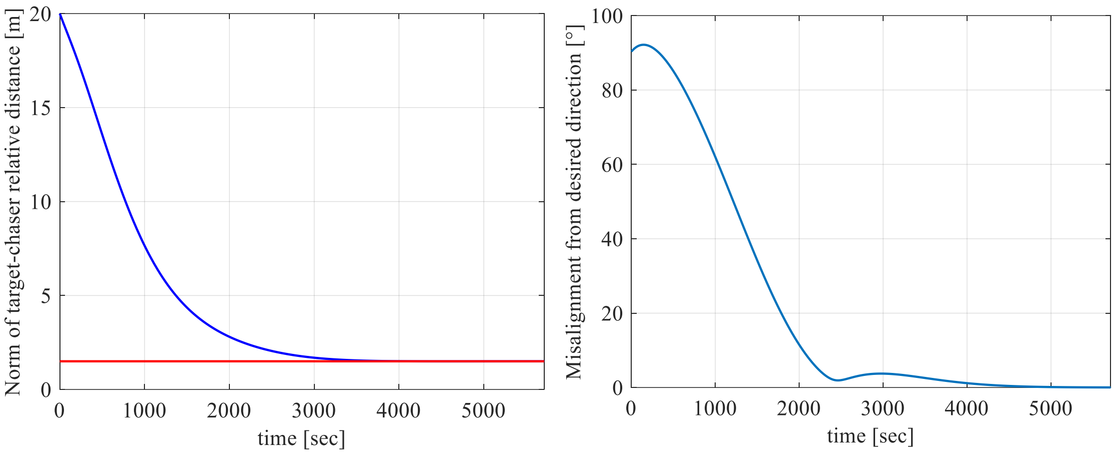

Figure 4.5: Relative distance between target and chaser (left) and misalignment angle during rendezvous (right)

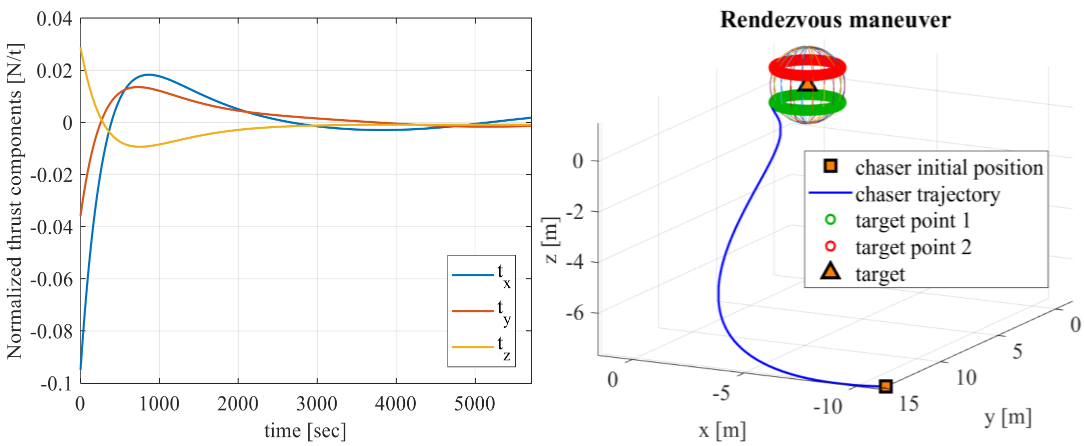

Figure 4.6: Thrust acceleration components (left) and rendezvous trajectory (right)

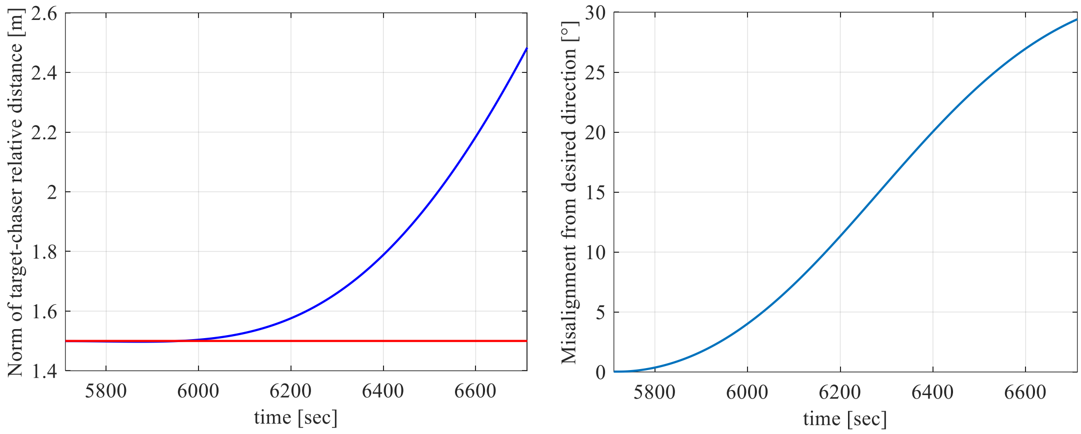

Figure 4.7: Relative distance (left) and misalignment angle (right) – thruster off

maneuver. If the relative orbit motion is propagated after the thruster has been switched off, Figure 4.7 is obtained. From the inspection of this figure, it is apparent that the misalignment is more critical than the increase of the relative distance that occurs in the absence of relative orbit control. Therefore, if the misalignment threshold is set to 10°, the time interval of the pre-manipulation and manipulation operations must be less than 460 seconds.

Once the rendezvous has ended, the thruster is switched off and a reorientation maneuver is carried out, such that body axis $\hat{b}_1$ points toward the spin axis of the target. Results of this attitude maneuver are reported in Figures 4.8-4.9. The reduced-attitude control law (3.64) is employed to carry out the reorientation maneuver, which is assumed to end when the angular distance between desired and actual $\hat{b}_1$ axis is less than

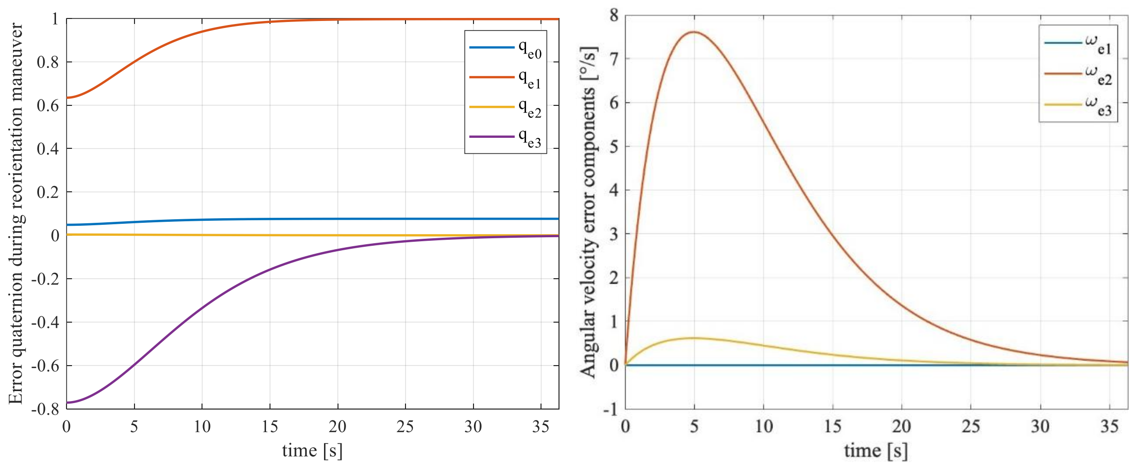

Figure 4.8: Error quaternion (left) and angular velocity error (right) in the reorientation maneuver

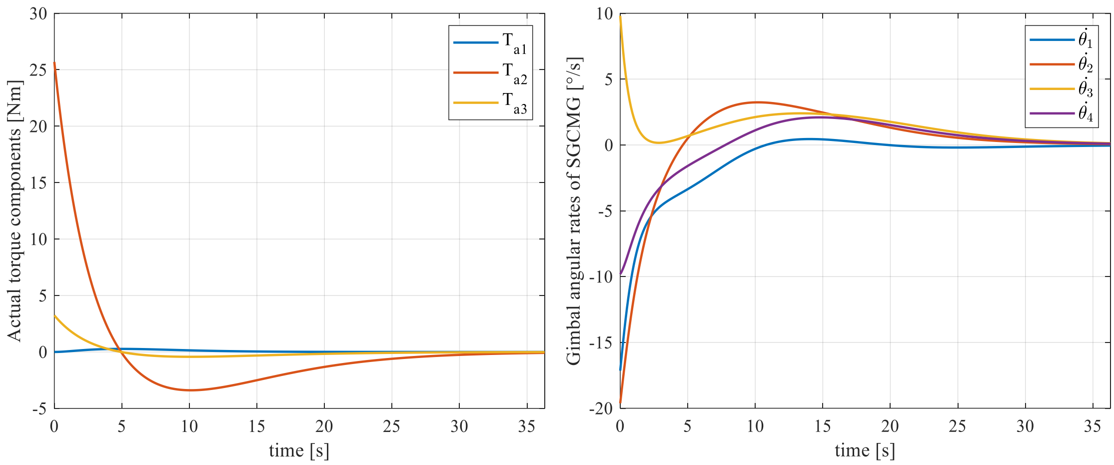

Figure 4.9: Actuator torque (left) and gimbal angular rates (right) in the reorientation maneuver

0.3 degrees. This maneuver takes 36 seconds. Figure 4.8 shows that convergence is achieved in terms of pointing error and error angular velocity. Furthermore, Figure 4.9 portrays the time histories of actuation torque and gimbal rates of the SG-CMGs employed to actuate the commanded torque. The gains in Eq. (3.64) are set in order to avoid exceeding a maximum torque magnitude of 25 Nm, well below the maximum available torque. As a consequence, also the gimbal angular rates reported in Figure 4.9 can be supplied by the actuators with no difficulty.

4.1.5. Arms opening and spin-rate synchronization

After the correct alignment has been achieved, the robotic arms are deployed, starting from their stowed configuration, to reach the configuration shown in the left plot in Figure 4.10. As previously specified, arms deployment is divided into two subphases, the first one regarding the joint variables $\theta_{22}, \theta_3, \theta_{42}, \theta_5$ and the second one regarding θ_{21}, θ_{41}. The numerical results for this phase are reported in Figure 4.11. Specifically, the time histories of the joint variables and their time derivatives are reported for the case of the left arm. The trend for the right arm are analogous, because the motion is planned to be symmetrical so that the reactions at joints Q_2 and Q_4 on the bus can compensate, and the chaser maintains the desired attitude as a result. Moreover, the right plot in Figure 4.10 shows the time histories of the control torques for the first subphase. In the second subphase the involved torsional inertia is much lower than the inertia in the first subphase, therefore the motor torque is lower and easily suppliable.

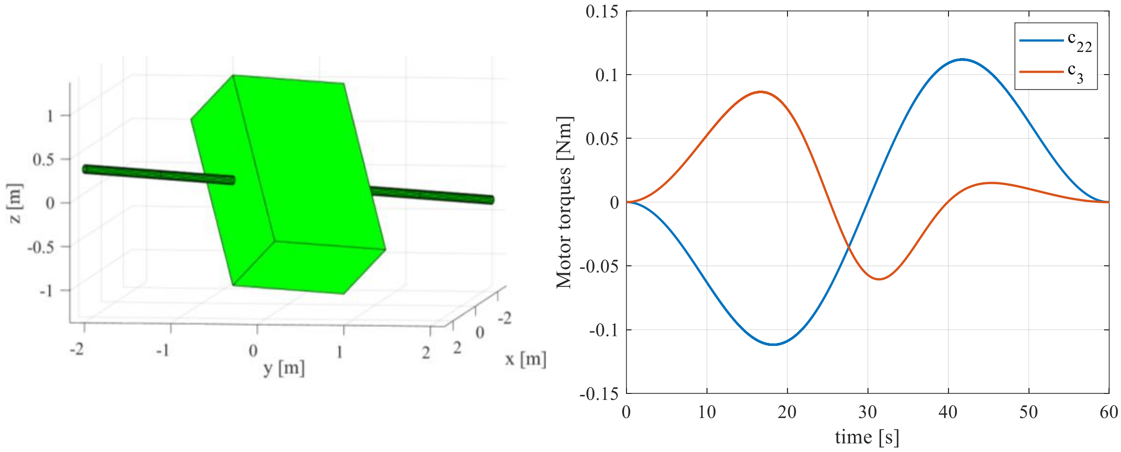

Figure 4.10: Configuration after arms opening (left) and motor torques during arms opening (right)

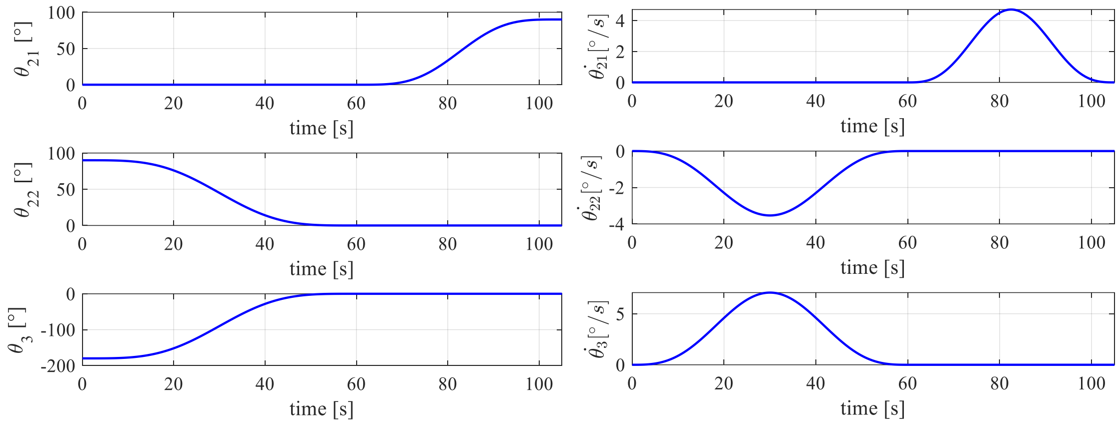

Figure 4.11: Joint angles (left) and joint rates (right) during arms opening

As mentioned in Section 4.1.3, the maneuver to open the arms can be executed during the rendezvous. The symmetrical motion of the two arms, as discussed in the preceding section, avoids any misalignment of the overall center of mass of the manipulator, which remains aligned with the thruster axis. Consequently, there is no disturbance torque due to thrust misalignment during the orbital maneuver. This strategy clearly economizes the time required for the arms opening. However, the increased inertia in the deployed configuration leads to a longer reorientation maneuver. Therefore, it becomes essential to assess the duration of the combined (and longer) reorientation maneuver, in comparison with the original, sequential reorientation maneuver. This analysis is presented in Section 4.1.7. However, plots for a specific case of the combined maneuver are omitted, as no significant difference can be discerned in comparison to the time histories associated with the original sequence.

Because the target is spinning, the synchronization maneuver described Section 4.1.3 is carried out. Figures 4.12-4.13 refer to this maneuver. From inspection of the left plot in Figure 4.12, it is apparent that the required spinning synchronization around axis $\hat{b}_1$ is successfully achieved, with acceptable control effort. However, a low entity nutation-like motion is triggered related to the combination of the spin around axis $\hat{b}_1$ and the rotation about axes $\hat{b}_2$ and $\hat{b}_3$ induced by the control torques, which aim at maintaining the desired pointing. As a result, axis $\hat{b}_1$ oscillates around the desired direction, because of the (slow) time variation of the control torque that acts on the chaser. This trend is recognizable from Figure 4.13, where it is also apparent that the amplitude of the (undesired) nutation motion increases with the spin rate.

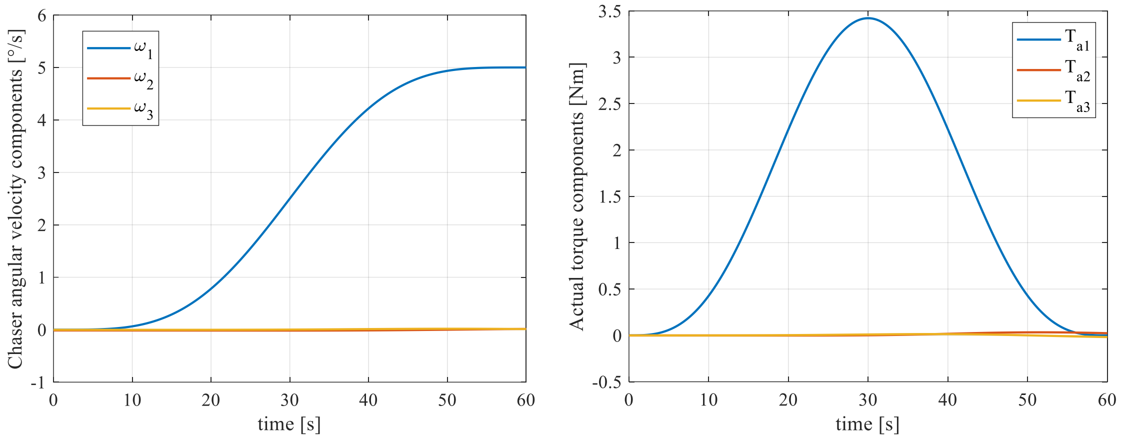

Figure 4.12: Spacecraft angular velocity (left) and actuator torque (right) during spin synchronization

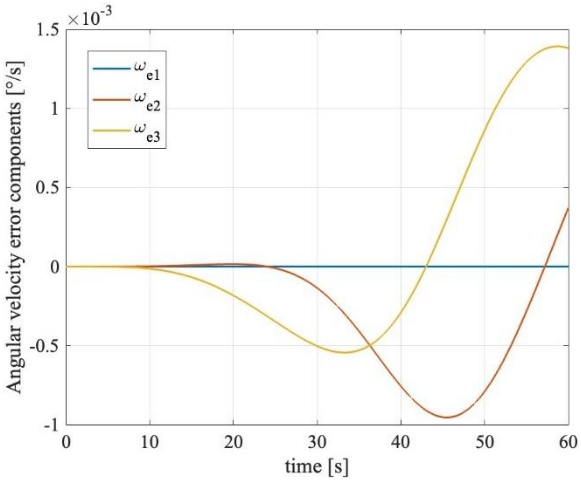

Figure 4.13: Angular velocity error during spin synchronization

4.1.6. Manipulation phase

In the manipulation phase, the operations start from the scenario depicted in the left plot of Figure 4.14. The final goal is in reaching the situation of the right plot of Figure 4.14, where both the end effectors are located at the grasping points. Considering a Chebyschev distribution of the path points, Figure 4.15 and the left plot in Figure 4.16 are obtained for the three trajectories described in Section 4.1.3. From inspection of these plots, it is apparent that the elliptic trajectory provides the smoothest trend of the motor torques, while the linear trajectory requires a much faster response of the actuators, especially in the first phase of the arm motion. For the mixed trajectory, the trend of the motor torque is close to the elliptical trajectory, but there is a limited but fast variation for

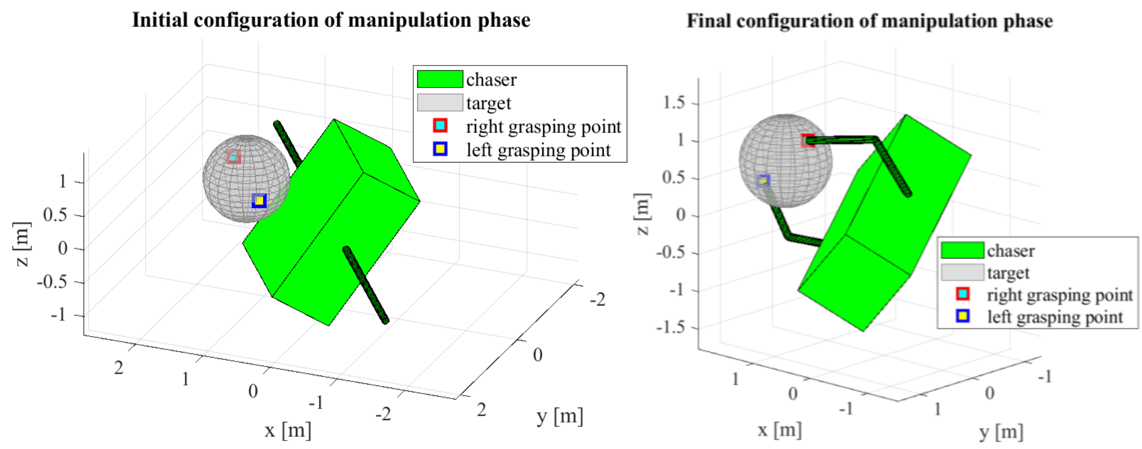

Figure 4.14: Initial (left) and final (right) configuration of manipulation

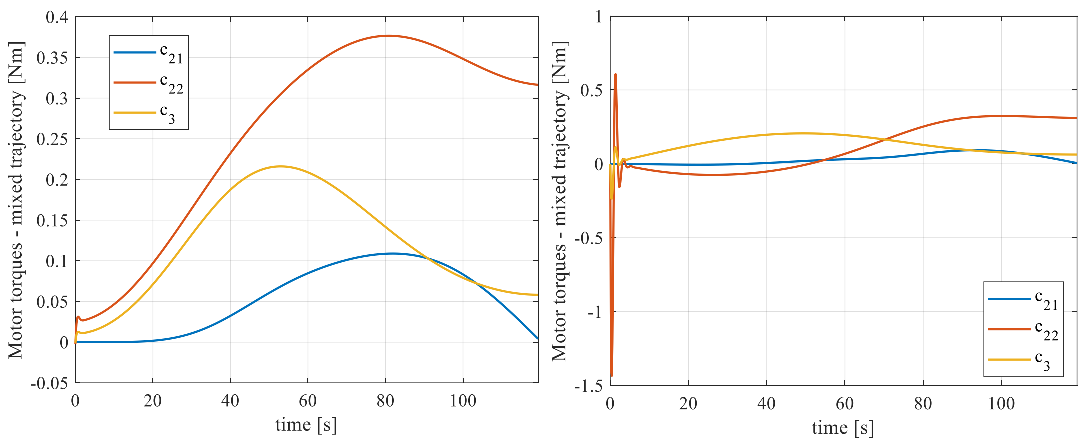

Figure 4.15: Motor torques for elliptic trajectory (left) and linear trajectory (right)

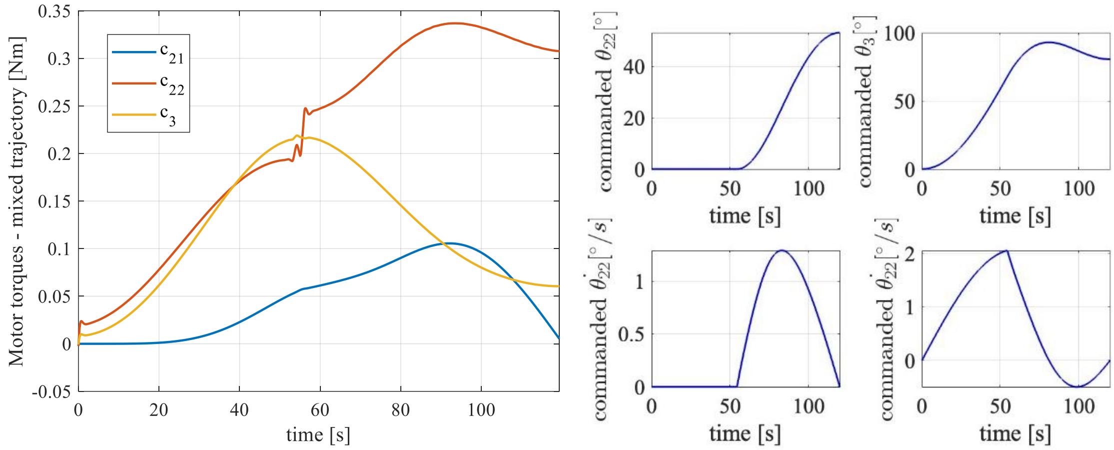

Figure 4.16: Motor torques (left) and commanded joint variables during manipulation (right) – mixed trajectory

the torque that acts on θ_{21} when the transition from the circular arc to the linear segment occurs. This behavior is due to the required joint motion coming from the trajectory planning algorithm, whose time histories are shown in the right plot of Figure 4.16. The two parts of the trajectory are clearly distinguishable in the joint space and this separation is the cause of the mentioned behavior. In conclusion, the elliptical trajectory is preferable, in terms of smoothness of the motor torques time histories.

With reference to the elliptical path, Figures 4.17-4.19 are obtained and describe the manipulation scenario. During the manipulation, the nutation induced by the spin rate characterizes the motion of the chaser but does not degrade the maneuver performance, because of its modest amplitude. Furthermore, the arms motion reduces the chaser inertia about axis $\hat{b}_1$, leading to an increase of the spin rate that is compensated by the control action with a certain delay, as represented in Figure 4.17. The phase shift due to this variation of the spin rate is evaluated through the numerical integration of the blue curve in the left plot of this figure, which yields a value of 2.58 deg, easily compensated through arm motion. Furthermore, Figure 4.18 shows the pointing error associated with axis $\hat{b}_1$, which shows very low values, meaning that attitude control succeeds in maintaining the pointing error within a certain threshold. Finally, Figure 4.19 illustrates the time histories of the most demanding joint variables (left plot) and the time histories of the relative distances between the two end effectors and the grasping points of the target (right plot).

To conclude the discussion about the manipulation phase, the constraint reactions at joint Q_2 are reported in Figure 4.20. Specifically, the rotary joints Q_2 allows two rotational degrees of freedom, thus the constraint reactions comprehend all the three force components and only a single torque component, which turns out to be modest and is not reported. The constraint forces components are obtained with respect to the reference frame

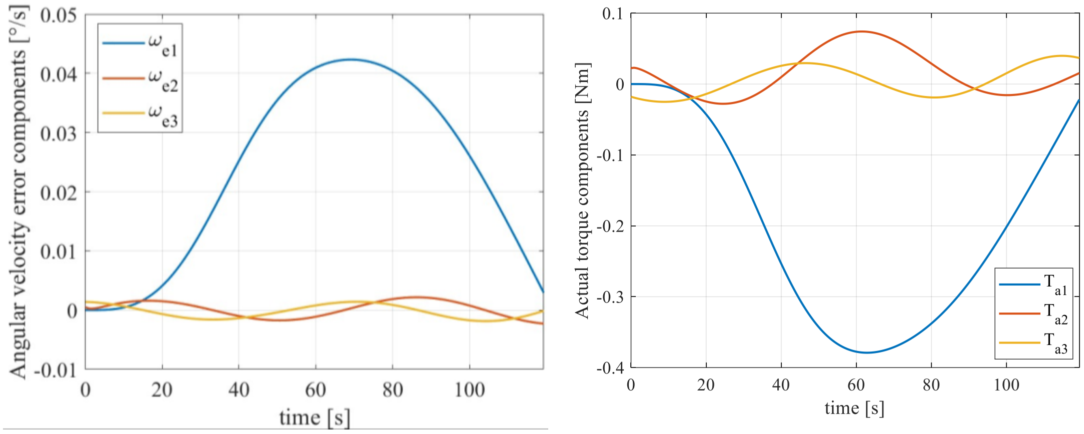

Figure 4.17: Spacecraft angular velocity (left) error and actuator torque (right) during manipulation

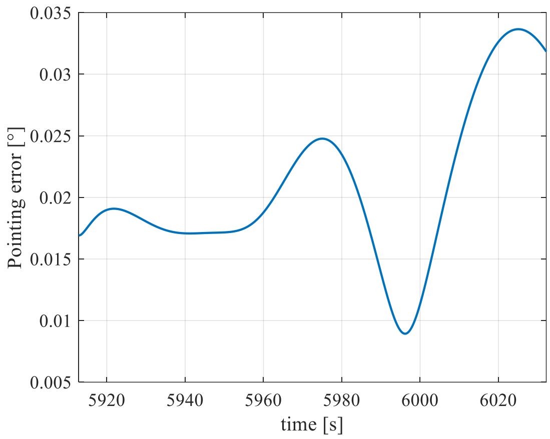

Figure 4.18: Pointing error during manipulation

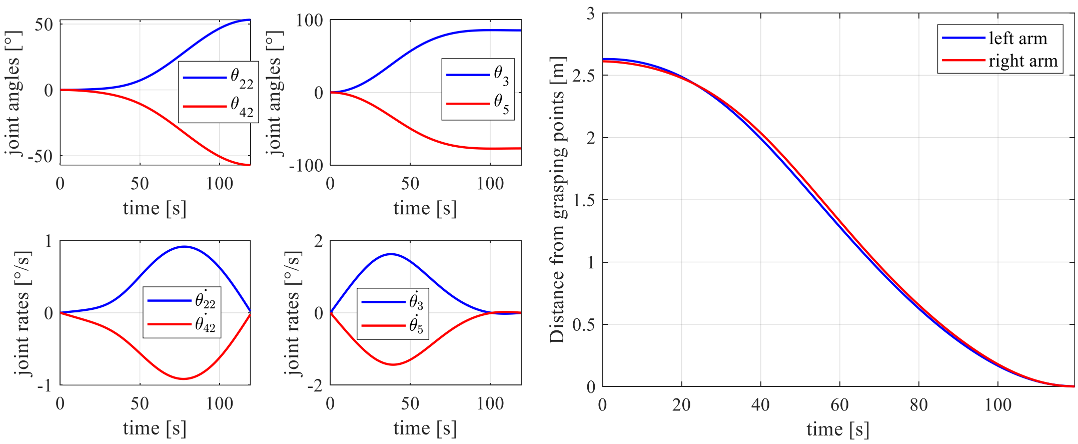

Figure 4.19: Joint variables (left) and end effectors/grasping points distances (right)

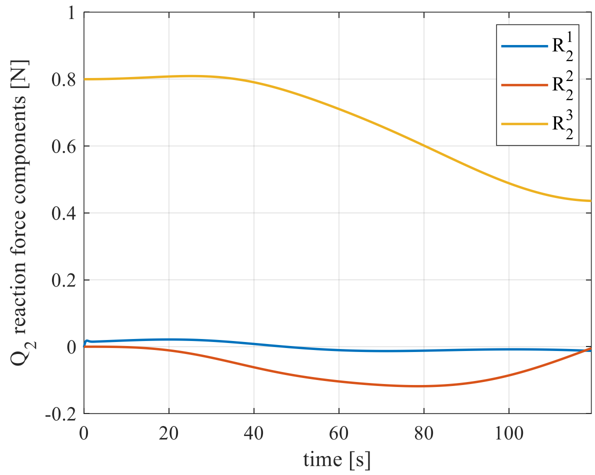

Figure 4.20: Reaction forces at joint Q_2

$\underline{\underline{B}}_1$. The main action is associated with the reaction to the centrifugal force induced by the spinning motion of the chaser. In fact, component R_2^3 is of the expected order of magnitude, using the following approximate relation:

$$F_C = m \cdot r \cdot \omega^2 \approx 60\text{kg} \cdot 1\text{m} \cdot \left(5° / \text{s}\right)^2 = 0.46\text{N} \tag{4.14}$$

where *m* here is the mass of a single dual-link arm, *r* is the distance between the spin axis of the manipulator and the center of mass of the arm and ω is the spin rate of the manipulator. This constraint force decreases in time because of the arm motion, which drives the center of mass of the arm toward the spin axis.

4.1.7. Operational window and safety requirements

To assess the suitability of the proposed strategy for a wide range of scenarios, two Monte Carlo campaigns were run:

1. Rendezvous Simulation (1000 runs): this campaign aims at verifying if the control strategy meets safety requirements while finding the average value of the operational window.
2. Reorientation Maneuver Simulation (200 runs): the objective of this campaign is in establishing the average duration of the reorientation operation. This duration is closely related to the initial conditions. Additionally, the campaign aims at determining whether arms opening before the reorientation maneuver represents an advantageous approach.

With regard to the first analysis, the parameters involved in the Monte Carlo campaign are the initial direction of the relative radius and the direction of $\hat{h}_{sp}$, which are uniformly distributed over a sphere, and the initial relative velocity, which is normally distributed with zero average value and 2 cm/s of standard deviation (truncation set to 5 cm/s). Results are presented in Figure 4.21.

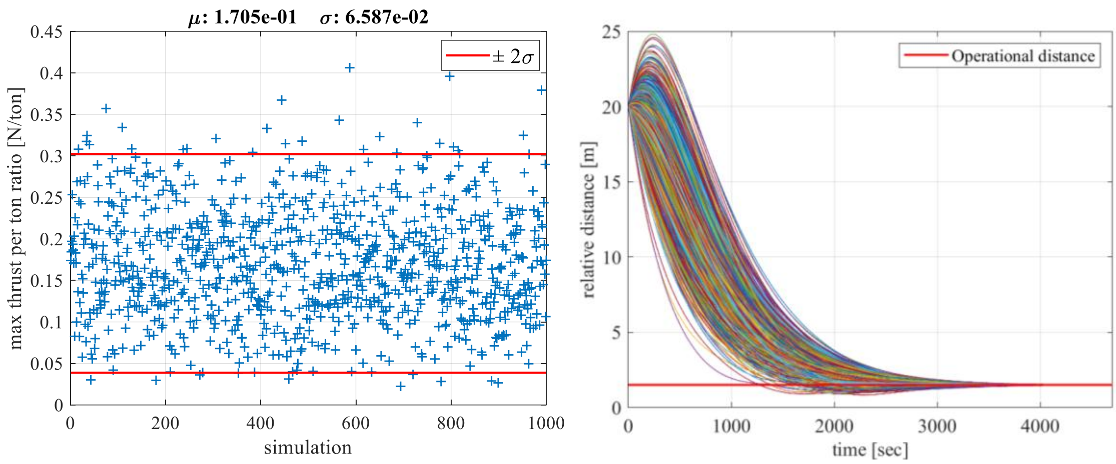

Figure 4.21: Distribution of the max normalized thrust (left) and time histories of the norm of relative distance (right) – simple guidance case

It is apparent that (i) the thrust is always below the threshold of $1 \ \mathrm{N/ton}$, and (ii) the control logic ensures the desired convergence to the operational distance of 1.5 m. In several cases the instantaneous distance falls below 1.4 m, which is assumed as the minimum safety distance, posing a potential risk of collision. This indicates that a more advanced guidance logic must be adopted, in place of the simple use of Eqs. (4.7), (4.8) and (4.9).

As an alternative and safer option, simulations are computed again using a via-point strategy, similar to the one adopted for the manipulation phase. From inspection of Figure 4.21, it is apparent that a suitable choice for the rendezvous time is 1 hour, which is roughly the average convergence time that allows carrying out the maneuver with feasible control values. The desired trajectory can be selected as a segment connecting the initial state, associated with time t_0, to the final one, associated with time t_f, i.e.

$$\underline{X}_d(t_0) = \underline{X}(t_0) \tag{4.15}$$

$$\underline{X}_d(t_f) = \pm \underset{L\leftarrow N}{R}(t_f)\underline{h}_{sp}^{(N)} d_{op} \tag{4.16}$$

where the sign in Eq. (4.16) is selected by choosing the shortest one between the two possible segments. Using spline interpolation, it is also possible to require that the desired velocity matches the initial and final conditions, which are

$$\underline{\dot{X}}_d(t_0) = \underline{\dot{X}}(t_0) \tag{4.17}$$

$$\underline{\dot{X}}_d(t_f) = \pm \underset{K\leftarrow N}{\dot{R}}(t_f)\,\underline{h}_{sp}^{(N)}d_{op} \tag{4.18}$$

With 10 via points, the results illustrated in Figure 4.22 are obtained. It is apparent that the safety constraints are met with this new approach, while the control effort remains modest. In fact, the number of via points is selected as a trade-off between the fulfillment of the safety requirements and the need of not overcoming the actuator capabilities. With regard to the duration of the reorientation maneuver, Figure 4.23 is obtained as a secondary result of the rendezvous campaign: for each computed case, the final rendezvous conditions are the new initial conditions of a further propagation in free-floating motion. The threshold is calculated by setting the upper bound of the operational

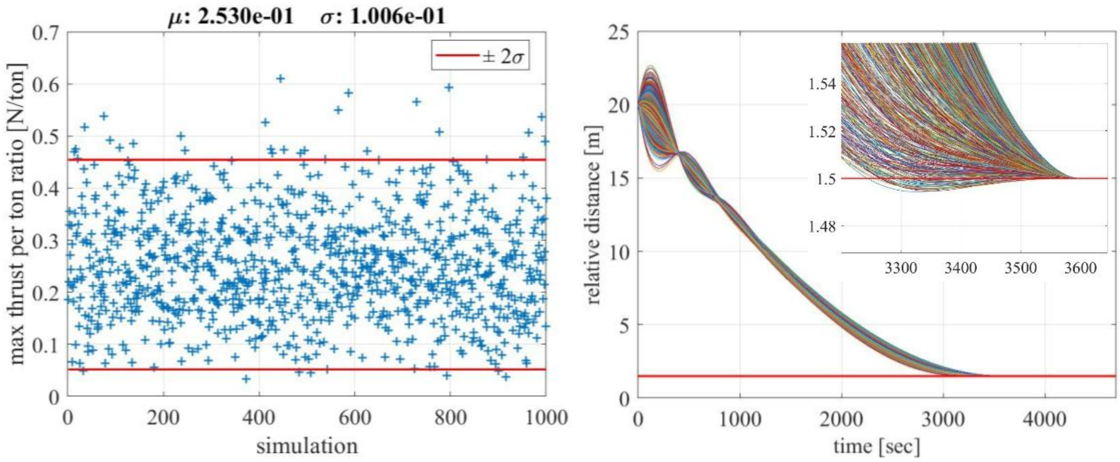

Figure 4.22: Distribution of the max normalized thrust (left) and time histories of the norm of relative distance (right) – via-points guidance case

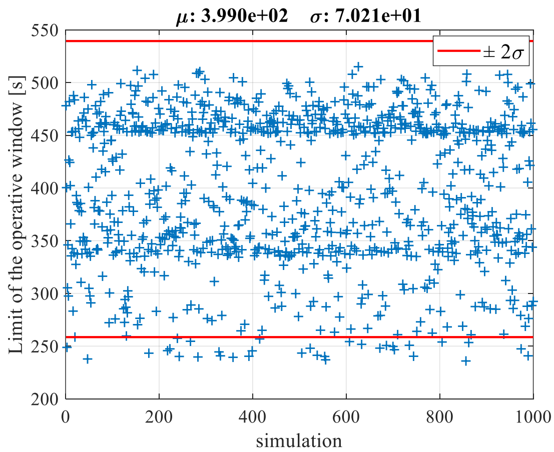

Figure 4.23: Distribution of the upper limit of the operational

window as the instant when the misalignment exceeds 10° or the relative distance increases by 10 cm with respect to the operational distance. Violation of each of these constraints represents about 50% of the total number of violations. From inspection of Figure 4.23 it is clear that in many cases the time for the maneuver must be less than 320 seconds, which is the total duration when the aforementioned sequential approach is considered.

If arms opening is carried out during the rendezvous, 105 seconds required for the operation are saved. However, the delay in the reorientation maneuver caused by the increased inertia of the spacecraft in its deployed configuration must be evaluated through a second Monte Carlo campaign. The only parameter involved in this case is the initial orientation of the spacecraft, which is uniformly distributed over a sphere. The results are reported in Table 4.8. Clearly, starting the arms deployment in advance offers a significant advantage in terms of mission duration. For the simulated case (not shown for the sake of brevity), the duration is reduced to approximately 230 seconds, which falls below the 2σ threshold indicated in Figure 4.23. Plots for this alternative sequence of operations are not reported because changing the order of operations does not have any significant impact on the time histories of the dynamic quantities obtained in the preceding sections.

Table 4.8: Statistical properties of convergence time for stowed and deployed configuration

	Stowed	Deployed
μ	41.53 s	48.36 s
σ	7.59 s	8.97 s

4.1.8. Post-grasping phase

After the capture phase, which is not modeled in this study case, the post grasping operations are simulated using the formulation presented in Section 1.4.2. The sequence of operations follows the subsequent steps: first, the chaser performs a de-spinning maneuver while maintaining the target at 1.5 m of distance. This phase lasts for 180 seconds. Then, after 60 additional seconds where the final state of the de-spinning phase is maintained, a manipulation maneuver is carried out. During this maneuver, which lasts 120 seconds, the relative distance between the target and the chaser is reduced from 1.5 m to 0.75 m. The mission concludes after additional 240 seconds, during which the spacecraft maintains the desired final state. Numerical results are reported in Figures 4.24-4.26. The results show that both the de-spinning and the manipulation of the target are successfully achieved within the depicted time span. Furthermore, the control efforts are modest for this mission, facilitating straightforward implementation in terms of actuator sizing. Although the constraint are imposed in the acceleration form, the

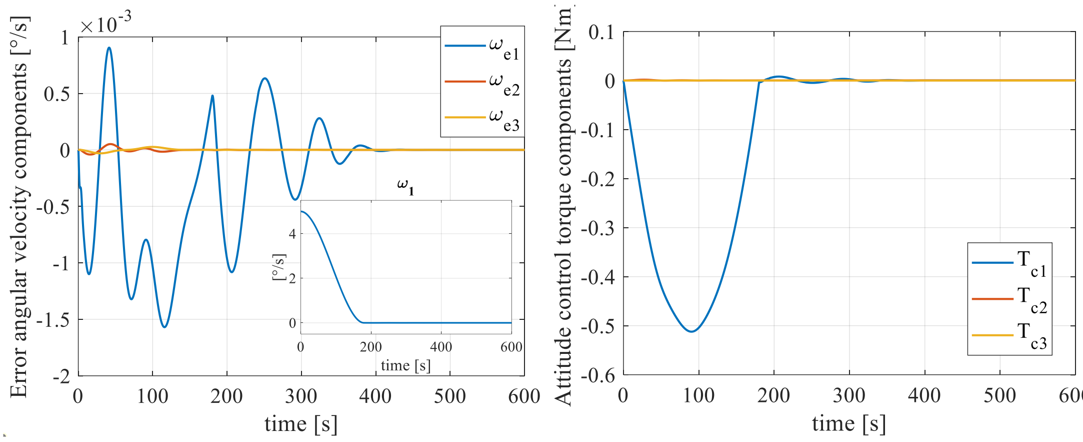

Figure 4.24: Error angular velocity components and absolute angular rate along b1 (left) and attitude control torque components (right)

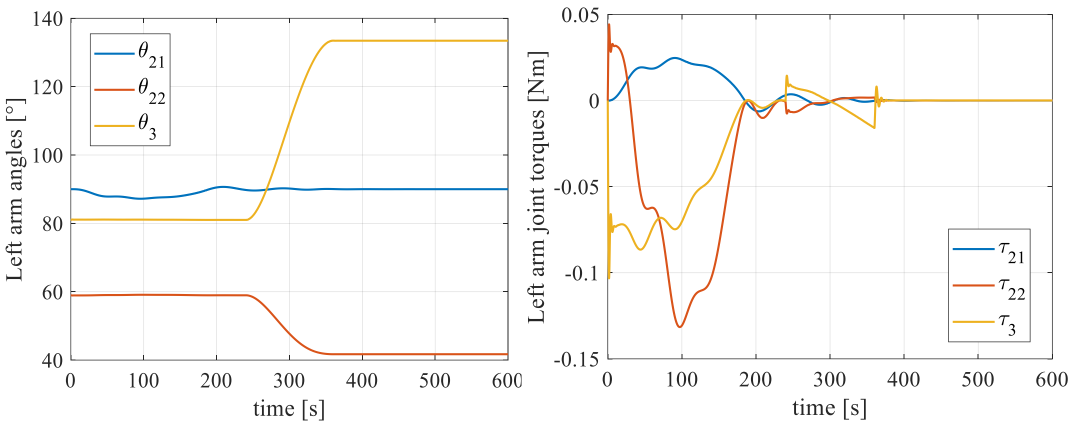

Figure 4.25: Angles of the left arm (left) and joint control torques for the left arm (right)

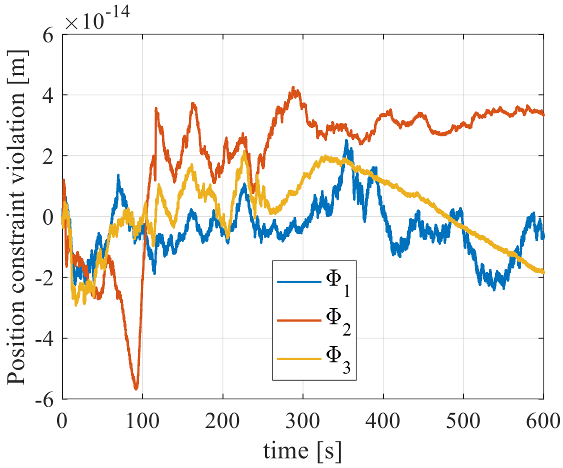

Figure 4.26: Violation of the position form of the constraint

violation of the constraint in the position form (in correspondence of the cut joint) is negligible, and no further numerical stabilization method is needed

4.1.9. Concluding remarks

This study case deals with the challenges of modeling and control of the overall dynamics of a space manipulator system designed for orbit berthing operations. The spacecraft at hand is equipped with two dual-link arms. This section addresses the design and numerical testing of the control architecture for relative trajectory, attitude, and robotic arms motion. Relative orbit dynamics is investigated using the Battin-Giorgi formulation of the Encke's method presented in Section 3.7. The related kinematics is incorporated into the Kane's formulation – reported in the first chapter – adopted to describe the overall dynamics of the (multibody) space manipulator system. Specific indications are obtained that constrain the duration of the rendezvous and berthing maneuver, in order to avoid excessive drift (i.e., increase of the relative distance) or misalignment. Moreover, two different sequences of operations (including rendezvous, reorientation, arms opening, synchronization, and manipulation) are proposed, simulated, and compared. Additionally, three different trajectories for the end effectors are designed and evaluated, pointing out the respective advantages and shortcomings. All the mission phases are simulated and discussed, pointing out some peculiar dynamical behaviors, such as the occurrence of spin-induced nutation. Two distinct guidance approaches are proposed, based on two different definitions of the rendezvous trajectory, and the via-point guidance is shown to be able to perform safe approach (without collisions) and grasping even from dispersed initial conditions. Finally, the post-grasping operations are modeled basing on the formulation reported in Sections 1.4.1-1.4.2, and the dynamic and control parameters concerning a de-spinning of the debris have been evaluated.

4.2. Attitude maneuvering of a large flexible spacecraft

This section presents a study focused on the agile attitude maneuvering of a spacecraft equipped with two flexible solar panels, in response to alert-triggered operational scenarios in space. Specifically, two distinct cases are addressed: one involving the tracking of a non-threatening piece of debris to enhance trajectory estimation, and another requiring an active collision avoidance maneuver to ensure spacecraft safety. The spacecraft is modeled as a multibody system with flexible appendages modeled as Euler-Bernoulli clamped-free beams. To meet the distinct requirements of each scenario, specific strategies for solar panel reorientation are implemented – either to optimize power generation or to suppress structural vibrations. Nonlinear reduced-attitude control is employed, using a pyramidal configuration of control momentum gyroscopes with a singularity avoidance algorithm. Numerical simulations demonstrate that the proposed approach its effectiveness in achieving mission objectives.

4.2.1. Vehicle and scenario description

The space vehicle considered in this application is modeled as a multibody structure, composed of a cylindrical rigid bus and two flexible solar panels. These can rotate about their own longitudinal axis, as illustrated in Figure 4.27, which also portrays the reference frames associated with the three bodies. In this work, the two solar panels are assumed to simultaneously rotate by angle β. Furthermore, for the sake of simplicity, the longitudinal axes of the solar panels are aligned with the center of mass of the rigid bus.

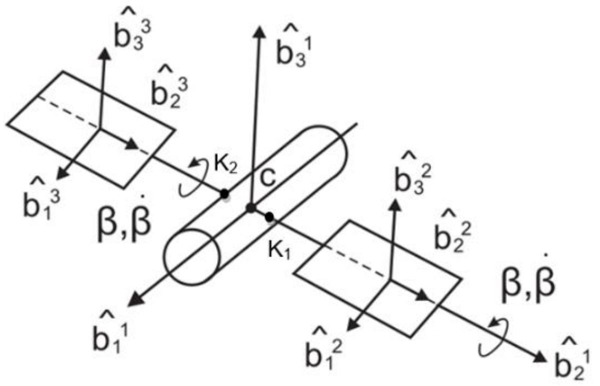

Figure 4.27: Geometry and elements of the multibody spacecraft

Geometry, sizing, and inertia parameters (i.e. total mass and principal inertia moments J_1, J_2, J_3) of the spacecraft of interest are identified referring to the Automated Transfer Vehicle (ATV) datasheet. Specifications for the cylindrical bus are shown in Table 4.9, whereas the geometric and inertia characteristics of the elastic solar panels are reported in Table 4.10. In this study case, flexibility is modeled through the linear approximation discussed in Chapter 2. No stiffening effect is included in the model, since the overall angular motion is expected to be on the order of 1°/s (≈ 0.0028 Hz), which is much lower than the lowest natural frequency of the structure. Therefore, stress stiffening can be considered negligible in this case.

The spacecraft mounts a pyramidal array of four single gimbal control momentum gyroscopes (SG-CMG) to provide the required control torque. SG-CMGs are momentum exchange devices, thus a limit exists on the maximum torque that they can transfer to the spacecraft before reaching saturation.

Table 4.11 collects the specifications of a specific type of commercial device, with performance appropriate to the dynamical scenarios of interest [96]. The symbols h, I_s,

ω_r, $\dot{\theta}_{max}$, T_{max} denote the axial angular momentum, inertia moment, rotor angular velocity, and maximum torque of the commercial device selected in this research.

The collision avoidance maneuver is carried out by means of a thruster aligned with axis $\hat{b}_1^1$ of the spacecraft, which provides constant thrust aligned with $\hat{b}_1^1$. For this application, a device with modest thrust level (compared to the large inertia of the entire spacecraft) is chosen (cf. Table 4.12), to prove feasibility of an efficient collision avoidance maneuver without any need of large thrust magnitudes.

Table 4.9: BUS specifications

Main Body (BUS)	
length (m)	9.79
diameter (m)	4.48
mass (kg)	16000
J_1 (kg m^2)	50000
J_2 (kg m^2)	100000
J_3 (kg m^2)	100000

Table 4.10: Solar panels: geometric and mechanical data

Solar panels	
length (m)	8.92
width (m)	1.16
thickness (cm)	2
density (kg/m3)	2700
Young's modulus (GPa)	70
mass (kg)	140

Table 4.11: SG-CMG specifications

SG-CMG M1300 Honeywell	
h (Nm sec)	2000
I_s (kg m^2)	2.938
ω_r (rpm)	6500
$\dot{\theta}_{max}$ (rad/s)	1
T_{max} (Nm)	2000
Mass (kg)	125

Table 4.12: Thruster specifications

Astrium 10 N Bi-Propellant Thruster	
specific impulse (s)	291
maximum thrust level (N)	10
mass depletion rate (g/s)	3.5

4.2.2. Tracking of a moving object: mission scenario

In the first scenario, a space debris is approaching the spacecraft, and no risk of collision is detected. For improving the accuracy in the space debris orbit determination, the spacecraft must direct a secondary payload (aligned with axis $\hat{b}_1^1$) toward the orbit debris. This provides the opportunity of observing debris while refining its orbit determination.

At time t_0, the presence of the debris is reported to the spacecraft, which stops performing its primary task and is reoriented in such a way to point the debris with the detector's axis ($\hat{b}_1^1$). Relative orbit dynamics leads to defining the commanded attitude and angular rate. However, as the debris approaches the observing spacecraft, relative orbit motion becomes faster. Attitude tracking proceeds until the commanded angular velocity and acceleration exceed the tracking capabilities, at time t_1 (less than one minute before the maximum approach occurs). Tracking is interrupted and a new attitude maneuver is carried out to reorient the satellite toward the point when a new tracking phase begins. Because the commanded angular velocity and acceleration show symmetric time histories with respect to the minimum distance point, tracking is resumed at a point symmetrical (with respect to the minimum distance point) to that where it was interrupted, i.e. at time $t_2 = t_1 + 2\left(t_{\min dist} - t_1\right)$.

During tracking arcs, the commanded attitude is defined as follows: first, the detector's axis must be aligned with $\underline{b}_{C_1}^{(N)}$ – the first axis of the commanded frame $\underline{\underline{C}}$ –, which collects the three components (in the inertial frame) of the debris position relative to the active spacecraft. A possible choice for the other two axes is

$$\hat{b}_{C_2} = \frac{\hat{b}_{C_1} \times \underrightarrow{h_B}}{\left\| \hat{b}_{C_1} \times \underrightarrow{h_B} \right\|} \qquad \hat{b}_{C_3} = \hat{b}_{C_1} \times \hat{b}_{C_2} \tag{4.19}$$

where $\underrightarrow{h_B}$ is the orbital angular momentum of the spacecraft. If $\hat{b}_{C_1}$ becomes parallel to $\underrightarrow{h_B}$, it is not possible to find the other two commanded axes; to avoid this singularity, it is possible to replace $\underrightarrow{h}_B$ with the spacecraft position vector (taken from the Earth center). Once the commanded axes are defined, one can directly write the associated rotation matrix as

$$\underset{C \leftarrow N}{R} = \begin{bmatrix} \underline{b}_{C_1}^{(N)T} \\ \underline{b}_{C_2}^{(N)T} \\ \underline{b}_{C_3}^{(N)T} \end{bmatrix} \tag{4.20}$$

and the commanded angular velocity is obtained from the Eq. (3.2), i.e.

$$\underset{C \leftarrow N}{\dot{R}} = -\underline{\tilde{\omega}}_C^{(C)} \underset{C \leftarrow N}{R} \Rightarrow \underline{\tilde{\omega}}_C^{(C)} = -\underset{C \leftarrow N}{\dot{R}} \underset{N \leftarrow C}{R} \tag{4.21}$$

Finally, the time derivative of $\underline{\omega}_C$ yields $\underline{\dot{\omega}}_C$.

In this application, solar panels are oriented with the objective of maximizing solar power storage. This corresponds to identifying the time history $\beta(t)$ that maximizes the dot product $\hat{r}_S \cdot \hat{\zeta}$, where unit vector $\hat{r}_S$ is aligned with the Earth-Sun direction, whereas unit vector $\hat{\zeta}$ is normal to the solar panels. To do this, it is first necessary to identify the Sun position with respect to the Earth Centered Inertial (ECI) frame though the angles ε_s and χ_s depicted in Figure 4.28. It is apparent that χ_s corresponds to the inclination of the ecliptic plane with respect to the equatorial plane, so it is equal to 23.4°. Instead, angle ε_s is equal to

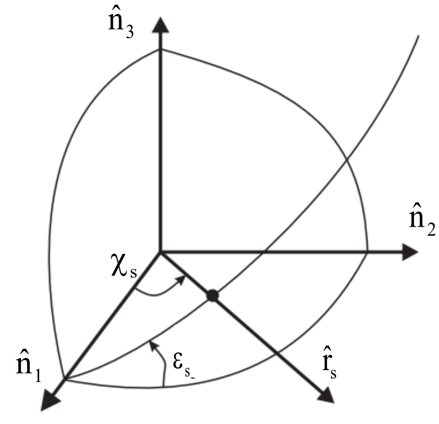

Figure 4.28: Sun position in the ECI frame

$$\chi_s = \chi_{s0} + \omega_s (t - t_0) \tag{4.22}$$

where ω_s is the angular velocity of the Earth orbit around the Sun, i.e. $\omega_s = \frac{2\pi}{1\text{yr}}$, wile χ_{s0} is the value of χ_s at the initial time t_0. Then, $\hat{r}_s$ becomes

$$\hat{r}_s = \underline{\underline{N}} \begin{bmatrix} \cos\chi_s \\ \sin\chi_s \cos\varepsilon_s \\ \sin\chi_s \sin\varepsilon_s \end{bmatrix} = \underline{\underline{N}}\underline{r}_s^{(N)} \tag{4.23}$$

and the time derivatives of Eq. (4.23) are

$$\dot{\underline{r}}_s^{(N)} = \dot{\chi}_s \begin{bmatrix} -\sin\chi_s \\ \cos\chi_s \cos\varepsilon_s \\ \cos\chi_s \sin\varepsilon_s \end{bmatrix} \tag{4.24}$$

$$\ddot{\underline{r}}_s^{(N)} = -\dot{\chi}_s^2 \begin{bmatrix} \cos\chi_s \\ \sin\chi_s \cos\varepsilon_s \\ \sin\chi_s \sin\varepsilon_s \end{bmatrix} \tag{4.25}$$

Moreover, with reference to Figure 4.29, the unit vector normal to the panel can be written as

$$\hat{\zeta} = \underline{\underline{B}} \begin{bmatrix} \sin\beta \\ 0 \\ \cos\beta \end{bmatrix} = \underline{\underline{N}} \underset{N \leftarrow B}{R} \begin{bmatrix} \sin\beta \\ 0 \\ \cos\beta \end{bmatrix} \tag{4.26}$$

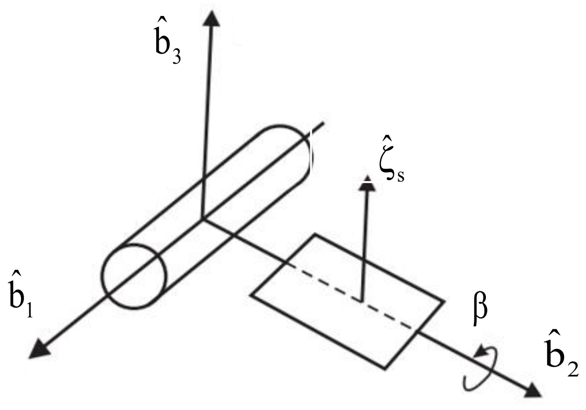

Figure 4.29: Panel orientation when $\beta = 0°$

To obtain β, it is needed to write $\hat{r}_s$ in components with respect to the spacecraft frame, i.e.

$$\hat{r}_s = \underline{\underline{N}}\,\underline{r}_s^{(N)} = \underline{\underline{B}}\,\underset{B\leftarrow N}{R}\,\underline{r}_s^{(N)} \triangleq \underline{\underline{B}}\,\underline{\xi} \tag{4.27}$$

Requiring the maximum irradiation implies the maximization of the scalar product $\hat{r}_S \cdot \hat{\zeta}$, which means that the normal to the panel $\hat{\zeta}$ is aligned with the projection of the Sun direction $\hat{r}_S$ onto the plane defined by axes $\hat{b}_1$ and $\hat{b}_3$. Then, angle β is derived from the following relations (cf. Figure 4.30):

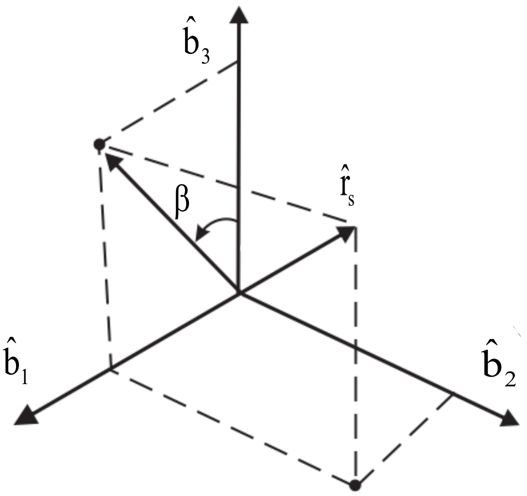

Figure 4.30: Relation between β and $\hat{r}_s$ in the spacecraft body frame

$$\begin{cases} \sin\beta = \dfrac{\xi_1}{\sqrt{\xi_1^2 + \xi_3^2}} \\ \cos\beta = \dfrac{\xi_3}{\sqrt{\xi_1^2 + \xi_3^2}} \end{cases} \tag{4.28}$$

The first time derivative of β is obtained from Eq. (4.28) as

$$\dot{\beta} = \frac{\dot{\xi}_1 \xi_3 - \dot{\xi}_3 \xi_1}{\xi_1^2 + \xi_3^2} \tag{4.29}$$

where $\dot{\underline{\xi}}$ is obtained by taking the derivative of Eq. (4.27), i.e.

$$\dot{\underline{\xi}} = -\underline{\tilde{\omega}}\,\underset{B\leftarrow N}{R}\,\underline{r}_s^{(N)} + \underset{B\leftarrow N}{R}\,\dot{\underline{r}}_s^{(N)} \tag{4.30}$$

Applying the same procedure for the second time, one also obtains

$$\ddot{\beta} = \frac{(\ddot{\xi}_1\xi_3 - \ddot{\xi}_3\xi_1)(\xi_1^2 + \xi_3^2) - 2(\dot{\xi}_1\xi_3 - \dot{\xi}_3\xi_1)(\xi_1\dot{\xi}_1 + \xi_3\dot{\xi}_3)}{(\xi_1^2 + \xi_3^2)^2} \tag{4.31}$$

with

$$\ddot{\underline{\xi}} = -\dot{\underline{\tilde{\omega}}} \underset{B\leftarrow N}{R} \underline{r}_s^{(N)} + \underline{\tilde{\omega}}\left(\underline{\tilde{\omega}} \underset{B\leftarrow N}{R} \underline{r}_s^{(N)}\right) - 2\underline{\tilde{\omega}} \underset{B\leftarrow N}{R} \dot{\underline{r}}_s^{(N)} \tag{4.32}$$

4.2.3. Tracking of a moving object: numerical results

As a first step, a single simulation was performed, to present and comment on some relevant time histories. In this case, results are obtained using the reduced-attitude control law (3.78) with $\gamma = 1/2$. The Classical Orbital Elements (COE) of spacecraft and debris are reported in Table 4.13. They yield closest approach approximately equal to 500 meters. The spacecraft initial nominal attitude conditions are

$$\begin{aligned} q_0 &= 0.8924 \\ \underline{q} &= \begin{bmatrix} 0.2391 & -0.0990 & 0.3696 \end{bmatrix} \\ \underline{\omega} &= \begin{bmatrix} -0.005 & 0.003 & -0.005 \end{bmatrix} \text{ rad/s} \end{aligned} \tag{4.33}$$

The order of magnitude of the angular velocity is chosen by assuming that the satellite is carrying out an Earth observation task.

Table 4.13: Initial orbit elements for scenario 1

	Spacecraft	Debris
semimajor axis (km)	7000	7000.47
eccentricity	0.01	0.01
inclination (deg)	1	11
RAAN (deg)	0	0
arg. of periapsis (deg)	0	0
true anomaly at t_0 (deg)	-60.005	-60

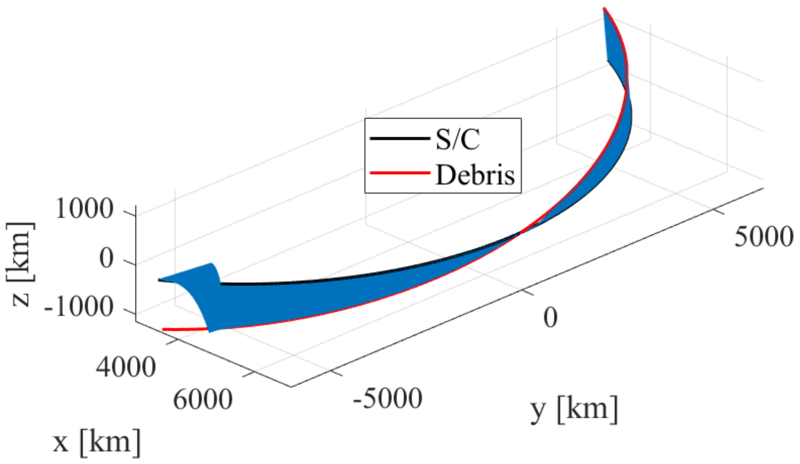

Figure 4.31: Orbits and time-varying directions of $\hat{b}_1$ (blue lines)

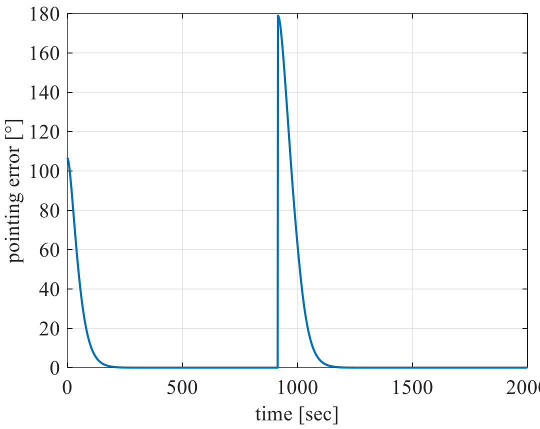

Figure 4.32: Pointing error

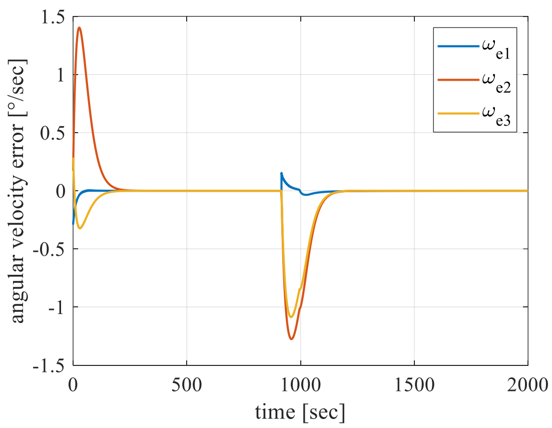

Figure 4.33: Angular velocity error

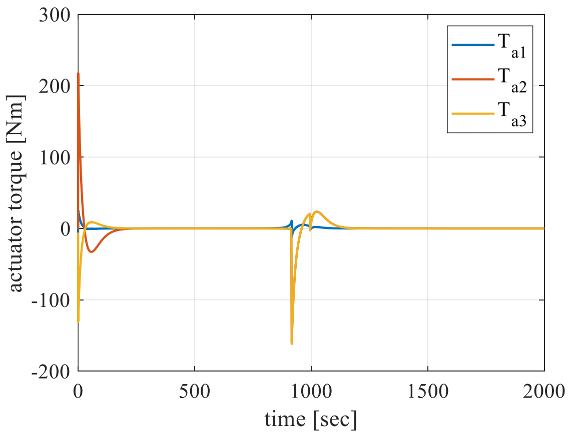

Figure 4.34: Actuator torque

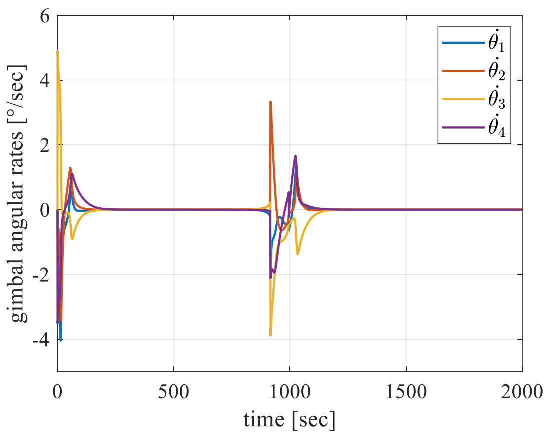

Figure 4.35: SG-CMG gimbal angular

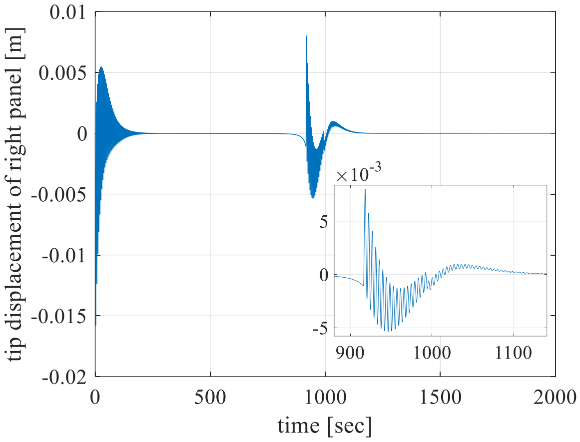

Figure 4.36: Tip transverse displacement of the right panel (body 2)

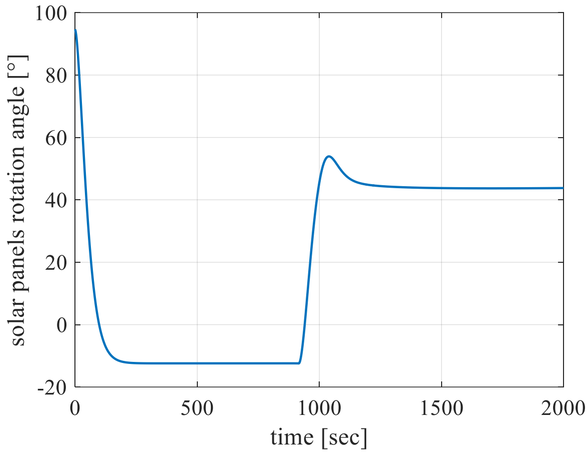

Figure 4.37: Rotation angle of the solar panels

Figure 4.31 depicts the time histories of the two orbits and axis $\hat{b}_1$, whereas Figure 4.32 through Figure 4.37 portray the pointing error, angular velocity error, actuator torque, gimbal velocities, tip displacement of body 2 (right panel in Figure 4.27), and panel rotation angle. Figures 4.31 and 4.32 show that, after a first period of acquisition, tracking is maintained during almost the entire mission duration. As previously remarked, reorientation is needed around the point of closest approach because the commanded angular velocities and accelerations are too large. However, this phase is not visible in Figure 4.31 due to the modest distance between spacecraft and debris that occurs during the reorientation interval. Figures 4.33- 4.37 show changes in their trends when the control logic is modified. In fact, discontinuity of the commanded attitude causes rapid variations of the actual torque and all the other quantities as a result. This abrupt change affects the flexural behavior, and time-varying torques can either trigger the flexible oscillations or (sometimes) damp them. In fact, Figures 4.34 and 4.36 point out that the first two sudden variations of the actual torque increase the tip oscillations, while the third one reduces their amplitude. Furthermore, the impact of structural damping can be assessed by examining Figure 4.36, which displays the continuous damping of the oscillations along the three arcs of the mission.

A Monte Carlo campaign was completed, to investigate feasibility of attitude maneuvering regardless of the initial attitude conditions and in the presence of some uncertainties on the mass of the bus and on the flexural stiffness of the solar panels (see Table 4.14). As in the nominal case, the modified reduced control law is used and orbital initial conditions are the same reported in Table 4.13. The campaign is composed of 100 simulations, with random initial attitude conditions and uncertainties in both the flexural properties of the solar panels and the mass distribution. Specifically, two-point masses are added symmetrically with respect to the center of mass. Their position is defined using cylindrical coordinates (r_A, λ, l_1), defined in relation to the three body axes of the

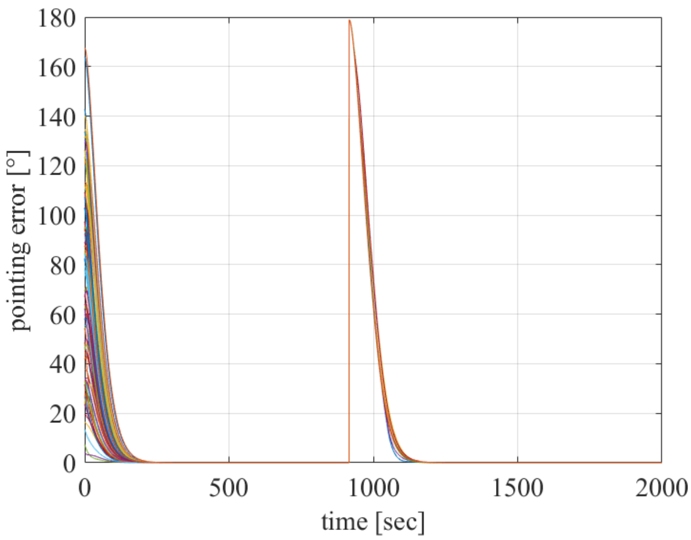

Figure 4.38: Time histories of the pointing error (Monte Carlo campaign)

Table 4.14: parameters of Monte Carlo simulations

(*) values corresponding to 10% uncertainty

	Description	Distribution
m	one point mass [kg]	Normal, $\mu = 0, \sigma = 500$ Constrained to $[0 \quad 1500]$
r_A	radial distance [m]	Uniform in $[0 \quad 2]$
λ	azimuth [rad]	Uniform in $[0 \quad 2\pi]$
l_1	height [m]	Normal, $\mu = 0, \sigma = 1$ Constrained to $[0 \quad 3]$
$\underline{e}$	eigenaxis direction	Uniform on a unit sphere
ϕ	eigenangle [rad]	Uniform in $[0 \quad \pi]$
ω_i	initial angular velocity components [deg/sec]	Normal, $\mu = 0, \sigma = 0.5$ constrained to $[-1.5 \quad 1.5]$
EI	flexural stiffness $[\mathrm{Pa} \cdot \mathrm{m}^4]$	Uniform in $[4.3772 \quad 6.5388] \cdot 10^4$ *

cylindrical body. Random attitude is defined by assuming that the eigenaxis components have uniform distribution over a unit sphere. The angular velocity components have normal distribution, with specified average value and standard deviation. For all uncertain quantities with normal distributions, symbols μ and σ denote the respective mean values and standard deviations (cf. Table 4.14).

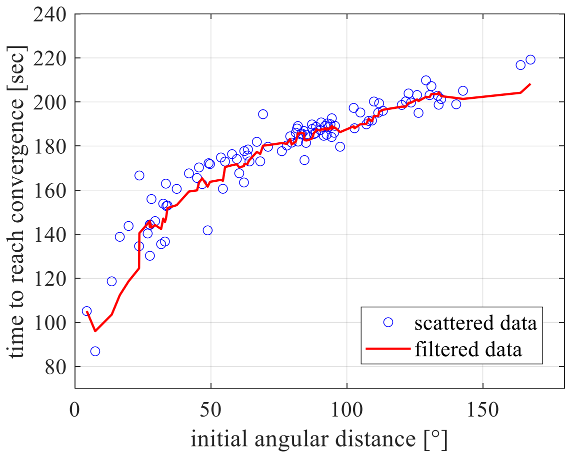

Figure 4.39: Correlation between initial angular displacement and convergence time (1st tracking interval)

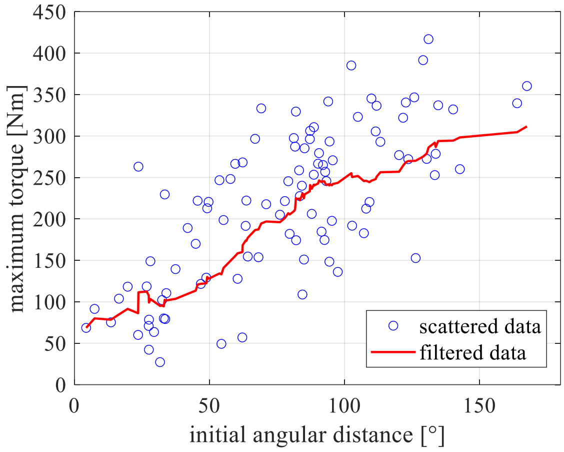

Figure 4.40: Correlation between initial angular displacement and maximum actuator torque (1st tracking interval)

Some results coming from the Monte Carlo simulations are illustrated in Figures 4.38-4.40. Figure 4.38 shows the pointing errors in all cases. For a deeper analysis of these simulations, it is convenient to divide each tracking interval in two subarcs, i.e. acquisition and continuous tracking. For each tracking interval, the following quantities can be computed: (a) convergence time t_{conv} (needed to reduce the pointing error below a specified threshold value, set to 0.5 deg), (b) maximum actuator torque $(T_a)_{max}$, (c) maximum tip displacement $[y(L)]_{max}$, and (d) mean (integral) value of the pointing error $\bar{\varepsilon}$ (computed between t_{conv} and the end of continuous tracking). Average values and standard deviations are evaluated and reported in Table 4.15

Table 4.16 for the two tracking phases. It is worth remarking that the first phase begins with different (random) initial conditions, while the second tracking interval starts with near identical initial attitude conditions for all the Monte Carlo simulations. For all simulations, the mission is successfully accomplished by the spacecraft. Inspection of Table 4.15

Table 4.16 reveals that random initial conditions lead to results of interval 1 that are much more dispersed than those of the second interval. Conversely, the mean values of the pointing error are similar because they are evaluated over time intervals where convergence has already been achieved. Focusing on the first arc, the evaluation of the

Table 4.15: Statistics for tracking interval 1

	μ	σ
t_{conv} (sec)	$1.774 \cdot 10^{2}$	$2.354 \cdot 10$
$(T_a)_{max}$ (Nm)	$2.176 \cdot 10^{2}$	$9.247 \cdot 10$
$[y(L)]_{max}$ (m)	$1.313 \cdot 10^{-2}$	$1.034 \cdot 10^{-2}$
$\bar{\varepsilon}$ (deg)	$1.902 \cdot 10^{-2}$	$8.486 \cdot 10^{-4}$

Table 4.16: Statistics for tracking interval 2

	μ	σ
t_{conv} (sec)	$2.407 \cdot 10^{2}$	5.242
$(T_a)_{max}$ (Nm)	$2.250 \cdot 10^{2}$	$1.144 \cdot 10$
$[y(L)]_{max}$ (m)	$8.785 \cdot 10^{-3}$	$4.023 \cdot 10^{-3}$
$\bar{\varepsilon}$ (deg)	$1.687 \cdot 10^{-2}$	$1.162 \cdot 10^{-3}$

performance of the attitude control system can be carried out through the inspection of Figures 4.39-4.40. They report the scattered and filtered trends of t_{conv} and $(T_a)_{max}$, respectively, as a function of the initial pointing error. The maximum actuator torque shows greater dispersion than the convergence time because it is more affected by the initial angular velocity.

4.2.4. Collision avoidance maneuvering: mission scenario

In the second application, a debris is assumed to be on a collision course toward the active spacecraft, and a collision avoidance maneuver is needed as a result. Simulations start around 50 minutes before the predicted impact. First, the optimal thrust direction that minimizes propellant consumption is computed. Because an efficient, real-time strategy is sought, optimization of the collision avoidance maneuver employs the impulsive thrust approximation. The time t_1 when the main thruster is ignited is specified a priori and set to 20 minutes before the impact. Optimal trajectory correction is performed by minimizing the cost function $J = \|\Delta \underset{\rightarrow}{v}\|$ (where $\Delta \underset{\rightarrow}{v}$ denotes the impulsive velocity change) under the constraint that the minimum relative distance must be greater than a threshold safety value, set to 100 m. The optimal trajectory correction is computed using MATLAB's "fmincon" algorithm, which performs constrained nonlinear optimization by applying an interior-point method by default.

Attitude maneuvering, aimed at aligning the main thruster with the optimal thrust direction, starts 50 minutes before the impact. In this way, all the elastic oscillations are already damped out at the time when the thruster is ignited, and the avoidance maneuver can be carried out in safety conditions. After identifying the optimal thrust direction, the attitude maneuver starts. Axis $\hat{b}_1^1$ (aligned with the thruster mounting) must point toward the optimal thrust direction. The commanded angular velocity is set to zero because the optimal direction must be maintained during the entire (short-duration) ignition of the main thruster. At time t_1, thrust is ignited, then it is switched off when the desired safety conditions are met. An orbit propagation is performed with a sampling time of 5 seconds to estimate the distance of closest approach. When this exceeds the threshold value of 100 m, thrust is turned off and the maneuver ends. The value of the sampling time is chosen as a compromise between the requirement of reducing propellant expenditure and the need of guaranteeing computational feasibility of a real-time estimation of the distance of closest approach. In this mission scenario, panels are rotated to maintain their normal direction orthogonal to axis $\hat{b}_1^1$, so that disturbance torques due to flexural oscillations are parallel to $\hat{b}_1^1$ and do not affect its alignment, which is crucial for the avoidance maneuver to succeed. As for the first scenario, results are obtained using the reduced-attitude control law (3.78) with $\gamma = 1/2$.

4.2.5. Collision avoidance maneuvering: numerical results

The orbital initial conditions are reported in Table 4.17. They lead to collision if no avoidance maneuver is carried out. The initial nominal attitude conditions are

$$\begin{aligned} q_0 &= 0.8924 \\ \underline{q} &= \begin{bmatrix} 0.2391 & -0.0990 & 0.3696 \end{bmatrix} \\ \underline{\omega} &= \begin{bmatrix} -0.005 & 0.003 & -0.005 \end{bmatrix} \text{ rad/s} \end{aligned} \tag{4.34}$$

Results are reported in Figures 4.41-4.46, where only the first 300 seconds of the time histories are reported, where the attitude maneuver is appreciable. In fact, after convergence has been reached, no further variation can be seen on these plots. In these figures, the order of magnitudes of the plotted quantities are comparable to the ones of the first scenario because the initial angular displacements are similar in the two cases. Considering the tip displacement of the solar panel, switching on and off the thruster does not trigger any oscillations because solar panels have been oriented with their normal direction orthogonal to the thrust direction, as specified before. For illustrative purposes, Figure 4.46 shows a zoom of the time history of the tip displacement in the "worst case", i.e. when the normal direction of the panels is parallel to the thrust direction. In this case, oscillation of small amplitude (because of the low thrust) are triggered by both switching on and off the thruster. Similarly to the previous case, in the tracking application, the structural damping also exerts a noticeable influence on the elastic behavior of the panels.

Table 4.17: Initial orbit elements for scenario 2

	Spacecraft	Debris
semimajor axis (km)	7000	7000
eccentricity	0.01	0.01
inclination (deg)	1	11
RAAN (deg)	0	0
arg. of periapsis (deg)	0	0
true anomaly at t_0 (deg)	-178	-178

Also in this scenario, a Monte Carlo analysis is carried out through a set of 100 simulations. Nonnominal conditions are identical to those introduced for mission scenario 1 (cf. Table 4.14). In addition, an oscillation term is introduced to perturb the thrust magnitude, with the intent of investigating its effect on the avoidance maneuver. This perturbing term has the following form:

$$\sum_{k=1}^{N} A_k \sin\left(\frac{2\pi kt}{t_{b_0}}\right) + B_k \cos\left(\frac{2\pi kt}{t_{b_0}}\right) \tag{4.35}$$

where t_{b_0} is a term of the same order of magnitude of the burning time, N is equal to 5 and A_k, B_k are random variables with normal distribution. Mean value and standard deviations are $\mu = 0$ N and $\sigma = 0.5$ N, and the values of A_k and B_k are constrained to the interval $[0\text{ N} \quad 1\text{ N}]$. Similarly to the first application, results are shown in terms of t_{conv}, $(T_a)_{max}$, $[y(L)]_{max}$ and $\bar{\varepsilon}$, whose statistical properties are evaluated. In addition, performance of the orbital maneuver is evaluated in terms of burning time and $\|\Delta\underline{v}\|$. The latter quantity is evaluated in terms of impulsive velocity change $\|\Delta\underline{v}\|_{imp}$ (found through optimization) and effective velocity change $\|\Delta\underline{v}\|_{FT}$ (obtained using finite thrust through the steps described in this section).

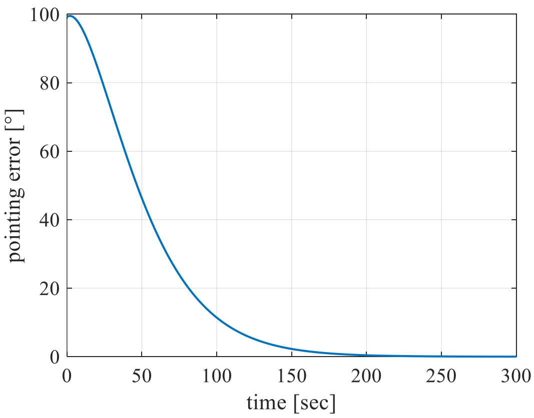

Figure 4.41: Pointing error

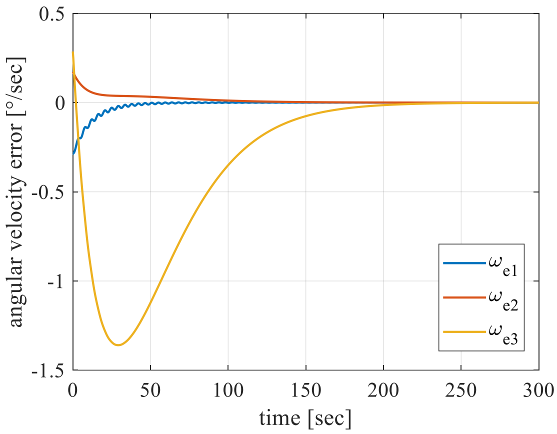

Figure 4.42: Angular velocity error

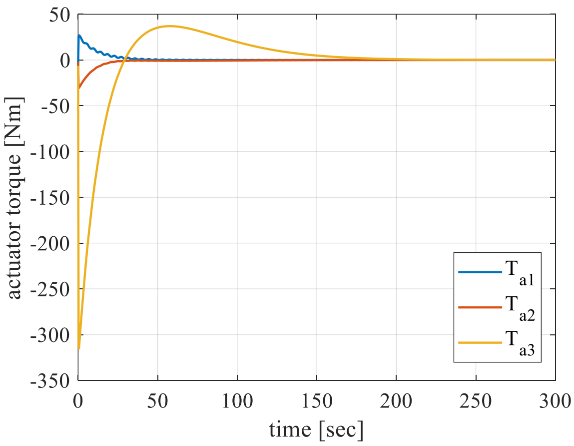

Figure 4.43: Actuator torque

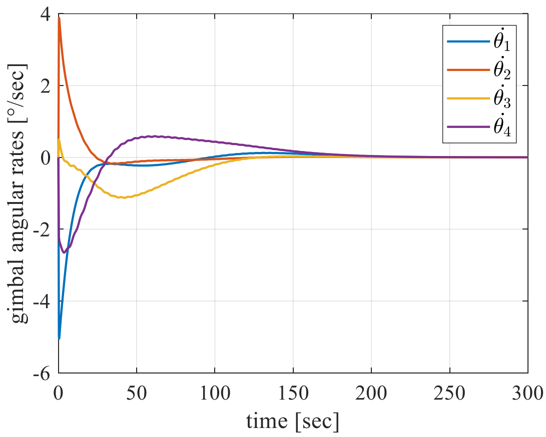

Figure 4.44: SG-CMG gimbal angular rates

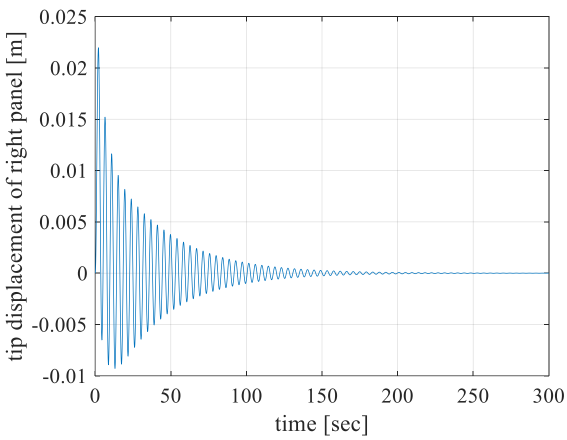

Figure 4.45: Tip transverse displacement of body 2 – attitude reorientation

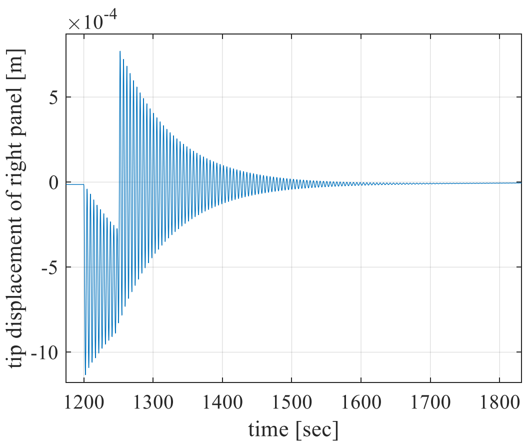

Figure 4.46: Tip transverse displacement of body 2 – thruster ignition

The reorientation maneuver is successfully accomplished in all cases. In particular, the desired attitude is always reached in relatively short time (cf. Figure 4.47), despite different initial orientation, angular velocity, mass distribution and flexural properties. It implies that, for all the cases, there is sufficient time to damp out even the long-period oscillations as those due to sloshing of propellants, which are not dynamically modeled in this application but nevertheless were considered for the choice of the mission scheduling. As in the previous case, performance of the attitude control system can be evaluated through inspection of Figures 4.49-4.50 and Table 4.18, while the control effort in the collision avoidance maneuver is evaluated by inspection of Table 4.19.

Table 4.18: Meaningful parameters of the reorientation maneuver

	μ	σ
t_{conv} (s)	$1.775 \cdot 10^2$	$2.008 \cdot 10$
$(T_a)_{max}$ (Nm)	$2.184 \cdot 10^2$	$9.966 \cdot 10$
$[y(L)]_{max}$ (m)	$1.447 \cdot 10^{-2}$	$1.018 \cdot 10^{-2}$
$\bar{\varepsilon}$ (deg)	$5.252 \cdot 10^{-3}$	$6.522 \cdot 10^{-4}$

Table 4.19: Performance of the collision avoidance maneuver

burning time (sec)	50
$\|\Delta \underset{\rightarrow}{v}\|_{imp}$ (cm/sec)	2.85
$\|\Delta \underset{\rightarrow}{v}\|_{FT}$ (cm/sec)	3.12

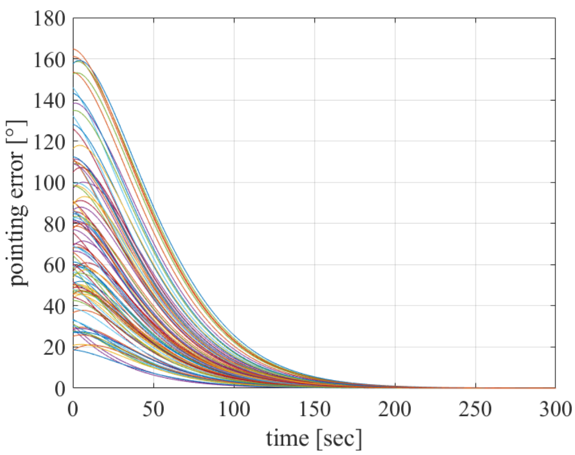

Figure 4.47: Time histories of the misalignment angle (MC campaign)

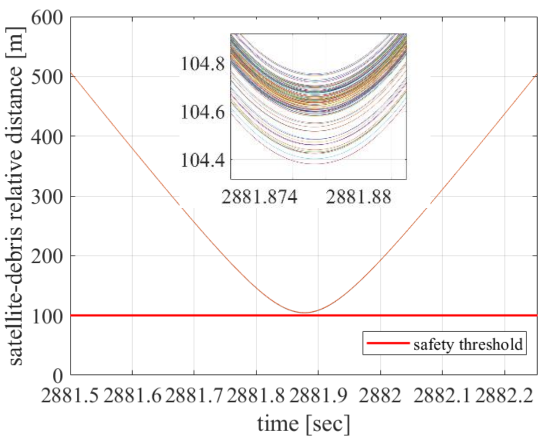

Figure 4.48: Time histories of the relative distance at the closest approach

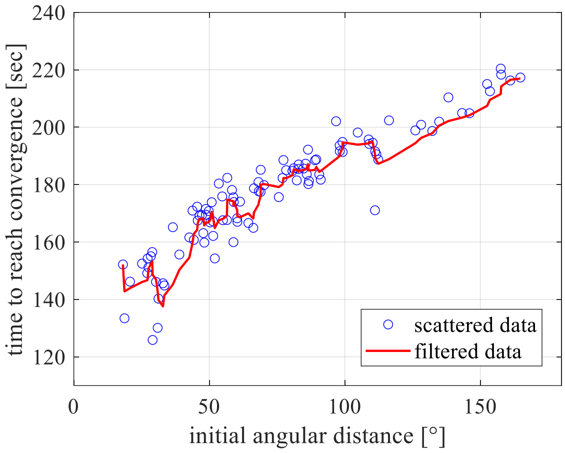

Figure 4.49: Correlation between initial angular displacement and convergence time

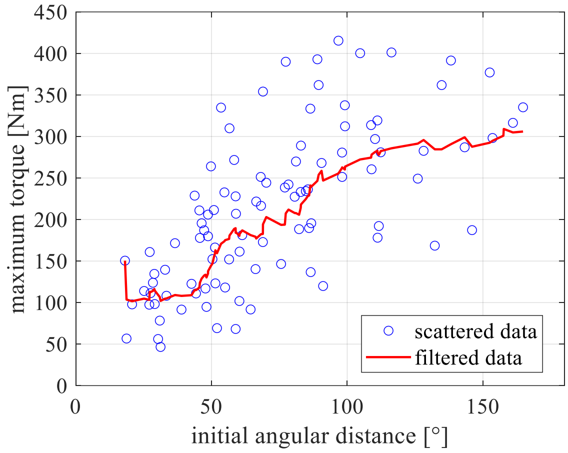

Figure 4.50: Correlation between initial angular displacement and maximum actuator torque

In the simulations, the burning time is the same for all cases. This means that the thrust oscillations do not alter the performance of the collision avoidance maneuver. This occurs also because the condition for switching off the main thruster is evaluated with sampling time interval of 5 sec, which is a relatively relaxed interval. If this interval reduces, the effect of thrust oscillations on the burning time increases. On the other hand, inspection of Figure 4.48 reveals that the distance of closest approach exceeds 100 m, but only of a few meters, thus there is no need to further reduce the sampling time interval. Anyway, the numerical results show that the collision avoidance maneuver is successfully completed, and safety requirements are met in short times, despite the low thrust level.

4.2.6. Concluding remarks

This study case addresses the problem of trajectory and attitude maneuvers of a spacecraft equipped with two flexible solar panels, in two distinct operational scenarios: (a) tracking of an approaching debris and (b) collision avoidance maneuvering. The dynamics of the flexible spacecraft is described using the formulation presented in the first two chapters. Efficient strategies are introduced to rotate the solar panels, for the purpose of maximizing their irradiation. Actuation for attitude control is modeled as well, by assuming the use of a pyramidal array of four single-gimbal control momentum gyroscopes. The control and actuation architecture at hand is tested in nonnominal flight conditions, through Monte Carlo numerical simulations, and allows performing safe and effective maneuvers in both mission scenarios, with limited elastic oscillations.

4.3. Spacecraft mounting a large rotating flexible antenna

The growing need for high-resolution Earth observation has led to the advancement of sophisticated satellite architectures featuring complex, deployable instruments. A particularly innovative configuration involves an Earth observation satellite equipped with a large, rotating antenna mounted on flexible booms. This design significantly enhances observational capabilities by widening the scanned area and improving temporal resolution. However, the inclusion of a spinning, flexible payload introduces intricate dynamic interactions, presenting significant challenges in modeling, simulation, and control system design [99]. The coupling of rigid and flexible components, particularly in deployable structures such as solar arrays and antennas, requires careful vibration analysis to ensure dynamic stability and control accuracy.

Notable examples of this class of satellites include NASA's Soil Moisture Active Passive (SMAP) mission, launched in 2015 [100], and the European Copernicus Imaging Microwave Radiometer (CIMR) mission, developed by the European Space Agency (ESA) and Thales Alenia Space [11]. The CIMR mission comprises two satellites, with a potential extension to a third, as part of the Copernicus Space Component program, a collaborative initiative between ESA and the European Commission. The mission aims to provide critical data for environmental monitoring, climate change assessment, and natural disaster evaluation, thereby contributing directly to societal well-being in Europe. Additionally, CIMR supports the European Union's Arctic Policy, which seeks to ensure a safe, sustainable, and prosperous Arctic environment [10].

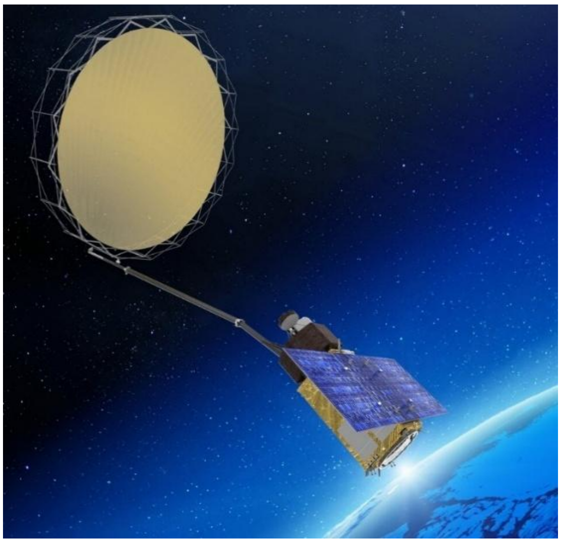

Figure 4.51: The CIMR satellite

The primary instrument of the CIMR mission is a microwave radiometer designed to measure sea-surface temperature (SST), sea-ice concentration (SIC), and sea-surface salinity (SSS). Operating in a near-polar, sun-synchronous orbit at an altitude of 817 km, the satellite is equipped with an 8-meter mesh reflector mounted on an 8-meter arm, spinning across five frequency bands (L/C/X/Ku/Ka). This configuration enables data collection over a 1900 km-wide ground swath, significantly enhancing temporal sampling. SST is measured at a 15 km resolution, while SIC and SSS are captured at a 5 km resolution, each with distinct temporal sampling rates [9].

The rotational motion of the payload is designed to optimize data acquisition efficiency by increasing the scanned area and reducing measurement time. However, this setup also complicates the spacecraft dynamic behavior, requiring an integrated approach to control-structure interaction [101]. The interplay between flexibility, rigid-body motion, and control system dynamics must be carefully addressed to prevent observation degradation [102]. The spinning antenna induces inertial loads and couples with the spacecraft overall attitude motion, leading to periodic and steady-state deformations that affect observation accuracy.

4.3.1. Vehicle description

The CIMR spacecraft is modeled as a multibody system comprising a rigid bus, a payload consisting of a rigid crate, a flexible large deployable reflector system (LDRS), and flexible solar arrays. The payload rotates around the spacecraft's vertical axis, as depicted in Figure 4.52. To accurately describe the spacecraft's mechanical behavior, two primary reference frames are introduced:

1. Spacecraft Mechanical Reference Frame (MRF):
    - Origin: Center of the satellite bottom panel.
    - z axis: Perpendicular to the bottom panel and aligned with the instrument rotation axis in its deployed configuration.
    - y axis: Orthogonal to the body-mounted solar panels.
    - x axis: Defined according to the Cartesian right-hand rule.
2. Instrument Spun Reference Frame (ISRF):
    - Origin: Intersection point of the rotating instrument interface plane with the rotation axis. The coordinates of the origin expressed in the MRF are $\begin{bmatrix} 0 & 0 & 2.84 \end{bmatrix}$m.

- z axis: Aligned with the instrument rotation axis
- x and y axes: Lie in the plane orthogonal to the z axis and follow the Cartesian right-hand rule.

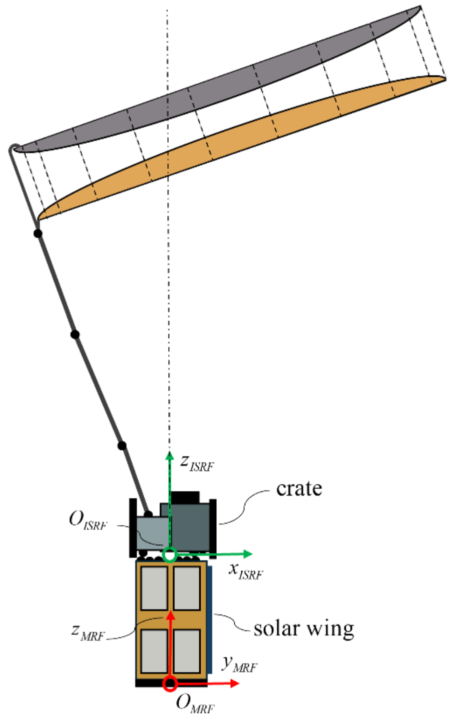

Figure 4.52: Schematics of CIMR spacecraft and body reference frames

The payload is connected to the spacecraft main platform at a hinge point corresponding to the origin of the ISRF. This frame is rigidly attached to the instrument rotating section and follows its motion around the z-axis. The specifications of the spacecraft components, including the bus, LDRS and solar arrays, are summarized in Tables 4.20-4.22.

Table 4.20: Bus specifications (Moment of Inertia are evaluated w.r.t. Mechanical Reference Frame)

Main Body (BUS)	
Mass (kg)	1089
I_{xx} (kg·m^2)	2448
I_{yy} (kg·m2)	2471
I_{zz} (kg·m2)	286

Table 4.21: LDRS specifications (Moment of Inertia are evaluated w.r.t. the ISRF)

LDRS		
Reflector	Radius (m)	7.74
Reflector	Height (m)	1.65
Reflector	Mass (kg)	104
Boom	Length (m)	8.37
Boom	Radius (cm)	9
	I_{xx} ($kg{\cdot}m^2$)	5893
	I_{yy} ($kg{\cdot}m^2$)	6242
	I_{zz} ($kg{\cdot}m^2$)	892

Table 4.22: Solar Wing: geometric and inertial data (Moment of Inertia are evaluated w.r.t. Mechanical Reference Frame)

Solar Wing	
Dimensions (m)	2.10 x 2.36 x 0.022
Mass (kg)	54
I_{xx} ($kg{\cdot}m^2$)	152
I_{yy} ($kg{\cdot}m^2$)	307
I_{zz} ($kg{\cdot}m^2$)	222

To achieve precise attitude stabilization and control, the spacecraft is equipped with two types of actuators:

- Momentum control wheel (MCW): Aligned with the instrument's rotation axis, the MCW compensates for reaction torques generated during spin-up and spin-down phases. It is positioned at $\begin{bmatrix}0 & 0 & 0.133\end{bmatrix}\mathrm{m}$ relative to the MRF.

- Pyramidal array of 4 reaction wheels (RWs): This array provides the necessary control torque for attitude reorientation and maintaining the desired nadir-pointing direction.

Tables 4.23- 4.24 provide details on the geometric and inertial properties of the MCW and reaction wheels.

The CIMR reflector comprises a deployable rim structure reinforced by two curved geodesic trusses (front and rear nets) constructed from rigid composite filaments. These trusses are stabilized by tension ties, with a reflective mesh stretched over the front net to

Table 4.23: MCW: geometric and inertial data (Moment of Inertia are evaluated w.r.t. the wheel center of mass)

MCW	
Mass (kg)	65
Axial inertia (kg·m^2)	8.23
Transversal inertia (kg·m^2)	4.33

Table 4.24: RWs: geometric and inertial data (Moment of Inertia are evaluated w.r.t. the wheel center of mass)

RW	
Mass (kg)	8
Axial inertia (kg·m^2)	$1.20 \cdot 10^{-1}$
Transversal inertia (kg·m^2)	$6.96 \cdot 10^{-2}$

enhance observational accuracy. While specific mechanical properties remain confidential and cannot be reported here, this study provides key insights into the first modal shapes and natural frequencies of the LDRS, as detailed in Table 4.25. In fact, in this study case flexibility is modeled using the eigenmodes strategy, where modal shapes and natural frequencies are provided by a modal analysis carried out through the commercial software MSC Nastran. The first three modal shapes exhibit pure bending and torsion behavior. However, beginning with the fourth mode, coupled motions and localized deformations become more pronounced. The cumulative modal mass of the first five modes represents 98% of the LDRS total mass, ensuring a comprehensive dynamic model that captures both rigid and flexible motion interactions.

Additionally, the spacecraft features a solar wing, which contributes to overall structural flexibility. The first four natural frequencies of the solar panels are summarized in Table 4.26. Notably, the first and third modes correspond to the right panel ($+x_{MRF}$), whereas the second and fourth modes correspond to the left panel ($-x_{MRF}$). Due to the asymmetric mounting configuration, the first and second modes of the right panel do not precisely match those of the left panel, introducing slight variations in structural response.

4.3.2. Multibody model validation

The dynamic equations are derived – according to the theory presented in the first two chapters – for the CIMR spacecraft, which is modeled as a system of seven bodies, organized as follows:

Table 4.25: Fundamental Frequencies and Modal Shapes of LDRS

Mode	Hz	Modal shape
1 (bending about X-axis)	0.601	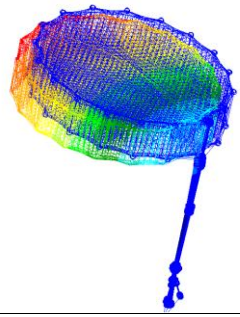
2 (bending about Y-axis)	0.634	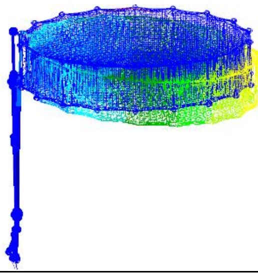
3 (torsion about X-axis)	1.091	
4 (bending/local)	1.672	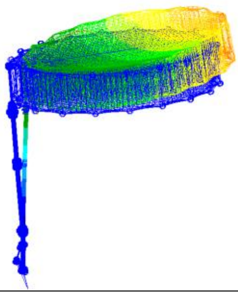
5 (torsion/local)	2.313	

Table 4.26: Solar Panels Natural Frequencies

Mode 1 - bending, $+x_{MRF}$ panel (Hz)	1.700
Mode 2 - bending, $-x_{MRF}$ panel (Hz)	1.761
Mode 3 - torsion, $+x_{MRF}$ panel (Hz)	3.973
Mode 4 - torsion, $-x_{MRF}$ panel (Hz)	4.030

- Body 1: rigid bus and flexible solar panels
- Body 2: rigid crate and flexible LDRS
- Body 3: momentum control wheel
- Bodies 4-7: reaction wheels

To simplify the model while maintaining accuracy, the rigid bus and solar panels, as well as the crate and LDRS, are treated as single entities. Their interconnection through locking joints justifies this approach, reducing computational complexity without introducing significant approximations.

In this section, the multibody dynamics model of the CIMR spacecraft is validated using the commercial software MSC Adams [103]. This validation is essential as it provides a benchmark comparison against a widely recognized simulation tool, reinforcing the credibility of the proposed dynamic model. MSC Adams is a well-established software known for its robust capability to simulate the behavior of complex mechanical systems, including flexible multibody spacecraft.

The inertial properties of the spacecraft are applied to both the Kane-developed model and the MSC Adams model. In this scenario, the solar panels are modeled as rigid, while the LDRS is treated as the sole flexible component. Flexibility is incorporated in both MSC Adams and the Kane-based model using modal analysis results obtained from MSC Nastran. In MSC Adams, all elasticity-related terms are retained in the simulation, whereas in the Kane-based model, two different conditions are considered:

1. The variation in the moment of inertia due to flexible deformation (that is the term reported in Eq. (2.63)) is neglected, ignoring also the terms associated with the modes cross-correlation, i.e. Eq. (2.62) and the term depending on the elastic coordinates in Eq. (2.73).
2. The variation in the moment of inertia is taken into account, while the cross-correlation is neglected also in this case.

The first case represents a commonly used simplification in dynamic modeling. Neglecting all the elasticity-related terms in Eq. (2.74) except for the modal participation factors to translation (2.58) and to rotation (2.60) significantly simplifies the computational process, as they can be directly obtained from MSC Nastran [104]. While this approximation introduces some level of error, it is generally acceptable depending on the specific analysis requirements. Its validity must be assessed on a case-by-case basis. On the other hand, accounting for the variation in the moment of inertia requires additional computational effort. This involves extracting the modal shapes corresponding to the selected elastic modes at all body nodes, performing numerical integration over the body volume, and computing mass distribution values for each element of the discretized structure. The importance of considering this term will be examined in the next section, where numerical results are presented. The cross-correlations terms are neglected also in this second case in order to distinguish the contribution solely provided by the variation of the inertia, but their computation does not introduce any further complexity with respect to what is required to obtain the elastic variation of the inertia matrix.

For validation purposes, a simplified scenario is considered. The spacecraft is assumed to be in deep space, free from external control and gravitational forces, allowing for an analysis of its unconstrained dynamic behavior. he simulation spans a predetermined time frame $\left(t \in \left[0s \quad 600s\right]\right)$ during which the spacecraft is initially at rest. The reaction wheels are allowed to rotate freely, while a torque is applied to both the payload and the momentum control wheel (MCW) following to a predefined time profile:

- Spin-up phase: From $t = 20s$ to $t = 250s$ a constant torque of 3.82 Nm is applied to the payload while an equal and opposite torque is applied to the MCW. By the end of this phase, the payload achieves a relative angular velocity of 46.8 °/s.
- Free dynamics phase: From $t = 250s$ to $t = 350s$ No external torque is applied, allowing the system to evolve naturally and reach a steady-state regime.
- Spin-down phase: From $t = 350s$ to $t = 580s$ a constant torque of -3.82 Nm is applied to the payload with an equal and opposite torque applied to the MCW.

The results of the validation scenario are analyzed by comparing the time histories of the spacecraft's angular velocity components from both the Kane-based model and MSC Adams. This comparison provides insight into the dynamic behavior of spacecraft, particularly the influence of both rigid and flexible dynamics.

Figure 4.53 compares the angular velocity components around the x and y axes – the ones with highest magnitude – between the Kane-based model (including inertia variation) and MSC Adams. The dynamics of the spin-up and spin-down maneuvers reveal the significant impact of elasticity on the spacecraft behavior. The results highlight two key interactions:

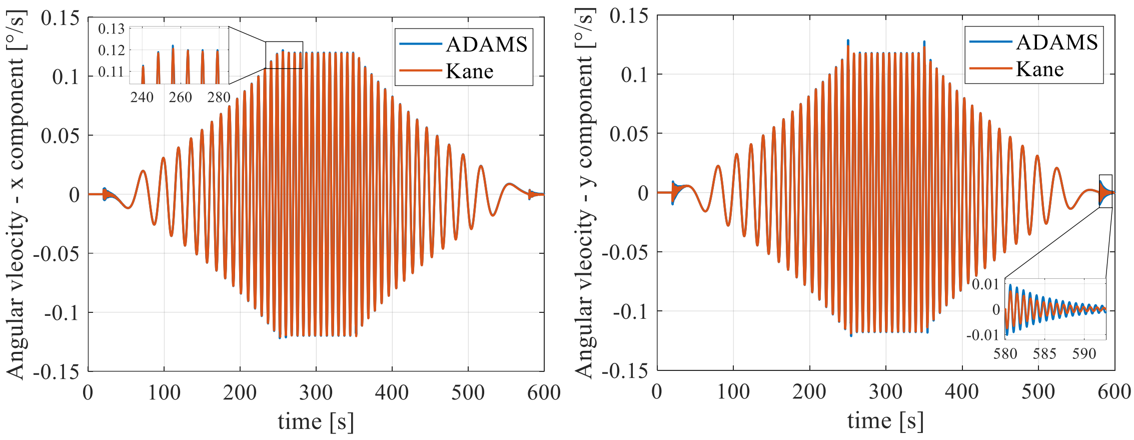

Figure 4.53: Comparison of the components of the angular velocity around x and y axis between Adams and the Kane-model code

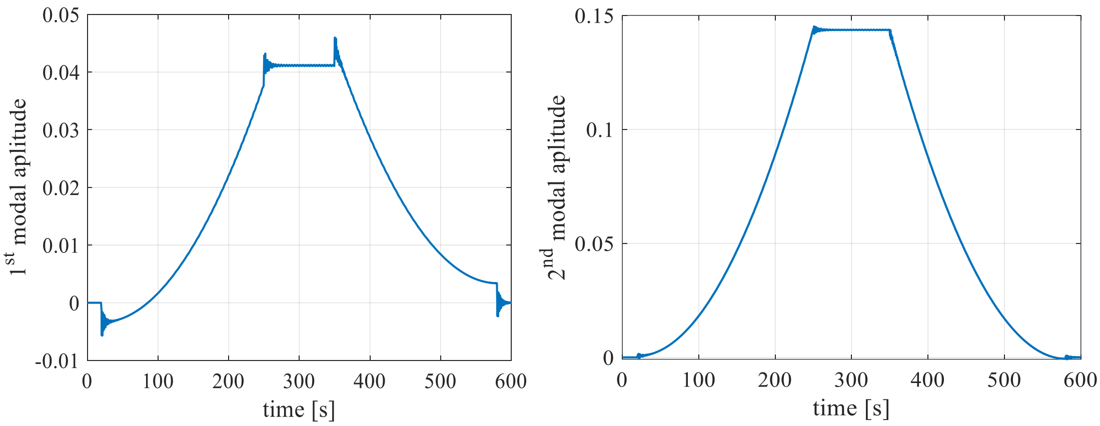

Figure 4.54: Time histories of the amplitudes of the first two modes of the LDRS

1. Nutation amplitude variation: The oscillations induced by static and dynamic imbalances of the rotating payload are significantly affected by centrifugal forces acting on the deformed structure.

2. Transient oscillations: Short-duration oscillations appear when torque is applied or removed but are gradually damped out over time.

These interactions are further demonstrated in Figure 4.54, which illustrates the time histories of the first two elastic mode amplitudes. The close agreement between the Kane-based model and MSC Adams confirms the validity of the proposed approach. Minor discrepancies are observed, which are likely attributable to differences in the number and nature of the modal integrals considered, as well as to some modeling aspects internal to

MSC Adams that are not fully transparent. Nevertheless, these differences do not significantly affect the overall consistency of the results.

To evaluate the effect of neglecting inertia variation, an additional simulation is conducted where the influence of flexibility on the moment of inertia is omitted. The time histories of the angular velocity are presented in Figure 4.55. A comparison between Figures 4.53 and 4.55 reveals significant differences in the nutation motion. Specifically, the x and y components of angular velocity exhibit oscillatory trends that are inaccurately captured when inertia variation is ignored, indicating that neglecting the variation of inertia leads to incorrect results. This confirms that for spacecraft with large rotating payloads, the influence of centrifugal force on the elastic deformation (cf. Eq. (2.71)) is critical in accurately modeling system dynamics. Relying solely on modal participation factors, as is commonly done in standard applications, proves insufficient

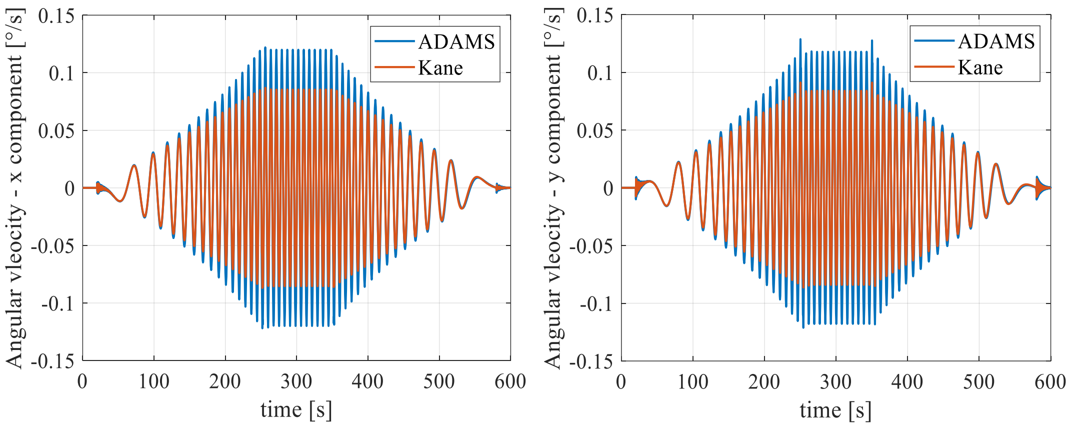

Figure 4.55: Comparison of the components of the angular velocity around x and y axes between Adams and the Kane-model code – elastic variation of inertia neglected

for precise dynamic simulations. The overall results demonstrate that incorporating inertia variation due to flexibility is essential for accurately capturing spacecraft dynamics. The Kane-based model successfully replicates the behavior observed in MSC Adams, verifying its suitability for analyzing multibody spacecraft with spinning flexible appendages.

As stated in the previous section, the terms related to the cross-correlation among the elastic modes are not included in the dynamical model to clearly isolate the effect of inertia variation due to elasticity in achieving consistent results. These terms could be introduced to perform a numerical simulation based on a more comprehensive dynamical model. However, the results of these simulations are nearly identical to the previously presented plots. As evidence of this, Figure 4.56 shows the angular velocity component along the x-axis for both cases – with and without the cross-correlation terms – demonstrating an almost perfect match. In fact, in this specific scenario, the cross-correlation terms do not significantly affect the system dynamics. Since payload rotation is the defining feature of this case, the key role is played by the variation of the inertia moments induced by the elastic deformation, which almost entirely captures the interaction between the centrifugal forces and payload elasticity.

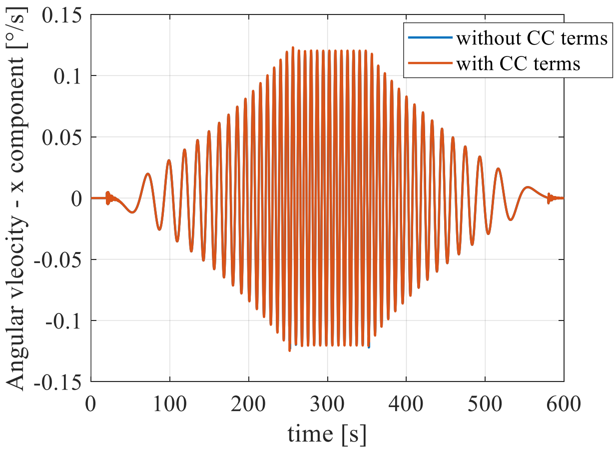

Figure 4.56: Comparison of the x-component of the angular velocity in the Kane-model code, with and without the cross-correlation terms

4.3.3. Deformation Analysis

Additional results from the Kane-based model, including the variation of inertia, further emphasize the elastic behavior of the spacecraft's structure. Figure 4.57 identifies key nodes of interest on the LDRS, while Figure 4.58 quantifies the elastic deformation by presenting the norm of the displacement differences between selected node pairs. This analysis provides a comprehensive assessment of the structural response during spin-up, spin-down, and operational phases.

In steady-state conditions, the maximum displacements are on the order of centimeters, characterizing the extent of LDRS deformation. Notably, significant deformations occur in:

- Tip bending displacement of the boom: Observed between node 10 and node 14, indicating notable structural flexibility in response to centrifugal forces.
- Ring deformation: Identified as the displacements of nodes 2, 4, 6 and 8 with respect to node 1, highlighting the structural response of the reflector to dynamic loading conditions.

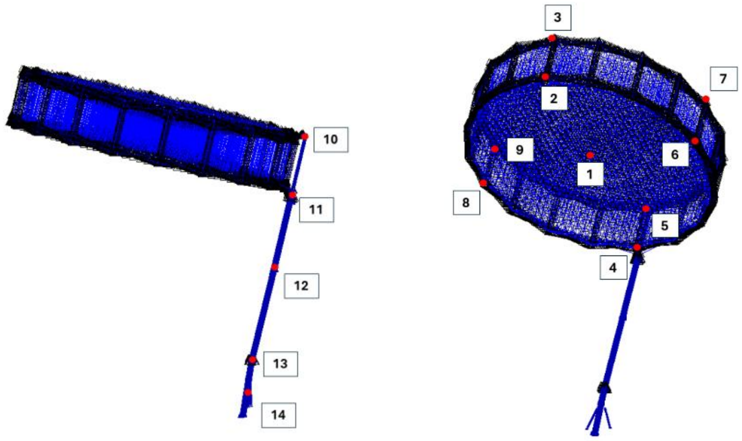

Figure 4.57: Position of the nodes of interests on the LDRS

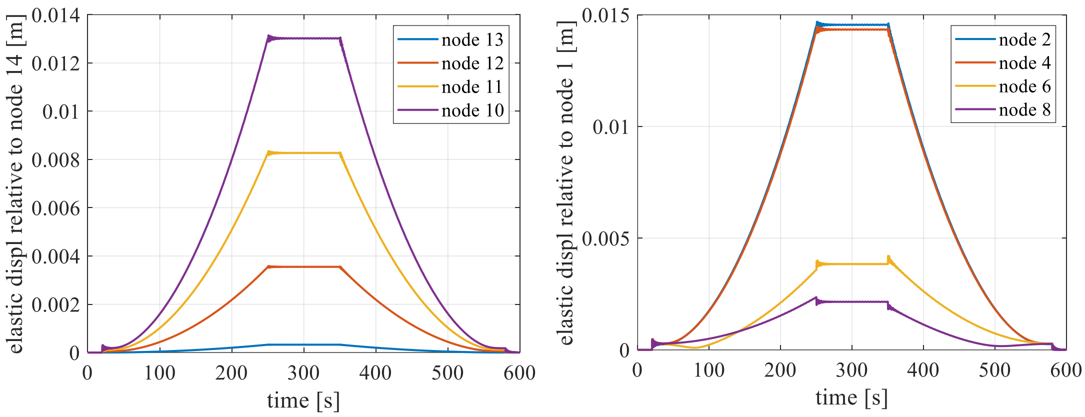

Figure 4.58: Elastic displacements between relevant pairs of nodes

These results underline the importance of considering structural elasticity in spacecraft dynamic simulations. By capturing these deformations, the Kane-based model provides valuable insights into how flexible appendages interact with overall spacecraft motion, reinforcing the need for comprehensive multibody modeling approaches in spacecraft design and analysis.

4.3.4. Preliminary analysis of the operational scenario

To establish a realistic framework, this analysis examines the impact of control-structure interaction on the elastic deformation of the LDRS during spacecraft reorientation and payload spin-up. The spacecraft is assumed to operate in a near-polar, sun-synchronous orbit at an altitude of 817 km. Following separation from the launch vehicle, the satellite typically undergoes a detumbling maneuver before deploying its payload. These initial phases, which are not simulated in this study, may leave the satellite in an attitude configuration different from the desired operational state. Consequently, before initiating the payload spin-up, the spacecraft must be reoriented to achieve the commanded nadir-pointing attitude. The simulated scenario is divided into two phases:

1. Attitude Reorientation: The deployed payload remains fixed to the bus while the spacecraft undergoes a reorientation maneuver to achieve the desired nadir-pointing attitude.

2. Payload Spin-Up: While maintaining nadir tracking, the payload spin-up is initiated and continues until operational conditions are met.

The desired attitude aligns the spacecraft $-z_{MRF}$ axis with the nadir direction, while the y_{MRF} axis (perpendicular to the solar panels) is oriented toward the Sun, assumed to be aligned with the orbital angular momentum vector. The attitude control is demanded to a pyramidal array of four reaction wheels opportunely steered according to the procedure described in Section 3.6.1, while the commanded torque is obtained using Eq. (3.22). The initial attitude conditions are defined in terms of angular velocity and quaternions:

$$\omega(t_0) = [1 \quad 1 \quad 1]^T * 10^{-3} \text{ rad/s} \tag{4.36}$$

$$\begin{cases} q_0(t_0) = 1 \\ \underline{q}(t_0) = [0 \quad 0 \quad 0]^T \end{cases} \tag{4.37}$$

At the beginning, all components of the spacecraft are at rest relative to the bus. A saturation logic is incorporated into the control system at two levels:

a) The commanded control torque is capped at 1 Nm.

b) Reaction wheel angular velocities are limited to 3000 rpm, which is the assumed maximum operational speed.

The reorientation maneuver (phase 1) is completed within 750 seconds. Following this, the spin-up phase begins and is concluded at time $t = 950\,\text{s}$, when the payload angular rate reaches the target value of 46.8°/s. The simulation continues beyond this point until $t = 1200\,\text{s}$ to observe steady-state behavior. The spin-up is carried out through a proportional control on the payload and MCW angular velocities, where the desired time histories of the angular velocities follow a cubic profile with horizontal tangent at the end points.

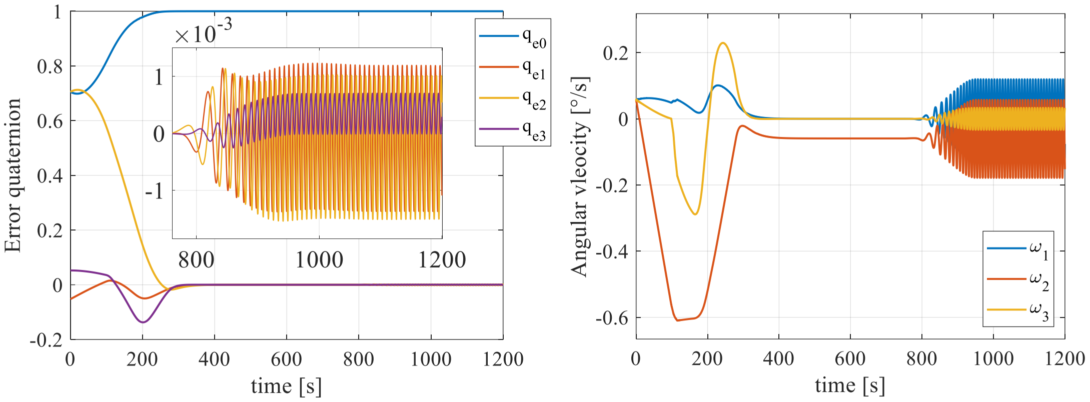

Figure 4.59: Error quaternion (left) and spacecraft angular velocity (right)

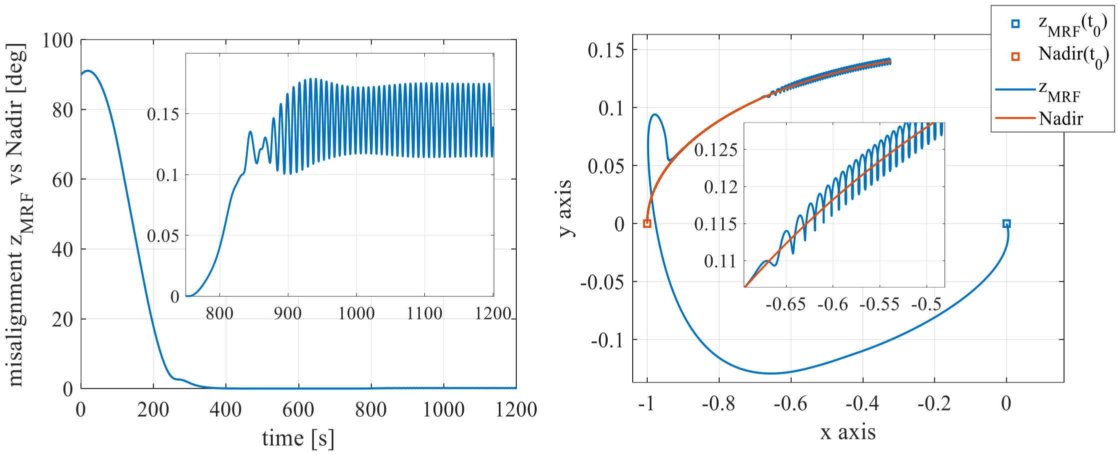

Figure 4.60: Pointing error evaluated as the misalignment between $-z_{MRF}$ and the Nadir direction (left) and projection on the plane xy belonging to the Earth Centered Inertial frame of the path described by the unit vectors associated with $-z_{MRF}$ and the Nadir direction (right)

The simulation results are presented in Figures 4.59-4.63. During the first phase, the spacecraft successfully completes the attitude reorientation, aligning the $-z_{MRF}$ axis with the nadir direction. However, the payload rotation introduces a disturbance, resulting in a nutation motion where the z_{MRF} axis traces a conical trajectory in the body frame. This nutation is not mitigated through active balancing or dedicated attitude control strategies, as the actual mission tolerates such behavior provided it remains below predefined thresholds. The results obtained confirm that the nutation stays well within these acceptable limits, thereby complying with mission requirements. Specifically, as shown in Figure 4.60, the nadir direction lies within this nutation cone but does not coincide with the cone axis, leading to oscillations visible in the zoomed views. Figure 4.61 further illustrates the performance of the attitude maneuver, depicting the control effort in terms of commanded torque and reaction wheel velocities. The trends align with expected behavior, including the effects of the implemented saturation logic. Figures 4.62-4.63 display the first three modal amplitudes of the LDRS and the first and

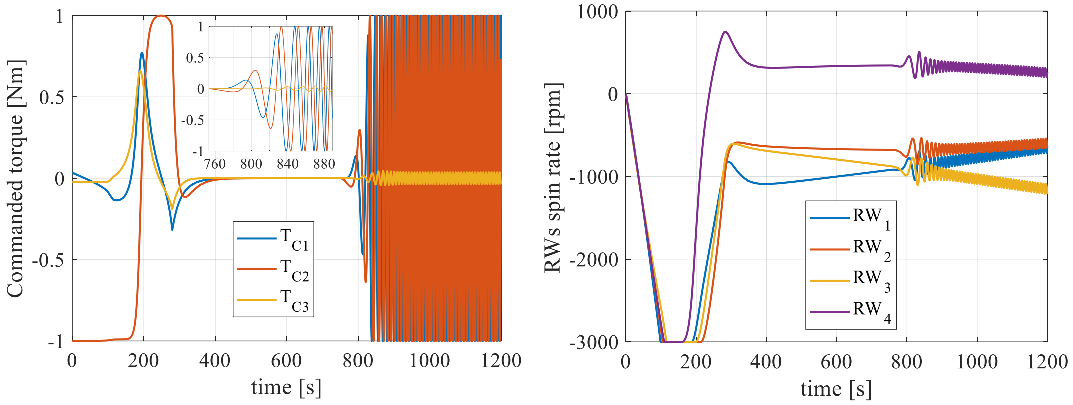

Figure 4.61: Actuator torque (left) and reaction wheels angular rates (right)

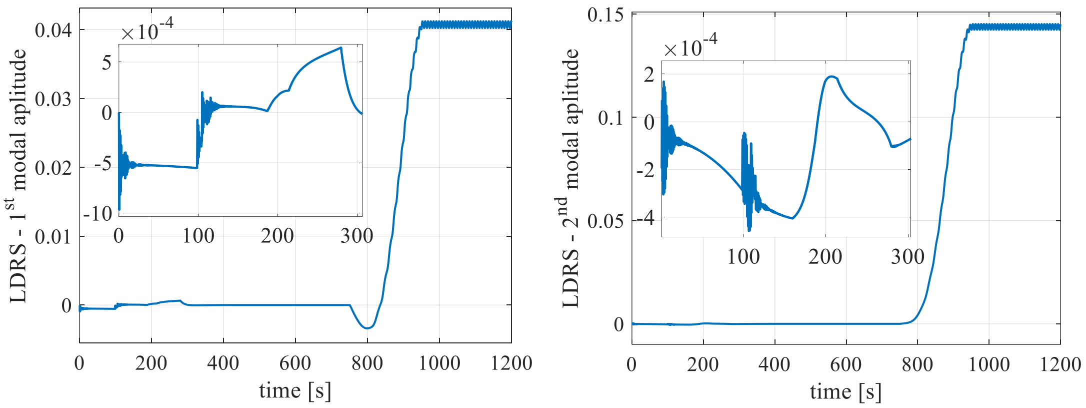

Figure 4.62: First and second modal amplitudes of the LDRS (left and right lots respectively)

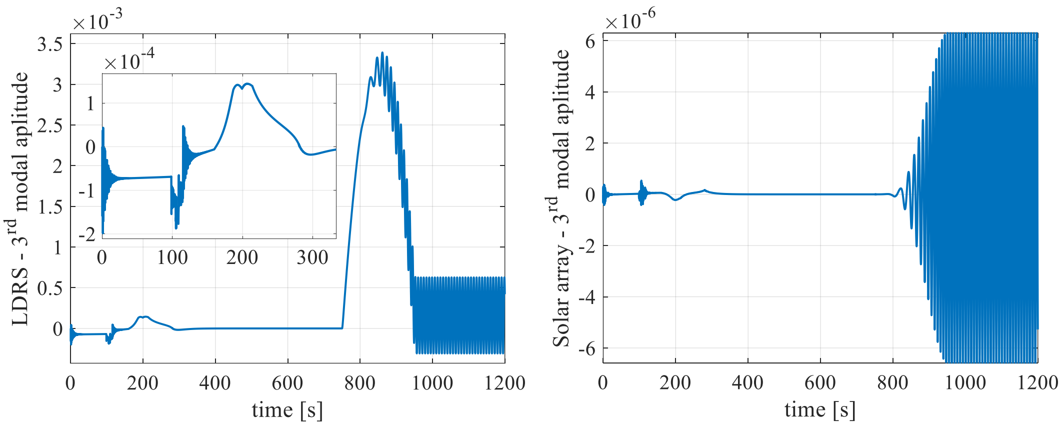

Figure 4.63: Third modal amplitude off the LDRS (left) and first modal amplitude of the right panel (left)

third modal amplitudes of the solar arrays, corresponding to the first two modes on the right-hand $\left(+x_{MRF}\right)$ panel. The results indicate that:

- Primary deformations occur during payload rotation, while the attitude maneuver induces comparatively smaller structural responses.
- The first two LDRS modes exhibit trends similar to the validation scenario. However, in steady-state conditions, oscillations persist due to continuous excitation from attitude control torques.
- Impulsive torque-switching oscillations are absent, as smoother gear torques prevent abrupt excitation. This behavior is evident by comparing the third modal amplitude trends of the LDRS in the validation and operational scenarios. The centrifugal forces do not significantly influence this mode, which is excited only by inertial torques resulting from angular acceleration. Consequently, the operational scenario shows a parabolic trend, due to the cubic profile of the desired angular velocity of the payload, in contrast to the oscillatory behavior seen in the validation case.
- Solar array modal amplitudes are influenced primarily by inertial effects due to nutation motion, as depicted in Figure 4.63.

4.3.5. Evaluation of stress stiffening effects

In this section, the effect of stress stiffening are evaluated for the CIMR satellite within the framework of linear elasticity (cf. Section 2.3.4). An equivalent analysis in MSC Adams would require the adoption of pre-stressed modal reduction, in which the flexible modes are computed on a structure subjected to centrifugal preload and subsequently imported into the multibody environment. While this strategy enables the inclusion of stress stiffening in a nominal operating point, it remains intrinsically limited, since the resulting modal basis is valid only for the specific preloaded state considered. Consequently, any variation in load levels or dynamic conditions – such as during the spin-up or spin-down of the CIMR antenna – would be consistently represented only if pre-stressed modes were computed over a wider range of configurations, which significantly increases the complexity of the method.

In this framework, an alternative model of the spacecraft is considered. In fact, as specified in Section 2.3.4, the evaluation of stress stiffening for a FEM-modeled structure requires a significant numerical effort in computing a series of numerical analysis with a FEM software [74, 105]. Then, a preliminary analysis is carried out on a simplified model of the spacecraft, where the flexible LDRS is replaced by an elastic beam and a rigid reflector. In fact, only the bending eigenmodes of the beam are considered in this analysis, where the reflector rigidly rotates with the beam (cf. Table 4.25). The reason of the high stiffness of the reflector lies in its peculiar design, in which tensioned cables are employed to guarantee that the reflector shape is maintained. This avoids compromising the device performance.

The specifications of the version of the CIMR spacecraft used in this analysis are reported in Tables 4.27-4.29, and the spacecraft is depicted in Figure 4.64. As shown in Figure 4.64, the flexible boom forms an angle α with respect to the plane parallel to the upper face of the bus. This angle is a design parameter, and is varied in this study, to investigate its effect on stress stiffening. The specifications for the rigid components, namely the bus and reflector, are reported in Tables 4.27 and 4.28, respectively. The principal moments of inertia are taken with respect to the centers of mass and are referred to the body frames depicted in Figure 4.64. Additionally, Table 4.29 provides information on the geometric, inertia, and elasticity properties of the flexible boom. It is worth noting that the elastic frequencies of the boom are computed by considering the overall inertia of the spacecraft. It is important to note that these data differ from those presented previously, as they refer to an earlier design of the spacecraft. Notably, the payload exhibits larger unbalances, and the elastic frequencies are lower in this configuration.

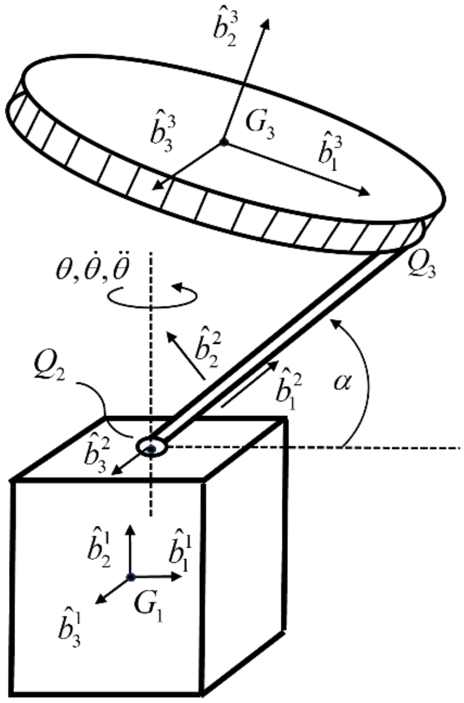

Figure 4.64: CIMR simplified configuration

Table 4.27: Bus specification

Main Body (BUS)	
Height (m)	2.5
Width (m)	1.5
Depth (m)	1.5
Mass (kg)	1695
J_1 (kg m^2)	3550
J_2 (kg m^2)	1150
J_3 (kg m^2)	3200

Table 4.28: Reflector specifications

Reflector	
Radius (m)	2.78
Height (m)	0.83
Mass (kg)	55
J_1 (kg m^2)	153
J_2 (kg m^2)	418
J_3 (kg m^2)	153

Table 4.29: Flexible boom: geometric and mechanical data

Boom	
Length (m)	5
Radius (cm)	5
Density (kg/m)	10
Young's modulus (GPa)	70
Second area moment (m^4)	4.675
First bending frequency (Hz)	0.3206
Second bending frequency (Hz)	0.3336
Third bending frequency (Hz)	2.7173
Forth bending frequency (Hz)	3.1953

Recalling the scenario of the previous section, additional simulations are conducted, focusing solely on the spin-up phase. The initial conditions correspond to the final state of the reorientation maneuver. At this stage, only the variation of the angular rate of the payload is considered by setting the final angular rate as $\dot{\theta}_f = k\dot{\theta}_{f,n}$ with $k = 1, 2, 3$ and $\dot{\theta}_{f,n} = 46.8° / s$ as in the previous section. Moreover, the angle α is maintained equal to its nominal value, i.e. 67.5°. The results are depicted in Figures 4.65-4.67. In all three cases the elastic displacements show the same qualitative behavior, both for the components along $\hat{b}_2^2$ and $\hat{b}_3^2$. The former shows an higher magnitude of displacement because of the specific spin-up profile that has been selected. In fact, the centrifugal force at steady state is significantly larger than the inertia torque due to angular acceleration. Nevertheless, the time histories exhibit a stiffening effect attributed to axial stretching strains that affect the flexible boom.

The strains arise from the combined action of two main non-inertial contributions: (i) the centrifugal force due to the spinning motion of the payload, and (ii) the non-inertial action (with the centrifugal force playing a major role also in this case) due to the attitude motion of the entire spacecraft, which is characterized by the previously discussed nutation motion. For the considered scenario, the second contribution plays a major role. In fact, (a) the value $\alpha = 67.5°$ implies that only a small component of the centrifugal force is directed along the longitudinal direction of the boom, so the main part of centrifugal force does not contribute to the axial strains. Moreover, (b) because α is the value that guarantees the static balance of the payload, the distance of the center of mass of the payload from the spin axis is small and only due to elastic displacement. This means that, for a statically balanced payload, the spinning motion has mainly an indirect relation with the stress stiffening phenomenon. In fact, dynamic imbalances are responsible for the nutation motion of the spacecraft, which determines the main part of the state of strains in the boom. It is worth noting that the attitude overall motion is also responsible for the nonzero mean value at steady state of the elastic displacement along $\hat{b}_3^2$.

Furthermore, the comparison of the results with different angular rate, especially the components along $\hat{b}_2^2$, shows that the relative effect of stress stiffening does not present significant variations with angular velocity. In fact, one can define the relative contribution of stress stiffening as

$$\delta_{ss} = \left| \frac{\max \left\| \underline{w}\left(Q_3^*\right)\big|_{cl} \right\| - \max \left\| \underline{w}\left(Q_3^*\right)\big|_{pl} \right\|}{\max \left\| \underline{w}\left(Q_3^*\right)\big|_{cl} \right\|} \right| \tag{4.38}$$

where $\underline{w}\left(Q_3^*\right)$ is the boom elastic displacement measured at the tip, while subscripts *cl* and *pl* stand for correct linearization (with stress stiffening) and premature linearization (without stress stiffening) respectively. Hence, it is possible to estimate the value of δ_{ss} for the three presented cases, which corresponds to 3.25%, 2.32% and 1.65% for $\dot{\theta}_f = k\dot{\theta}_{f,n}$ with $k = 1, 2, 3$. In fact, for cases with higher spin rate, the control system considered in this study case is unable to fully compensate for the large amplitude rotational motion. Then, instead of the internal strain, the nutation motion amplitudes increases.

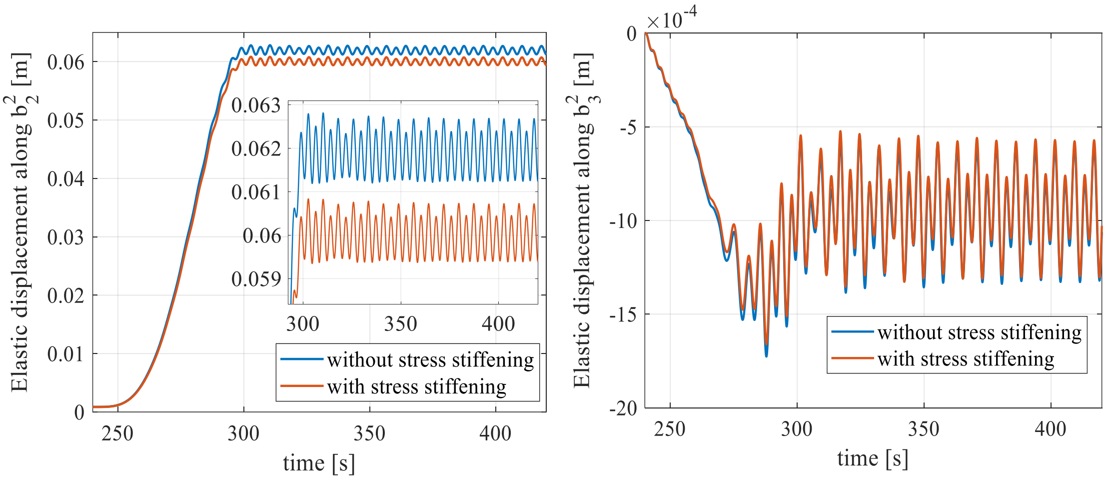

Figure 4.65: Elastic displacement along $\hat{b}_2^2$ (left) and $\hat{b}_3^2$ (right) and for $\alpha = 67.5°$ and $\dot{\theta}_f = 46.8°/s$ with and without stress stiffening

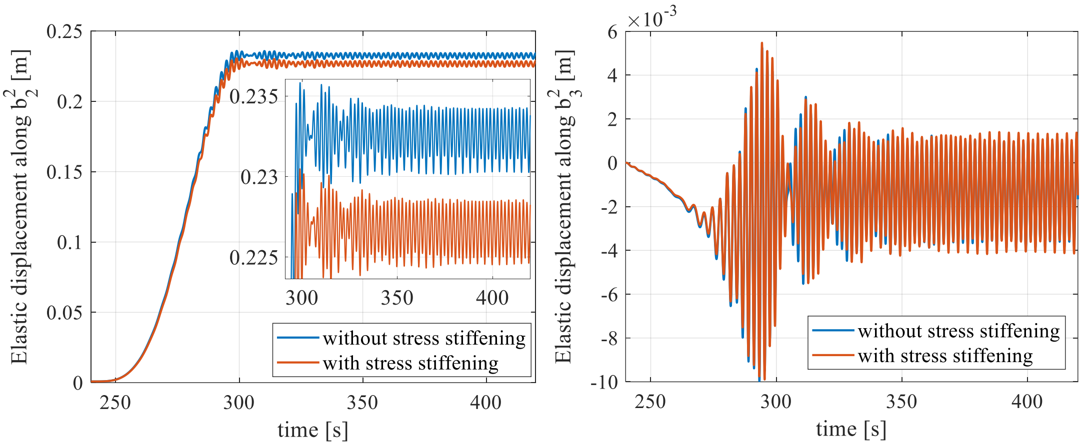

Figure 4.66: Elastic displacement along $\hat{b}_2^2$ (left) and $\hat{b}_3^2$ (right) and for $\alpha = 67.5°$ and $\dot{\theta}_f = 93.6°/s$ with and without stress stiffening

A more comprehensive analysis is conducted, by considering several combinations of the two design parameters, including the angle α. This involves conducting a series of simulations to assess the errors resulting from premature linearization. In this case, the spacecraft is assumed to be in the nadir-pointing operational configuration, i.e. the same scenario described in the previous section. The variations in the two design parameters fall within the following intervals

- α is varied in [0,90]°;
- $\dot{\theta}_f$ is varied in [46.8,140.4]°/s.

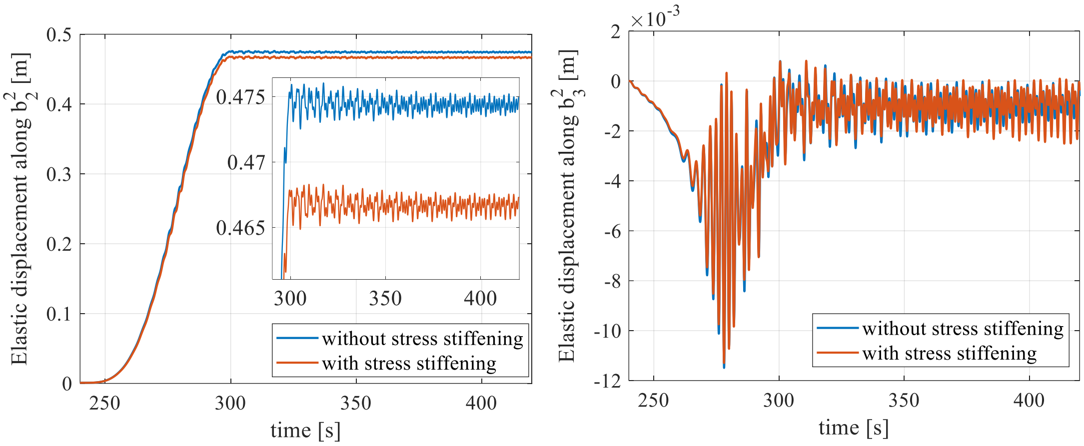

Figure 4.67: Elastic displacement along $\hat{b}_2^2$ (left) and $\hat{b}_3^2$ (right) and for $\alpha = 67.5°$ and $\dot{\theta}_f = 140.4°/s$ with and without stress stiffening

When the angular velocity of the rotating antenna is examined, establishing a connection of its absolute value with the first natural frequency of its supporting boom becomes meaningful. Hence, results report in the x-axis the ratio between $\dot{\theta}_f$ and the first frequency of the boom reported in Table 4.29. Figures 4.68-4.69 illustrate the maximum elastic displacement at the tip of the boom for each combination of design parameters, considering premature and correct linearization respectively. The white regions correspond to tip displacements greater than 10% of the boom length (evaluated for the premature linearization case), which is assumed as the upper bound for the linear approximation to be sufficiently accurate. It is worth noting that Figures 4.68-4.69 only show the absolute value of the maximum elastic displacements in order to easily evaluate which combinations of the design parameters lead to higher displacements. From inspection of both figures, it appears that

1. the absolute value of elastic displacements grows with the final angular velocity of the payload. In fact, as observed in the previous section, an increasing angular velocity implies a larger centrifugal action because of the relative rotation itself and the wider-amplitude attitude motion;

2. the relationship between the elastic displacement and the angle α is more complex than the previous one. In fact, maximum elastic displacements are observed in two regions, for α between 15° and 40° and larger than 70°. The latter case is easier to be explained: angles close to 90° imply that the centrifugal action is almost completely directed orthogonally to the boom longitudinal axis, mainly affecting the bending displacements. On the other hand, the angles in the first region are those that maximize the combined effect of payload unbalances (that lead to the larger nutation motion) and the orthogonal component of the centrifugal force. Instead, angles close to 0° are characterized by very low values of the orthogonal

component of the centrifugal action, while angles between 40° and 70° reduce the previously discussed coupling effect. In this context, it is worth noting that the value of α characterized by the lowest elastic displacements is far beyond the static balance value of 67.5° (it is close to 56°). Hence, a better balancing condition at the rotating steady state, where elastic displacement occur, can be reached if the rotating antenna is designed to have a suitable initial unbalance in the rigid configuration.

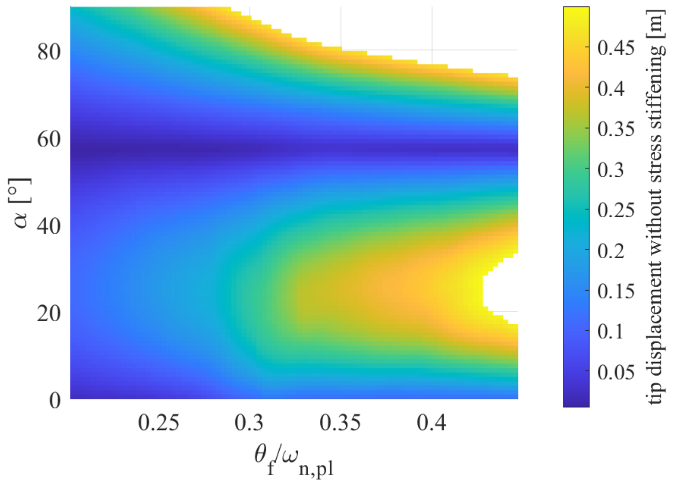

Figure 4.68: Maximum tip displacement (absolute values) – premature linearization

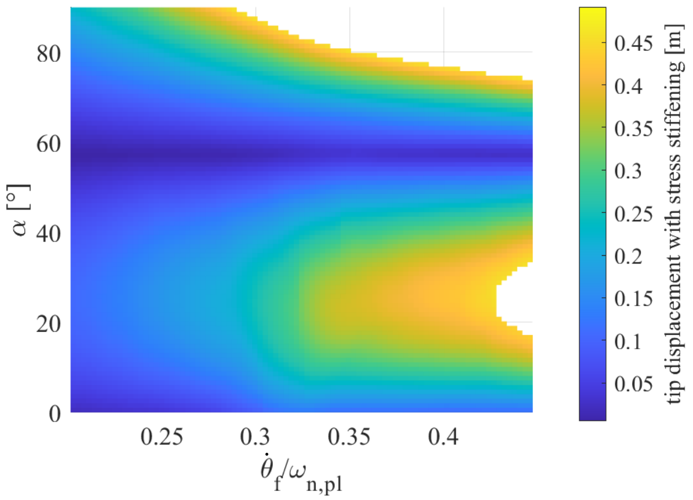

Figure 4.69: Maximum tip displacement (absolute values) – correct linearization

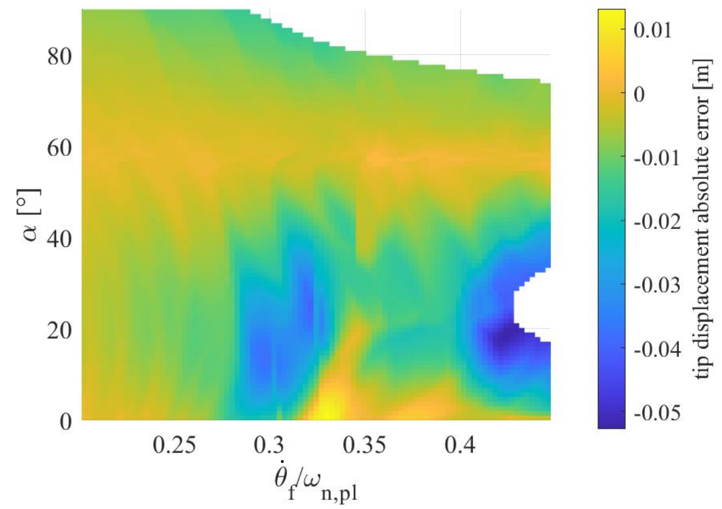

Figure 4.70: Error in maximum tip displacements – correct vs premature linearization

Figure 4.70 depicts the effect of neglecting the stress stiffening phenomenon in the model, i.e. the difference between the maximum tip displacements computed with and without considering the stress stiffening. Unlike the previous two plots, in this figure also the sign is reported, to assess if either a stiffening or a softening effect occurs. Specifically, negative values correspond to stiffening, while positive values represent softening. In fact, while the stretch of the boom implies a stiffening of the structure, the opposite condition of a state of compression strains leads to softening of the bending stiffness, as observed in the analysis of the buckling phenomenon. From inspection of Figure 4.70 it is evident that higher stiffening occurs generally for lower values of α. In fact, in these cases the component of the centrifugal force is almost completely directed along the longitudinal axis, thus stretching the boom. This effect is enhanced by the angular rate, and larger stiffening is just observed in the previously discussed region, where the centrifugal force is maximized. In fact, the region with values of α between 15° and 40° not only maximize the orthogonal component of the centrifugal force, but also its magnitude. Hence, both larger elastic displacement and larger stiffening effects are observed in this region. However, for these values of α, the displacement does not increase monotonically with $\dot{\theta}_f$. This is due to the overall dynamics, which includes attitude motion and elastic displacements and the related nonlinear coupling effects. In the rest of the domain, stress stiffening shows a lower effect, which however, is nonnegligible for the purpose of precise modeling of the antenna performance.

4.3.6. Concluding remarks

In this study case, a comprehensive dynamic model for an Earth observation satellite equipped with a large, spinning flexible antenna is developed, addressing the complex interactions between the spacecraft's rigid motion, flexible components, and control system. By validating the model through simulations with MSC Adams, the coupled rigid-flexible dynamics is analyzed, demonstrating the significant influence of structural flexibility on the spacecraft motion. The findings emphasize the necessity of considering variations in the moment of inertia due to flexibility, particularly for spacecraft with spinning flexible components. Neglecting these variations can introduce substantial errors in predicting spacecraft behavior, leading to inaccurate assessments of attitude dynamics and control effectiveness. A further analysis of the spacecraft operational scenario, where the satellite is first reoriented and then kept in the nadir-pointing configuration while the antenna rotates, shows that attitude maneuvers with a fixed payload have a secondary influence compared to the nutation motion induced by antenna rotation. The findings reveal that periodic antenna oscillations in steady-state conditions are amplified by the control action, underscoring the importance of accounting for the control law effects when performing pointing budget analysis.

Finally, a simplified model of the CIMR spacecraft is used to evaluate the impact of stress stiffening resulting from non-inertial actions, in relation to the angular velocity of the payload and its misalignment with the axis of rotation. With this regard, several numerical results in the operational nadir-pointing scenario are presented. First, specific subcases are computed considering the spacecraft in its nominal design and varying only the payload angular velocities. From these results, relevant parameters of the mission are observed, and the coupling between the attitude motion of the satellite (strongly affected by the control system) and the relative effect of stress stiffening has been outlined. Finally, an analysis in terms of the two design parameters, i.e. payload angular velocity and inclination, is conducted to extend and generalize the discussion. The elastic behavior of the structure is investigated both in terms of absolute displacements and relative contribution of stress stiffening. The existence of an inclination angle that minimizes the unbalances at steady state but different from the one that guarantees the static balanced rest was observed. Configurations that are close to this angle allow neglecting the stress stiffening effect in the dynamical modeling. In the other cases, an accurate modeling necessarily requires the inclusion of this effect if the spacecraft dynamics and especially the antenna deformation must be evaluated with high levels of accuracy.

4.4. Deployment of a Tubular Telescopic Mast structure

In this study case, the dynamics of a spacecraft equipped with a Telescopic Tubular Mast (TTM) [106, 107], a one-dimensional deployable structure composed of nested flexible tubes, is investigated. The deployment of such a structure introduces a rich set of dynamics due to the interplay between the spacecraft rigid-body motion and the elastic deformations of the extending boom. The complexity of this system is further increased by its inherently time-varying geometry, which affects both the mass distribution and structural properties throughout the deployment process. To accurately capture these effects, a possibility consists of representing the TTM as a series of interconnected flexible elements. Each tube segment is modeled as an independent elastic body with fixed geometry, discretized using a finite element method (FEM) formulation to account for the distributed structural flexibility. In fact, differently from the previous study cases, in this application flexibility is modeled directly using FEM interpolation functions as modal shapes.

To validate and benchmark the consistency and computational efficiency of the Kane-based FEM model, results are compared with the ones obtained using an alternative formulation based on the Hybrid Coordinate (HC) method. The HC approach treats the deployable mast as a single flexible continuum with time-dependent parameters, such as length and cross-sectional properties, which evolve during deployment. By deriving the system energy expressions in hybrid coordinates, this method enables a compact yet flexible description of the system elastic and rigid-body dynamics. The theory behind this approach is not reported in the following because it does not represent a contribution of the author's work and deserves a detailed discussion, but further insight about this topic is provided in Ref. [108].

4.4.1. Vehicle description

The spacecraft system analyzed in this work consists of a rigid cubic central hub, two rigid containers, and two deployable TTMs, as shown in Figure 4.71. This TTM concept, initially developed in 2005, was built, tested, and later expanded for broader applications in large spacecraft. It consists of N_z ($N_z = 17$, excluding the rigid container) flexible tube sections of varying radii housed within a rigid container. Initially, all tubes are nested inside the container and deploy sequentially, starting with the thinnest section. Upon full deployment, the boom extends to 51 m in length, with its radius $r_{out}(x)$ decreasing from 31.8 cm at the base to 11.4 cm at the tip. The length of each tube l_p is 3 m. The first section has a thickness $h(x)$ of 0.51 mm, while the final (17-th) section is 1.02 mm thick. Other properties remain consistent with those in reference and are not repeated here. The velocity of the deploying motion maintains a constant value v_0 for each tube's motion. Additionally, there is a time interval ts between the movement of successive tube sections to reduce the flexible vibrations induced by the locking behavior. After this interval, the next section replicates the same motion as the previous one.

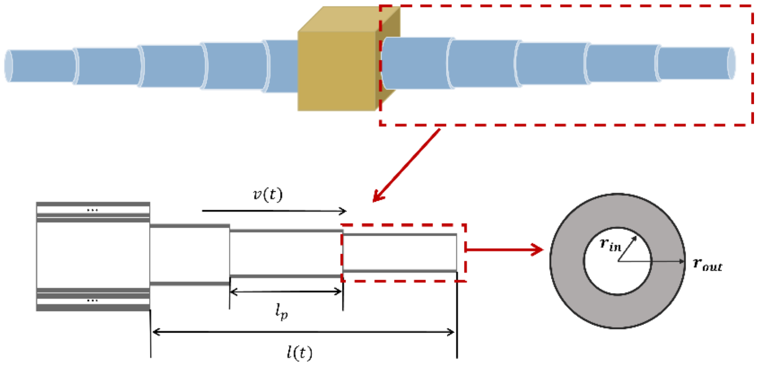

Figure 4.71: Sketch of spacecraft system with two deployable TTMs

4.4.2. Kinematic and dynamic relevant quantities

The development of significative kinematics and dynamic entities already presented in Section 2.3.1 is now reported. Before starting the discussion, it is necessary to specify that this study case involves a 2D (planar) scenario. The kinematics of an arbitrary point mass P of the system is described as:

$$\underline{r}_P = \underline{r}_O + \underset{N \leftarrow B}{R}\,\underline{d} \tag{4.39}$$

where $\underline{r}_P$ denotes the position of the point P in an inertial frame (Earth-centered), whose position in the body-fixed frame is $\underline{d}$. The body-fixed frame is centered at the spacecraft's center of mass (CM), with its axes aligned with the principal axes of inertia. In this analysis, no distinction is made between the deformed and undeformed configurations of the body. The spacecraft position in the inertial frame is further defined by the position $\underline{r}_O$ of its CM (which is assumed to remain fixed relatively to the body). Additionally, the rotation matrix $\underset{N \leftarrow B}{R}$, describing the passage from body axes to inertial axes, can be expressed as:

$$\underset{N \leftarrow B}{R} = \begin{bmatrix} \cos\gamma & -\sin\gamma \\ \sin\gamma & \cos\gamma \end{bmatrix} \tag{4.40}$$

where γ is the angle of the spacecraft system with respect to the inertial reference frame

For this study, the spacecraft is considered in a circular orbit. The coordinate systems and variable descriptions are illustrated in Figure 4.72. The rotation matrix from central body fixed coordinate system $O_b - x_b y_b$ to the inertial system $O - XY$ is $\underset{N \leftarrow B}{R}$, as in Eq. (4.40), where $\gamma = \alpha + \theta$, α is the attitude angle and θ is the true anomaly.

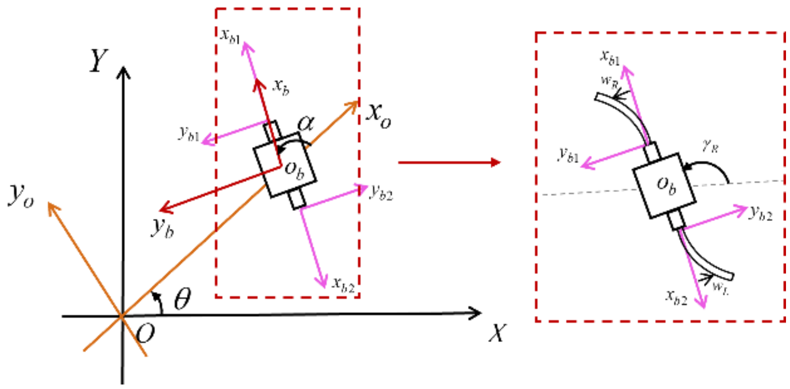

Figure 4.72: Coordinate systems and variable descriptions of the spacecraft system

For the rigid hub of the spacecraft, the position vector $\underline{d}$ used in Eq. (4.40) corresponds to the position vector of the rigid part in its body-fixed coordinate system $O_b - x_b y_b$. This can be expressed as $\underline{d}_h$:

$$\underline{d}_h = \begin{bmatrix} x & 0 \end{bmatrix}^T \tag{1.41}$$

By taking the derivative of Eq. (1.41), the velocity vector of point on the rigid hub is obtained as:

$$\dot{\underline{r}}_{Ph} = \dot{\underline{r}}_o + \dot{\gamma}\, \tilde{I} \underset{N \leftarrow B}{R}\, \underline{d}_h \tag{4.42}$$

where matrix

$$\tilde{I} = \begin{bmatrix} 0 & -1 \\ 1 & 0 \end{bmatrix} \quad \Rightarrow \quad \tilde{I}^T \tilde{I} = -I_{2\times2} \tag{4.43}$$

is employed to compute the cross product between a vector in the 2D plane and the angular velocity, which is orthogonal to that plane. The rigid containers are symmetrically positioned on both sides of the central bus, leading to different rotational angles for each side. The rotational angle for the left side is $\gamma_L = \gamma + \pi$, while for the right side, it is $\gamma_R = \gamma$. Therefore, the velocity of the containers can be expressed as:

$$\dot{\underline{r}}_{Pc} = \dot{\underline{r}}_o + \dot{\gamma}_{L/R}\, \tilde{I} \underset{N \leftarrow B_{L/R}}{R}\, \underline{d}_c \tag{4.44}$$

where $\underline{d}_c = \begin{bmatrix} x + a & 0 \end{bmatrix}^T$, being $2a$ the length of the hub. Here the subscript L/R denotes Left and Right elements relative to the spacecraft body-fixed reference frame. For the deployable TTMs, the position vector for the left and right side of the spacecraft is given by:

$$\underline{d}_b = [x + a + l_p, w_{L/R}]^T \tag{4.45}$$

where l_p is the length of each tube, and w is the elastic displacement evaluated at the axial coordinate x.

In the context of multibody formulation, it is necessary to introduce the i-th tube frames $(O_i - x_i y_i)$, as depicted in Figure 4.73 for the simplified case of a 3-tube TTM.

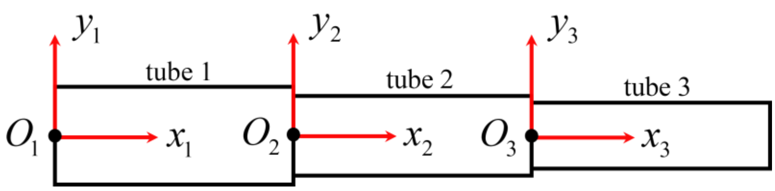

Figure 4.73: Tube reference frames for a 3-tubes TTM

The origin of the *i*-th tube frame is positioned at the center of the "root" face (the left one for the right TTM and vice versa) of the i-th tube. At this location, where the *i*-th tube is connected to the $(i-1)$-th tube by a prismatic joint, the relative motion during deployment occurs.

During the deployment, point O_i moves along the $(i-1)$-th tube from its left end to the right end (for the right TTM). In the rigid case, all the tube frames are aligned with the body frame $(O_b - x_b y_b)$. The only relative rotations between the tubes result from the elastic motion of the TTM, as the axes x_i are assumed to be tangent to the tube axes at points O_i.

To model the flexural behavior of the structure within the standard multibody approach, each tube of the TTM is considered as an independent body, specifically modeled as an equivalent Euler-Bernoulli beam. The modal basis is provided by the cubic interpolating functions associated with the finite element analysis (FEA). Each tube can be considered as a single 1D beam element or can be subdivided into two or more elements for a finer mesh, yielding more accurate results. In this context, the elastic displacement of the r-th beam element is evaluated as the "absolute" difference between its deformed and undeformed configurations, as depicted in Figure 4.74.

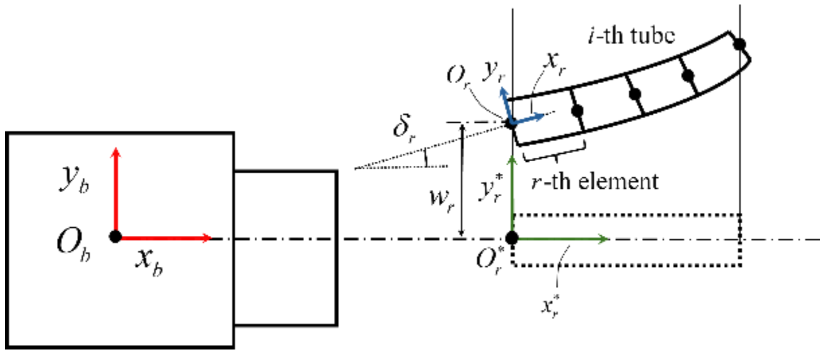

Figure 4.74: Absolute elastic displacement and rotation

In fact, two different frames are associated with the beam element: (i) $\left(O_r - x_r y_r\right)$ the deformed element frame, defined similarly to the tube frame in the previous case, and (ii) $\left(O_r^* - x_r^* y_r^*\right)$ the undeformed element frame, which is used to compute the elastic displacement of the element.

The elastic displacement of the r-th beam element is then expressed as follows:

$$w_r = \sum_{s=1}^{4} \psi_{r,s}\left(x_r^*\right) z_{r,s}\left(t\right) = \underline{\psi}_r^T \underline{z}_r \tag{4.46}$$

where $\psi_{r,s}\left(x_r^*\right)$ represents the s-th cubic interpolation function associated with the r-th beam element, while $z_{r,s}\left(t\right)$ is the *s*-th variable defining the elastic configuration of the *r*-th element, i.e.

$$\begin{cases} \psi_{r,1} = 1 - \dfrac{3x_r^{*2}}{l_d^2} + \dfrac{3x_r^{*3}}{l_d^3} \\ \psi_{r,2} = x_r^* - \dfrac{2x_r^{*2}}{l_d} + \dfrac{x_r^{*3}}{l_d^2} \\ \psi_{r,3} = \dfrac{3x_r^{*2}}{l_d^2} - \dfrac{2x_r^{*3}}{l_d^3} \\ \psi_{r,4} = -\dfrac{x_r^{*2}}{l_d} + \dfrac{x_r^{*3}}{l_d^3} \end{cases} \tag{4.47}$$

Scalars $z_{r,1}$ and $z_{r,3}$ are the absolute elastic displacement of the left and right ends of the element respectively, while $z_{r,2}$ and $z_{r,4}$ are the absolute rotation of the two ends. The choice of an absolute modal coordinates formulation to represent the flexibility in the multibody approach has been driven by the high number of interconnections between flexible bodies, which require accurate fulfillment of the boundary conditions at the interfaces. Specifically, in the current case, the boundary conditions at the connection between two consecutive booms are satisfied by imposing the following condition:

$$\begin{cases} z_{r,1} = z_{r-1,3} \\ z_{r,2} = z_{r-1,4} \end{cases} \tag{4.48}$$

Due to this compatibility conditions all the variables $z_{r,s}$ can be reorganized in a new vector $\underline{z}$ that eliminates redundancies, such that

$$w_r = \underline{\psi}_r^T \, \underline{z}\big|_{2(r-1)+s}, \quad s = 1,2,3,4 \tag{4.49}$$

with

$$\underline{z} = \begin{bmatrix} z_{1,1} & z_{1,2} & z_{1,3} & z_{1,4} & z_{2,3} & z_{2,4} & \cdots & z_{n_e,3} & z_{n_e,4} \end{bmatrix}^T \tag{4.50}$$

where $\underline{z}$ is a vector of dimension $2n_e + 2$ (with n_e number of beam elements). It is worth noting that, to enforce the locking of the TTM to the main platform, the first two components of vector $\underline{z}$ must be set to zero at each time (or, alternatively, removed from $\underline{z}$).

In this study case, each tube is modeled using one or more beam elements, depending on the required computational accuracy. For simplicity, it is assumed that all tubes consist of the same number of elements, n_e, though this approach can be easily extended to cases where different tubes have varying element counts. Consequently, Eqs. (4.46)-(4.49) remain valid, with $r = 1, \cdots, N_z \times n_e$ ($N_z = 17$, number of tubes). Within this framework, the vector of the tube shape functions $\overline{\underline{\psi}}_i\left(x_i^*\right)$ associated with the undeformed i-th tube frame is defined as:

$$\overline{\underline{\psi}}_i\left(x_i^*\right) = \begin{cases} \underline{\psi}_{i,1}\left(x_i^*\right), \ x_i^* \in \left[0 \quad l_d\right] \\ \underline{\psi}_{i,2}\left(x_i^* - l_d\right), x_i^* \in \left(l_d \quad 2l_d\right] \\ \underline{\psi}_{i,3}\left(x_i^* - 2l_d\right), x_i^* \in \left(2l_d \quad 3l_d\right] \\ \vdots \\ \underline{\psi}_{i,n_e}\left(x_i^* - \left(n_e - 1\right)l_d\right), x_i^* \in \left(\left(n_e - 1\right)l_d \quad n_e l_d\right] \end{cases} \tag{4.51}$$

where subscripts $1,2,\ldots,n_e$ refer to the element, while subscript i has been added to associate the element modal shapes to the tube to which the element belongs. The tube modal shapes are defined relatively to the undeformed tube frame $\left(O_i^* - x_i^* y_i^*\right)$, which is aligned with the main body frame $\left(O_b - x_b y_b\right)$.

The system dynamics equations are obtained following the procedure described in Sections 2.2.2 and 2.3.1. In this framework, it is important to remark that:

- As the left end of the first tube is clamped to the container, it is necessary to exclude the first two components of $\underline{z}$ and its time derivative from the degrees of freedom of the system, because $z_{1,1} = z_{1,2} = 0 \ \ \forall t$.
- Since the elastic displacements are evaluated with respect to the undeformed configuration of the overall appendage and not of the single element (cf. Figure 4.74), terms associated with elasticity do not appear in the partial velocities matrices and remainder acceleration vectors. Consequently, in the context of this modeling choice, flexibility is limited to the terms containing the modal integrals.
- Because of the discretization of the single tube into a certain number of elements, the expression of modal integrals associated with the i-th tube are obtained as a summation of element modal integrals. To clarify this concept, the expression of modal participation factors to translation and rotation are reported:

$$\underline{\bar{b}}_{i,k} = \int_0^{l_p} \underline{\bar{\psi}}_{i,k}\left(x_i^*\right) dm_i = \sum_{j=1}^{n_e} \int_0^{l_e} \underline{\psi}_{i,j,k}\left(x_j^*\right) dm_j = \sum_{j=1}^{n_e} \underline{b}_{i,j,k} \tag{4.52}$$

$$\begin{aligned} \bar{c}_{i,k} &= \int_0^{l_p} x_i \bar{\psi}_{i,k}\left(x_i^*\right) dm_i = \sum_{j=1}^{n_e} \int_0^{l_e} \left[x_j^* + (j-1) l_e\right] \psi_{i,j,k}\left(x_j^*\right) dm_j \\ &= \sum_{j=1}^{n_e} \left[\int_0^{l_e} x_j \psi_{i,j,k}\left(x_j^*\right) dm_j + (j-1) l_e \int_0^{l_e} \psi_{i,j,k}\left(x_j^*\right) dm_j\right] \\ &= \sum_{j=1}^{n_e} \left[c_{i,j,k} + (j-1) l_e b_{i,j,k}\right] \end{aligned} \tag{4.53}$$

  where index i refers to the tube, j to the element, k to the elastic degree of freedom. Moreover, l_e is the length of a single element. It is worth noting that the modal participation factor to rotation and terms contained in the related equations are scalars, because of the planar nature of the scenario and the consequent scalar equation associated with rotational motion. In this framework, $\psi_{i,j,k} = \left|\underline{\psi}_{i,j,k}\right|$ and $b_{i,j,k} = \left|\underline{b}_{i,j,k}\right|$.

4.4.3. Numerical results and comparison with HC model

This section presents the simulation results obtained from different modeling methods. The deployment velocities is set to 0.1 m/s, while the locking and restarting time is equal to $ts = 0.05\,s$. Moreover, the orbital radius is assumed as $r_0 = 6700\,km$. Under these conditions, the variations in the satellite's attitude angle and angular velocity during the deployment process are illustrated in Figure 4.75. The satellite begins in a gravitationally stabilized state, maintaining an Earth-pointing orientation, with the TTMs completely stowed. Consequently, any observed deviation from the Nadir-pointing configuration (corresponding to $\alpha = 0°$) is solely attributed to the unfolding process. The simulation results obtained using the two modeling methods demonstrate a high degree of consistency.

The flexible displacement of the boom tip point, driven by the interaction between the deployment process and the rigid-flexible coupling phenomenon, is shown in Figure 4.76.

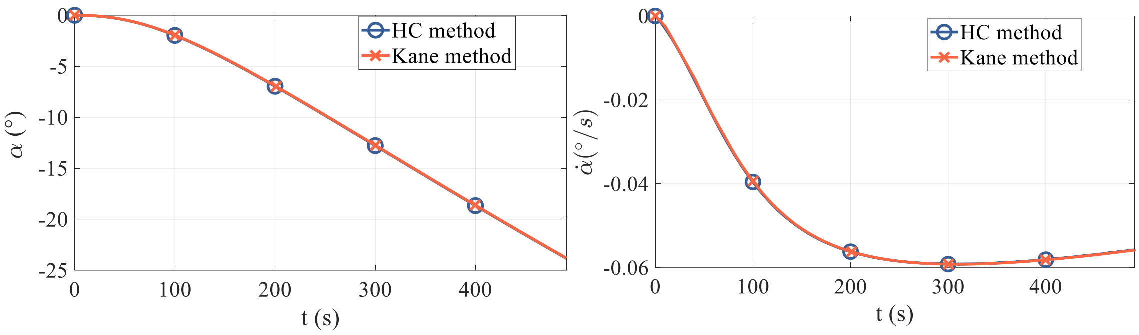

Figure 4.75: Satellite attitude angle (left) and angular velocity (left) during the deployment phase

In this context, it is necessary to mention that the HC method – which considers the TTM as a single beam with time-varying length and constant piecewise physical properties – fully accounts for the time-varying components of the shape function that introduce additional terms in both the stiffness and damping matrices. In fact, the deployment process implies that the flexible part of the TTM varies over time, leading to a time dependance of the shape function, which is not accounted in the multibody dynamic model employed in this study case. To facilitate direct comparison with the multibody formulation, a simplified variant, the "Reduced HC Method", is introduced by neglecting these time-dependent terms. Inspection of Figure 4.76 shows that, under the same assumptions, the Reduced HC method and the multibody approach, produce similar results, providing a cross-validation of both methodologies Furthermore, a second result, depicted in Figure 4.77, is produced while considering also the time-dependency of the modal shapes. The obtained curve shows a different trend with respect the previous outcome, leading to conclude that the specific contribution of time variation of modal shapes should not be neglected when modeling morphing structures, with a deployment velocity that does not allow to consider the phenomenon as quasi-stationary.

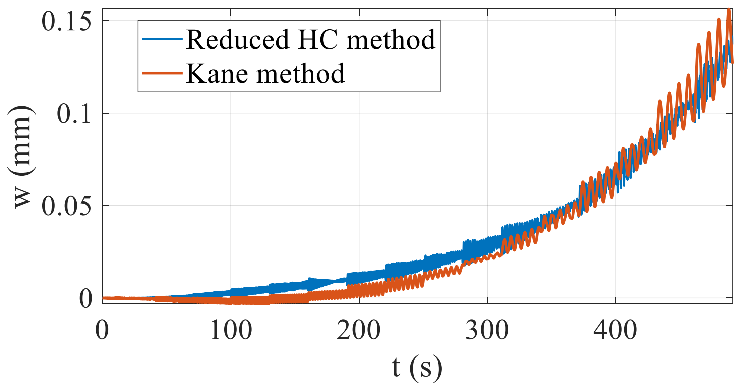

Figure 4.76: Flexible vibration at the tip of the deployable boom – reduced HC method vs Kane's method

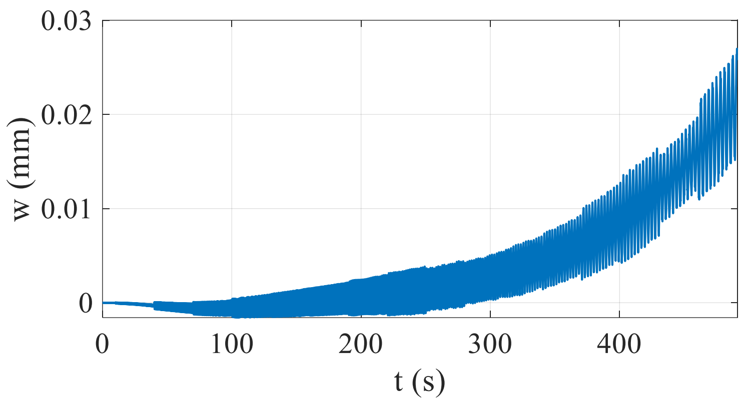

Figure 4.77: Flexible vibration at the tip of the deployable boom – complete HC method

From a computational point of view, the HC method exhibits better performance than the multibody approach. This is mainly because, in the HC method, the TTM is modeled as a single beam using approximate modal shapes, which are precomputed before the dynamic simulation for a selected number of possible TTM configurations, as described in Section 2.2.2. Conversely, in the multibody approach, a FEM formulation combined with a modal reduction technique (cf. Section 2.3.3) is used to model the elastic TTM. Although the number of elastic modes considered is the same in both methods, the computation of the approximate shapes results in lower computational effort. This is simply because the approximate mode shapes are calculated only for a limited set of configurations that the TTM can assume during deployment. When the TTM reaches a different configuration not included in the precomputed set, its elastic properties are obtained by interpolating the results across the previously computed configurations. In contrast, in the FEM-based approach, the modal reduction technique must be applied at each time step during the dynamic simulation, resulting in a higher number of numerical operations and therefore a greater computational effort. The difference in computational efficiency between the two methods is further influenced by the number of elements used to discretize each beam (in this study, $n_e = 10$). In fact, for a higher number of elements, the discrepancy between the two approaches in the total number of operations required for a single dynamic simulation clearly increases.

4.4.4. Concluding remarks

This study case presents a comprehensive analysis of the dynamic behavior of deployable Telescopic Tubular Masts (TTMs), incorporating both rigid-body and flexible motion effects. The step-by-step derivation of the elastic dynamics equations of the TTMs using the FEM shape functions in conjunction with the group-based approach, as described in in Section 2.2.2, was presented and discussed. Two modeling approaches – Hybrid Coordinate (HC) and Kane's method – were employed and cross-validated through a deployment simulation, and the differences in modeling capabilities and computational performance have been discussed. Moreover, the results demonstrate that the time variation of shape functions significantly affects the final outcome in the case of morphing structures, especially for large rate of variation of the structure configuration (the deployment velocity in the TTM case). Furthermore, the effect on computational performance of the modal-based and FEM-based approaches discussed in Section 2.2.2 have been compared and discussed, pointing out that, if the conditions reported in Section 2.2.2 do not verify, the former guarantees a faster computation, while the latter outperforms in terms of model fidelity.

4.5. Autonomous guidance and control for rendezvous and mating with Gateway

This application addresses the autonomous rendezvous and mating operations of a chaser spacecraft with Gateway, a critical infrastructure element in NASA's Artemis program and future deep space missions [109]. Gateway will operate in a Near Rectilinear Halo Orbit (NRHO) around the Moon [110], a dynamically favorable configuration offering prolonged visibility to both Earth and the lunar South Pole – key for sustained human presence and logistics in cislunar space[111]. Its role as a permanent orbital outpost entails regular interactions with crewed and uncrewed spacecraft, making robust and autonomous proximity operations essential. Unlike Earth-orbiting rendezvous scenarios, operations around Gateway occur in a strongly perturbed "multibody" (in this context, this term assumes the astrodynamics sense) environment, dominated by the gravitational influence of the Moon, Earth, and Sun.

The application focuses specifically on the terminal phases of proximity operations: close-range rendezvous, terminal approach, and final mating. These phases require high-precision, coordinated control of both translational and rotational motion, especially under stringent safety constraints, in an ephemeris-based dynamical framework. The analysis encompasses nonnominal conditions, such as when the final mating interface lies on the opposite side of Gateway relative to the approach path, and investigates the possibility of failures in the propulsion system. Although the current work does not regard a multibody spacecraft, it demonstrates a framework that is highly adaptable to berthing operations involving robotic systems, where dynamic coupling between spacecraft and robotic arms must be considered. This is reflected in the explicit inclusion of berthing as a potential mating scenario, in addition to traditional docking.

4.5.1. Vehicle description

This section is focused on the mass distribution, actuators, and geometry of the chaser spacecraft in relation to Gateway. Given the modular construction nature of Gateway and its evolving geometry, in the absence of specific information, Gateway is modeled as a sphere with a radius of 5 m, for the sake of simplicity. It is worth remarking that the control algorithm, though designed for a spherical target, can adapt to more complex geometries of Gateway. The chaser spacecraft has its geometry based on a cylinder and represents a scaled version of the Autonomous Transfer Vehicle in its stowed configuration. The radius, length, and mass of the spacecraft are reported in Table 4.30. Based on the geometry of the spacecraft, the inertia matrix is

$$\mathrm{J_C} = \begin{bmatrix} 3375 & 0 & 0 \\ 0 & 9250 & 0 \\ 0 & 0 & 9250 \end{bmatrix} \mathrm{kg\,m^2} \tag{4.54}$$

Equipped with a low-thrust engine, the chaser propulsion system is characterized by the parameters in Table 4.31.

Table 4.30: Chaser geometry and mass parameters

radius (m)	1.5
length (m)	5.5
mass (kg)	3600

Table 4.31: Propulsion system specifications $\left(g_0 = 9.8\,\mathrm{m/s^2}\right)$

effective exhaust velocity (km/s)	1.5
maximum thrust acceleration (m/s^2)	$5\times10^{-5}\cdot g_0$

Table 4.32: Reaction wheels parameters (referred to a single device)

axial moment of inertia (kg m^2)	0.84
maximum torque (Nm)	0.80
maximum spin rate (rpm)	3000

The spacecraft attitude control system relies on a set of four (non-coplanar) reaction wheels arranged in a pyramidal configuration. The parameters of these reaction wheels are summarized in Table 4.32. The maximum wheel angular acceleration is obtained dividing the maximum torque by the axial moment of inertia.

4.5.2. Mission scenarios and phases

The rendezvous and mating mission is divided into three distinct phases, which are illustrated in Figure 4.78:

i. Close-Range Rendezvous, from the spacecraft initial position until the communication point, which is assumed to be located at distance of 150 m. During this phase, the primary focus is on orbital control, using low-thrust propulsion to drive the chaser spacecraft toward Gateway. Attitude is assumed to be ideal, i.e. the actual direction of the longitudinal axis coincides with the desired thrust direction. This assumption is reasonable because no rapid steering of thrust direction occurs in this time interval. For this reason, only translational motion is modeled, and nonlinear hybrid predictive orbit control is employed. This exploits a first saturated phase (with maximum thrust), aimed at reducing the initial relative distance and velocity. The reference trajectory is generated by means of a cubic spline that connects two relative states, associated with each component of the relative position and velocity.

ii. Terminal Approach, covering the spacecraft path from the communication point until the final natural (unpowered) drift starts. In this phase, joint control of both trajectory and attitude is required to achieve successful mating, while avoiding collision with Gateway. The spacecraft attitude is dictated by the desired thrust direction, identified by means of a classic constant-gain feedback linearization approach and aimed at adjusting the relative trajectory. The chaser repeatedly updates its reference path following the trajectory planning algorithm described in Section 4.5.4. Actuation of attitude maneuvers through reaction wheels is also modeled.

iii. Final Drift and Mating, which is the conclusion of the approaching maneuver. The spacecraft is subject to natural drift (with no active translational control), while attitude control and actuation through reaction wheels is aimed at correct alignment for safe mating with Gateway. It is worth remarking that in the terminal approach the commanded attitude is based on the commanded thrust direction computed through the trajectory control, while in the final drift the commanded attitude is dictated by the mating conditions.

The mission scenarios include both docking and berthing operations, each with its specific terminal approach conditions. The control system must be designed to achieve the desired final conditions in both cases. If docking is pursued, mating between the spacecraft and Gateway must occur at Gateway docking port, assumed similar to that developed by ESA [112]. This mechanism allows Gateway to absorb the impact with the incoming spacecraft. The final relative conditions for docking are

$$\begin{cases} \rho_f = 7.75\,\mathrm{m} \\ \dot{\rho}_f = -1\,\mathrm{cm/s} \end{cases} \tag{1.55}$$

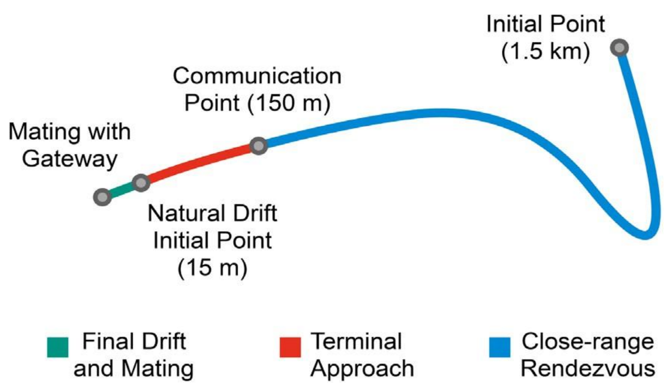

Figure 4.78: Mission phases

where ρ_f and $\dot{\rho}_f$ represent the chaser relative distance and its time derivative, termed relative velocity henceforth. Successful docking corresponds to the circular base of the chaser in touch with Gateway (cf. Figure 4.79), in such a way that the main thruster is pointed in the direction opposite to Gateway.

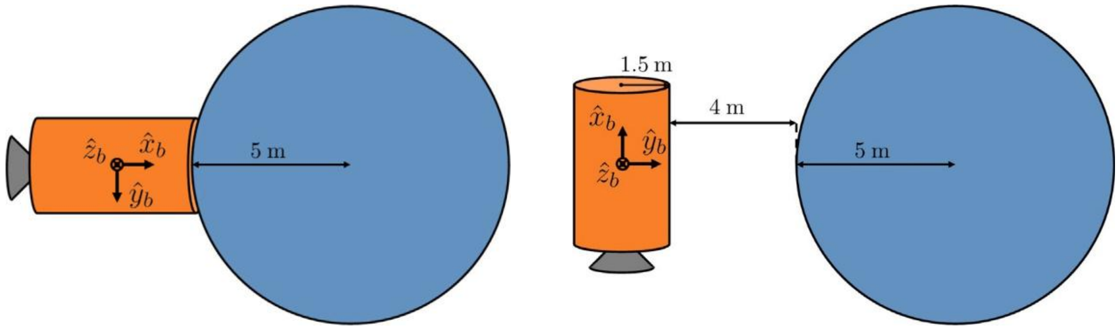

Figure 4.79: Geometry of docking (left) and berthing (right)

If berthing is pursued, a robotic arm attached to Gateway is responsible for establishing contact between the two spacecraft. This choice requires the spacecraft to reach Gateway with lower relative velocity to guarantee a smooth contact, and with a specific attitude to allow grasping (cf. Figure 4.79). To do this, for the chaser the final relative position and corresponding time derivative are enforced to be [113]

$$\begin{cases} \rho_f = 10.50\,\text{m} \\ \dot{\rho}_f = -0.5\,\text{cm/s} \end{cases} \tag{4.56}$$

These values are chosen to comply with a hypothetical robotic arm configuration, where it is assumed that a robotic arm in a partially folded configuration occupies 4 m. The chaser is also assumed to be equipped with a handle located on its lateral surface along the $\hat{y}_b$ direction (arm and handle are not shown in Figure 4.79).

4.5.3. Orbital motion of Gateway

The orbit designated for Gateway is a southern NRHO in the proximity of the exterior collinear libration point L_2. The selection of this orbit was determined by a variety of factors [114]. Firstly, an L_2 NRHO offers better visibility for communications with the far side of the Moon compared to a L_1 NRHO [115]. Additionally, L_2 NRHOs demonstrate better stability characteristics than L_1 NRHOs, which leads to reduced orbit maintenance costs [116]. At the same time, this kind of orbit enables a very long coverage of the lunar south pole, an area of significant interest due to the presence of substantial water ice deposits in crater shadows. Moreover, connection with Lunar south pole even requires less propellant consumption if compared to the effort required to collocate a spacecraft in a northern NHRO [117]. Lastly, the 9:2 lunar synodic resonance with the Moon's orbital period helps preventing eclipses by the Earth [118]. Since Earth eclipses can last longer than current hardware capabilities, avoiding them was a key design objective for this orbit. While lunar eclipses occur fairly frequently, several times each year, they never last more than 80 min and thus do not pose a significant risk. The orbit that results from previous criteria has a periselenium radius between 3196 and 3557 km, with an average value of 3366 km, and a mean orbital period of 6.562 days. Gateway's ephemerides data are stored in an SPK-type file produced by the NASA's Navigation and Ancillary Information. These ephemerides were calculated considering the perturbing influences of the gravitational fields of Earth, Sun, and Jupiter, as well as several harmonics of the

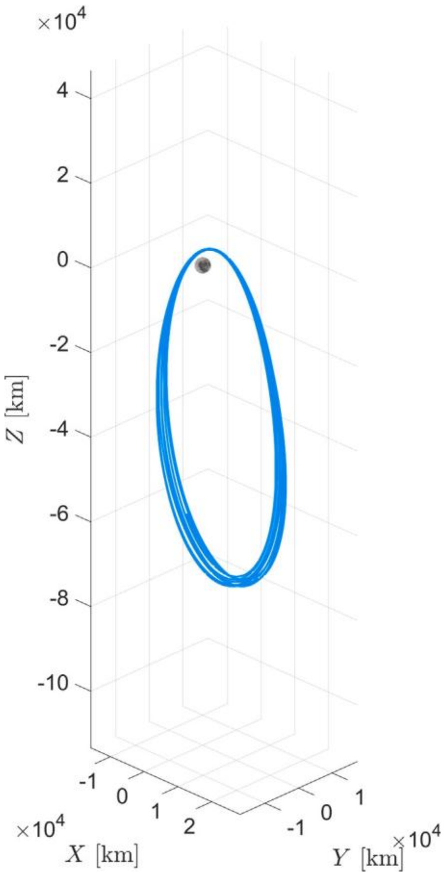

Figure 4.80: Gateway trajectory in the Earth-Moon synodic reference frame (10 periods)

selenopotential. Additionally, minor aposelenium maneuvers of few millimeters per second were incorporated for stationkeeping purposes. As a matter of fact, even if this orbit is periodic in the Circular Restricted Three Body Problem (CR3BP), it is quasi-periodic in a more accurate dynamic model. Therefore, without maintenance, Gateway would drift from the nominal CR3BP orbit after more than nine revolutions [119]. Figure 4.80 depicts the Gateway trajectory derived from the ephemerides in the Earth-Moon synodic reference frame, with origin at the center of the Moon.

4.5.4. Reference trajectory planning

To ensure a successful and safe docking, it is essential to develop a refined trajectory planning algorithm. The challenge lies in devising a reference trajectory that not only leads the spacecraft to the mating port but also maintains a safe distance from Gateway. A novel approach to trajectory planning is introduced, based on the definition of an exclusion sphere, a forbidden region around Gateway with a radius of 15 m, i.e. 3 times the radius of Gateway (modeled as a sphere). The exclusion sphere serves as a safety threshold to avoid collision with Gateway before reaching the mating port. This methodology is particularly relevant during terminal approach, in the presence of nonnominal conditions.

The algorithm determines the desired via-points based on the logic described below and generates the corresponding relative trajectory using cubic spline interpolation, with derivative boundary conditions imposed according to proper criteria. Moreover, the relative path is updated to become tangent to the sphere if the initial relative trajectory turns out to cross the sphere itself. This ensures safety while maintaining proximity for mating. Two primary strategies are employed for establishing this reference trajectory, using either (i) two via points or (ii) three via points.

Two via points. Using two via points represents the standard approach, accompanied by cubic spline interpolation between the initial and final states (i.e. relative position and velocity components), corresponding to times t_0 and t_f. In order to find the coefficients of the spline functions, a set of boundary conditions must be enforced. For the purpose of generating the reference path, the desired initial relative velocity is set to 0 at the beginning of phase 1 (close-range rendezvous). Then the boundary conditions are:

- First via point: actual initial state
- Second via point: desired final state

Instead, in phase 2 (terminal approach) the spline is updated at each sampling time t_k, based on the current state. Therefore, the initial boundary conditions (referred to the updated first via point) for phase 2 are the current relative position and velocity, while the second via point is characterized by the same final conditions. However, if the trajectory intersects the exclusion sphere, two via points are no longer sufficient.

Three via points. Three via points are employed in phase 2 when the preceding approach based on two via points implies violating the exclusion sphere. This approach introduces a third via point to ensure that the trajectory becomes tangent to the exclusion sphere. The key steps to design this new reference path are

i. defining the time of tangency: the trajectory derived from the two point interpolation is analyzed to identify the point of closest approach to Gateway. If it intersects the exclusion sphere, the time of tangency t_1 is defined as the time at which the distance between the reference trajectory and Gateway is minimum.

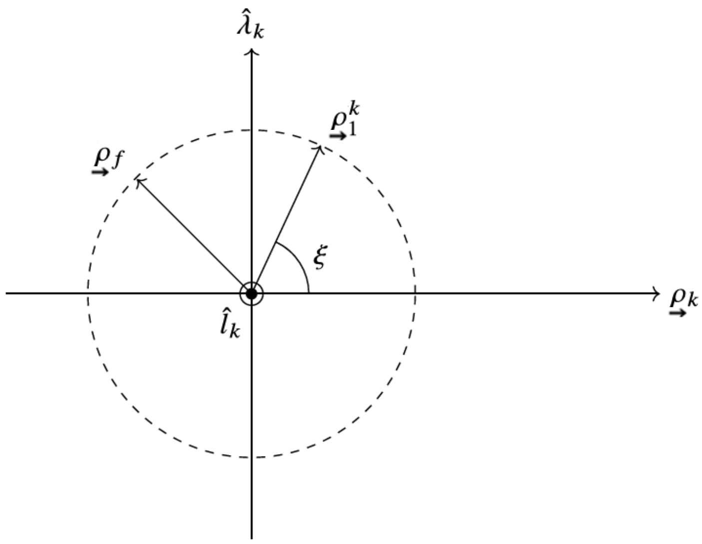

Figure 4.81: Geometry for the three-point reference trajectory

ii. determining the point of tangency: the tangency point, corresponding to $\underset{\rightarrow}{\rho}_1^k$, is calculated to ensure that the trajectory is tangent to the exclusion sphere, avoiding intersection. This calculation is performed in the reference frame $\underline{\underline{H}}_k = \begin{bmatrix} \hat{\rho}_k & \hat{\lambda}_k & \hat{l}_k \end{bmatrix}$, shown in Figure 4.81. This step and the previous one are repeated at each sampling time t_k.

The reference frame $\underline{\underline{H}}_k$ is defined as

$$\underline{\underline{H}}_k \triangleq \left\{ \hat{\rho}_k = \frac{\underset{\rightarrow}{\rho}_k}{\left|\underset{\rightarrow}{\rho}_k\right|} \quad \hat{\lambda}_k = \frac{\hat{l}_k \times \hat{\rho}_k}{\left|\hat{l}_k \times \hat{\rho}_k\right|} \quad \hat{l}_k = \frac{\hat{\rho}_k \times \underset{\rightarrow}{\rho}_f}{\left|\hat{\rho}_k \times \underset{\rightarrow}{\rho}_f\right|} \right\} \tag{4.57}$$

where $\underset{\rightarrow}{\rho}_k$ and $\underset{\leftarrow}{\rho}_f$ denote the current and final (desired) relative position vectors, respectively. Then, two separate branches must be considered, the first one from the initial state to the tangent point, while the second one starts in the tangent point and ends in the desired final state. For the first branch, the boundary conditions are

- First via point: actual initial relative position and velocity
- Second via point: relative position at the tangent point

while for the second branch one has

- First via point: relative position at the tangent point
- Second via point: desired final relative position and velocity

It is apparent that, for both branches, 3 vector conditions (corresponding to 9 scalar conditions) are imposed. However, the cubic spline interpolation of the trajectory – represented as a vector – requires 12 scalar conditions for each branch to be completely defined. This allows to impose further 6 scalar conditions to the time derivative of the relative position vector in the tangent point. A possibility consists in directly assigning the relative velocity in the tangent point. One of the possible choices consists of requiring a precise value of the relative velocity vector in the tangent point. However, it is not possible to predict a suitable value to ensure smooth trends in velocity and acceleration time histories. Then, it is preferred to apply the following constraints:

- continuity of the relative velocity in the tangent point (3 scalar conditions);
- tangency of the trajectory with the sphere, i.e. $\underset{\rightarrow 1}{\rho}^{k} \cdot \underset{\rightarrow 1}{\dot{\rho}}^{k} = 0$;
- coplanarity between $\underset{\rightarrow 1}{\dot{\rho}}^{k}$ and the $\left(\underset{\rightarrow k}{\rho}, \underset{\leftarrow f}{\rho}\right)$-plane, i.e. $\underset{\rightarrow 1}{\dot{\rho}}^{k} \cdot \hat{1}_{k} = 0$;
- continuity of the acceleration component that is parallel to the velocity, which is defined as $\underset{\rightarrow 1}{\hat{\dot{\rho}}}^{k} \cdot \underset{\rightarrow 1}{\ddot{\rho}}^{k}$

Through these adjustments, the three-via-point approach improves safety and reliability by ensuring that the reference trajectory avoids the exclusion sphere, in agreement with the goals of safe and efficient mating operations.

4.5.5. Control strategy

The attitude and orbit control actions employed during the approach of the chaser toward Gateway depend on the ongoing phase of the rendezvous maneuver. With reference to Section 4.5.2, the first phase coincides with the close-range rendezvous, where the relative motion control relies on the HPC law discussed in Section 3.8.2. Instead, the terminal approach phase employs (constant-gain) feedback linearization control law, with no saturation of the thrust magnitude. In fact, in the proximity of Gateway the main goal is in precise trajectory tracking while maintaining a safe distance, rather than reducing the approach time through maximum thrust. This fixed-gain feedback control law is integrated into an iterative guidance and control algorithm that incorporates the spacecraft attitude dynamics. The algorithm computes the desired thrust acceleration $\vec{a}_{t,c}$ – in terms of magnitude and direction – based on the desired trajectory. However, instead of assuming ideal attitude alignment, the thrust is applied along axis $\hat{x}_b$ of the spacecraft, considering its actual orientation. This approach accounts for any misalignment between commanded and actual attitude. The iterative guidance scheme operates with a sampling time of 1 min. At each iteration, the algorithm updates the reference trajectory and computes the corresponding commanded attitude, which is then fed to the attitude control system. Because the spacecraft main thruster points toward axis 1 of the spacecraft $\hat{x}_b$, the new commanded axis $\hat{x}_c$ is $\hat{x}_c = \hat{a}_{t,c}$. The other two commanded axes are chosen to complete the right-handed orthogonal triad. To guarantee a slow time-variation of the commanded frame, the other two axes at each sampling time are defined as

$$\hat{y}_c(t_k) = \frac{\hat{z}_c(t_{k-1}) \times \hat{x}_c(t_k)}{\left|\hat{z}_c(t_{k-1}) \times \hat{x}_c(t_k)\right|} \qquad \hat{z}_c(t_k) = \frac{\hat{x}_c(t_k) \times \hat{y}_c(t_k)}{\left|\hat{x}_c(t_k) \times \hat{y}_c(t_k)\right|} \tag{4.58}$$

This closed-loop approach allows the spacecraft to dynamically adjust its orientation to match the desired thrust direction, even in the presence of disturbances or nonnominal conditions. This integrated guidance and control strategy is aimed at safely driving the spacecraft during the terminal approach that precedes final drift and mating.

Maintaining a safe distance between the chaser and the target is critical in orbital in orbital rendezvous operations. In the terminal approach framework, an emergency maneuver is designed to address scenarios where the distance between the mass centers of chaser and target drops below 14.8 m. Once activated, this maneuver starts a hysteresis cycle to ensure the chaser regains a safe distance before resuming ordinary operations. During the hysteresis cycle, illustrated in Figure 4.82, the chaser's orbital control system applies maximum thrust aligned with

$$\hat{t} = \frac{\hat{\eta} \times \vec{\rho}}{\left|\hat{\eta} \times \vec{\rho}\right|} \tag{4.59}$$

with

$$\hat{\eta} = \frac{\vec{\rho} \times \vec{\rho}_f}{\left|\vec{\rho} \times \vec{\rho}_f\right|} \tag{4.60}$$

where $\underset{\rightarrow}{\rho}$ is the instantaneous relative position of the chaser. This leads the chaser to move away from Gateway without thrusting toward it. The emergency maneuver remains active until the relative distance exceeds 15.2 m. Figure 4.82 shows that the emergency maneuver is ignited only if the distance drops below 14.8 m and ends when the distance exceeds 15.2 m. Once this condition is met, the constant-gain feedback linearization control is resumed to continue the rendezvous process safely.

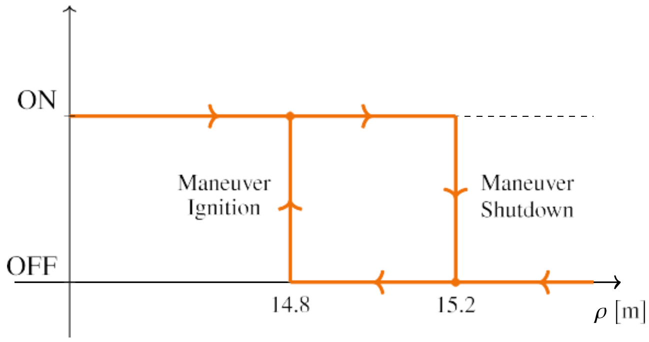

Figure 4.82: Illustration of the hysteresis cycle in the emergency maneuver

The final phase of the maneuver, characterized by a natural drift trajectory, is exclusively dedicated to attitude control. This is essential for achieving the precise alignment required for a successful mating with Gateway. With the propulsion system deactivated, the spacecraft trajectory is governed by its natural orbital motion, while the attitude control system actively reorients the spacecraft to match the desired mating configuration. Successful docking is achieved when the chaser comes in contact with Gateway with its thruster in the direction opposite to the target. This is based on the assumption that the docking mechanism will be mounted on the tip of the chaser (cf. the left plot of Figure 4.79). This condition can be enforced by requiring that at the final time the chaser longitudinal axis, aligned with $\hat{x}_c$, points toward the docking interface direction (taken from the center of mass of Gateway). The other axes of the commanded reference frame can be computed by following the same approach previously introduced in this section. In the berthing scenario, the final phase involves a natural drift of the spacecraft toward Gateway, while the attitude control system actively reorients the chaser for capture by the robotic arm. In this phase the chaser attitude must converge to a specific orientation. This configuration corresponds to the robotic arm grasping a handle mounted on the side of the cylindrically-shaped chaser along the $\hat{y}_b$ direction as shown in the right plot of Figure 4.79, ensuring a successful berthing operation. Thus, the desired attitude is

$$\hat{y}_c = -\frac{\underset{\rightarrow}{\rho}_f}{\rho_f} \qquad \hat{z}_c = \hat{1}_k \qquad \hat{x}_c = \frac{\hat{y}_c \times \hat{z}_c}{|\hat{y}_c \times \hat{z}_c|} \tag{4.61}$$

where $\hat{1}_k$ is illustrated in Figure 4.81.

4.5.6. Numerical results: rendezvous and docking

For the sake of brevity, results are presented only for the docking case. In fact, results related to docking and berthing cases are similar, and for each case several plots are required. Nevertheless, results concerning the latter case are reported in Ref. . The rendezvous maneuver of the chaser is assumed to begin from a distance of 1.5 km from Gateway along the radial direction, with relative velocity components of −1 m/s along $\hat{\theta}$ and $\hat{h}$. These initial conditions are realistic at the end of an orbit transfer that precedes rendezvous. The initial relative state can be expressed in the LVLH-T frame as

$$\underline{\rho}(t_0) = \underline{\rho}_0 = \begin{bmatrix} 1.5 \\ 0 \\ 0 \end{bmatrix} \text{km} \qquad \dot{\underline{\rho}}(t_0) = \dot{\underline{\rho}}_0 = \begin{bmatrix} 0 \\ -1 \\ -1 \end{bmatrix} \text{m/s} \tag{4.62}$$

The duration of the complete maneuver is set to 12 h, from May 23, 2025, 9:56:10 UTC to 21:56:10 UTC, consistent with similar Soyuz docking maneuvers.

In this first phase of the mission, it is assumed that the mating port is initially oriented toward the chaser initial position. Using the values of $\underline{\rho}_f$ and $\dot{\underline{\rho}}_f$ from Eq. (1.55), one can define the final desired state as

$$\underline{\rho}_f = \rho_f \frac{\underline{\rho}_0}{\rho_0} \qquad \text{and} \qquad \dot{\underline{\rho}}_f = \dot{\rho}_f \frac{\dot{\underline{\rho}}_0}{\dot{\rho}_0} \tag{4.63}$$

The final desired state for this phase is obtained by means of a free-dynamics backward propagation in time from these state values until the boundary of the exclusion sphere is reached, by numerical integration of Eq. (3.125), setting $\underline{a}_{t,c} = \underline{0}$. This state is the one that is targeted by the nonlinear HPC. Once the spacecraft reaches the communication point, the real attitude of the docking port is communicated and the second phase of the rendezvous maneuver begins. The chaser trajectory from the initial position to the communication point is depicted in Figure 4.83.

After completing the close-range rendezvous, the initial conditions for the terminal approach phase coincide with the spacecraft position and velocity at the communication point, denoted $\underline{\rho}_c$ and $\dot{\underline{\rho}}_c$, respectively. Then, the final docking conditions are computed by performing a backward free-dynamics (natural drift) propagation from the following conditions:

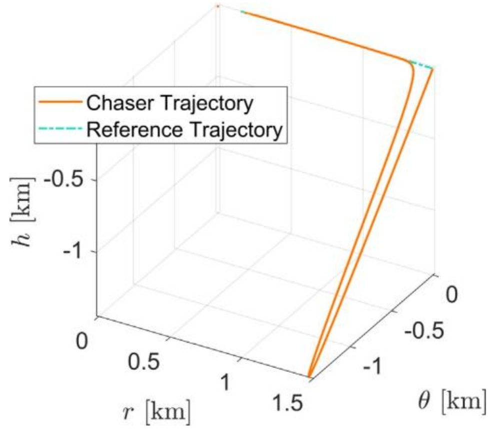

Figure 4.83: Close-range rendezvous trajectory in LVLH-frame

$$\underline{\rho}_f = -\rho_f \frac{\underline{\rho}_c}{\rho_c} \quad \text{and} \quad \dot{\underline{\rho}}_f = -\dot{\rho}_f \frac{\dot{\underline{\rho}}_c}{\dot{\rho}_c} \tag{4.64}$$

These conditions allow testing the guidance and control architecture in the worst case scenario, as the final position is placed at the opposite side of Gateway with respect to the incoming direction. A Monte Carlo campaign of 100 simulations is carried out to assess the control system performance. The following nonnominal conditions at the communication point are also assumed:

- initial state perturbations: the error on each state component has Gaussian distribution, with average value equal to 0 and standard deviation equal to 5% of the respective nominal value;

- temporary unavailability of the propulsion system: this is assumed to occur before the tangency point; the failure duration has uniform distribution in the interval $[0, 5]$ min, and the starting time is uniformly distributed between the time corresponding to the communication point t_c and t_1;

- thrust misalignment: the actual thrust direction has a random displaced direction identified through two angles, i.e. γ and β (cf. Figure 4.84), referred to the nominal thrust direction (aligned with $\hat{u}_n$, cf. Figure 4.84). Their time histories are generated through sinusoidal interpolation of equally-spaced values. These values (for both γ and β) are generated at sampling times and have stochastic distributions. In particular, γ has Gaussian distribution with average value and standard deviation σ equal to 0 and 1 deg, respectively, while β has uniform distribution in the interval [0, 360] deg. The random values selected for γ are truncated in the interval $[-3\sigma, 3\sigma]$.

As shown in Figure 4.85, the Monte Carlo simulations for the docking maneuver reveal the effectiveness of the guidance system in directing the spacecraft along a smooth trajectory toward Gateway. The approaching paths depicted in the plot point out that the guidance and control system successfully drive the chaser toward the desired docking location, in spite of initial dispersed conditions. Further insight on the control system performance is shown in Figure 4.86, which depict the relative distance and velocity over time. These figures show that the chaser smoothly approaches Gateway, up to the point in which the natural drift starts. It is worth noting that the velocity components reduce, to meet the requirements for docking. The thrust acceleration components for a single docking simulation are shown in Figure 4.87, which highlights smooth, continuous thrust acceleration with nonnegligible variations during critical phases, such as encountering the communication point and the beginning of the final drift. The chaser attitude is illustrated through the error quaternions and angular velocity components in Figure 4.88, which shows convergence to the desired orientation. The actual torque components and the corresponding spin rates of the reaction wheels are reported in Figure 4.89, which illustrates the adjustments during the terminal approach. The results of the Monte Carlo

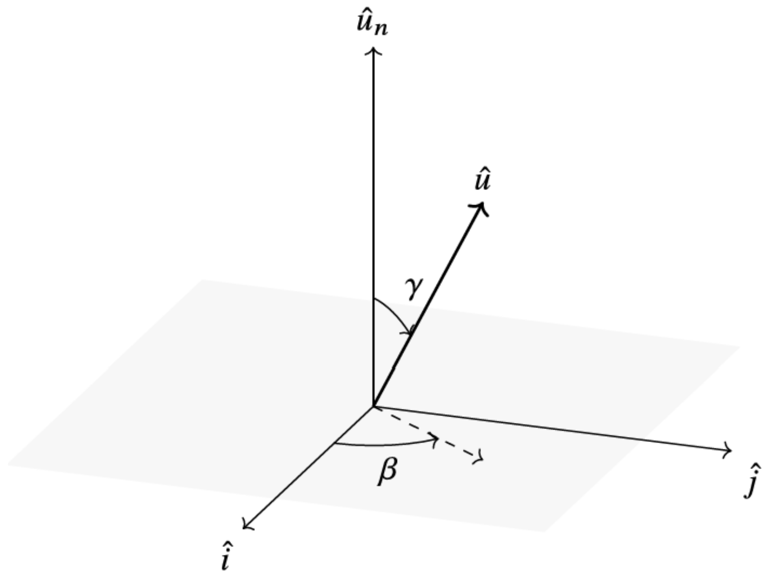

Figure 4.84: Illustration of the misalignment angles

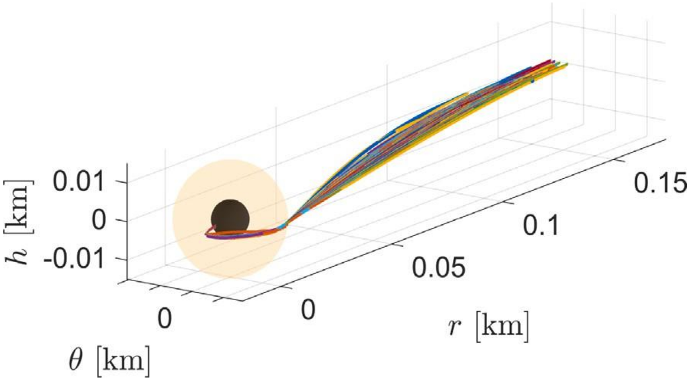

Figure 4.85: Rendezvous and docking: trajectories in the LVLH-T frame (phases 2 and 3)

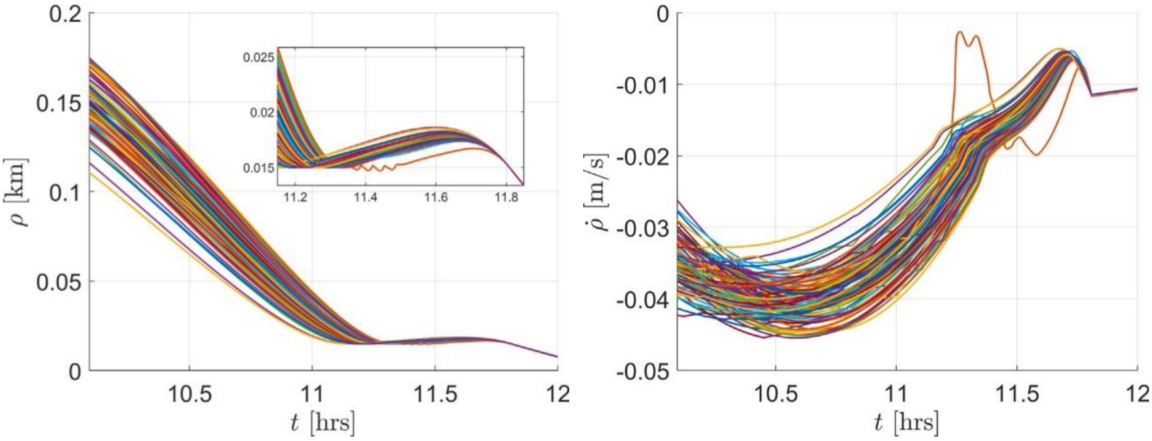

Figure 4.86: Rendezvous and docking: relative distance (left) and relative velocity (left) (phases 2 and 3)

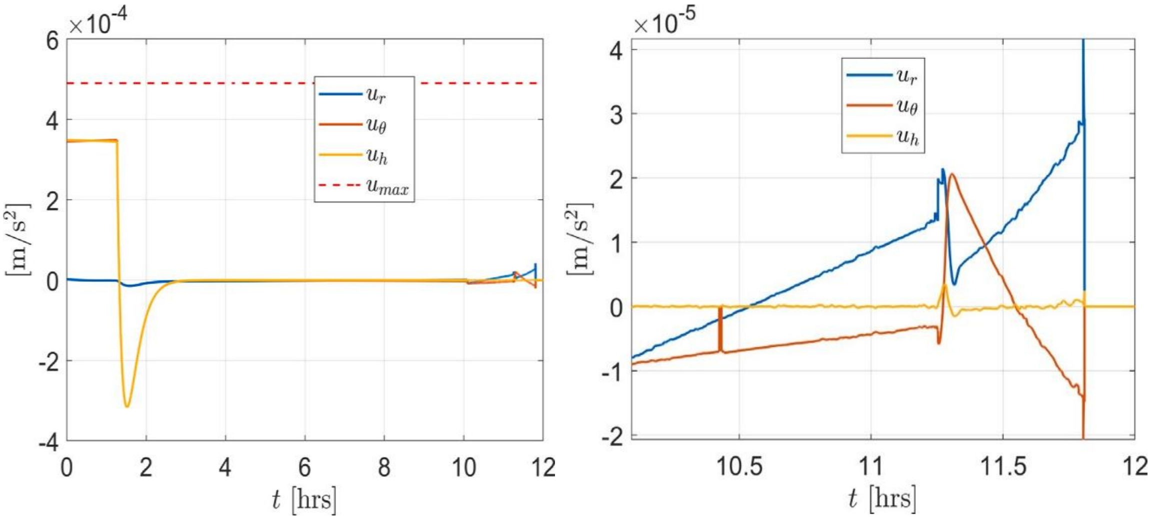

Figure 4.87: Rendezvous and docking: thrust acceleration components in phases 1 through 3 (left) and the details regarding only phases 2 and 3 (right)

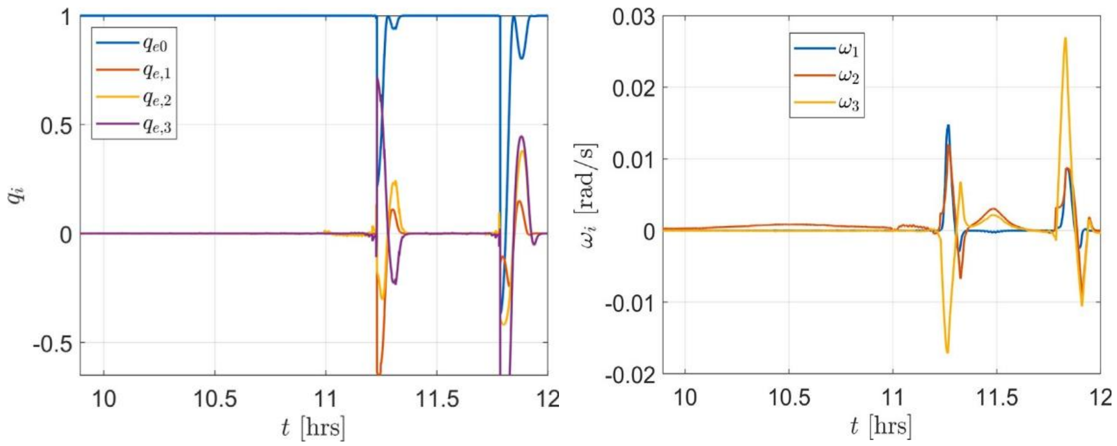

Figure 4.88: Rendezvous and docking: error quaternion (left) and error angular velocity (right) in phases 2 and 3

simulations in the docking scenario are summarized in Table 4.33. This table provides an overview of the mean and standard deviation of the final values of the errors on relative distance, relative velocity, as well as the final angular velocity error and the pointing error.

Analysis of the outputs of the previously mentioned Monte Carlo campaign reveals that the emergency maneuver, described in Section 4.5.5, is needed in a single simulation. This occurs when the relative distance drops below 14.8 m. Figures 4.90 through 4.92 depict the relative distance, trajectory, the thrust acceleration components, the error quaternion, and the actual torque components during the last hour before mating for the case that requires the emergency maneuver. In particular, the left plot in Figure 4.91 shows that the relative distance oscillates between 14.8 and 15.2 m during the emergency

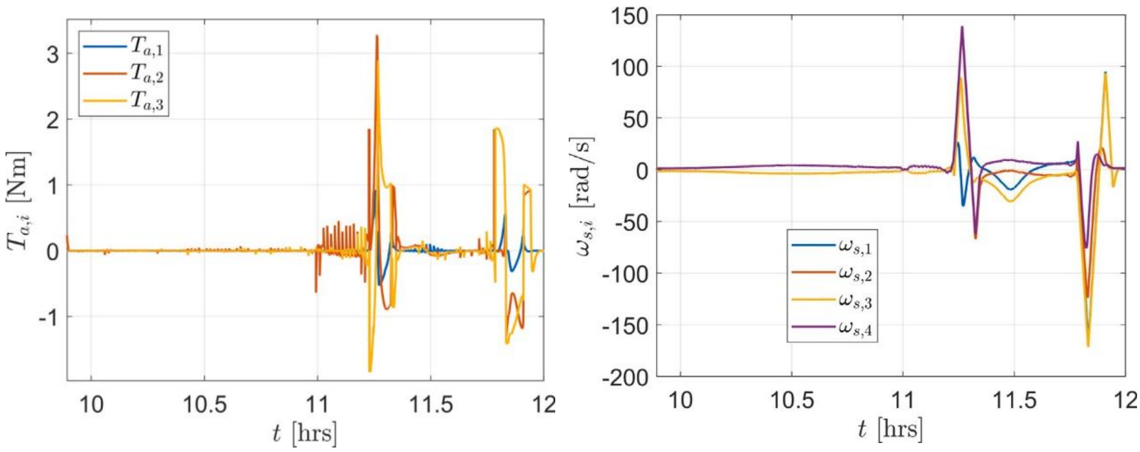

Figure 4.89: Rendezvous and docking: actual torque (left) and wheels angular rates (right) in phases 2 and 3

Table 4.33: Results of the Monte Carlo campaign in the docking scenario

	mean value	standard deviation
relative distance error [mm]	5.547	9.113
relative velocity error [mm/s]	$5.785 \cdot 10^{-2}$	$4.988 \cdot 10^{-2}$
angular velocity error [deg/s]	$1.862 \cdot 10^{-7}$	$1.362 \cdot 10^{-7}$
pointing error [deg]	$1.309 \cdot 10^{-3}$	$9.455 \cdot 10^{-3}$

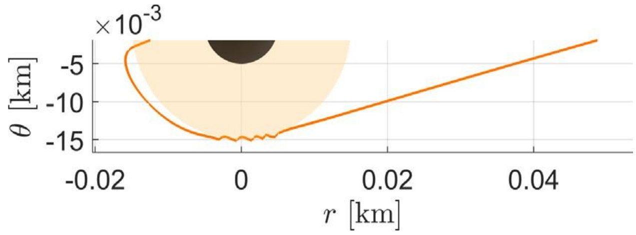

Figure 4.90: Trajectory in the LVLH-T frame during the emergency maneuver

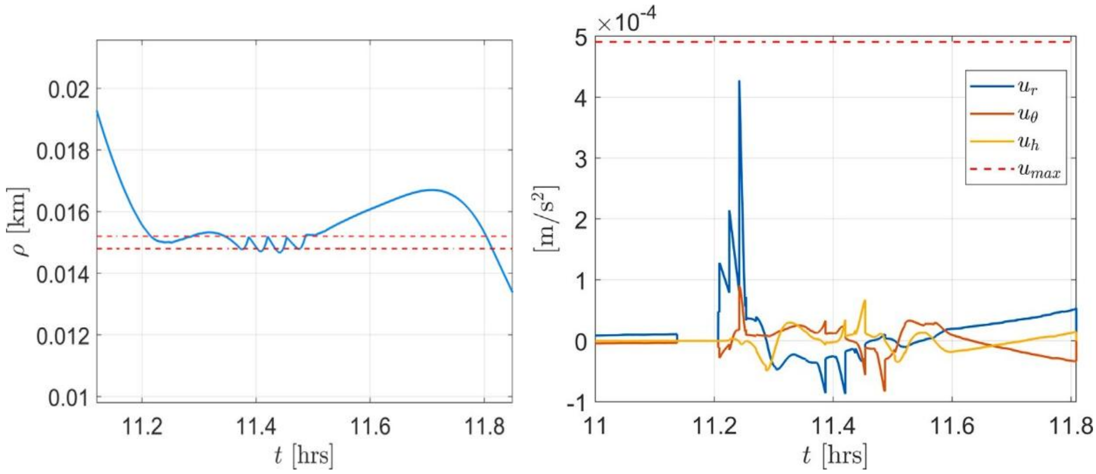

Figure 4.91: Relative distance (left) and thrust acceleration (right) during the emergency maneuver

maneuver, which is consistent with the hysteresis cycle introduced in Section 4.5.5. This behavior is also apparent from inspection of Figure 4.90. The thrust acceleration components, responsible for carrying out collision avoidance, oscillate with greater amplitudes with respect to the remaining portion of the approaching path, as shown in the right plot in Figure 4.91. Inspection of Figure 4.92 reveals that the error quaternion is subject to oscillations as well, but finally correct orientation is gained before mating takes place. Moreover, the attitude control system appears particularly solicited during the emergency maneuver, which nevertheless is performed successfully.

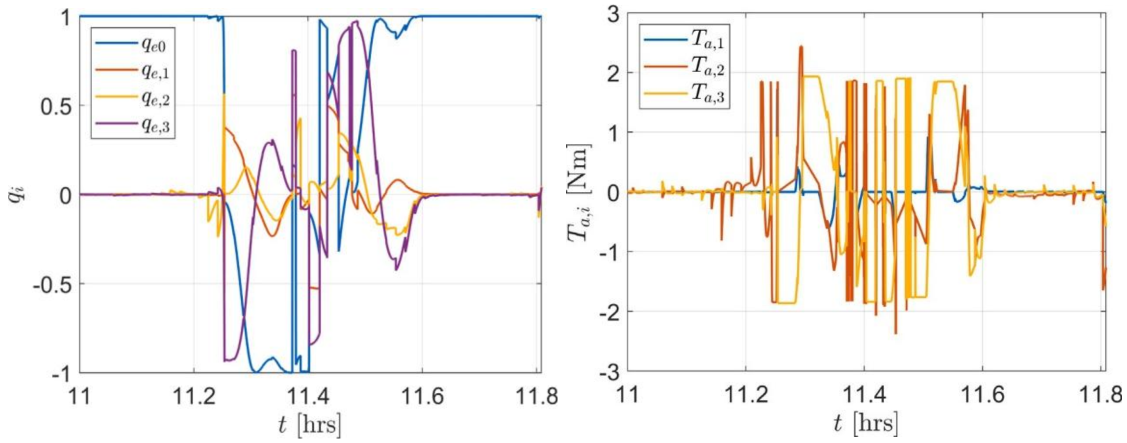

Figure 4.92: Thrust acceleration (left) and error quaternion (right) during the emergency maneuver

4.5.7. Concluding remarks

In this case study a novel guidance and control architecture (including actuation) for autonomous rendezvous and mating with Gateway is designed and tested. Because orbit dynamics in the proximity of Gateway is strongly perturbed, it is modeled in a high fidelity multibody dynamical framework, with the inclusion of all relevant orbit perturbations. Motion relative to Gateway is described using the modified Battin-Giorgi approach (cf. Section 3.7) that considers Gateway as the reference vehicle, unlike former contributions that usually assume that the reference spacecraft travels a Keplerian orbit. The rendezvous and mating maneuver is split in three phases: (1) close-range rendezvous, starting from a relatively short distance, (2) terminal approach, and (3) final drift and mating. In phase (1), the hybrid predictive control law described in Section 3.8.2 is applied and tested. Phase (2) starts when the distance from Gateway reduces to 150 m, and requires tight coordinated trajectory and attitude control, with the use of low thrust, aimed at driving the chaser toward Gateway. In this application, strict collision avoidance constraints, with the definition of a suitable exclusion region, are introduced and used in the real-time iterative update of the tracked trajectory. This is designed based on two different ordinary strategies (using either a two- or a three-via-point relative path), in conjunction with an effective hysteretic emergency maneuver. In phase (2), the time-varying thrust components identify the commanded pointing direction of the spacecraft, which is achieved using a nonlinear attitude control algorithm. Phase (2) ends with final conditions such that in phase (3) the spacecraft naturally drifts toward Gateway, with no propulsion. In this way, in phase (3) attitude maneuvering has no effect on trajectory and can be designed in order to achieve the final correct orientation. Actuation is demanded to an array of reaction wheels. Numerical simulations in nonnominal conditions show that the nonlinear control techniques presented in the third chapter and incorporated in a unified guidance and attitude control architecture are effective for autonomous spacecraft rendezvous and mating with Gateway.

4.6. Final discussion

Chapter 4 demonstrated the practical application of the advanced modeling and control techniques developed in the previous chapters, through a series of realistic space mission scenarios. These applications span a broad spectrum of operational contexts, addressing the increasing complexity of modern space systems and validating the versatility of the proposed multibody framework. A common feature across all scenarios was the accurate and efficient integration of the Kane-based multibody formulation with advanced nonlinear control techniques – except for the last application, where only nonlinear control is addressed in a complex orbital scenario. The simulations encompassed various operational contexts, ranging from proximity operations and manipulation to attitude maneuvers and structural deployment, thereby demonstrating the versatility of the unified framework. In the proposed cases, the dynamic coupling between flexible elements, rigid-body motion, and control actions was fully captured, confirming the capability of the formulation to model complex space systems with high fidelity. Importantly, the chapter demonstrated that the same core modeling and control architecture can be systematically applied across diverse mission scenarios without the need for significant reformulation. This highlights one of the key objectives of the thesis: to develop a general-purpose methodology that is modular and adaptable to the evolving demands of space missions. Overall, Chapter 4 showed the practical applicability and scalability of the methodologies developed in this work. The results confirm that the combined modeling and control approach can effectively support the dynamic analysis, guidance, and control of complex spacecraft in future operational environments, including on-orbit servicing, debris removal, and the deployment and operation of large space structures. The generality and flexibility of the framework provide a solid foundation for further industrial applications and future research in this rapidly evolving sector.

Conclusion

This PhD thesis has addressed the increasing complexity of modern spacecraft dynamics through the development of a general, efficient, and modular framework for the modeling and control of rigid and flexible multibody systems in the space environment. The work has been driven by real industrial needs – particularly those arising from the CIMR mission – while aiming at broader applicability to the future challenges of space mission design and operations.

On the modeling side, the thesis has established a systematic and recursive formulation for multibody dynamics based on Kane's method, which was chosen for its balance between physical interpretability and computational efficiency. The derivation of the dynamic equations accommodates both rigid and flexible bodies and can be applied to complex spacecraft configurations, including those involving closed kinematic chains and sloshing dynamics. Moreover, the application of the proposed formulation to the modeling of space manipulators has been thoroughly investigated, with particular attention to the correspondence between the key elements of Kane's method and the characteristic quantities used in robotics. In this context, the entire manipulator capture process has been addressed, enabling the simulation and analysis not only of pre- and post-grasping phases, but also of the capture maneuver itself.

The treatment of structural flexibility has been developed with great attention to both theoretical generality and practical implementation. By analyzing both the modal and finite element bases, the framework enables the modeling of elastic deformations also when the spacecraft exhibits complex configurations. This is further allowed by modeling strategies as the grouping approach and the modal reduction technique. The interaction between elastic dynamics and environmental forces – particularly gravity – has been integrated, with the development of a series of "gravitational modal integrals" that play a crucial role in the accurate representation of the elastic deformation in space structures. Moreover, stress stiffening has been analyzed and formally included within the formulation (for beam-like structures) to further enhance the model fidelity. These capabilities are critical for assessing performance and safety in scenarios involving large and lightweight structures – especially when arranged in complex dynamic configurations – such as rotating antennas and deployable structures.

In parallel with the modeling contributions, this thesis has advanced the design of nonlinear control techniques tailored to space applications. New control laws for attitude tracking and relative orbital motion have been proposed, analyzed for stability, and benchmarked against state-of-the-art solutions. The use of these enhanced approaches has demonstrated clear advantages, including improved convergence speed and better exploitation of actuator capabilities. Steering laws for momentum exchange devices and strategies for proximity operations have also been addressed, reinforcing the applicability of the control framework to complex operational scenarios.

A major contribution of this thesis lies in the effort to integrate the developed modeling and control strategies into realistic and operationally relevant applications. Five mission scenarios have been studied, ranging from debris capture with space manipulators to complex maneuvers involving large flexible spacecraft and advanced proximity operations. These applications demonstrate the maturity and versatility of the proposed methodologies, highlighting their capability to support mission design, validation, and safety analysis. Among the various study cases examined in this work, particular emphasis has been placed on the CIMR spacecraft dynamics, which constitutes the central application scenario of this PhD research. In this context, the developed methodologies have yielded significant insights into the satellite dynamic behavior in its operational configuration, providing critical information for both safety assessment and functional performance evaluation.

Complementing the theoretical contributions, a dedicated multibody simulation tool – presented in the Appendix – has been developed in MATLAB and delivered to Thales Alenia Space Italia. The software implements the recursive Kane-based formulation and supports tree-like multibody configurations, orbital dynamics, and control input integration. Despite being in a preliminary state, the tool already allows non-expert users to perform advanced dynamic simulations with a high degree of automation and flexibility. Preliminary comparisons with commercial software have shown promising results, with the in-house tool demonstrating lower computational costs and improved numerical accuracy, particularly in scenarios involving combined orbital and attitude dynamics. These encouraging outcomes suggest that the tool can be further refined and expanded to become a fully structured and mission-oriented simulation environment.

Appendix

Development of a generalized multibody simulation tool

A.1 Motivation

The request to develop an in-house multibody software originated directly from a clear need identified by Thales Alenia Space Italia (TAS-I). The department involved in this PhD work, which focuses primarily on multibody dynamics analysis of individual mechanisms and entire satellites, currently uses the commercial software MSC Adams for its simulations [103]. While MSC Adams already offers high-fidelity modeling capabilities across a wide range of applications, including both rigid and flexible bodies, TAS-I has identified several areas for improvement that could be addressed through the development of proprietary software. Specifically:

- MSC Adams is a general-purpose software and is not specifically tailored for space applications. This becomes particularly evident when attempting to include orbital dynamics in dynamic simulations. While it is technically possible to incorporate such dynamics into MSC Adams, doing so often results in a decline in computational performance, leading to significantly longer integration times compared to codes specifically designed for space applications. Furthermore, several features critical to space operations are either missing or not natively supported in the software. These include, for example:
    - the representation of orbital motion using classical orbital elements,
    - the modeling of orbital perturbations,
    - the ability to represent the relative orbital motion between two bodies using dedicated formulations,
    - the effects of the Earth's magnetic field on magnetic sensors and attitude actuators such as magnetorquers.

  All these factors can significantly influence both the trajectory and the attitude dynamics of a spacecraft.

- When testing a specific control law – especially a feedback control law – a co-simulation procedure with external software such as MATLAB/Simulink is typically required [120]. In this setup, the MSC Adams model functions as the plant within the control scheme. While this approach is feasible, it is not straightforward and can introduce complications into the overall simulation architecture. In contrast, the ability to implement both the plant and the control system within the same programming environment would greatly simplify the simulation process and enhance integration efficiency.

- Although several user guides and manuals are available, MSC Adams remains an external commercial tool and, as such, functions to some extent as a "black box." This limits the company's ability to gain a deep and complete understanding of its internal mechanisms or to modify it according to the specific and unique needs of different mission scenarios. In contrast, an in-house software solution offers full transparency and flexibility, as it is entirely owned and developed within the company. This allows for unrestricted customization and the integration of mission-specific features, including functionalities that may not strictly fall within the domain of dynamics, such as power budget analysis or ground track computation. Such additions can significantly expand the software's applicability, enabling its use in broader system-level analyses across a wide range of missions.

For all these reasons, the company supported the development of a generalized multibody simulation tool for space applications within the framework of this PhD work. Although the development is still ongoing, a first version of the software, written in MATLAB programming language, has been delivered. Although a different choice would have ensured better numerical performance, the MATLAB environment offers a wide library of functions and is very simple to use, facilitating the programming work at least at this preliminary stages. If the software proves to be convenient for the company, it can be decided to transfer it on a more convenient – from the performance point of view – programming language.

A.2 Code structure

The theoretical framework of the code is based on Kane's method, as presented in the first two chapters. This formulation is particularly well-suited for numerical applications due to its computational efficiency and its ability to be generalized through the recursive structures of partial velocities and remainder accelerations, as previously discussed. Therefore, to avoid redundancy, no additional details on the mathematical formulation of multibody dynamics are provided in this section.

In this section, the first delivered version of the software is presented, along with an analysis and discussion of its features and limitations. Additionally, strategies to overcome some of these limitations are discussed. Most of these improvements have already been implemented in the current, enhanced second version of the software, which is still under development.

A.2.1 Assembling procedure

The main input process in the software consists of constructing the multibody model of the spacecraft. This section explains how this construction is handled within the code. It is important to note that the first version of the software supports only tree-like spacecraft configurations, as the procedure for handling closed kinematic loops has not yet been implemented. The current assembly process begins with the first body, which is treated as the root of the tree structure. From there, additional bodies can be added in any order to form the desired configuration. Denoting C as the center of mass, Q as the "root joint", and $\underline{\underline{B}}$ as the reference triad of a body, the assembly process follows the scheme described below (cf. Figure A.1):

- First, the user is prompted to specify which existing body the new body should be attached to. In this discussion, the new (added) body is referred to as the *j*-th body, while the body it is attached to is referred to as the *i*-th body.

- Then, the following data are requested:
  - Vector connecting C_i to Q_j in components with respect to body frame $\underline{\underline{B}}_i$, i.e. $\underline{r}^{(i)}_{C_iQ_j}$
  - Vector connecting Q_j to C_j in components with respect to body frame $\underline{\underline{B}}_j$, i.e. $\underline{r}^{(j)}_{Q_jC_j}$
  - relative mounting orientation of $\underline{\underline{B}}_j$ with respect to $\underline{\underline{B}}_i$, i.e. $\underset{j\leftarrow i}{R}$.

It is worth noting that, to simplify the input process, vectors must be provided with their components expressed in the reference frame associated with the body to which they belong. Additionally, the relative mounting orientation between connected bodies can be specified using different parameterizations. For ease of use, the 3-2-1 Euler angle sequence is selected as the default parameterization, although other options are also available. During the assembly of the multibody structure, the configuration array (see Section 1.2.2) of the spacecraft is simultaneously constructed. This array, by itself, provides all the information needed to apply the recursive multibody formulation described in the first two chapters. Specifically, the configuration array decomposes the multibody structure into individual kinematic chains, clearly and uniquely identifying the links between the bodies that make up the system. The three key inputs required for each body during the assembly process are sufficient to fully define the relative position and orientation of the *j*-th body with respect to the *i*-th one. However, additional information is needed at this stage to complete the definition of the multibody configuration.

In particular, the user must specify the type of joint connecting the two bodies, with a focus on the number and type of relative degrees of freedom (DOFs) allowed. The current version of the code supports both prismatic and revolute joints, each of which can allow from 1 to 3 relative DOFs.

For revolute joints:

- In the 1-DOF case, the direction of the joint axis must be specified.
- In the 2-DOF and 3-DOF cases, the user must define the rotation sequence, following the logic described in Section 1.2.4.

For prismatic joints:

- In the 1-DOF and 2-DOF cases, the axis or plane of motion must be specified.
- In the 3-DOF case, the child body is allowed to translate freely in 3D space.

Additionally, the mounting values of the joint variables and their velocities must be provided. These mounting states are distinguished from the initial conditions in order to allow for a more flexible and comprehensive modeling capability.

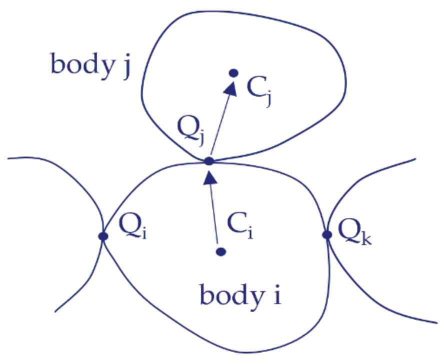

Figure A.1: Sketch of j-th body being attached to i-th body

A.2.2. List of modeling features

This section presents a complete list of the modeling features currently available in the software.

(a) The code can model any multibody system with a tree-like configuration, without restrictions on the number of bodies in the system. The interconnection between two bodies can be either a prismatic or a revolute joint, each allowing from 1 to 3 relative degrees of freedom. The two main limitations of the current version are: (i) only rigid bodies are supported, and (ii) only open-chain (tree-like) configurations are allowed. However, the theoretical framework required to extend the code to include flexible bodies and closed-loop kinematic chains has already been developed and systematized (see Chapters 1 and 2), and these features are planned for implementation in a future version.

(b) The code allows the user to impose prescribed time laws on one or more degrees of freedom of the multibody spacecraft, following the procedure described in Section 1.2.8. These time histories can either be autogenerated using an embedded function that constructs piecewise polynomial functions of time (up to third degree), or they can be imported directly from external files in .txt or .mat format.

(c) The prescribed time laws described in point (b) can also be used to impose internal torques or forces between interconnected bodies, or serve as reference trajectories for joint kinematic variables that are tracked using PD controllers.

(d) Linear or torsional spring-damper elements can also be assigned at joint locations.

(e) For more advanced control logic or to represent complex physical phenomena, the software can interface with external codes (if appropriately developed) that use the state vector to generate the required internal or external forces and torques.

(f) The spacecraft can be initialized in a desired orbit, defined either by position and velocity vectors or by Classical Orbital Elements (COE). When gravity forces are included, the code also models the corresponding gravity gradient torque.

With this capability, it is already possible to model a wide range of spacecraft configurations. However, the scope can be further expanded by first addressing the limitations mentioned in point (a), and then by introducing new features specifically related to space environment modeling and the inclusion of more advanced constraints.

A.2.3 User interface

At While the core part of the code is being developed, a user interface is also necessary to receive input data and provide graphical representation of the results. In the first delivered version, the input architecture relies on a series of dialog boxes generated within the MATLAB environment. The entire assembly process, along with the setting of initial conditions and some of the features discussed in the previous section, is managed through these dialog boxes. As an example, Figure A.2 shows the dialog box used to input data for attaching body 2 to body 1. The structure of these dialog boxes closely follows the process described in Section 0. Additionally, the final prompt in the dialog (on the right side) offers the option to enable a graphical representation of the bodies in 3D space. The software allows each body to be associated with a geometric solid (such as a cylinder, sphere, or box) or a CAD file. This enables not only an initial visualization of the assembled multibody system but also the creation of an animation depicting the system motion based on the dynamic simulation results, as in the CIMR case reported in Figure A.3. The animation is generated as part of a post-processing module that manipulates the time histories of the state vector, obtained from numerical integration, to produce time histories of other relevant quantities such as constraint reaction forces at the joints. This module also generates the required plots.

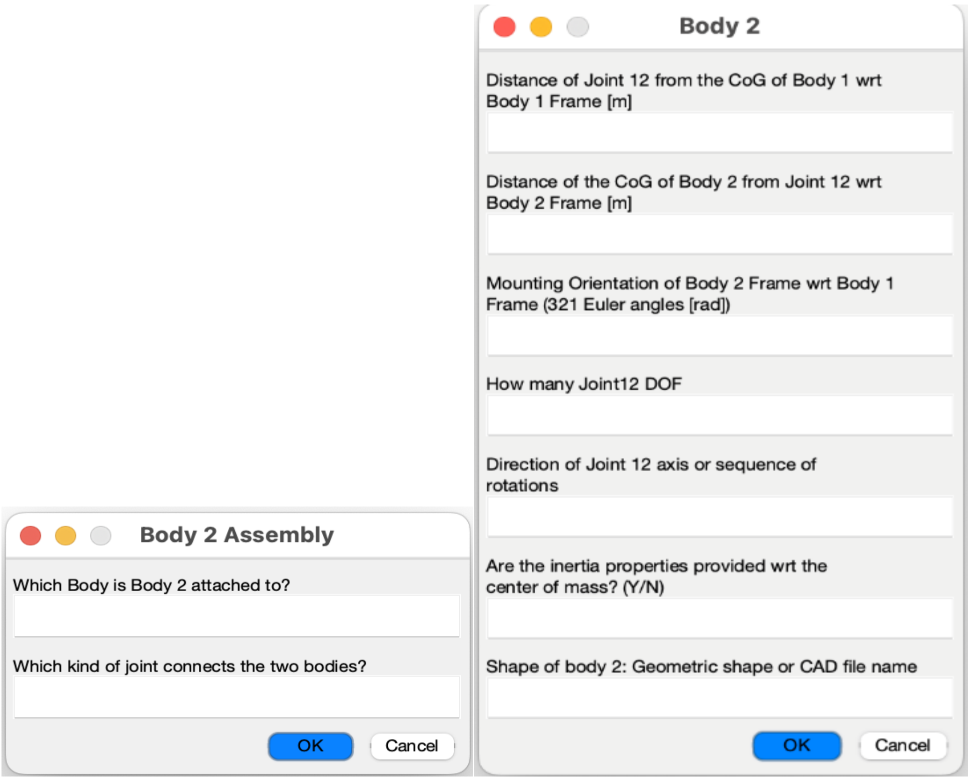

Figure A.2: Example of dialog box input

At the current stage, the user interface is still underdeveloped. The use of successive dialog boxes does not provide the desired modularity or ease in the input process. However, a new version of the interface is under development. This upcoming version aims to replace the dialog boxes with a comprehensive input window, allowing users to interact with the multibody structure via a pointer while the geometric representation remains visible throughout the entire assembly process. To achieve this, the existing geometric representation in the code is leveraged, and a series of subroutines have been developed and introduced to make the construction of the configuration array more flexible and modular. Nonetheless, this new interface is not yet fully defined, and further work is needed to finalize the software architecture and communication protocols.

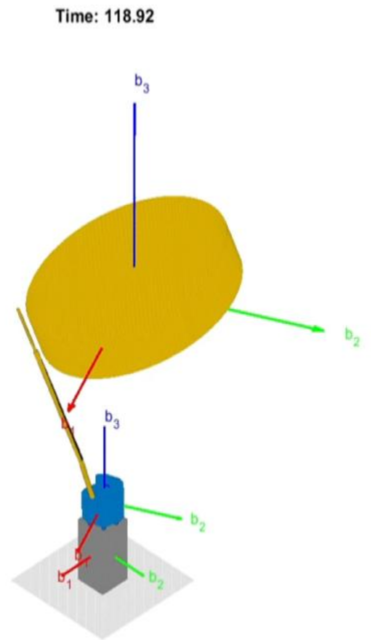

Figure A.3: Graphic representation of CIMR multibody spacecraft

As a concluding remark, it is worth noting that, although flexibility has not yet been fully integrated into the core code, some user interface tools for working with flexible bodies have already been developed. These tools were initially implemented in the model-based code created to simulate the dynamics of the CIMR spacecraft, which includes elastic components. Specifically, these tools are applied to the output stage and include: (i) the ability to select a specific node or group of nodes using the mouse pointer and visualize the associated deformation, including the option to display the relative elastic displacement between two selected points; and (ii) the ability to animate the elastic deflection of a flexible body, as illustrated in Figures A.4-A.5 for the case of the CIMR spacecraft LDRS. In the bottom-left corner of the figures, some interactive buttons and drop-down menus can be seen. These interface elements were implemented in the software to allow the user to interact with the animation and select the desired visualization parameters.

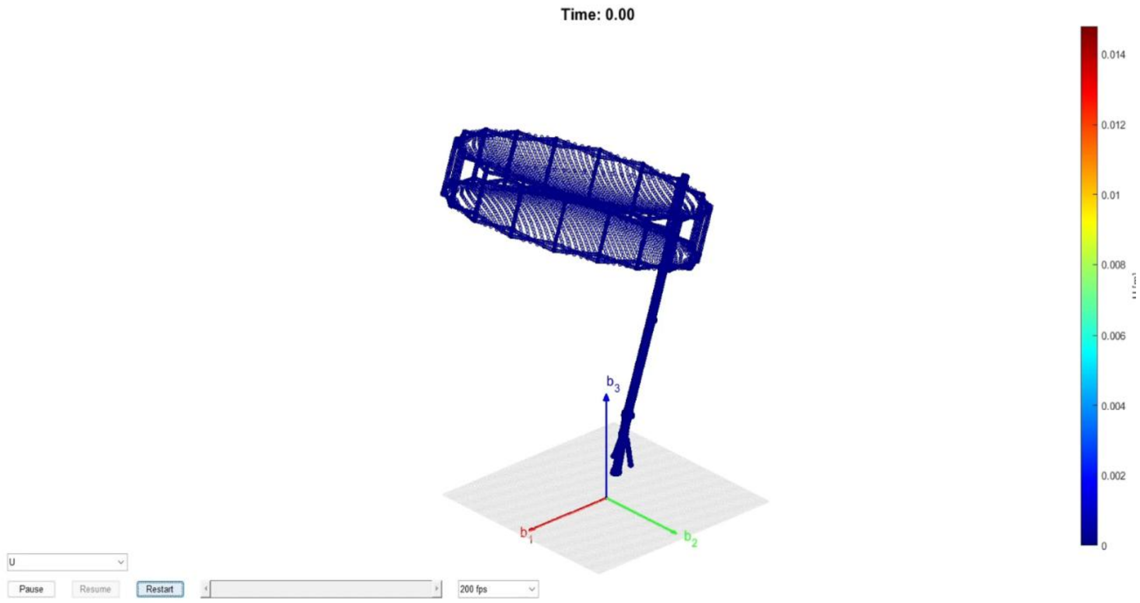

Figure A.4; CIMR elastic payload – undeformed configuration

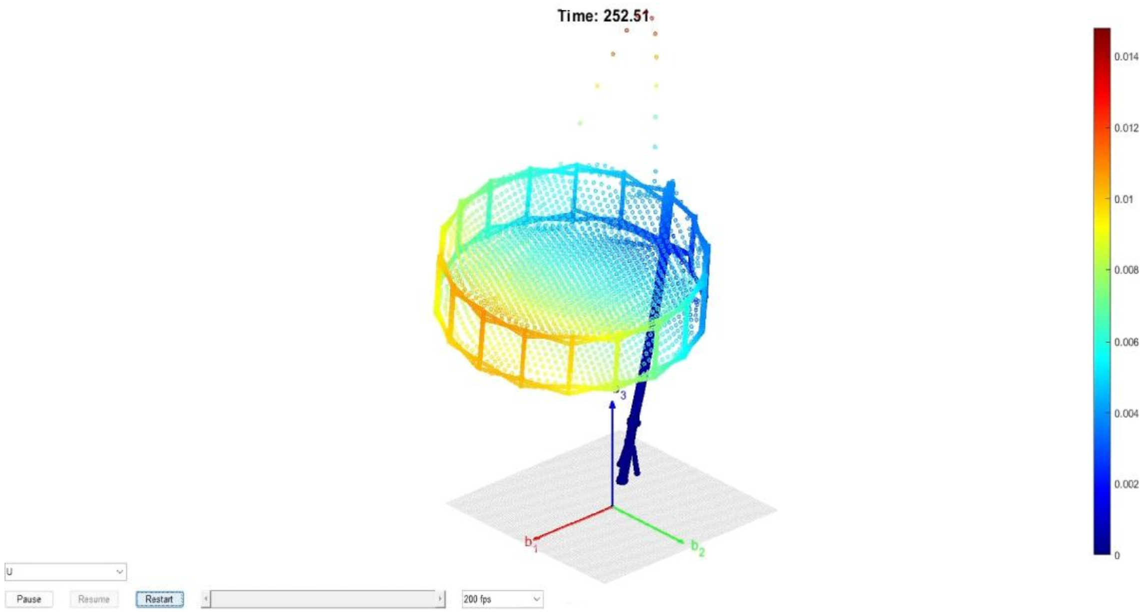

Figure A.5: CIMR elastic payload – deformed configuration

A.3 Numerical indications from preliminary results

Preliminary analyses – although not conducted in a systematic or comprehensive manner – have already been performed to gain a first insight into the actual advantages offered by the in-house developed software. It is important to emphasize that, from a numerical standpoint, the observed computational performance is entirely attributable to the use of Kane's formulation, since the software itself essentially acts as a generalized implementation of these equations, equipped with a user-friendly input interface.

Given that no extensive simulation campaign has yet been carried out, the considerations presented here are limited to a few isolated cases in which comparative simulations were run using both MSC Adams and the in-house code. In these cases, specific numerical aspects were evaluated. Overall, these initial comparisons indicated a consistent reduction in computational cost when using the in-house software. This performance gain was observed in both deep-space scenarios and simulations involving satellites in defined orbits. Notably, in the latter category – where both attitude and orbital dynamics had to be integrated simultaneously – the performance gap widened significantly. The improved efficiency in such cases is likely due to the software ability to leverage MATLAB built-in integrators, such as ode113 and ode45 [121], which adapt the integration step based on the instantaneous numerical stiffness of the system. By contrast, despite various parameter tuning options, the MSC Adams integrator was never able to match the performance of the custom tool.

In fact, the in-house software consistently outperformed MSC Adams not only in terms of faster execution times but also in terms of numerical accuracy. This was assessed in two ways: (i) for simulations conducted in deep space – i.e., in the absence of external forces and torques – the conservation of total linear and angular momenta (cf. Section 1.3.5) was used as a benchmark; (ii) for orbit-based simulations without perturbations, the conservation of the classical orbital elements (excluding true anomaly) was evaluated. In both cases, the custom software yielded smaller deviations from expected conservation laws than MSC Adams.

Although these results remain preliminary and not yet conclusive, they are nonetheless promising. They support the continuation of the software development effort and suggest that, especially for space mission simulations, the in-house code offers tangible benefits over general-purpose commercial tools, particularly in terms of flexibility, performance, and suitability for space-specific applications.

A.4 Concluding remarks

In this appendix, the development of an in-house multibody simulation tool within the framework of this PhD research is presented and discussed. Starting from a clear industrial need identified by Thales Alenia Space Italia, the work addressed critical limitations of commercial software – particularly in terms of flexibility, transparency, and the integration of space-specific functionalities. The Kane's method is adopted as the theoretical foundation because of its recursive structure and computational efficiency, which are especially valuable in numerical implementations. The first delivered version of the software can model tree-like multibody configurations with a reasonable degree of automation and user interaction, even within a high-level environment such as MATLAB. The modular input structure, the modeling features described in this appendix, and the preliminary user interface with basic 3D visualization capabilities already allow for the simulation of a wide variety of realistic spacecraft scenarios. Nonetheless, the current version still presents some limitations, including the restriction to rigid bodies and open-chain architectures, as well as the lack of a fully developed graphical interface. These shortcomings have already been acknowledged, and strategies for addressing them have been outlined. In particular, the integration of flexible components and closed kinematic loops will considerably enhance the tool modeling capabilities. The same applies to the transition from dialog-based input to an interactive and more intuitive graphical interface, which is currently under development. The preliminary results showed encouraging performance of the developed tool if compared to the general-purpose commercial software, leading to further motivation to continue its development and progressively transform it into a more structured and comprehensive simulation environment.

References

[1] D. Tripathi *et al.*, "The Aditya-L1 mission of ISRO," in *Proceedings of the International Astronomical Union*, vol. 18, Cambridge University Press, 2022, pp. 17–27. doi: 10.1017/S1743921323001230.

[2] M. Arcioni *et al.*, "The Biomass mission, status of the satellite system," in *2014 IEEE Geoscience and Remote Sensing Symposium*, IEEE, Jul. 2014, pp. 1413–1416. doi: 10.1109/IGARSS.2014.6946700.

[3] M. R. Bolcar, "The Large UV/Optical/Infrared (LUVOIR) surveyor: engineering design and technology overview," in *UV/Optical/IR Space Telescopes and Instruments: Innovative Technologies and Concepts IX*, J. B. Breckinridge, H. P. Stahl, and A. A. Barto, Eds., SPIE, Sep. 2019, p. 24. doi: 10.1117/12.2530456.

[4] P. Xaypraseuth, R. Satish, and A. Chatterjee, "NISAR spacecraft concept overview: Design challenges for a proposed flagship dual-frequency SAR mission," in *2015 IEEE Aerospace Conference*, IEEE, Mar. 2015, pp. 1–11. doi: 10.1109/AERO.2015.7118935.

[5] K. Kellogg *et al.*, "NASA's Soil Moisture Active Passive (SMAP) observatory," in *2013 IEEE Aerospace Conference*, IEEE, Mar. 2013, pp. 1–20. doi: 10.1109/AERO.2013.6496938.

[6] Y. Cui, P. Lan, H. Zhou, and Z. Yu, "The Rigid-Flexible-Thermal Coupled Analysis for Spacecraft Carrying Large-Aperture Paraboloid Antenna," *J Comput Nonlinear Dyn*, vol. 15, no. 3, Mar. 2020, doi: 10.1115/1.4045890.

[7] M. K. Chamberlain, S. H. Kiefer, M. LaPointe, and P. LaCorte, "On-orbit flight testing of the Roll-Out Solar Array," *Acta Astronaut*, vol. 179, pp. 407–414, Feb. 2021, doi: 10.1016/j.actaastro.2020.10.024.

[8] M. A. Roa, K. Nottensteiner, A. Wedler, and G. Grunwald, "Robotic Technologies for In-Space Assembly Operations."

[9] L. Kilic *et al.*, "Expected Performances of the Copernicus Imaging Microwave Radiometer (CIMR) for an All-Weather and High Spatial Resolution Estimation of Ocean and Sea Ice Parameters," *J Geophys Res Oceans*, vol. 123, no. 10, pp. 7564–7580, Oct. 2018, doi: 10.1029/2018JC014408.

[10] C. Jiménez *et al.*, “Ocean and Sea Ice Retrievals From an End-To-End Simulation of the Copernicus Imaging Microwave Radiometer (CIMR) 1.4–36.5 GHz Measurements,” *J Geophys Res Oceans*, vol. 126, no. 12, Dec. 2021, doi: 10.1029/2021JC017610.

[11] D. Ciani, R. Santoleri, G. L. Liberti, C. Prigent, C. Donlon, and B. B. Nardelli, “Copernicus Imaging Microwave Radiometer (CIMR) benefits for the copernicus level 4 Sea-Surface Salinity processing chain,” *Remote Sens (Basel)*, vol. 11, no. 15, Aug. 2019, doi: 10.3390/rs11151818.

[12] P. Li, C. Liu, Q. Tian, H. Hu, and Y. Song, “Dynamics of a Deployable Mesh Reflector of Satellite Antenna: Parallel Computation and Deployment Simulation1,” *J Comput Nonlinear Dyn*, vol. 11, no. 6, Nov. 2016, doi: 10.1115/1.4033657.

[13] F. Zhang and G.-R. Duan, “Integrated relative position and attitude control of spacecraft in proximity operation missions,” *International Journal of Automation and Computing*, vol. 9, no. 4, pp. 342–351, Aug. 2012, doi: 10.1007/s11633-012-0654-0.

[14] P. E. Nikravesh, “An Overview of Several Formulations for Multibody Dynamics,” in *Product Engineering*, Dordrecht: Kluwer Academic Publishers, pp. 189–226. doi: 10.1007/1-4020-2933-0_13.

[15] P. Santini and P. Gasbarri, “Dynamics of multibody systems in space environment; Lagrangian vs. Eulerian approach,” *Acta Astronaut*, vol. 54, no. 1, pp. 1–24, Jan. 2004, doi: 10.1016/S0094-5765(02)00277-1.

[16] A. Pisculli, L. Felicetti, M. Sabatini, P. Gasbarri, and G. B. Palmerini, “A Hybrid Formulation for Modelling Multibody Spacecraft,” *Aerotecnica Missili & Spazio*, vol. 94, no. 2, pp. 91–101, Apr. 2015, doi: 10.1007/BF03404692.

[17] A. A. Shabana, “Flexible Multibody Dynamics: Review of Past and Recent Developments,” *Multibody Syst Dyn*, vol. 1, no. 2, pp. 189–222, Jun. 1997, doi: 10.1023/A:1009773505418.

[18] C. Gontier and Y. Li, “Lagrangian formulation and linearization of multibody system equations,” *Comput Struct*, vol. 57, no. 2, pp. 317–331, Oct. 1995, doi: 10.1016/0045-7949(94)00599-X.

[19] F. Amirouche and S. Ider, “Numerical Stability of Constrained Multibody Systems,” in *Fundamentals of Multibody Dynamics*, Boston, MA: Birkhäuser Boston, pp. 395–428. doi: 10.1007/0-8176-4406-7_8.

[20] T. R. Kane, P. W. Likins, and D. A. Levinson, *Spacecraft Dyanimcs*. McGraw Hill, 1983.

[21] E. Stoneking, "Newton-Euler Dynamic Equations of Motion for a Multi-Body Spacecraft," in *AIAA Guidance, Navigation and Control Conference and Exhibit*, Reston, Virigina: American Institute of Aeronautics and Astronautics, Aug. 2007. doi: 10.2514/6.2007-6441.

[22] T. R. Kane and D. A. Levinson, "Formulation of Equations of Motion for Complex Spacecraft," *Journal of Guidance and Control*, vol. 3, no. 2, pp. 99–112, Mar. 1980, doi: 10.2514/3.55956.

[23] J. Vaz Carneiro, C. Allard, and H. Schaub, "Effector Dynamics For Sequentially Rotating Rigid Body Spacecraft Components," in *AAS/AIAA Astrodynamics Specialist Conference*, Big Sky, Montana, Aug. 2023.

[24] J. Vaz Carneiro, P. Johnson, and H. Schaub, "Backsubstitution Method For Spacecraft With Generally Translating Appendages," in *AAS Astrodynamics Specialist Conference*, Broomfield, CO, Aug. 2024.

[25] A. A. Al-Qaisia and B. O. Al-Bedoor, "Evaluation of different methods for the consideration of the effect of rotation on the stiffening of rotating beams," *J Sound Vib*, vol. 280, no. 3–5, pp. 531–553, Feb. 2005, doi: 10.1016/j.jsv.2003.12.049.

[26] Z. Xian, P. Lertkultanon, and Q.-C. Pham, "Closed-Chain Manipulation of Large Objects by Multi-Arm Robotic Systems," *IEEE Robot Autom Lett*, vol. 2, no. 4, pp. 1832–1839, Oct. 2017, doi: 10.1109/LRA.2017.2708134.

[27] A. E. P. Veldman, J. Gerrits, R. Luppes, J. A. Helder, and J. P. B. Vreeburg, "The numerical simulation of liquid sloshing on board spacecraft," *J Comput Phys*, vol. 224, no. 1, pp. 82–99, May 2007, doi: 10.1016/j.jcp.2006.12.020.

[28] W. Yu, D. I. Wilson, and B. R. Young, "A comparison of nonlinear control performance assessment techniques for nonlinear processes," *Can J Chem Eng*, vol. 90, no. 6, pp. 1442–1449, Dec. 2012, doi: 10.1002/cjce.21733.

[29] M. Pontani, A. Pianalto, S. Carletta, and P. Teofilatto, "Near-Optimal Guidance and Pulse-Modulated Reduced-Attitude Control for Orbit Injection," 2023, pp. 301–329. doi: 10.1007/978-3-031-24812-2_11.

[30] J. T.-Y. Wen and K. Kreutz-Delgado, “The attitude control problem,” *IEEE Trans Automat Contr*, vol. 36, no. 10, pp. 1148–1162, 1991, doi: 10.1109/9.90228.

[31] F. L. Markley and J. L. Crassidis, *Fundamentals of Spacecraft Attitude Determination and Control*. New York, NY: Springer New York, 2014. doi: 10.1007/978-1-4939-0802-8.

[32] A. Daniel Ogundele, “Nonlinear Dynamics and Control of Spacecraft Relative Motion,” Auburn University, Auburn, Alabama, 2017. doi: 10.13140/RG.2.2.35073.48484.

[33] M. J. Doshi, N. M. Pathak, and E. I. Abouelmagd, “Periodic orbits of the perturbed relative motion,” *Advances in Space Research*, vol. 72, no. 6, pp. 2020–2038, Sep. 2023, doi: 10.1016/j.asr.2023.05.053.

[34] R. Santoro and M. Pontani, “Orbit acquisition, rendezvous, and docking with a noncooperative capsule in a Mars sample return mission,” *Acta Astronaut*, vol. 211, pp. 950–962, Oct. 2023, doi: 10.1016/j.actaastro.2023.04.043.

[35] Z.-F. Fu and J. He, *Modal analysis*. Elsevier, 2001.

[36] S. Giorgi, *Una Formulazione Caratteristica del Metodo di Encke in Vista dell'Applicazione Numerica*. Rome: Scuola di Ingegneria Aerospaziale, 1964.

[37] M. Pontani, *Advanced Spacecraft Dynamics*. Rome: Edizioni Efesto, 2023.

[38] M. W. Sayers, “Symbolic vector/dyadic multibody formalism for tree-topology systems,” *Journal of Guidance, Control, and Dynamics*, vol. 14, no. 6, pp. 1240–1250, Nov. 1991, doi: 10.2514/3.20780.

[39] G. A. Sohl and J. E. Bobrow, “A Recursive Multibody Dynamics and Sensitivity Algorithm for Branched Kinematic Chains,” *J Dyn Syst Meas Control*, vol. 123, no. 3, pp. 391–399, Sep. 2001, doi: 10.1115/1.1376121.

[40] E. Stoneking, “Implementation of Kane's Method for a Spacecraft Composed of Multiple Rigid Bodies,” in *AIAA Guidance, Navigation, and Control (GNC) Conference*, Reston, Virginia: American Institute of Aeronautics and Astronautics, Aug. 2013. doi: 10.2514/6.2013-4649.

[41] A. Pisculli, L. Felicetti, M. Sabatini, P. Gasbarri, and G. B. Palmerini, “A Hybrid Formulation for Modelling Multibody Spacecraft,” *Aerotecnica*

Missili & Spazio, vol. 94, no. 2, pp. 91–101, Apr. 2015, doi: 10.1007/BF03404692.

[42] G. R. Hintz, “Survey of Orbit Element Sets,” *Journal of Guidance, Control, and Dynamics*, vol. 31, no. 3, pp. 785–790, May 2008, doi: 10.2514/1.32237.

[43] J. R. Phillips and F. Amirouche, “A momentum form of Kane’s equations for scleronomic systems,” *Math Comput Model Dyn Syst*, vol. 24, no. 2, pp. 143–169, Mar. 2018, doi: 10.1080/13873954.2017.1385638.

[44] C. M. Pappalardo and D. Guida, “On the Lagrange multipliers of the intrinsic constraint equations of rigid multibody mechanical systems,” *Archive of Applied Mechanics*, vol. 88, no. 3, pp. 419–451, Mar. 2018, doi: 10.1007/s00419-017-1317-y.

[45] F. E. Udwadia and A. D. Schutte, “Equations of motion for general constrained systems in Lagrangian mechanics,” *Acta Mech*, vol. 213, no. 1–2, pp. 111–129, Aug. 2010, doi: 10.1007/s00707-009-0272-2.

[46] A. H. Bajodah, D. H. Hodges, and Y.-H. Chen, “New Form of Kane’s Equations of Motion for Constrained Systems,” *Journal of Guidance, Control, and Dynamics*, vol. 26, no. 1, pp. 79–88, Jan. 2003, doi: 10.2514/2.5017.

[47] F. Marques, I. Roupa, M. T. Silva, P. Flores, and H. M. Lankarani, “Examination and comparison of different methods to model closed loop kinematic chains using Lagrangian formulation with cut joint, clearance joint constraint and elastic joint approaches,” *Mech Mach Theory*, vol. 160, p. 104294, Jun. 2021, doi: 10.1016/j.mechmachtheory.2021.104294.

[48] Y.-C. Li and H.-L. Gou, “Modeling Problem of Equivalent Mechanical Models of a Sloshing Fluid,” *Shock and Vibration*, vol. 2018, no. 1, Jan. 2018, doi: 10.1155/2018/2350716.

[49] Z. Zhou and H. Huang, “Constraint surface model for large amplitude sloshing of the spacecraft with multiple tanks,” *Acta Astronaut*, vol. 111, pp. 222–229, Jun. 2015, doi: 10.1016/j.actaastro.2015.02.023.

[50] L. Feng, Y. Baozeng, A. K. Banerjee, T. Yong, W. Wenjun, and L. Zhengyong, “Large Motion Dynamics of In-Orbit Flexible Spacecraft with Large-Amplitude Propellant Slosh,” *Journal of Guidance, Control, and Dynamics*, vol. 43, no. 3, pp. 438–450, Mar. 2020, doi: 10.2514/1.G004685.

[51] M. Nosonovsky, “Model for solid-liquid and solid-solid friction of rough surfaces with adhesion hysteresis,” *J Chem Phys*, vol. 126, no. 22, Jun. 2007, doi: 10.1063/1.2739525.

[52] G. G. Adams and M. Nosonovsky, “Contact modeling — forces,” *Tribol Int*, vol. 33, no. 5–6, pp. 431–442, May 2000, doi: 10.1016/S0301-679X(00)00063-3.

[53] B. Siciliano, L. Sciavicco, L. Villani, and G. Oriolo, *Robotics*. London: Springer London, 2009. doi: 10.1007/978-1-84628-642-1.

[54] T. R. Kane and D. A. Levinson, “The Use of Kane’s Dynamical Equations in Robotics,” *Int J Rob Res*, vol. 2, no. 3, pp. 3–21, Sep. 1983, doi: 10.1177/027836498300200301.

[55] E. Papadopoulos, F. Aghili, O. Ma, and R. Lampariello, “Robotic Manipulation and Capture in Space: A Survey,” *Front Robot AI*, vol. 8, Jul. 2021, doi: 10.3389/frobt.2021.686723.

[56] A. Stolfi, P. Gasbarri, and M. Sabatini, “A combined impedance-PD approach for controlling a dual-arm space manipulator in the capture of a non-cooperative target,” *Acta Astronaut*, vol. 139, pp. 243–253, Oct. 2017, doi: 10.1016/j.actaastro.2017.07.014.

[57] J. He, H. Zheng, F. Gao, and H. Zhang, “Dynamics and control of a 7-DOF hybrid manipulator for capturing a non-cooperative target in space,” *Mech Mach Theory*, vol. 140, pp. 83–103, Oct. 2019, doi: 10.1016/j.mechmachtheory.2019.05.020.

[58] Y. Zheng, “Collision Effects on Two Coordinating Robots in Assembly and the Effect Minimization,” *IEEE Trans Syst Man Cybern*, vol. 17, no. 1, pp. 108–116, Jan. 1987, doi: 10.1109/TSMC.1987.289340.

[59] Liang-Boon Wee and M. W. Walker, “On the dynamics of contact between space robots and configuration control for impact minimization,” *IEEE Transactions on Robotics and Automation*, vol. 9, no. 5, pp. 581–591, 1993, doi: 10.1109/70.258051.

[60] F. Feng, L. Tang, J. Xu, H. Liu, and Y. Liu, “A review of the end-effector of large space manipulator with capabilities of misalignment tolerance and soft capture,” *Sci China Technol Sci*, vol. 59, no. 11, pp. 1621–1638, Nov. 2016, doi: 10.1007/s11431-016-0084-7.

[61] A. H. Nayfeh and P. F. Pai, *Linear and Nonlinear Structural Mechanics*. Wiley, 2004. doi: 10.1002/9783527617562.

[62] O. C. Zienkiewicz, R. L. Taylor, and D. Fox, *The Finite Element Method for Solid and Structural Mechanics*. Elsevier, 2014. doi: 10.1016/C2009-0-26332-X.

[63] S. S. Rao, *Vibration of Continuous Systems*. Wiley, 2006. doi: 10.1002/9780470117866.

[64] A. K. Banerjee and M. E. Lemak, "Multi-Flexible Body Dynamics Capturing Motion-Induced Stiffness," *J Appl Mech*, vol. 58, no. 3, pp. 766–775, Sep. 1991, doi: 10.1115/1.2897262.

[65] A. A. Shabana and G. Wang, "Durability analysis and implementation of the floating frame of reference formulation," *Proceedings of the Institution of Mechanical Engineers, Part K: Journal of Multi-body Dynamics*, vol. 232, no. 3, pp. 295–313, Sep. 2018, doi: 10.1177/1464419317731707.

[66] A. K. . Banerjee, *Flexible multibody dynamics : efficient formulations and applications*. Wiley, 2016.

[67] M. Gürgöze and S. Zeren, "The influences of both offset and mass moment of inertia of a tip mass on the dynamics of a centrifugally stiffened visco-elastic beam," *Meccanica*, vol. 46, no. 6, pp. 1401–1412, Dec. 2011, doi: 10.1007/s11012-010-9396-7.

[68] M. Nieto, M. Elsayed, and D. Walch, "Modal Participation Factors And Their Potential Applications In Aerospace: A Review," in *Progress in Canadian Mechanical Engineering*, York University Libraries, May 2018. doi: 10.25071/10315/35254.

[69] K. Zhang, S. Wu, and Z. Wu, "Effect Analysis of Gravity Gradient on Attitude–Elastic Motion of a Solar Power Satellite," *AIAA Journal*, vol. 60, no. 10, pp. 6041–6048, Oct. 2022, doi: 10.2514/1.J061914.

[70] L. Rouleau, J.-F. Deü, and A. Legay, "A comparison of model reduction techniques based on modal projection for structures with frequency-dependent damping," *Mech Syst Signal Process*, vol. 90, pp. 110–125, Jun. 2017, doi: 10.1016/j.ymssp.2016.12.013.

[71] J. H. Seinfeld, L. Lapidus, and M. Hwang, "Review of Numerical Integration Techniques for Stiff Ordinary Differential Equations,"

Industrial & Engineering Chemistry Fundamentals, vol. 9, no. 2, pp. 266–275, May 1970, doi: 10.1021/i160034a013.

[72] B. Szabó and G. Királyfalvi, "Linear models of buckling and stress-stiffening," *Comput Methods Appl Mech Eng*, vol. 171, no. 1–2, pp. 43–59, Mar. 1999, doi: 10.1016/S0045-7825(98)00241-2.

[73] C. M. Roithmayr and D. H. Hodges, "Dynamics: Theory and Application of Kane's Method," *J Comput Nonlinear Dyn*, vol. 11, no. 6, Nov. 2016, doi: 10.1115/1.4034731.

[74] A. K. Banerjee and J. M. Dickens, "Dynamics of an arbitrary flexible body in large rotation and translation," *Journal of Guidance, Control, and Dynamics*, vol. 13, no. 2, pp. 221–227, Mar. 1990, doi: 10.2514/3.20540.

[75] T. R. Kane, R. R. Ryan, and A. K. Banerjeer, "Dynamics of a cantilever beam attached to a moving base," *Journal of Guidance, Control, and Dynamics*, vol. 10, no. 2, pp. 139–151, Mar. 1987, doi: 10.2514/3.20195.

[76] A. M. Long, M. G. Richards, and D. E. Hastings, "On-Orbit Servicing: A New Value Proposition for Satellite Design and Operation," *J Spacecr Rockets*, vol. 44, no. 4, pp. 964–976, Jul. 2007, doi: 10.2514/1.27117.

[77] D. Malyh, S. Vaulin, V. Fedorov, R. Peshkov, and M. Shalashov, "A brief review on in-orbit refueling projects and critical techniques," *Aerospace Systems*, vol. 5, no. 2, pp. 185–196, Jun. 2022, doi: 10.1007/s42401-022-00132-2.

[78] G. Arantes and L. S. Martins-Filho, "Guidance and Control of Position and Attitude for Rendezvous and Dock/Berthing with a Noncooperative/Target Spacecraft," *Math Probl Eng*, vol. 2014, no. 1, Jan. 2014, doi: 10.1155/2014/508516.

[79] F. Gao, J. Li, and G. Sun, "Efficient and accurate flexible multibody dynamics modeling for complex spacecraft with integrated control applications," *Acta Astronaut*, vol. 219, pp. 818–825, Jun. 2024, doi: 10.1016/j.actaastro.2024.03.071.

[80] S. Tafazoli and K. Khorasani, "Nonlinear control and stability analysis of spacecraft attitude recovery," *IEEE Trans Aerosp Electron Syst*, vol. 42, no. 3, pp. 825–845, Jul. 2006, doi: 10.1109/TAES.2006.248187.

[81] L. Ravikumar, R. Padhi, and N. K. Philip, "Trajectory optimization for Rendezvous and Docking using Nonlinear Model Predictive Control,"

IFAC-PapersOnLine, vol. 53, no. 1, pp. 518–523, 2020, doi: 10.1016/j.ifacol.2020.06.087.

[82] P. C. Hughes, *Spacecraft Attitude Dynamics*. Dover Publications, 2004.

[83] G. Q. Xing and S. A. Parvez, "Nonlinear Attitude State Tracking Control for Spacecraft," *Journal of Guidance, Control, and Dynamics*, vol. 24, no. 3, pp. 624–626, May 2001, doi: 10.2514/2.4754.

[84] H. K. Khalil, *Nonlinear Systems*. Upper Saddle River, NJ: Prentice-Hall, 2002.

[85] G. Avanzini and F. Giulietti, "Constrained Slews for Single-Axis Pointing," *Journal of Guidance, Control, and Dynamics*, vol. 31, no. 6, pp. 1814–1817, Nov. 2008, doi: 10.2514/1.38291.

[86] M. Yu. Ovchinnikov, D. S. Roldugin, and V. I. Penkov, "Asymptotic study of a complete magnetic attitude control cycle providing a single-axis orientation," *Acta Astronaut*, vol. 77, pp. 48–60, Aug. 2012, doi: 10.1016/j.actaastro.2012.03.001.

[87] F. A. Leve, B. J. Hamilton, and M. A. Peck, *Spacecraft Momentum Control Systems*. Cham: Springer International Publishing, 2015. doi: 10.1007/978-3-319-22563-0.

[88] S. Pan, Z. Xu, and C. Zhao, "A novel single-gimbal control moment gyroscope driven by an ultrasonic motor," *Advances in Mechanical Engineering*, vol. 11, no. 4, Apr. 2019, doi: 10.1177/1687814019844382.

[89] J. C. A. Barata and M. S. Hussein, "The Moore–Penrose Pseudoinverse: A Tutorial Review of the Theory," *Brazilian Journal of Physics*, vol. 42, no. 1–2, pp. 146–165, Apr. 2012, doi: 10.1007/s13538-011-0052-z.

[90] J. A. Kéchichian, *Orbital Relative Motion and Terminal Rendezvous*. Cham: Springer International Publishing, 2021. doi: 10.1007/978-3-030-64657-8.

[91] Z. Dang, "Solutions of Tschauner–Hempel Equations," *Journal of Guidance, Control, and Dynamics*, vol. 40, no. 11, pp. 2956–2960, Nov. 2017, doi: 10.2514/1.G002774.

[92] I. Napoli and M. Pontani, "Discrete-Variable-Thrust Guidance for Orbital Rendezvous Based on Feedback Linearization," *Aerotecnica Missili & Spazio*, vol. 101, no. 4, pp. 351–360, Dec. 2022, doi: 10.1007/s42496-022-00124-7.

[93] D. Sanna, D. P. Madonna, M. Pontani, and P. Gasbarri, "Orbit Rendezvous Maneuvers in Cislunar Space via Nonlinear Hybrid Predictive Control," *Dynamics*, vol. 4, no. 3, pp. 609–642, Aug. 2024, doi: 10.3390/dynamics4030032.

[94] L. Felicetti, P. Gasbarri, A. Pisculli, M. Sabatini, and G. B. Palmerini, "Design of robotic manipulators for orbit removal of spent launchers' stages," *Acta Astronaut*, vol. 119, pp. 118–130, Feb. 2016, doi: 10.1016/j.actaastro.2015.11.012.

[95] A. De Bonis, F. Angeletti, P. Iannelli, and P. Gasbarri, "Mixed Kane–Newton Multi-Body Analysis of a Dual-Arm Robotic System for On-Orbit Servicing Missions," *Aerotecnica Missili & Spazio*, vol. 100, no. 4, pp. 375–386, Dec. 2021, doi: 10.1007/s42496-021-00088-0.

[96] F. A. Leve, "Development of the spacecraft orientation buoyancy experimental kiosk," University of Florida, Gainesville, 2008.

[97] K. Holste *et al.*, "Ion thrusters for electric propulsion: Scientific issues developing a niche technology into a game changer," *Review of Scientific Instruments*, vol. 91, no. 6, p. 061101, Jun. 2020, doi: 10.1063/5.0010134.

[98] E. De Pasquale, "ATV Jules Verne: a Step by Step Approach for In- Orbit Demonstration of New Rendezvous Technologies," in *SpaceOps 2012 Conference*, Reston, Virigina: American Institute of Aeronautics and Astronautics, Jun. 2012. doi: 10.2514/6.2012-1314619.

[99] P. Gasbarri, R. Monti, C. De Angelis, and M. Sabatini, "Effects of uncertainties and flexible dynamic contributions on the control of a spacecraft full-coupled model," *Acta Astronaut*, vol. 94, no. 1, pp. 515–526, Jan. 2014, doi: 10.1016/j.actaastro.2012.08.018.

[100] A. Eremenko, J. Kastner, and P. Hoffman, "SMAP Observatory configuration, from concept to preliminary design," in *2010 IEEE Aerospace Conference*, IEEE, Mar. 2010, pp. 1–11. doi: 10.1109/AERO.2010.5446761.

[101] G. Zhang, S. Qiu, and F. Wang, "Adaptive Fuzzy Fault-Tolerant Control of Flexible Spacecraft with Rotating Appendages," *International Journal of Fuzzy Systems*, vol. 25, no. 1, pp. 326–337, Feb. 2023, doi: 10.1007/s40815-022-01338-4.

[102] G. L. Ketner, "Survey of historical incidences with Controls-Structures Interaction and recommended technology improvements needed to put

hardware in space," Richland, WA (United States), Mar. 1989. doi: 10.2172/6179780.

[103] R. R. Ryan, "ADAMS — Multibody System Analysis Software," in *Multibody Systems Handbook*, Berlin, Heidelberg: Springer Berlin Heidelberg, 1990, pp. 361–402. doi: 10.1007/978-3-642-50995-7_21.

[104] R. H. MacNeal and C. W. McCormick, "The NASTRAN computer program for structural analysis," *Comput Struct*, vol. 1, no. 3, pp. 389–412, Oct. 1971, doi: 10.1016/0045-7949(71)90021-6.

[105] R. Rodrigues, D. Alazard, F. Sanfedino, T. Mauriello, and P. Iannelli, "Modeling and analysis of a flexible spinning Euler-Bernoulli beam with centrifugal stiffening and softening: A linear fractional representation approach with application to spinning spacecraft," *Appl Math Model*, vol. 137, p. 115699, Jan. 2025, doi: 10.1016/j.apm.2024.115699.

[106] L. Bourrec, L. Bernabé, V. Pires, and S. Tremolieres, "Telescopic Boom for Space Applications - Engineering Model," in *14th European Space Mechanisms & Tribology Symposium–ESMATS Constance*, Germany, 2011.

[107] M. Mobrem and C. Spier, "Design and performance of the telescopic tubular mast," in *41st Aerospace Mechanisms Symposium*, Washington DC: NASA, 2012.

[108] T. Sun *et al.*, "Dynamic Modeling and Analysis of Deployable Telescope Tubular Mast (TTM) in Spacecraft Systems using Hybrid Coordinate and Kane's Methods," in *IAF Materials and Structures Symposium*, Paris, France: International Astronautical Federation (IAF), 2024, pp. 109–122. doi: 10.52202/078369-0014.

[109] M. Smith *et al.*, "The Artemis Program: An Overview of NASA's Activities to Return Humans to the Moon," in *2020 IEEE Aerospace Conference*, IEEE, Mar. 2020, pp. 1–10. doi: 10.1109/AERO47225.2020.9172323.

[110] L. Liu and Y. Liu, "A note on the computation of multi-revolution NRHO under the ephemeris model," *Advances in Space Research*, vol. 75, no. 3, pp. 2889–2907, Feb. 2025, doi: 10.1016/j.asr.2024.11.001.

[111] W. C. Feldman, S. Maurice, A. B. Binder, B. L. Barraclough, R. C. Elphic, and D. J. Lawrence, "Fluxes of Fast and Epithermal Neutrons from Lunar Prospector: Evidence for Water Ice at the Lunar Poles," *Science (1979)*, vol.

281, no. 5382, pp. 1496–1500, Sep. 1998, doi: 10.1126/science.281.5382.1496.

[112] J. M. Pairot, M. Frezet, J. Tailhades, W. Fehse, A. Tobias, and A. Getzschmann, “European rendezvous and docking system,” *Acta Astronaut*, vol. 28, pp. 31–42, Aug. 1992, doi: 10.1016/0094-5765(92)90007-6.

[113] C. D’Souza, C. Hannak, P. Spehar, F. Clark, and M. Jackson, “Orion Rendezvous, Proximity Operations and Docking Design and Analysis,” in *AIAA Guidance, Navigation and Control Conference and Exhibit*, Reston, Virigina: American Institute of Aeronautics and Astronautics, Aug. 2007. doi: 10.2514/6.2007-6683.

[114] D. E. Lee, “White paper: Gateway destination orbit model: A continuous 15 year nrho reference trajectory,” 2019.

[115] R. Whitley and R. Martinez, “Options for staging orbits in cislunar space,” in *2016 IEEE Aerospace Conference*, IEEE, Mar. 2016, pp. 1–9. doi: 10.1109/AERO.2016.7500635.

[116] D. C. Davis, S. M. Phillips, K. C. Howell, S. Vutukuri, and B. P. McCarthy, “Stationkeeping and transfer trajectory design for spacecraft in cislunar space,” in *AAS/AIAA Astrodynamics Specialist Conference*, London: Springer NAture, 2017.

[117] S. Li *et al.*, “Direct evidence of surface exposed water ice in the lunar polar regions,” *Proceedings of the National Academy of Sciences*, vol. 115, no. 36, pp. 8907–8912, Sep. 2018, doi: 10.1073/pnas.1802345115.

[118] M. L. McGuire, S. L. McCarty, and L. M. Burke, “Power and propulsion element (PPE) spacecraft reference trajectory document,” 2020.

[119] E. M. Zimovan-Spreen, D. C. Davis, and K. C. Howell, “Recovery Traejctories for Inadvertent Departures from an NRHO,” in *AAS/AIAA Spaceflight Mechanics Meeting, AAS 21-345*, NASA, 2021.

[120] D. K. Chaturvedi, *Modeling and Simulation of Systems Using MATLAB® and Simulink®*. CRC Press, 2017. doi: 10.1201/9781315218335.

[121] R. Ashino, M. Nagase, and R. Vaillancourt, “Behind and beyond the Matlab ODE suite,” *Computers & Mathematics with Applications*, vol. 40, no. 4–5, pp. 491–512, Aug. 2000, doi: 10.1016/S0898-1221(00)00175-9.

List of author’s publications

Journal papers

[1] L. Russo, D. Sanna, D. P. Madonna, M. Pontani, P. Gasbarri, “Autonomous guidance and control for rendezvous and mating with gateway with collision avoidance maneuvering”, *Acta Astronautica*, Vol. 232, Pages 678-692, 2025

[2] D. Sanna, D. P. Madonna, M. Pontani, P. Gasbarri, “Orbit Rendezvous Maneuvers in Cislunar Space via Nonlinear Hybrid Predictive Control”. *Dynamics* 2024, 4, 609-642

[3] D. P. Madonna, M. Pontani, P. Gasbarri, F. Gennari, “Stress stiffening effects in flexible Earth observation satellites with spinning appendage”, *Acta Astronautica*, Vol. 222, Pages 705-720, 2024

[4] D. P. Madonna, M. Pontani, P. Gasbarri, “Berthing proximity maneuvers and trajectory planning of a space manipulator via Kane’s formulation”, *Acta Astronautica*, Vol. 222, Pages 674-691, 2024

[5] D. P. Madonna, M. Pontani, P. Gasbarri, “Nonlinear Attitude Maneuvering of a Flexible Spacecraft for Space Debris Tracking and Collision Avoidance”, *Acta Astronautica*, Vol. 210, Pages 268-288, 2023

Conference papers

[1] D. P. Madonna, M. Carattoli, F. Angeletti, M. Pontani, P. Gasbarri, M. Sabatini, “Experimental Evaluation of Robotic Grasping Strategies for On-Orbit Servicing”, *Proceedings of the 76th International Astronautical Congress*, Paper IAC-25,C2,4,2,x96445, 2025.

[2] M. Carattoli, A. Ceccotti, D. P. Madonna, M. Pontani, M. Sabatini, P. Gasbarri, “A Geometric Approach to Near-Optimal Feedback Spacecraft Reorientation with Exclusion Cones”, *Proceedings of the 76th International Astronautical Congress*, Paper IAC-25,C1,1,2,x96513, 2025.

[3] T. Sun, D. P. Madonna, P. Gasbarri, F. Angeletti, L. Du, Z. Deng, “Dynamic Modeling and Analysis of Deployable Telescope Tubular Mast (TTM) in Spacecraft Systems Using Hybrid Coordinate and Kane's Methods”, *Proceedings of the 75th International Astronautical Congress*, Paper IAC-24,C2,2,5,x83938, 2024.

[4] D. P. Madonna, P. Gasbarri, F. Angeletti, M. Sabatini, M. Pontani, D. E. Pratesi, F. Gennari, L. Scialanga, A. Marchetti, "Modeling and Control of an Earth Observation Satellite Equipped with a Spinning Flexible Antenna", *Proceedings of the 75th International Astronautical Congress*, Paper IAC-24-C.2.4.5.x85596, 2024.

[5] D. Sanna, L. Russo, D. P. Madonna, M. Pontani, P. Gasbarri, "Constrained rendezvous and mating with Gateway using nonlinear control techniques", *Proceedings of the 75th International Astronautical Congress*, Paper IAC-24,C1,2,1,x8488, 2024.

[6] D. P. Madonna, "Simulation of post-grasping operations in closed-chain configuration using Kane's method", *Materials Research Proceedings*, Vol. 42, pp 66-71, 2024

[7] D. P. Madonna. M. Pontani, P. Gasbarri, "Attitude control and trajectory planning of a space manipulator system using Kane's formulation", *Proceedings of the 74th International Astronautical Congress*, Paper IAC-23,C1,2,2,x76301, 2023.

[8] D. P. Madonna, P. Gasbarri, M. Pontani, F. Gennari, "Non-Inertial Structural Effects in Flexible Spacecraft with Spinning Appendage", *Proceedings of the 74th International Astronautical Congres*s, Paper IAC-23,C2,2,6,x76303, 2023.

[9] D.P. Madonna, P. Gasbarri, M. Pontani, F. Gennari, L. Scialanga, A. Marchetti, "A revised and general Kane's formulation applied to very flexible multibody spacecraft*", in: Material Research Proceedings* vol. 37, September 2023, pp. 487–494. *Proceedings of the AIDAA XXVII International Congress*, Padua, 4-7 September 2023.

[10] D. P. Madonna, "Recent advances in dynamical modeling and attitude control of flexible spacecraft", *Materials Research Proceedings*, Vol. 33, pp 140-147, 2023

[11] D. P. Madonna, M. Pontani, P. Gasbarri, "Attitude maneuvers of a flexible spacecraft for space debris detection and collision avoidance", *Proceedings of the 73rd International Astronautical Congress*, Paper IAC-22,C1,2,1,x68387, 2022